



Thesis for the degree of Doctor of Philosophy

Unveiling the Nature of Dark Matter with Direct Detection Experiments

DISSERTATION BY:

Vanessa Zema

THESIS ADVISORS:

Dr. rer. nat. Karoline Schöffner

Assoc. Prof. Riccardo Catena

EXAMINER:

Prof. Gabriele Ferretti

OPPONENT:

Prof. Nicolao Fornengo

PhD program in Astroparticle Physics, XXXII cycle, Gran Sasso Science Institute
L'Aquila, Italy 2020

Department of Physics, Chalmers University of Technology
Göteborg, Sweden 2020

Contents

Acknowledgements	v
Abstract	vii
List of publications	ix
Acronymous	xiii
Introduction	1
1 Evidence for dark matter	7
1.1 Basics of modern cosmology	7
1.2 How many baryons are in the Universe? Estimation from BBN and CMB	10
1.2.1 Estimation of baryon content from BBN	11
1.2.2 Estimation of baryon content from CMB	11
1.3 Does the Universe contain non-baryonic matter?	13
1.3.1 Evidence for DM from CMB and other probes	13
1.3.2 Evidence for DM from large scale structure formation	14
1.3.3 Evidence for DM from gravitational lensing observation	15
1.3.4 Evidence for DM from the rotation curves of spiral galaxies	15
2 Selected dark matter particle models	19
2.1 QCD axion	20
2.2 Sterile neutrino	22
2.3 WIMPs	25
3 Generalities of dark matter direct detection	29
3.1 Dark matter galactic halo	30
3.1.1 Dark matter density profile	30
3.1.2 Dark matter velocity distribution	31
3.2 Two direct detection observables	33
3.2.1 Expected energy spectrum	34
3.2.2 Annual modulating event rate	34
3.3 DM-nucleus scattering cross section	35

3.4	Direct detection experiments and latest results	38
4	Dark matter direct detection effective theory: two applications	43
4.1	Non-relativistic effective theory of DM direct detection (NREFT)	43
4.1.1	NREFT application, limitations and subsequent developments	47
4.2	Annual modulation in NREFT	49
4.2.1	Theoretical Framework	50
4.2.2	Systematic study of the annual modulation signal properties in NREFT	53
4.3	Search for dark matter with polarised nuclei	59
4.3.1	Double differential DM-nucleus scattering rate	60
4.3.2	DM-nucleus effective Lagrangian	61
4.3.3	Polarised scattering amplitude	64
4.3.4	Discussion	66
5	Dark matter search with the CRESST experiment	69
5.1	CRESST-III experiment	69
5.2	Spin-dependent search in ${}^7\text{Li}$ target	72
5.2.1	Expected SD differential scattering rate off lithium	76
5.2.2	DM result with CRESST Li_2MoO_4 prototype	77
5.3	Annual modulation phenomenology in CRESST-III	80
5.3.1	Dark matter signal calculation: Cross-check with previous literature	80
5.3.2	CRESST background	81
5.3.3	Statistical theory	84
5.3.4	Methodology for p-value computation	85
5.3.5	Results on signal discovery	88
5.3.6	Results on model selection	94
6	COSINUS phenomenology	99
6.1	COSINUS scientific motivation	99
6.2	Experimental concept	100
6.3	COSINUS pulse-shape model	104
6.3.1	Original pulse shape model (PSM)	104
6.3.2	Extended Pulse-Shape Model (EPSM)	109
6.3.3	Validation of the EPSM with experimental data	114
6.4	Outlook of studies on phonon propagation in NaI	117
6.4.1	Thermal properties of crystals: Debye model	119
6.4.2	Elastic theory of lattice dynamics	120
6.4.3	Molecular Dynamics Simulations	121
6.4.4	NaI(Tl) structural properties characterisation using the XAS experimental method	130
	Conclusions	131

A	133
A.1 Strong CP-violation	133
A.2 The role of sterile neutrinos in the neutrino mass term	135
A.3 SUSY: motivations and consequences	140
B	145
B.1 Gravitational focusing: practical suggestion	145
B.2 Elastic scattering kinematics	145
C	147
C.1 NREFT DM-response functions	147
C.2 Dark matter magnetic dipole moment	148
D	151
D.1 Spin-dependent differential rate	151
D.2 Analytical derivation of the likelihood ratio	153
E	155
E.1 $^{127}\text{I}(n,\gamma)^{128}\text{I}$ process and following atomic relaxation	155
References	157

Acknowledgements

This work has been funded by the Gran Sasso Science Institute (GSSI), the Chalmers University of Technology (CHALMERS) and the National Institute of Nuclear Physics (INFN). It was hosted also by the National Laboratory of Gran Sasso (LNGS) and the University of L'Aquila.

The research presented in this thesis is the result of the close collaboration and the continuous learnings transmitted by Karoline Schäffner, Riccardo Catena, Francesco Vissani and Paolo Gorla. All of them supported this “experimental” program in between theory and experiment, in agreement between GSSI and CHALMERS, and gave me the freedom to undertake the most suitable path for myself. Thank you for your wise advices, your commitment, enthusiasm and flexibility. A special thank goes to Karoline Schäffner. Her deep knowledge and scientific rigour, combined with her strength and passion, have been a daily profound inspiration for my scientific and personal growth in these years. I can remember many occasions where your description of the great scientists who supervised you in the past coincided with my consideration of you. I particularly thank Riccardo Catena for his constant engagement and determination which made possible the realisation of this double doctoral degree program. Thank you for your welcome in CHALMERS, for sharing your wide expertises on the question of the dark matter search and for always showing your appreciation for the multidisciplinary character of this thesis. I thank Francesco Vissani, who advised me during these years as during my Master thesis and I profoundly esteem for the immense scientist he is and for his elevated scientific ethic. I thank him for being both a severe advisor and a dear friend. I am grateful to Paolo Gorla for supporting at any time my research, for his straight advices and for always prioritising the scientific development of his students over all the rest. I thank also Gabriele Ferretti for accepting to be my examiner at CHALMERS.

The work presented in the final part of this thesis was developed with Gianni Profeta and Adriano Filipponi. I am grateful to them for the insightful discussions, for their time and interest and for hosting me in L'Aquila University. Some of the articles and the results discussed in the next pages are the outcome of the collaboration with Guido Fantini, Andrea Gallo Rosso, Kåre Fridell, Florian Reindl, Michele Mancuso and

Elia Bertoldo. Besides the results presented here, I referred to Florian Reindl in many different occasions during my PhD path. I am very grateful for your constant availability, consideration and support. I will be always grateful to Martin Stahlberg for the impressive work done to validate the model described in the last chapter of this thesis, and whose results are also presented therein. I thank Stefano Di Lorenzo for realising the COSINUS detector scheme shown in the last chapter. I also thank Martin Krauss and Timon Emken: sharing the office at CHALMERS was a great opportunity for continuous exchanges and funny stories.

For the second chapter of this thesis I refer to the review made for my Master thesis, supervised by Francesco Vissani and Antonio Capone, who I thank for the teachings and advises which are of guidance today as in the past.

A crucial and pleasant aspect of my PhD has been the relation with many scientists: Giuseppe Di Carlo, who I deeply thank for his advices and frequent discussions, Matteo Agostini, Vitaly Kudryavtsev, Giovanni F. Ciani, Matthias Laubenstein, Oliviero Cremonesi, Lorenzo Pagnanini, Luca Gironi, Luciano Pandola, Vladimir Tretyak, Zurab Berezhiani, Christian Forssén, Andreas Ekström, Stefano Pirro, Franz Pröbst, Johannes Rothe, Federica Petricca, Natalia Di Marco, the members of the CRESST and COSINUS collaborations, Massimo Mannarelli, Paolo Panci, my precious colleagues and close friends of the XXXII Cycle of doctoral studies in Astroparticle Physics in GSSI: Miriam Olmi, Enrico Peretti, Stefano Di Lorenzo, Zhaoming Wang, Benedetta Belfatto, Alex Gnech, Odysse Halim, Carlo Mascaretti and Guido Fantini.

Finally, I thank my dear family, which is my biggest strength, and my friends, who are always present and supportive, despite of the distance.

Abstract

The desire of discovery is an anthropic need which characterises and connects the human being over the eras. In particular, observing the sky is an instinctive drive exerted by the curiosity of the mysteries which it retains. At the present time, the tremendous advances in the exploration of space have opened even more challenges than back in the days. One of the most urgent question is unveiling the nature of dark matter (DM). As stated by Neta A. Bahcall (Professor at Princeton University), “Cosmology has revealed an amazing universe, filled with a “dark sector” that composes 95% of the energy density of our cosmos [...]” (*Dark matter universe*, PNAS, 2015). About one-third of this dark sector is associated to an invisible and still undetected form of matter, the so-called dark matter, whose gravitational effect manifests at all cosmological scales. Both theoretical and experimental observations based on ordinary gravity reinforced the evidences for the existence of DM, since its first appearance in the pioneering calculations of F. Zwicky (1933). This PhD project explores the hypothesis that DM is made of new particles beyond the standard model. More specifically, it focuses on those DM particles which are trapped into the galactic gravitational field and populate the galactic halo. If DM interacts with ordinary particles, extremely sensitive detectors operating in very low-background environments, are expected to detect galactic DM particles scattering off their target material. This widely employed experimental technique is known as DM direct detection and it is the focus of my studies, where I consider the further hypothesis that DM interacts with atomic nuclei. The research I conducted during my PhD program consists of two main parts: the first part focused on purely phenomenology aspects of the DM direct detection (namely on the DM annual modulation treated using a non-relativistic effective theory and on the scattering of spin-1 DM particles off polarised nuclei) and the second one is more closely connected to experimental applications. The latter has been strongly stimulated by my collaboration with the two DM direct detection experiments CRESST and COSINUS. For CRESST, I compute the DM-nucleus cross-section for the conventional spin-dependent interactions, used to analyse the data collected with a prototype Li-based detector module, and I derive some prospects for a time dependent analysis of CRESST-III data, using a statistical frequentist approach based on Monte Carlo simulations. For COSINUS, I provide a significant extension of the pulse shape model currently used by CRESST and COSINUS in order to explain experimental observations related to the COSINUS detector response. Finally, I contribute to ongoing studies on the phonon propagation in NaI crystals based on solid state physics. This PhD thesis has been oriented to fill the gap between theoretical and experimental efforts in the DM field. This approach has facilitated the exchange of expertise, has driven the trend of my research and has stimulated the development of the ideas and methods described in this PhD thesis.

List of publications

This thesis is based on:

1. **Introduction to the Formalism of Neutrino Oscillation** - G. Fantini (GSSI), A. Gallo Rosso (GSSI), F. Vissani (GSSI) and V. Zema (GSSI) – *Adv. Ser. Direct. High Energy Phys.* 28 (2018) 37-119 · *e-Print: 1802.05781* [1]
2. **Direct detection of fermionic and vector dark matter with polarised targets** - R. Catena (Chalmers U. Tech.), K. Fridell (Chalmers U. Tech.), V. Zema (Chalmers U. Tech. and GSSI) – *JCAP* 11 (2018) 018 · *e-Print: 1810.01515* [2]
3. **First results on sub-GeV spin-dependent dark matter interactions with ${}^7\text{Li}$** - A.H. Abdelhameed et al. [CRESST Collaboration] – *Eur. Phys. J. C* 79 (2019) 7, 630 · *e-Print: 1902.07587* [3]
4. **First results from the CRESST-III low-mass dark matter program** - A.H. Abdelhameed et al. [CRESST Collaboration] – *Phys. Rev. D* 100 (2019) 10, 102002 · *e-Print: 1904.00498* [4]
5. **COSINUS: A NaI-based cryogenic calorimeter for direct dark matter search** - V. Zema (Chalmers U. Tech. and GSSI) for the COSINUS Collaboration – *Nuovo Cim. C* 42 (2020) 5, 228 · *Contribution to: SIF 2018, 228* [5]
6. **COSINUS: Cryogenic Calorimeters for the Direct Dark Matter Search with NaI Crystals** - G. Angloher et al. [COSINUS Collaboration] – *J. Low Temp. Phys.* (2020) [6]
7. **Studies for DM signal discovery and model selection via timing information in the CRESST experiment** - R. Catena (Chalmers U. Tech.) and V. Zema (Chalmers U. Tech. and GSSI). *In manuscript*.

Journal articles and reviewed proceedings:

8. **Limits on Dark Matter Effective Field Theory Parameters with CRESST-II** - G. Angloher et al. [CRESST Collaboration] – *Eur. Phys. J. C* 79 (2019) 1, 43 · *e-Print: 1809.03753* [7]
9. **Geant4-based electromagnetic background model for the CRESST dark matter experiment** - A.H. Abdelhameed et al. [CRESST Collaboration]– *Eur. Phys. J. C* 79 (2019) 12, 987 · *e-Print: 1908.06755* [8]
10. **Lithium-Containing Crystals for Light Dark Matter Search Experiments** - E. Bertoldo et al. [CRESST Collaboration] – *J. Low Temp. Phys.* 199 (2019) 1-2, 510-518 · *Contribution to: LTD 18, 510-518* [9]
11. **Searches for Light Dark Matter with the CRESST-III Experiment** - M. Mancuso et al. [CRESST Collaboration] – *J. Low Temp. Phys.* 199 (2020) 1-2, 547-555 · *Contribution to: LTD 18, 547-555* [10]
12. **Latest results of CRESST-III's search for sub-GeV/c² dark matter** - H. Kluck et al. [CRESST Collaboration] – *J. Phys. Conf. Ser.* 1468 (2020) 1, 012038 · *Contribution to: TAUP 2019* [11]
13. **Local lattice relaxation around Tl substitutional impurities in a NaI(Tl) scintillator crystal** - A. Filipponi (U. L'Aquila) G. Profeta (U. L'Aquila) , N. Di Marco (GSSI), V. Zema (Chalmers U. Tech. and GSSI), K. Schäffner (MPP), F. Reindl (HEPHY, TU Wien), M. Harfouche (SESAME), A. Trapananti (U. of Camerino), A. Di Cicco (U. of Camerino) – *J. Rad. Phys. and Chem.* (2020) [12]

My contribution to papers (1-7):

1. I cross-checked the calculations, wrote some parts and reviewed the manuscript.
2. I computed the cross-sections for fermionic and vector dark matter scattering off polarised nuclei and reviewed the manuscript.
3. I computed the cross-section for the spin-dependent interaction of spin-1/2 dark matter off ⁷Li, wrote the theoretical part and reviewed the manuscript.
4. I contributed to the experimental operations related to CRESST run-34 and I contributed to the results on spin-dependent dark matter interactions.
5. I wrote the manuscript. Its publication was offered as part of the Società Italiana di Fisica (SIF) award for the best communications at 104th SIF Congress.
6. I wrote the manuscript.

7. I developed part of the ideas, I did all the calculations and the plots, I wrote part of the manuscript.

Acronymous

DM	Dark Matter
DD	Direct Detection
SM	Standard Model
MOND	MOdified Newtonian Dynamics theory
NREFT	Non-Relativistic Effective Field Theory
DAMA	DARk MATter
CRESST	Cryogenic Rare Event Search with Superconducting Thermometers
SI	Spin Independent
SD	Spin Dependent
MDDM	Magnetic Dipole Dark Matter
ADM	Anapole Dark Matter
COSINUS	Cryogenic Observatory for Signatures seen in Next-generation Underground Searches
CDM	Cold Dark Matter
CMB	Cosmic Microwave Background
BBN	Big Bang Nucleosynthesis
MACHO	MAcroscopic Compact Halo Objects
PBH	Primordial Black Holes
WIMP	Weakly Interactive Massive Particle
BSM	Beyond Standard Model
QCD	Quantum ChromoDynamics

SSB	Spontaneous Symmetry Breaking
NEDM	Neutron Electric Dipole Moment
CP	Charge conjugation and Parity
PQ	Peccei and Quinn
WWPQ	Weinberg, Wilczek, Peccei and Quinn
LEP	Large Electron-Positron collider
MSM	Minimal Standard Model
HDM	Hot Dark Matter
WDM	Warm Dark Matter
SUSY	SUperSYmmetry
NFW	Navarro, Frank and White
SHM	Standard Halo Model
NR	Non-Relativistic
ChEFT	Chiral Effective Field Theories
UV	UltraViolet
EM	ElectroMagnetic
GF	Gravitational Focusing
LNGS	Laboratori Nazionali del Gran Sasso
TES	Transition Edge Sensor
LY	Light Yield
EC	Electron Capture
1D (2D)	One-dimensional (Two-dimensional)
NP	Neyman-Pearson
PL	Profile-Likelihood
MC	Monte Carlo
W-TES	Tungsten Transition Edge Sensors
SQUID	Superconducting QUantum Interference Device

PSM	Pulse-Shape-Model
EPSM	Extended Pulse-Shape-Model
NTD	Neutron Transmutation Doped
PH	Pulse Height
LAMMPS	Large scale Atomic/Molecular Massively Parallel Simulator
PDOS	Phonon Density Of States
ILM	Intrinsic Localised Modes
IGM	Intrinsic Gap localised Modes
XAFS/XRF	X-ray Absorption Fine Structure and X-Ray Fluorescence
XAS	X-ray Absorption Spectroscopy
CM	Center of Mass

Introduction

The nature of Dark Matter (DM) is one of the most fundamental open questions of modern physics and finding an answer is a main challenge for Astroparticle Physics. Astroparticle Physics is the multidisciplinary and relatively recent branch of physics which connects the physics of elementary particles to the phenomena occurring in astrophysical environment and in cosmology. It includes and combines the study of cosmic messengers (gamma-rays, cosmic-rays, neutrinos and since very few years gravitational waves (GW)) and DM, to gain insights on the mechanisms ruling the Universe. The most recent and revolutionary example of discovery in this field is the detection of GW by the LIGO¹ and VIRGO² collaborations, observed for the first time as emission product of the merging event of two multi-solar mass black holes. Similarly, other important milestones, such as the detection of ultra high energy cosmic rays, identified as of extragalactic origin (Pierre Auger Observatory³), the joint detection of GW and of the electromagnetic counterpart (Fermi Gamma-ray Space Telescope⁴, the International Gamma-Ray Astrophysics Laboratory (INTEGRAL)⁵ and others), the detection of very high-energy neutrinos followed up by gamma-ray observations (IceCube⁶, Fermi Gamma-ray Space Telescope, MAGIC⁷ and others), the less recent proof of neutrino oscillations⁸ (SNO⁹ and Super-Kamiokande¹⁰ and the discovery of the Higgs boson, are all exciting examples of the extraordinary progress made in this field of research.

Although from one side gigantic steps forward have been done, there are still fundamental questions which wait for an answer. The Standard Model of Cosmology which describes the history and evolution of the Universe, combined with available cosmological and astrophysical data, predicts, in fact, that besides the known matter content, there is an additional 95% of matter and energy content in the Universe which we ignore the nature of. These undefined components are known as Dark Matter (DM) and Dark Energy

¹<https://www.ligo.caltech.edu>

²<http://www.virgo-gw.eu>

³<https://www.auger.org>

⁴<https://fermi.gsfc.nasa.gov>

⁵<https://www.cosmos.esa.int/web/integral/mission-overview>

⁶<https://icecube.wisc.edu>

⁷<https://magic.mpp.mpg.de>

⁸See [1] for an introduction on neutrino oscillations.

⁹<https://falcon.phy.queensu.ca/SNO/>

¹⁰<http://www-sk.icrr.u-tokyo.ac.jp/sk/index-e.html>

(DE). Some of the most precise and insightful cosmological data, which play a key role in the identification of DM and DE, are provided by the Planck mission¹¹ and the Atacama Cosmology Telescope¹², which, similarly to the previous NASA Explorer mission WMAP¹³, are designed to measure the temperature and polarisation anisotropies of the Cosmic Microwave Background Radiation. These data, combined with complementary measurements on large and small cosmological scales, allow to establish the contributions of the DM and DE to the total energy content of the Universe. The evidence for DM is also suggested by gravitational anomalies on astrophysical scales. For example, the mass content of galaxies and clusters of galaxies, as inferred by the velocity dispersion of the system, points towards the discrepancy between the luminous mass and the inferred mass in these astrophysical objects (see Chap. 1 for an overview on DM evidence).

The clues for the existence of DM have been found by applying the known laws of gravity. An open and hot question is whether the aforementioned gravitational anomalies are evidence for the failure of General Relativity and Newtonian laws in specific regimes, whose application to data would mimic the presence of an additional non-luminous component of matter, dark matter. While at galactic scales successful proposals have been advanced, such as the MODified Newtonian Dynamics theory (MOND) [13], a gravity theory which satisfies the observational requirements at all scales is still missing. However, any future discoveries in this context has the potential to revolutionise our comprehension of nature.

This PhD thesis explores the hypothesis that a large part of the matter content of the Universe is made from DM. More specifically, it assumes that DM is made of new particles beyond the Standard Model (SM) which so far escaped detection. The connection between the “DM problem” and particle physics, is strongly motivated by the hints for new physics encrypted in the SM. This new physics involves hypothetical particles which have not been postulated to solve the DM problem, but which have the properties to be the “DM particle”. For example, axions are the product of the Peccei-Quinn solution to the strong CP problem, sterile neutrinos are required by the see-saw mechanism proposed to explain the nature of neutrino mass, neutralino is a prediction of Supersymmetry, the theory proposed to solve the hierarchy (or naturalness) problem related to the radiative corrections to the Higgs mass (more details can be found in Chap. 2). Other models were proposed in the years, such as asymmetric DM, self-interacting massive particles, strongly-interacting massive particles, mirror DM, WIMPZILLAs and many others. The final competition among this plethora of models will be played on the experimental field.

The experimental effort dedicated to the DM particle search is tremendous. There are three classes of complementary DM detection techniques, known as DM direct detection, indirect detection and production at colliders. The DM indirect detection consists in the search for DM signatures in the SM particle fluxes (gamma-rays, cosmic-rays and neutrinos) arriving on Earth from astrophysical sources. If DM self-annihilates into

¹¹<https://www.cosmos.esa.int/web/planck>

¹²<https://act.princeton.edu>

¹³<https://map.gsfc.nasa.gov>

SM particles in high density environments, it produces visible lines or bumps in the energy spectrum of gamma-rays (detected *e.g.* by Fermi-LAT⁴, DAMPE¹⁴, MAGIC⁷, H.E.S.S.¹⁵ and VERITAS¹⁶), cosmic rays (electron-positron flux observed *e.g.* by Fermi-CREs⁴, AMS-02¹⁷ and DAMPE¹⁴ and hadronic flux *e.g.* by AMS-02¹⁷ and DAMPE¹⁴), and neutrino fluxes (measured *e.g.* by IceCube⁶, ANTARES¹⁸ and KM3NET¹⁹). The other DM detection technique is the DM production at colliders, among which the most renowned is obviously the Large Hadron Collider (LHC). In this case, the detection principle consists in the measurement of the missing transverse energy in the final state of proton-proton collisions. The results of DM production at colliders, together with the ones obtained by DM indirect detection experiments, can be translated into and compared with the results of the DM direct detection technique, which is the experimental approach this thesis focuses on.

DM direct detection (DD) consists in the observation of a DM signature left *directly* inside a target material. While for the DD of light axions, new kind of detectors are required to measure the coherent effects of the axion field²⁰, the direct search for galactic DM particles in the keV-TeV mass range can be performed using ordinary particle detectors located deep underground to obtain a natural shielding from cosmic radiation, mainly from muons. Under the assumption that DM particles are on average at rest in the galaxy, which is supported by N-body simulations and recent Gaia satellite²¹ data, the Solar System rotational velocity combined with the Earth proper motion is expected to induce time dependent DM-nucleus (for MeV-TeV DM mass range) and/or DM-electron (for keV-MeV DM mass range) scatterings inside the detector. The amount of energy released in the scattering process depends on the DM mass and the type of target. Both elastic (equal initial and final states) and inelastic (different initial and final states) scatterings can occur, therefore collected data can be analysed using both interpretations. Comparing DD experiments with theoretical predictions, a key aspect is the assumption on the type of DM-SM particle interaction, as very poor information can be extrapolated from the DM gravitational effects observed.

One of the goals of this thesis is to characterise the time dependence of the expected DM signal at DD experiments using a general theoretical framework known as *non-relativistic effective theory* (NREFT) of DM DD [14, 15] (manuscript in preparation). The motion of the Earth around the Sun is expected to cause a periodic annual variation in the DM count rate [16–18], whose properties (*e.g.* amplitude of modulation, time of maximal and minimal rate, amplitude of higher order harmonics) are shown to be a function of the DM galactic velocity distribution [19, 20] and the DM-nucleon interac-

¹⁴<http://dpnc.unige.ch/dampe/>

¹⁵<https://www.mpi-hd.mpg.de/hfm/HESS/>

¹⁶<https://veritas.sao.arizona.edu><https://veritas.sao.arizona.edu>

¹⁷<https://ams02.space>

¹⁸<https://antares.in2p3.fr>

¹⁹<https://www.km3net.org>

²⁰<https://indico.cern.ch/event/610112/contributions/2570059/attachments/1456873/2248556/Pheno.pdf>

²¹<https://sci.esa.int/web/gaia>

tions [21, 22]. The discussion is fervid as the DAMA/LIBRA collaboration has been detecting for more than 20 annual cycles a signal compatible with the DM-signature interpretation [23–25], while no DM signatures are present in the large part of DM DD experiments (*e.g.* [26–33]). The study presented in Sec. 4.2 contributes to this discussion: including the effect known as gravitational focusing [18, 34], it shows how the phase of the annual modulation can be used to classify possible DM-nucleon interactions parametrised within NREFT and it highlights the potential of low threshold experiments to extract information from this classification. The close collaboration with the CRESST experiment²² strengthened this study and results are presented for and extended to targets of interest for CRESST.

A second question addressed in this thesis deals with the scattering of DM particles off polarised nuclei and the possibility to extract information on the DM nature from the observation of this process [2]. Previous studies on the search for spin-1/2 DM particles using polarised targets [35], have been extended to spin-1 DM particles (see Sec. 4.3). The cross-section for this scattering is provided and the comparison of the results predicted for the two cases, spin-1/2 and spin-1, are shown to underline how the value of the DM spin can be extrapolated from the differential count rate using the nuclear-recoil directionality and energy distribution or just their energy spectrum. The results are presented as a function of the purely polarisation dependent part of the nuclear recoil spectrum (the ‘spin modulation’ obtained as the difference of the count rate collected inverting the nucleus polarisation direction). They show that in specific regions of the parameter space different nuclear recoil maps for the two cases (fermion and vector DM) are expected. Furthermore, it is found that the two scenarios exhibit different behaviours also in the one dimensional energy spectrum. Although these findings are intriguing, two points are stressed here: 1) very large exposures of the order of the DAMA/LIBRA experiment are necessary to distinguish the total energy spectrum from the spin modulation energy spectrum [35] and 2) these results are derived in the approximation of ideal detectors. In order to apply this formalism to realistic cases, estimations including experimental parameters (*e.g.* detector efficiency, energy resolutions and background rate) are necessary.

The leading motivation of this PhD project is the strong belief that a close and daily synergy between theoretical and experimental studies is not only beneficial, but inevitable to boost the DM search. Leveraging on this motivation, Chap. 5 and Chap. 6 present the projects inspired by the collaboration with the CRESST²² and COSINUS experiment²³.

CRESST is a cryogenic scintillating calorimeter working at milli-Kelvin temperature and employing transition edge sensors. It is designed to provide a double channel readout of the scattering particle energy release converted in heat and light, used to discriminate between nuclear recoils (signal) and β/γ events (background). The R&D is a crucial aspect of the CRESST collaboration, as new materials and techniques are constantly tested to improve the CRESST performance. As outcome of one of these investigations,

²²<https://www.cresst.de>

²³<http://cosinus.lngs.infn.it>

new results on the conventional spin-dependent (SD) DM-nucleon interactions are derived using the amount of ${}^7\text{Li}$ contained in 2.66 g of a Li_2MoO_4 crystal [3]. In this work the potential of Li-based target materials for the DM search is described and shown in terms of a sensitivity limit in the SD-DM-nucleon cross-section versus DM particle mass parameter space. This was the first SD-result provided by the CRESST collaboration and it inspired the calculation of a new SD limit using CRESST-III data collected by the best performing module, detector A, using the percentage of ${}^{17}\text{O}$ in CaWO_4 [4]. These and following studies beyond this PhD project, motivated the employment of Li-based targets for DM search, which are currently mounted in the CRESST-III cryostat.

A further project related to CRESST is based on last CRESST-III data release [4], where an energy spectrum showing an excess of events below 200 eV with exponential shape was present (manuscript in preparation). As stressed in the CRESST-III publication, at this energy the discrimination power between nuclear recoils and β/γ events vanishes, therefore the events populating the excess cannot be associated to a specific event class. The same phenomenology is present in all CRESST-III detectors with thresholds below 100 eV; since the shape of the energy spectrum of the excess is different from one detector to another, a single common explanation of this observation is hard to believe and further investigations on possible not yet identified detector physics are ongoing. Stimulated by these findings and by the study on the annual modulation phenomenology presented in Sec. 4.2, a statistical analysis aiming at determining the signal discrimination power associated with a time dependent analysis in CRESST-like detectors limited by an exponential background rate, was performed. The final goal was to establish if a 2-dimensional (2D) analysis in time and energy would be preferable to the 1D energy analysis in case only the phonon-channel read-out is available (the light yield is poor at low energies, that is why the discrimination power between nuclear recoils and β/γ events vanishes at low energies). The energy spectrum of CRESST-III is used as reference for the background model, rescaled as a function of the exposure considered. In addition, the opportunity to perform model selection in low threshold experiments is investigated, comparing the standard spin-independent interaction model with the magnetic dipole DM model. In all the configurations considered, the 1D and 2D analysis show similar results, a conclusion which tends to discourage the effort of an annual modulation search using current CRESST-III setup.

The final part of this PhD project was mostly dedicated to study the phenomenology of the COSINUS DD experiment [5, 6]. COSINUS²³ is a cryogenic scintillating calorimeter based on NaI target crystals operated at milli-Kelvin temperature, whose research goal is to provide a cross-check of the DAMA/LIBRA claim of DM detection. It is the first experiment which successfully operated NaI crystals as cryogenic calorimeters and the potential double read-out of light and phonons can provide insightful information on the nature of the signal detected by DAMA/LIBRA. To achieve this goal, the COSINUS detector characterisation is a key aspect and in this thesis a relevant contribution is given to explain COSINUS experimental findings related to the detector working principle. In particular, a considerable extension to the original model for cryogenic particle detectors published in 1995 by Pröbst et al. [36] is derived to describe the pulse shape

produced by particles interacting inside the COSINUS target material, which naturally provides the empirical terms added in [37] to fit the original model to data. Using this extended model, a new method for the energy reconstruction is proposed, which can be used to perform particle identification, that is to distinguish nuclear recoils from β/γ events. Such discrimination is, in fact, challenging when the original model and standard data analysis (similar as CRESST) are applied to COSINUS data.

In connection with the peculiar pulse shape observed in COSINUS data, a new study which aims at characterising COSINUS detectors using solid state physics started within this PhD thesis. This investigation benefit from a collaboration with the solid state group of L’Aquila University, who also joint the COSINUS collaboration. First studies based on solid state simulations of the NaI lattice are presented at the end of Chap. 6: the NaI phonon density of states simulated using molecular dynamics methods is compared with the one available in literature [38] and found in good agreement and the attempts to simulate the excitations, known as ‘breathers’ [39], are discussed. This new COSINUS research frontier which interfaces particle and solid state physics is very promising as it opens the way to a deeper understanding of individual processes involved in scattering events and therefore to a more precise description of the detector physics involved. It is worth noting that very recently this ‘contamination’ of expertises has become quite frequent and prolific, see *e.g.* [40–42].

The long-standing tension between DAMA/LIBRA results and the other DM DD experiments is an urgent problem which COSINUS, together with the other NaI-based experiments (*e.g.* [26, 27, 43]), will very likely within the next three years give a conclusive explanation to. In the meanwhile, new ideas and projects for DM DD are emerging both from theoretical and experimental sides, which aim at exploring the low-mass DM parameter space, whose large part is still uncovered. These new projects are based on DM-electron scattering (see *e.g.* SENSEI²⁴), on new insights from solid state physics [40, 44] or on other types of technologies suited for very light DM particles [45]. The region of SI DM-nucleus cross-sections between the current experimental upper limits for a DM mass larger than about 5 GeV and the expected neutrino floor²⁵ will be spanned by next generation of very large exposure experiments, *e.g.* XENONnT²⁶, PandaX-4T²⁷, LZ²⁸, DarkSide-20k [48] and DARWIN²⁹, while the sensitivity to regions dominated by the neutrino-induced background may be extended using directionality techniques, employed *e.g.* by NEWSdm³⁰, MIMAC [49], DRIFT [50] and the CYGNUS project [51]. Although has proved to be an intricate challenge, if DM particles are out there and interact with ordinary matter not only gravitationally, the “tentacular” strategy of the scientific community will allow to catch them, sooner or later.

²⁴<https://sensei-skipper.github.io/#>

²⁵The neutrino floor is the barrier in the DM parameter space below which DM DD experiments are limited by the background due to the coherent solar neutrino-nucleus scattering event rate [46, 47].

²⁶<https://science.purdue.edu/xenon1t/?tag=xenonnT>

²⁷<https://pandax.sjtu.edu.cn/pandax4>

²⁸<https://lz.lbl.gov>

²⁹<https://darwin.physik.uzh.ch>

³⁰<https://news-dm.lngs.infn.it>

Chapter 1

Evidence for dark matter

In this chapter the evidences which support the hypothesis of the existence of Dark Matter (DM) are described. The two cosmological periods known as the *Big Bang Nucleosynthesis (BBN)-era* and the *recombination-era* play a fundamental role in this description: the former is the time of formation of the light nuclei, which starts at around 1 second after the Big Bang at a temperature $T \sim 1$ MeV; the latter corresponds to the time of matter-radiation decoupling, which is the condition for the formation of neutral hydrogen and occurred when the Universe was about 370,000 years-old. After recombination the Universe becomes transparent to radiation, and photons can freely travel through space. Such photons are the cosmic electromagnetic background that we observed today, also known as the Cosmic Microwave Background Radiation (CMBR or, more commonly, CMB).

This chapter is organised as follows. In Sec 1.1 basics of modern cosmology are introduced, in Sec. 1.2 the current knowledge on the abundance of ordinary (or baryonic) matter in the Universe is reviewed, focusing on BBN and CMB observations. Section 1.3 explains why astronomical and cosmological observations point towards the existence of non-luminous and non baryonic matter in the Cosmos. This cosmological component is known as DM. Furthermore it is explained qualitatively how the physics of the evolution of primordial density fluctuations provides information on DM-properties and examples of anomalous observations at the scales of galaxy-clusters and galaxies, which stimulated the DM-search, are shown. In the various sections, the SM of particle physics and the SM of cosmology are the models implied and the consequences of these assumptions are discussed.

1.1 Basics of modern cosmology

Before moving to the evidences for DM, three concepts are briefly introduced: (i) the equation of state of the early Universe and the Friedmann equation (ii) the angular power spectrum, that is the observable related to CMB and (iii) the Λ CDM-model.

Equation of state and Friedmann equation. The SM of cosmology is based on the Friedmann-Lemaître-Robertson-Walker metric, which is built on the Cosmological Principle of a homogeneous and isotropic Universe [52]. The observation that the Universe is expanding and the assumption that its energy content can be treated as a set of perfect fluids, lead to the *Friedmann equation* [52, 53],

$$1 + \left(\frac{k}{aH} \right)^2 = \sum_i \Omega_i \quad (1.1)$$

where k can be $+1$, 0 or -1 for spaces of constant positive, zero, or negative spatial curvatures, respectively, $a(t)$ is the scale factor which multiplies the spatial part of the metric, $H = \frac{\dot{a}}{a}$ is the Hubble parameter and $\sum_i \Omega_i$ is the total energy density parameter. Ω_i is defined as the ratio between the energy density at time t of the i -cosmological fluid ρ_i , and the critical density, ρ_c , which is [54],

$$\rho_c = \frac{3H_0^2}{8\pi G_N} = 1.87834(4) \cdot 10^{-29} h^2 \text{ g cm}^{-3} \quad (1.2)$$

where

$$h = H_0 / (100 \text{ km s}^{-1} \text{ Mpc}^{-1}) = 0.674(5) \quad (1.3)$$

is the dimensionless Hubble parameter [55]¹, H_0 is the Hubble parameter today and $G_N = 6.67430(15) \cdot 10^{-11} \text{ m}^3 \text{ kg}^{-1} \text{ s}^{-2}$ is the gravitational constant [54]. Each cosmological fluid is characterised by an equation of state,

$$P_i = \omega_i \rho_i \quad (1.4)$$

where P_i is the pressure of the i -fluid, ρ_i is the corresponding energy density and $\omega_i = (\gamma_i - 1)$, where γ_i is the *polytropic index* [53]. For example, $\omega = 0$ corresponds to a matter fluid, while $\omega = 1/3$ to radiation.

CMB angular power spectrum. The CMB is a fundamental source of information about the physics of the Universe at recombination and a powerful tool for cosmological parameter estimation [54, 55]. CMB experiments, such as Planck and the Atacama Cosmology Telescope, measure the temperature fluctuations in the microwave background radiation. The angular autocorrelation-function of the CMB-temperature-fluctuations averaged over all the directions \mathbf{n}_1 and \mathbf{n}_2 , such that $\mathbf{n}_1 \cdot \mathbf{n}_2 = \cos \theta$, is defined as²,

$$D^{TT}(\theta) = \left\langle \frac{\delta T}{T}(n_1) \frac{\delta T}{T}(n_2) \right\rangle \equiv \frac{1}{4\pi} \sum_{\ell=2}^{\infty} (2\ell + 1) D_{\ell}^{TT} P_{\ell}(\cos \theta) \quad (1.5)$$

In the right hand side, ℓ is the index of multipole expansion, P_{ℓ} are Legendre polynomials and D_{ℓ} are multipole moments, which depend on the gravitational potential of scalar

¹Currently, there is some inconsistency between distance-ladder and CMB estimates of H_0 , for a discussion see Sec. 24 of [54].

²From here on, we will simply say ‘CMB-angular-power-spectrum’.

metric perturbations, Φ , and on the fluctuations of the radiation-energy-density, δ_γ [56]. Theoretical expectation and experimental data for the multipole moments $(2\ell + 1) D_\ell^{TT}$ are shown in Fig. 1.1.1. Low- ℓ values correspond to large angular scales, while large- ℓ values to small angular scales. The shape of the CMB-angular-power-spectrum depends on the cosmological parameters. The peaks, the most prominent at $\ell \simeq 200$, are the imprint of the baryon-photon-plasma-oscillations before recombination. They are usually defined as acoustic peaks and their properties are crucial for parameter estimation, as discussed in Secs. 1.2.2 and 1.3.1.

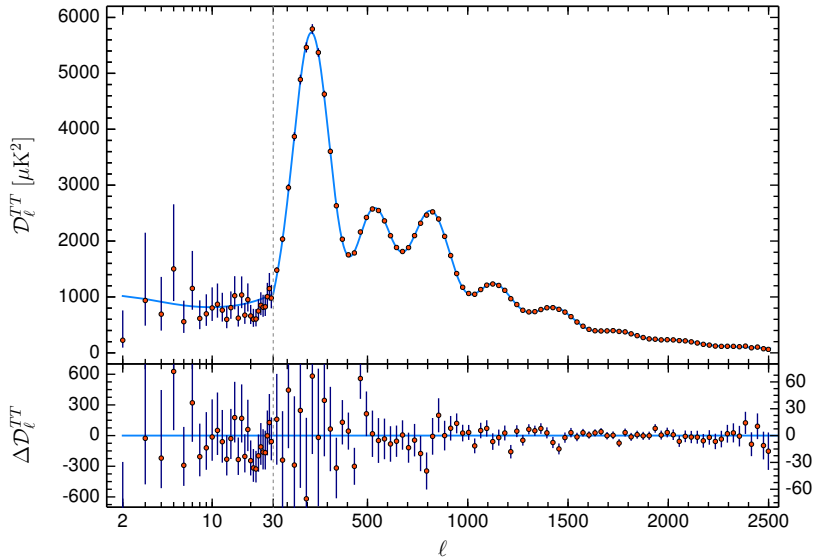


Figure 1.1.1: Multipole moments of the autocorrelation-function of CMB-temperature-fluctuations (Planck Collaboration [55]).

Λ CDM-model. The SM of cosmology is also defined as ‘base Λ CDM-model’ [55]. It is a spatially-flat 6-parameter model which includes the cosmological constant Λ and Cold Dark Matter (CDM). The cosmological constant is a contribution to the right hand side of Einstein equations, which provides a negative pressure component to the energy density ($\omega = -1$ in Eq. 1.4 [55]), known as *dark energy*, introduced to explain the acceleration of the Universe [53]³. CDM is a self-gravitating collisionless fluid decoupled from radiation both before and after recombination and characterised by $w = 0$, with a very small velocity dispersion [58]⁴. The six parameters of the base Λ CDM-model are: the Hubble parameter, H_0 , the matter parameter density, Ω_m , the baryonic density

³The nature of the cosmological constant is one of the main open issue in the SM [57].

⁴DM is cold if it decouples from thermal equilibrium when it is not relativistic (*e.g.* WIMPs, Sec. 2.3), or if it was never in thermal equilibrium (*e.g.* axions, Sec. 2.1).

parameter⁵, Ω_b , the CDM density parameter, Ω_c , the scalar spectral index⁶, n_s , and the optical depth⁷, τ [55].

The sum on the right-hand-side of Eq. 1.1 is made over the different contributions to the total energy density parameter, some of them are free parameters of the Λ CDM-model,

$$\Omega = \Omega_m + \Omega_\Lambda + \Omega_{rad} + \Omega_\nu \quad (1.6)$$

where Ω_Λ , Ω_{rad} and Ω_ν are the Λ , radiation and SM-neutrinos contributions, respectively, and $\Omega_m = \Omega_b + \Omega_c$. The value of the total energy density parameter is fixed once the parameter k related to the spatial curvature of the Universe in Eq. 1.1 is also fixed and in the Λ CDM model $k = 0$ ⁸. By solving the *continuity equation* [53],

$$\dot{\rho} + 3(\rho + P)\frac{\dot{a}}{a} = 0 \quad (1.7)$$

where P is defined in Eq. 1.4, the functional relation between the energy density, ρ (or equivalently the density parameter, Ω), and the scale parameter, a , can be derived. It is equal to $\rho = a^{-3\gamma}$, where $\gamma = 1, 4/3$ and 0 for matter, radiation and cosmological constant components, respectively. Ω_ν is defined in Eq. 1.17 and depends on the neutrino mass.

The presence of the different components in the total density parameter in Eq. 1.6 is suggested by theory and observations. Based on Eq. 1.6 only, these parameters are degenerate, *i.e.* an increase in one of them can be compensated by a decrease in another parameter. The question of how this degeneracy can be broken is qualitatively addressed in this chapter.

1.2 How many baryons are in the Universe? Estimation from BBN and CMB

In this section the motivations which support the hypothesis of the existence of *non-baryonic* DM are discussed. The discussion is divided in two parts: theoretical predictions and experimental observations for the formation of the lightest nuclei in the BBN-era are presented in Sec. 1.2.1 and the independent extrapolation of the number of baryons at the era of recombination by using information encoded in CMB is addressed in Sec. 1.2.2.

⁵In this context, nucleons (protons and neutrons) are called baryons, and ordinary matter is named baryonic-matter.

⁶The scalar spectral index describes how the density perturbations depend on the spatial scale.

⁷The optical depth is the mean free path for photon scattering, integrated from a certain time to the present-day.

⁸The term $\left(\frac{k}{aH}\right)^2$ in the left hand side of Eq. 1.1 can be incorporated into the right hand side as $\Omega_k = \left(\frac{k}{aH}\right)^2$, which is null in the Λ CDM model ($k = 0$).

1.2.1 Estimation of baryon content from BBN

The cosmological era of nucleosynthesis, predicted by G. Gamov and his collaborators [59–61] and subsequently developed by many others (*e.g.* [62–64]), is considered a powerful probe of SM physics [65] as theoretical predictions for the primordial abundances of light elements only depend on the baryon to photon density and accurate observations for some of these abundances are available (see *Sec. 23* of [54]).

Analytical expressions, provided *e.g.* in [56] and [65], show that primordial abundances of light elements, D, T, ${}^4\text{He}$, ${}^3\text{He}$, ${}^7\text{Li}$, are just function of the baryon-to-photon-density-ratio, η_{10} ,⁹,

$$\eta_{10} = 10^{10} \cdot \frac{n_b}{n_\gamma} \quad (1.8)$$

Measurements of the abundances of light elements provide estimations of η_{10} , which, in turn can be used to constrain the baryon-density-parameter, $\Omega_b = \rho_b/\rho_c$, where ρ_b is the mass density of baryons and the critical density, ρ_c , is defined in Eq. 1.2. In fact, there is a simple relation between η_{10} and Ω_b [65],

$$\eta_{10} = 10^{10} \frac{\rho_c}{\langle m \rangle n_\gamma^0} \Omega_b \quad (1.9)$$

where $\langle m \rangle$ is the mean mass per baryon (roughly the proton mass) and n_γ^0 is the number density of photons today. Theoretical predictions of the light element abundances as function of η_{10} for $N_\nu = 3$ are shown in Fig. 1.2.1 (solid lines), taken from Particle Data Group, 2019 [54]. The bands along the solid lines are theoretical uncertainties on the abundances due to uncertainties on the neutron lifetime. Yellow boxes indicate experimental observations¹⁰. Note that there is a yellow box also on top of the prediction of the Deuterium abundance. The two purple vertical lines mark the overlap between the experimental values of the abundance ratios ${}^4\text{He}/\text{H}$ and D/H . The correspondent range of values for η_{10} is [54],

$$5.8 \leq \eta_{10} \leq 6.5 \text{ (95\%CL)} \quad (1.10)$$

which implies the Ω_b -estimation,

$$0.021 \leq \Omega_b h^2 \leq 0.024 \text{ (95\%CL)} \quad (1.11)$$

The inconsistency between ${}^7\text{Li}/\text{H}$ abundance with the other observations is known as the *lithium problem*. It is an open question and its answer could be related to systematic errors in the measured abundances, astrophysical or nuclear uncertainties, or it could be the hint for physics beyond the SM [54, 65].

1.2.2 Estimation of baryon content from CMB

The baryon content can be estimated independently from BBN-theory and observations by fitting the ΛCDM model to the peaks of the CMB-angular-power-spectrum. Table 2

⁹It depends also on the number of light neutrinos N_ν , but within the SM it is fixed to three.

¹⁰For references about observational results see [54].

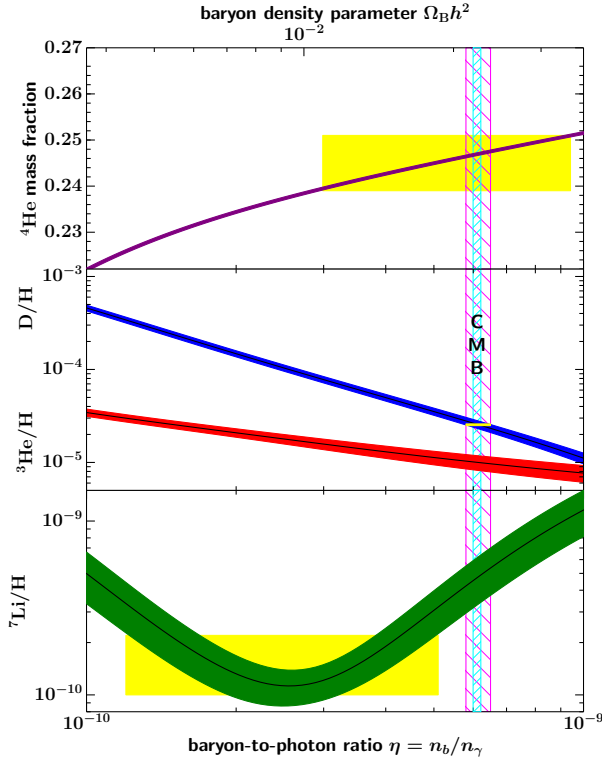


Figure 1.2.1: Theoretical prediction and experimental constraints on light element abundances as function of the baryon-to-photon ratio η_{10} [54]. Solid lines are theoretical predictions based on standard BBN. Bands along the solid lines show 95% CL on theoretical predictions due to uncertainties on neutron-life-time. Yellow boxes indicate experimental observations. Note that there is a yellow box also on top of the prediction of Deuterium abundance, between the two purple vertical lines. Shaded region confined by vertical purple lines indicates the region of D+ ^4He overlap. Cyan shaded region shows the estimation of η_{10} from CMB-data.

of [55] shows the result based on *Planck* TT , TE , $EE + lowE$ ¹¹ (6-column), which is,

$$\Omega_b h^2 = 0.02237 \pm 0.00015 \quad (1.12)$$

The result in Eq. 1.12 still depends on BBN because it is obtained by fixing the parameter related to ^4He -abundance. If the ^4He -abundance is left as free parameter, the *Planck* TT , TE , $EE + lowE$ estimation is (Tab. 5 of [55]),

$$\Omega_b h^2 = 0.02230 \pm 0.00020 \quad (1.13)$$

The two values for Ω_b in Eqs. 1.12 and 1.13 are used to identify the region of values of η_{10} compatible with CMB [54], which is shown within the two light blue vertical lines in Fig. 1.2.1. Although the era of recombination occurs thousands of years after the era of BBN, the abundance of baryons does not change during this period, therefore the baryon-to-photon ratio estimated at the era of recombination is expected to be numerically the same as during the BBN-era, according to ΛCDM model (Sec. 23 of [54]). The agreement between the value of η_{10} estimated by using CMB and BBN-data is considered a success of the SM of cosmology.

¹¹The labels TT , TE and EE refer to angular correlation-functions at large angular scales between: temperature-fluctuations, $D^{TT}(\theta) = \langle \frac{\delta T}{T}(n_1) \frac{\delta T}{T}(n_2) \rangle$, temperature-fluctuations and electric-field, $D^{TE}(\theta) = \langle \frac{\delta T}{T}(n_1) E(n_2) \rangle$, and electric-fields, $D^{EE}(\theta) = \langle E(n_1) E(n_2) \rangle$; *lowE* refers to EE at small angular scales. For more details about *Planck*-notation, see Sec. 2.2.4 of [55].

1.3 Does the Universe contain non-baryonic matter?

1.3.1 Evidence for DM from CMB and other probes

It is natural to wonder how to establish if $\Omega_m > \Omega_b$, which is crucial to admit the existence of non-baryonic matter. Historically, the existence of a non-baryonic component of matter was suggested by studies on large scale structure formation and gravitational lensing, considerations which inspired the idea of treating Ω_m and Ω_b as independent parameters. But, how can the contribution of these two parameters in Eq. 1.6 be disentangled? According to [56], the degeneracy between the baryon and the total-matter content is broken by fitting the Λ CDM model to the peaks of the CMB-angular-power-spectrum, which is shown in Fig. 1.1.1. In fact, in [56] V. Mukhanov derives analytical formula which show that $\Omega_m h^2$ and $\Omega_b h^2$ can be independently estimated by fitting the heights of the first ($\ell \simeq 200$) and second peak of the CMB-angular power spectrum, although a dependence on the Hubble parameter remains. In Sec. 24 of [54] (*Cosmological parameters*), O. Lahav and A.R. Liddle confirm that the relative heights of the peaks of the angular power spectrum allow the determination of $\Omega_b h^2$. They underline the strong degeneracy between the determination of the Hubble parameter H_0 and other parameters - *e.g.* $\Omega_m h^2$ and the neutrino mass - as discussed in the Planck paper [55]. This means that Ω_m can be uniquely determined only if CMB-data are combined with independent measurements of H_0 , which are available and provide similar result as *Planck*¹².

From the information given above, we conclude that the degeneracy between the baryon and the total matter content of the Universe can be broken by the combination of CMB-data with independent measurements of H_0 , which are discussed for example in [54]. The values of the cold-matter-density-parameter $\Omega_m h^2$ and the DM density parameter $\Omega_c h^2$ taken from [55] (Tab. 2, column 5) are,

$$\begin{aligned}\Omega_m h^2 &= 0.1430 \pm 0.0011 \\ \Omega_c h^2 &= 0.1200 \pm 0.0012\end{aligned}\tag{1.14}$$

which combined with Eq. 1.13 satisfy the relation,

$$\Omega_m h^2 = \Omega_b h^2 + \Omega_c h^2\tag{1.15}$$

Based on these results, derived within the SM of particles and of cosmology, one concludes that there is non-baryonic matter in the Universe and it constitutes about the 86% of the total matter content.

According to the literature mentioned in the previous section [54, 56], the first and second acoustic peaks of the CMB-angular-power-spectrum, combined with independent measurements of the Hubble parameter, provide an estimation of $\Omega_m h^2$ and $\Omega_b h^2$. If this information is combined with the location of the first peak of the CMB-angular power

¹²As already suggested before, for what concerns the ‘ H_0 -tension’ debate see Sec. 24 of Ref. [54].

spectrum, the parameter k in Eq. 1.1 can be estimated - the observations are consistent with a spatially-flat-Universe [54].

The photon-density-parameter is measured directly from CMB-data and it is (Sec. 24 of [54]),

$$\Omega_{rad} \simeq 2.47 \cdot 10^{-5} h^{-2} \quad (1.16)$$

The neutrino-density-parameter is (Sec. 25 of [54]),

$$\Omega_{\nu} = \frac{\sum_i m_{\nu_i}}{93.14 \text{eV}} \quad (1.17)$$

where $\sum_i m_{\nu_i}$ is the sum over the neutrino masses. The estimation of $\sum_i m_{\nu_i}$ from cosmological probes is rather complicated, as discussed in Sec. 7.5 of [55]. Among the plethora of different estimations given in [55], we show the conservative result based on *Planck TT, TE, EE + lowE*, which is,

$$\begin{aligned} \sum_i m_{\nu_i} &< 0.26 \text{ eV} \\ \Omega_{\nu} h^2 &\lesssim 0.0279 \end{aligned} \quad (1.18)$$

Since $\Omega_{\nu} h^2 \ll \Omega_c h^2$, neutrinos clearly cannot explain DM. Although neutrino and dark-energy density parameters depend on each other, combing results from independent observations - *e.g.* from high-redshift supernovae and galaxy cluster surveys [66] - allow to break the remaining degeneracy between Ω_m and Ω_{Λ} [55].

1.3.2 Evidence for DM from large scale structure formation

The structures we observe in the Universe (galaxies, galaxy clusters, etc...) are the final result of initial density perturbations imprinted by inflation in the early Universe and evolved into gravitational instabilities [56, 67]. By solving the differential equations which describe the evolution of density perturbations, one can predict how they grow as a function of time and it is found that, in order to reproduce observations, the matter density perturbations must start growing before the recombination era [68]. However, the tight coupling between baryonic matter and radiation counterbalances gravity and density perturbations cannot grow in baryonic matter before recombination. As a result, a non-baryonic component of matter with negligible interactions with radiation (dark matter) is required.

The evidence for non-baryonic DM based on the theory of large scale cosmological structure formation, is quantitatively confirmed by N-body simulations. The well-known representation of the DM *cosmic web*, shown for example in Fig. 1.3.1, left panel, is the result of N-body simulations, which follow the evolution of the structure formation starting from random initial conditions, sampled from CMB data. The statistical agreement between large-number-galaxy-system-observation and their N-body simulations, for example the one shown in Fig. 1.3.1, right panel, is considered a success of the Λ CDM-model and promoted N-body simulations as a powerful tool to predict the characteristics of the matter-power-spectrum as a function of different scales and DM particle models [71].

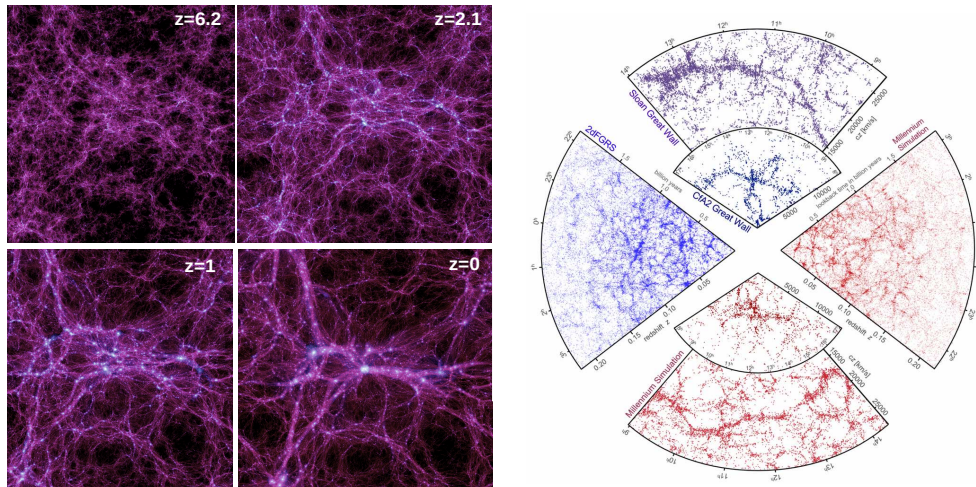


Figure 1.3.1: N-body Millennium-II simulations. **Left:** DM cosmic web for four different redshifts [69]. **Right:** comparison between observations and simulations of system of galaxies [70].

1.3.3 Evidence for DM from gravitational lensing observation

Gravitational lensing is the distortion of light passing through the space-time curved by a gravitational field. It is a prediction of general relativity and it is a pure gravitational effect. For this reason, it provides one of the strongest evidence for the presence of DM, an invisible and non-baryonic component of mass in the Universe [72, 73]. The gravitational lensing of the light emitted by sources which are nearby a strong gravitational field can be quantified and converted into a measure of the mass content of the system. The comparison of the mass content with the distribution of the electromagnetic emissions can reveal the presence of non-luminous matter, such as the common examples of the ‘Bullet Cluster’ 1E0657-56 or the ‘Baby bullet’ MACSJ0025.4-1222, shown in Fig. 1.3.2. In this figures, the pink and blue shadows trace the peaks of the X-ray emission and mass-content distributions, respectively. The blue shadow overlaps with the region were galaxies are located, which means that most of the matter in the cluster - which is dark - is not interacting, like galaxies. In the assumption that DM is made of particles, upper limits on the cross-section for the interactions of DM particles with ordinary matter can be derived on the basis of these observations (see *e.g.* Sec. 4 of [74]).

1.3.4 Evidence for DM from the rotation curves of spiral galaxies

Among the different classes of galaxies, late-type galaxies - spirals and irregular - present a disc of gas which extends beyond the region populated by stars [75]. The gas contribution to galactic rotation velocity can be established by using data based on the radiation emitted by the spin-flip of hydrogen first-excited-state [76]. Such contribution, together with the bulge, the stars and the hypothetical dark halo contributions, are shown in Fig. 1.3.3, for a selection of spiral galaxies. The experimental data in Fig. 1.3.3



Figure 1.3.2: Images of ‘Bullet Cluster’ 1E0657-56 (left panel) and the ‘Baby bullet’ MACSJ0025.4-1222 (right panel). The + spots are light nearby us, it is an optical effect of the telescope. Most of yellow galaxies are part of the clusters. The pink shadow traces X-ray emission from hot, intra-cluster gas. The blue shadow traces the picks of the mass distribution, reconstructed by the lensing map; it overlaps with the location of galaxies, which are not-interacting objects, showing that most part of the mass content of the clusters is not-interacting. The estimation of the total mass content shows that there is more mass than accounted in galaxies and stars, requiring the presence of DM [72].

are archived in the SPARC database [77]. The contribution of the dark-halo can be computed assuming specific models (see Sec. 3.1). The total rotation velocity curve is obtained by fitting Eq. 1.19 to data,

$$V_C(r) = \sqrt{V_{DM}(r)^2 + V_{gas}(r)^2 + M_*/L \cdot V_{stars}(r)^2} \quad (1.19)$$

where V_C is the total rotation-velocity curve, V_{DM} , V_{gas} and V_{stars} are the DM, the gas and the stars rotation velocity contributions and M_*/L is luminous mass over luminosity. It is evident that the dark-halo component is required to obtain a good fit. This observation is one of the first suggestions for the existence of a non-luminous component of matter in galaxies. More details on spiral-galaxy-velocity-rotation-curves can be found in [75].

Briefly on MOND. An alternative approach to solve the discrepancy between the spiral-galaxy-rotation-velocity-curves and the known matter content of galaxies relies on theoretical efforts to modify the theory of gravity. A notorious example is the modified law of gravity which is known as MODified-Newtonian-Dynamics (MOND) [13]. The central point is a modification of the gravity-acceleration g , which reads,

$$g_N = \mu(x) g = \begin{cases} g & \text{if } x \gg 1 \\ x \cdot g & \text{if } x \ll 1 \end{cases} \quad (1.20)$$

where g_N is the Newtonian gravity acceleration and $x = g/a_M$, with $a_M = 1.15 \cdot 10^{-10} \text{ m s}^{-2}$, estimated by fitting the model to experimental data. Since gravity-acceleration is

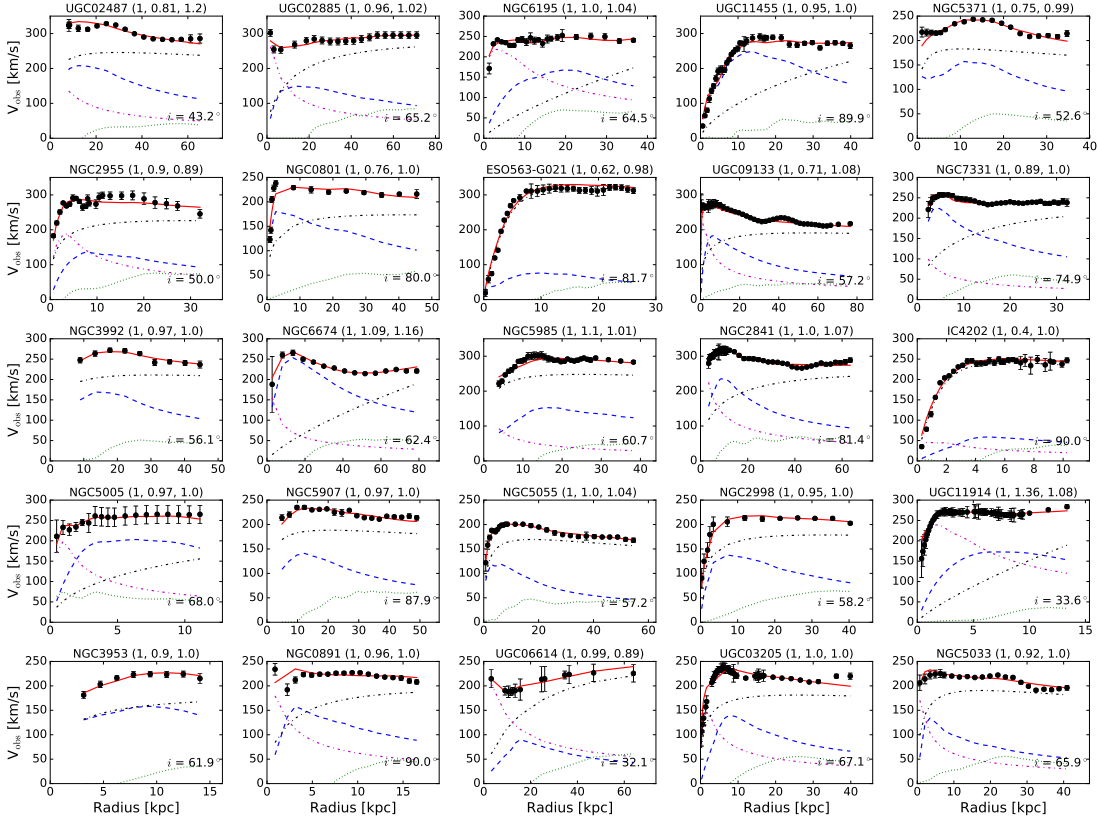


Figure 1.3.3: Selection of spiral galaxy rotation curves [77]. Velocity contributions of different components: gas (dotted-green), stars (dashed-blue), bulge (dot-dashed-purple), dark-halo (dot-dashed-black). Model fitting to data is Di Cintio et al. 2014 (DC14) [75].

expected to decrease at large radii, the prediction of this model is that, at large distances from the gravity-center, $g_N = g^2/a_M$ and the rotation-velocity curve [78],

$$V_C^4(r) \equiv g^2 \cdot r^2 = g_N \cdot a_M \cdot r^2 = G_N \cdot M_0 \cdot a_M = const \quad (1.21)$$

is flat, where M_0 is the luminous mass of the object, which is considered point like. Despite of the strong interest in alternative explanations of the *missing-mass* problem, not further details on MOND or similar attempts are given in this work, since this research explores the hypothesis of DM.

Chapter 2

Selected dark matter particle models

The list of cosmological and astrophysical observations supporting the DM existence reviewed in the first chapter and which have been collected in the last decades, strongly stimulate the formulation of hypotheses on the nature of DM. Among the most discussed proposals, the possibility that DM is constituted by macroscopic compact halo objects (MACHO), in particular in the form of Primordial Black Holes (PBHs), has been extensively discussed and received renewed attention since the first observation of gravitational waves produced by black holes merging [79]. However, recently it has been pointed out that PBHs and other MACHOs associated to LIGO gravitational wave detections are excluded as the dominant component of DM, as shown in Fig. 2.0.1 [80]. In this plot the fraction of DM that can be composed by PHBs is constrained to be lower than 40% in the whole PHBs mass range, reaching few percents for masses different from about $10 M_{\odot}$.

The research developed in this thesis is based on a second widely discussed hypothesis, namely, that DM consists of at least one new type of particle Beyond the Standard Model (BSM)¹. A very large number of possible DM particle candidates have been proposed during the last 40-50 years. They differ by their hypothetical cosmological production, couplings and mass scale. Historically, DM-particle-candidates found major fortune if they were embedded in some motivated extension of the SM. These were proposed to solve either actual open issues, such as for the case of *sterile neutrinos*, or ‘naturalness problems’, that is the unpleasant need in certain theories of fine-tuning the parameters to match observations, as in the case of *axions* and *neutralino*. This chapter presents the three candidates just mentioned, axions, sterile neutrinos and neutralino, the latter as a specific example of WIMPs, for Weakly Interactive Massive Particles. This selection of candidates is motivated both by their role in theories BSM and by the resonance they had for the DM problem.

¹SM neutrinos were the first DM-candidates hypothesised - beyond considerations about their velocity dispersion and the implications for the evolution of structure formation, Planck results reported in Eq. 1.18 definitely exclude such hypothesis.

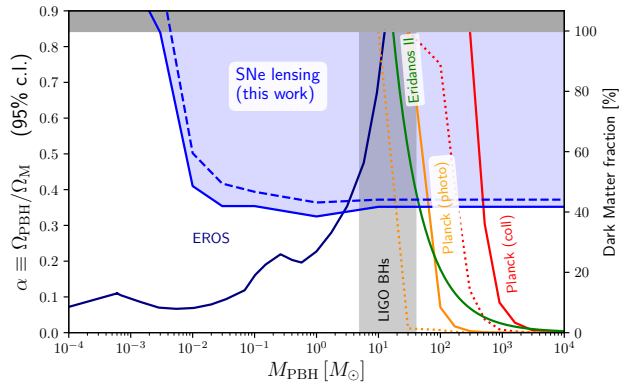


Figure 2.0.1: Constraints on the abundance of PBHs (left y-axis) and on the fraction of DM constituted by PBHs (right y-axis), as function of PBHs mass, M_{pbh} [80]. The analysis of SNe lensing performed in [80] using the joint light-curve analysis (JLA) of the SDSS Collaboration [81] (solid-blue) and the Union 2.1 SN Ia compilations [82] (dashed-blue) constrains the PBH abundance for $0.01M_{\odot} \lesssim M_{pbh}$, including the masses of the merging BH observed by LIGO (shaded-gray). Other constraints come from micro-lensing (EROS [83]), the stability of stellar compact systems (Eridanus II [84, 85]) and CMB [86, 87] (orange and red).

2.1 QCD axion

The axions are pseudoscalar fields identified by Weinberg [88] and Wilczek [89] as a consequence of Peccei and Quinn’s extension of the SM [90], which they proposed to solve the CP violation of strong interactions ([91], Chap. 2). Below, the reason why unobserved CP violations are expected in Quantum Chromodynamics (QCD) - the fundamental theory of strong interactions - is explained and then the QCD axion, as solution of this problem, is introduced.

In the limit of massless quarks, QCD is symmetric under global $U(2)_R \otimes U(2)_L$ chiral transformations or, similarly, under $U(2)_V \otimes U(2)_A$. Here, $U(2)_R$ ($U(2)_L$) is the group of unitary transformations of the right-handed (left-handed) up and down quark fields. The generators of $U(2)_V \otimes U(2)_A$ are linear combinations of $U(2)_R \otimes U(2)_L^2$. According to Goldstone theorem, the spontaneous global symmetry breaking (SSB) leads to the production of as many Nambu-Goldstone bosons as the number of broken generators. Since $m_q \neq 0$, the $U(2)_A$ SSB should be associated to four *pseudo* Nambu-Goldstone bosons. Since there are just three light candidates, the three pions π^{\pm}, π^0 , associated to the $SU(2)_A$ -SSB [92], $U(1)_A$ is not spontaneously broken. Indeed, it is explicitly broken³ due to the axial-vector current anomaly, that affects the current

²Consider the right and left currents $J_R^{\mu a} = \bar{q}_R \gamma^{\mu} \frac{\sigma^a}{2} q_R$ and $J_L^{\mu a} = \bar{q}_L \gamma^{\mu} \frac{\sigma^a}{2} q_L$. Then $J_V^{\mu a} = J_R^{\mu a} + J_L^{\mu a} = \bar{q} \gamma^{\mu} \frac{\sigma^a}{2} q$, while $J_A^{\mu a 5} = J_R^{\mu a} - J_L^{\mu a} = \bar{q} \gamma^{\mu} \gamma^5 \frac{\sigma^a}{2} q$, therefore $U(2)_R \otimes U(2)_L \rightarrow U(2)_V \otimes U(2)_A$.

³A symmetry can be explicitly broken either by terms added by hand for some theoretical or experimental reasons, or by non-renormalisable terms introduced within effective theories or, finally, by anomalies, caused by either quantum effects (the case of $U_A(1)$) or *cut-off* regularisation effects

quadri-divergence[93, 94],

$$\partial_\mu J^{\mu 5} = \frac{g^2 N}{32\pi^2} F_a^{\mu\nu} \tilde{F}_{\mu\nu}^a \quad (2.1)$$

where g is the strong coupling constant, N is the number of flavors, $F_a^{\mu\nu}$ is the colour field strength tensor and $\tilde{F}_{\mu\nu}^a$ its dual. This anomalous current allows for the presence of the Lagrangian term [95, 96],

$$L_{\bar{\theta}} = \bar{\theta} \frac{g^2}{32\pi^2} F_a^{\mu\nu} \tilde{F}^{\mu\nu a} \quad (2.2)$$

where $\bar{\theta}$ is a dimensionless parameter, sum of two independent contributions, $\bar{\theta} = \theta + \text{Arg det } M$, where θ is a free parameter, related to the non trivial structure of the QCD vacuum [97, 98], and $\text{Arg det } M$ is related to the diagonalisation of the complex quark mass matrix with respect to the physical basis. This Lagrangian term violates CP and it induces an unobserved neutron electric dipole moment (NEDM), as shown in Appendix A.1. There are experiments that are searching for NEDM to probe CP violations in strong interactions. The experiments actually impose an upper limit to NEDM equal to $|d_n| < 2.9 \times 10^{-26} \text{e}\cdot\text{cm}$ [99], that requires $\bar{\theta} \lesssim 10^{-10}$, as discussed in Appendix A.1. This small upper limit on $\bar{\theta}$ (which points towards $\bar{\theta} = 0$), implies a precise cancellation of the two independent terms θ and $\text{Arg det } M$. This cancellation between QCD and electroweak parameters is considered a fine-tuning, what is known as the strong CP problem.

Peccei and Quinn [90] propose a theory to explain $\bar{\theta} = 0$, suggesting an extension of the SM with the introduction of a new global chiral symmetry, $U(1)_{PQ}$ as called by Weinberg [88]. They introduce a field, $a(x)$, as a dynamical theta parameter, in a way that the shift symmetry $a(x) \rightarrow a(x) + \text{const}$ is respected except for anomalous couplings with the gauge fields. The θ -term can then be eliminated by the shift $a(x) \rightarrow a(x) - \theta f_A$. The remaining term multiplying $a(x)$ vanishes as the QCD dynamics predicts that the vacuum expectation value (vev) of $a(x)$ is $\langle a(x) \rangle = 0$ [100]. In this way, the CP violating term in Eq. 2.2 is re-absorbed and the strong CP problem finds a solution⁴. Weinberg and Wilczek independently inspect the consequences of Peccei and Quinn's theory, and predict the existence of light pseudoscalar bosons, the *axions* [88, 89].

This initial model was based on a $U(1)_{PQ}$ SSB scale f_a equal to the electroweak one ($f_a \approx v_{ew} = O(250\text{GeV})$), but this hypothesis was ruled out by the experiments; during the years, the model has been reexamined and now $f_a \gg v_{ew}$. There is a fixed relation between the QCD axion mass and the PQ scale f_a , which is (Sec. 112 of [54]),

$$m_a = 5.961(51) \left(\frac{10^9 \text{GeV}}{f_a} \right) \text{meV} \quad (2.3)$$

(<https://plato.stanford.edu/entries/symmetry-breaking>).

⁴For a presentation on axions see *Topology in QCD and Axion Dark Matter*, Andreas Ringwald (DESY) <https://www.rug.nl/research/vsi/events/groenewold/ringwald.pdf>.

A priori, neglecting experimental constraints, PQWW theory (Peccei, Quinn, Weinberg and Wilczek) admits an axion mass range of $10^{-12} - 10^6$ eV, while experimental constraints limit the range to $10^{-6} - 10^{-3}$ eV [54, 101]. The attractive feature of the PQWW theory is that in addition to its resolution of the strong-CP problem it naturally offers a particle-candidate for DM. To this aim, we require axions to be stable within the age of the Universe. Since they are light, their stability depends only on the two-photon decay channel (Sec. 112 of [54]),

$$\Gamma_{a\gamma\gamma} = \frac{g_{a\gamma\gamma}^2 m_a^3}{64\pi} = 1.1 \cdot 10^{-24} \text{s}^{-1} \left(\frac{m_a}{\text{eV}} \right)^5 \quad (2.4)$$

which requires $m_a < 20$ eV, in agreement with the not-excluded QCD-axion mass range.

Here the discussion is limited to the original PQWW theory to stress the motivations supporting the axion as possible new building block of the SM. However, several modifications to the initial proposal have been elaborated which also depart from the initial goal of solving the strong CP-problem. For a complete recent review of axion-like-models and constraints, see Sec. 112 of [54].

2.2 Sterile neutrino

The sterile neutrino is a hypothetical particle beyond the SM, that does not interact with any gauge boson of the electroweak theory - for this reason called ‘sterile’ ([91], Chap. 2). It can be thought as a right handed component of the neutrino field and its existence has been matter of speculation for long time. Today the sterile neutrino is strongly supported by the evidence of massive neutrinos. Similarly to the right handed projection of charged leptons, a right handed neutrino can take part in the generation of mass and can be involved in the mechanism that causes the hierarchy between neutrino and charged lepton masses ⁵ (see for example [102]). It could take part in the generation of the baryon asymmetry of the Universe [103]. Furthermore the sterile neutrino, if accomodated by ad hoc hypothesis, can account for DM. Clearly this last application is the most relevant one for the purposes of this work and is the focus of this section. However, the versatility of sterile neutrinos at explaining the different crucial problems in particle physics and cosmology just mentioned, increases considerably the interest in this particle and makes it a very attractive object of study in general.

Because of the LEP results on Z boson decay width, that implies a number of invisible decay channels equal to $N_\nu = 2.9840 \pm 0.0082$ - see *Particle listing* in [54] - the right-handed neutrinos must be either not coupled to the Z gauge bosons or more massive than $m_Z/2$. Since a particle coupled to electroweak-fields more massive than $m_Z/2$ would be highly unstable, the first possibility will be considered, that is a gauge singlet under electroweak interactions. Since it is not coupled to electroweak gauge bosons, the

⁵For more details, see Appendix A.2.

number of generations is not constrained by anomaly cancellations and, a priori, the number of generations is arbitrary. Since the mechanism for neutrino mass generation is not established, a priori sterile neutrino can have almost any mass [103].

This section considers the case one or more sterile neutrino can be relevant as a candidate for DM. For this reason, the interest is in sterile neutrinos with masses of $O(\text{keV})$, as this is the range suggested by cosmological and astrophysical constraints [104].

In the following, assume there are n heavy neutrinos, N_i , with $i = 1, \dots, n$, with masses $M_1 < M_2 < M_3 < \dots < M_n$. A common case is the one with 3 heavy neutrinos, with the lightest of $O(\text{keV})$ mass. Sterile neutrinos models mainly predict two main mass splitting schemes, the bottom-up and the top-down, shown in Fig. 2.2.1, where M_1 is the lightest sterile neutrino mass, M_2, M_3 are the heaviest sterile neutrino masses and $M_R \gg \text{keV}$ is some model dependent high energy scale [105]. Figure 2.2.1 assumes a total of three sterile neutrinos, but it can be generalised to an arbitrary number. The common tendency is to consider a starting configuration, in which M_2 and M_3 are of $O(M_R)$ and M_1 is either zero or $O(M_R)$; then some mechanism increases or suppresses the N_1 sterile neutrino mass up to the keV scale.

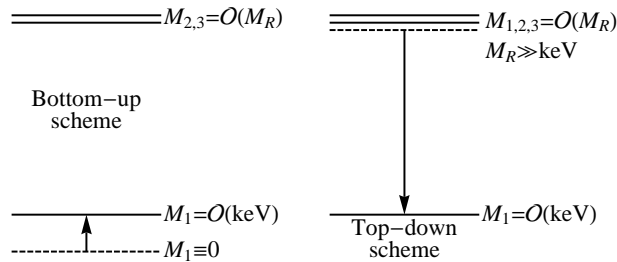


Figure 2.2.1: Left: The bottom-up scheme. The light neutrino mass initially is $M_1 = 0$ and is increased at the keV by some mechanism. The two heavier neutrino mass M_2, M_3 are of $O(M_R)$, where M_R is some high energy scale. Right: the top-down scheme. All three right handed neutrino masses initially are of $O(M_R)$ and some mechanism suppresses M_1 at the keV scale. Taken from [105].

A particularly interesting example of this scenario the νMSM (Neutrino Minimal SM) proposed by Asaka, Blanchet and Shaposhinokov in 2005 [106] as a minimal extension of the SM. It works within the $SU(2)_L \otimes U(1)_Y$ symmetry group and extends the SM particle content by three right-handed gauge singlets (N_1, N_2, N_3) ⁶. It accounts for,

1. standard neutrino masses;

⁶A comment on notation: in this work *right handed* and *sterile* neutrino is equivalently used to distinguish the three N_1, N_2, N_3 from the standard, left handed (or *active*) neutrinos. To identify instead the N_i from each other, in particular the keV neutrino from the others that are heavier, *light* or *heavy* is specified. Moreover, in the same way as the literature, N_1 is associated to the light sterile neutrino and N_2, N_3 to the heavier neutrinos.

2. warm DM⁷, through the accommodation of a light sterile neutrino of $O(\text{keV})$;
3. the baryon asymmetry, through the accommodation of two heavier right handed neutrinos ($M_{2,3} \geq 1 \text{ GeV}$).

The many issues that find solution in this *scenario*⁸ make it attractive; however, since it is a phenomenological theory that does not provide any explanation for the appearance of the keV scale and for the mass shift between the light and the two heavier right handed neutrino masses, additional effort in model building is required, as done for example in [108] and recently in [109].

Since *models* aim to provide a complete theory of neutrinos, they have to account also for the difference between neutrino and charged lepton masses. This task is commonly achieved involving the popular *seesaw mechanism*, whose simplest version is discussed in Appendix A.2. Besides the explanation of the charged lepton-neutrino mass departure, the seesaw mechanism implies the fundamental mixing between active neutrinos, ν_a , that are interaction-eigenstates, and sterile neutrinos, mixing that makes this latter not completely sterile. For example it could have a main decay channel, $N_1 \rightarrow \nu_a \nu_a \nu_a$, of amplitude [104],

$$\Gamma_{N_1 \rightarrow \nu_a \nu_a \nu_a} \approx \frac{G_F^2 M_1^5 \theta_1^2}{96\pi^3} = \frac{1}{4.7 \times 10^{10} \text{ sec}} \left(\frac{m_N}{50 \text{ keV}} \right)^5 \theta_1^2 \quad (2.5)$$

where G_F is the Fermi coupling constant and θ_1 is the active/light-sterile-neutrino mixing angle. The condition of stability imposed to the decay channel $N_1 \rightarrow \nu_a \nu_a \nu_a$ over the age of the Universe, $\tau_u \simeq 4 \cdot 10^{17} \text{ sec}$, imposes a limit on the mixing angle,

$$\theta_1^2 < 1.1 \times 10^{-7} \left(\frac{50 \text{ keV}}{m_N} \right)^5 \quad (2.6)$$

An important decay channel for observations is $N_1 \rightarrow \gamma \nu_a$, whose decay rate is [104],

⁷From the theory of large scale structure formation (see Sec. 1.3.2), information about the DM particle properties can be extrapolated, in particular on the velocity dispersion. Commonly, DM is classified in [68],

- Cold (CDM) particles if the velocity dispersion is small enough that the free-streaming length does not have any impact on the cosmological structure formation (the assumption implied in the Λ CDM model discussed in Sec. 1.1).
- Hot (HDM) *e.g.* neutrinos, if it consists of relativistic particles whose velocity dispersion is very large and the free-streaming length smooths out the matter density fluctuations at the galaxy and galaxy cluster scale.
- Warm (WDM) particles represent an intermediate case between CDM and HDM, whose specifics depend on the type of particle cosmological production [107].

⁸On terminology: Alexander Merle, in [105], classifies a sterile neutrino approach relative to the keV mass scale as a "[...]scenario, whenever it can accommodate for a keV sterile neutrino, but does not give any explanation for the appearance of the keV scale" and as a "[...]model whenever there is an explanation for the appearance of the keV scale or, rather, for a suitable mass hierarchy or the existence of a suitable new scale". In this view, the ν MSM would be an interesting *scenario*.

$$\Gamma_{N_1 \rightarrow \gamma \nu_a} = \frac{9\alpha G_F^2}{256 \cdot 4\pi^4} \sin^2 2\theta_1 M_1^5 \quad (2.7)$$

where α is the fine-structure constant. In fact, the correspondent search for monochromatic X-ray emission allows to constrain the (θ_1, M_1) parameter space and imposes an upper limit to the keV sterile neutrino equal to $M_1 < 50$ keV [104]. This bound, combined with the Tremaine-Gunn bound [110], constrains the keV sterile neutrino mass range to $1 \text{ keV} \lesssim M_1 \lesssim 50 \text{ keV}$. Experimental and theoretical constraints on the θ_1 and M_1 parameters are reviewed in [104, 111].

2.3 WIMPs

The assumption that the DM we observe today is the thermal-relic of a species which was in thermodynamical equilibrium with SM particles in the early Universe, historically led to the hypothesis that DM consists of Weakly Interacting Massive Particles (WIMPs)⁹ [52]. If during the radiation-dominated-era DM particles are in equilibrium with the primordial plasma, their number density n is kept constant by the annihilation-production rate balance. This equilibrium depends on the mass-temperature ratio x and holds while the temperature of the thermal bath T is larger than the mass of the species of interest, $T \gg m$. Since the Universe cools down during expansion, when the temperature drops below the particle-mass, $T \ll m$, the particle-production is inhibited but the annihilation process is still efficient, causing the depletion of the particle number. The reduction of the particle-number-density continues until the time-dependent expansion-rate equals the annihilation rate, conditions which mark the *particle freeze-out*. The particle phase space distribution function, $f(x^\mu, p^\mu)$ evolves according to the Boltzmann equation which equates the Liouville operator and the collisional operator, $L[\hat{f}] = C[f]$ [52]. In the Friedmann-Lemaître-Robertson-Walker model of an isotropic and homogeneous Universe, the number density evolution is described by [114],

$$\dot{n} + 3Hn = \langle \sigma v \rangle [(n_{eq})^2 - n^2] \quad (2.8)$$

where n_{eq} is the number density of particles in thermal equilibrium, given by the integration of the Fermi-Dirac or Bose-Einstein distribution function for the relativistic species ($T \gg m$ at freeze-out) and the Maxwell-Boltzmann distribution function for the non-relativistic ones ($T \ll m$ at freeze-out), H is the expansion rate and $\langle \sigma v \rangle$ is the annihilation rate times the velocity, averaged over the $\chi\bar{\chi}$ distribution functions.

Equation 2.8 is commonly solved by substituting n with $Y = n/s$ and $Y_{eq} = n_{eq}/s$, where s is the entropy in a comoving volume, a^3 , and a is the scale factor. With this substitution, the number density evolution equation is [114],

$$\frac{dY}{dx} = \frac{s\langle \sigma v \rangle}{Hx} \left[1 + \frac{1}{3} \frac{d(\ln g_{*s})}{d(\ln T)} \right] (Y_{eq}^2 - Y^2) \quad (2.9)$$

⁹Historically, the thermal relic hypothesis was associated to WIMPs. See [112, 113] for an example of DM thermal relic which is not WIMPs.

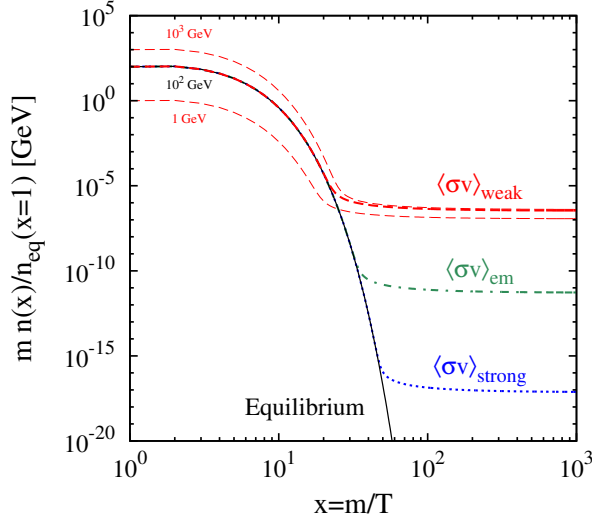


Figure 2.3.1: Number density evolution as a function of $x = m/T$. The number density is normalised to the number density at $x = 1$ and multiplied by the particle mass. The solid black line shows the evolution of the number density of particles at equilibrium with radiation. Red, green and blue dashed curves show at which mass-temperature ratio x the number density freeze-out occurs for different values of $\langle\sigma v\rangle$, in particular $\langle\sigma v\rangle_{weak} = 2 \times 10^{-26} \text{cm}^3 \text{s}^{-1}$, $\langle\sigma v\rangle_{em} = 2 \times 10^{-21} \text{cm}^3 \text{s}^{-1}$ and $\langle\sigma v\rangle_{strong} = 2 \times 10^{-15} \text{cm}^3 \text{s}^{-1}$. The two thin dashed red curves show the mass dependence of the number density for $\langle\sigma v\rangle_{weak}$ [114].

where $x = m_\chi/T$ and g_{*s} is,

$$g_{*s} \equiv \sum_B g_B \left(\frac{T_B}{T_\gamma} \right)^3 + \frac{7}{8} \sum_F g_F \left(\frac{T_F}{T_\gamma} \right)^3 \quad (2.10)$$

where $g_{B,F}$ are the number of degrees of freedom for each relativistic boson and fermion, $T_{B,F}$ the temperature of each species and T_γ the temperature of photons.

Equation 2.8 admits approximated analytical solutions [114] and can be solved numerically with high accuracy by means of computer programs [114]. As shown in Fig. 2.3.1 the present cosmological density of WIMPs mainly depend on $\langle\sigma v\rangle$ ¹⁰.

¹⁰A rather well known calculation can be found in [52] and [115]. It has the advantage of a more explicit solution for Eq. 2.9, that for the case of the decoupling of a non-relativistic species is,

$$Y_0 = \frac{3.79(n+1)\alpha g_*^{1/2} g_{*s}}{m_{Pl} m \langle\sigma v\rangle} x_f \quad (2.11)$$

where 0 stays for the present time, n is the index of the parameterisation $\langle\sigma v\rangle \sim \sigma_0 x^{-n}$, g_* is defined as g_{*s} with the third power substituted by the fourth power, m_{Pl} is the Planck scale, m the mass of the particle of interest and x_f is the mass-to-temperature ratio at the time of the particle ‘freeze-out’. Such solution makes evident the dependence on m and $\langle\sigma v\rangle$. Using Eq. 2.13, the DM parameter density is,

$$\Omega_c = \frac{\rho_\chi}{\rho_0} = \frac{m s_0 Y_0}{\rho_0} \equiv \frac{s_0}{\rho_0} \frac{3.79(n+1)\alpha g_*^{1/2} g_{*s}}{m_{Pl} \langle\sigma v\rangle} x_f \quad (2.12)$$

which only depends on the annihilation cross-section at freeze-out.

Once Y -dependence on $\langle\sigma v\rangle$ is made explicit, the mass density of DM today ρ_χ can be computed,

$$\rho_\chi = ms_0 Y_0 \quad (2.13)$$

where 0 stays for the present time. Using Eq. 2.13, the required order of magnitude for $\langle\sigma v\rangle$ can be estimated by matching the DM density parameter $\Omega_c = \frac{\rho_\chi}{\rho_0}$ with its observed value $\Omega_c h^2 = 0.1200 \pm 0.0012$ [55]. The result is that regardless of the DM-mass¹¹, one finds,

$$\langle\sigma v\rangle \sim 10^{-26} \text{cm}^3 \text{s}^{-1} \quad (2.14)$$

Consequently, the order of magnitude of the DM annihilation cross section is inherent in the hypothesis of DM-thermal-production. However, since we do not have information on the couplings, the mediator and the DM mass, we cannot establish the type of interaction. The first attempt in the past was to accommodate DM within the electroweak framework. The reason is the following. When the mediator mass is fixed at the order of the electroweak gauge bosons masses, $M \sim O(10^2 \text{ GeV})$, and we consider a typical electroweak cross-section,

$$\sigma \sim G_F^2 m_\chi^2 \propto \frac{g^4 m_\chi^2}{M^4} \quad (2.15)$$

where $G_F \sim 10^{-5} \text{ GeV}^{-2}$ in natural units is the Fermi constant, m_χ the DM particle mass and g the coupling constant, the resulting cross-section is in agreement with the prediction in Eq. 2.14. Within this assumption¹² a lower limit on the WIMP mass can be imposed, known as the ‘Lee-Weinberg limit’. In [116] Lee and Weinberg show that for a stable heavy neutrino produced as thermal relic, the condition to avoid the Universe overclosing (which is a more conservative condition than imposing that it constitutes all the DM) imposes a lower limit on the mass at about 2 GeV. In [117], it is derived that elementary particles which were in thermal equilibrium cannot have a mass greater than 340 TeV. For this reason historically the search for WIMPs focused on the GeV-TeV energy range. If the assumption on the mediator mass in Eq. 2.15 is relaxed, lower WIMP mass values are also possible. In Ref. [118] (2007), in fact, scenarios which contemplate a new light mediator are defined stating that they are ‘perhaps the only viable possibility for WIMP masses to lie well below the Lee-Weinberg window, and close to the MeV-scale’ and several models are proposed. More recently, the frontier of new light messengers has been extensively explored and results from accelerators, astrophysics, cosmology and direct detection have been combined to provide updated constraints on the WIMP low mass regime (see *e.g.* [119]) and discuss the prospects of the DM experimental search.

Various WIMP-models can be built playing with the parameters which enter in the estimation of the thermally averaged annihilation-cross section. Here the motivation for the most discussed WIMP-candidate, the supersymmetric neutralino, is addressed.

¹¹In [114] two regimes are identified, one for $m_\chi \lesssim 10 \text{ GeV}$ and one for $10 \text{ GeV} \lesssim m_\chi$, which show just a slight mass dependence.

¹²Such speculation used to be termed as the ‘WIMP miracle’.

Supersymmetry: Neutralino

SUPERSymmetry (SUSY) is a renowned theoretical proposal which extends the SM to relax the so called *hierarchy* or *naturalness problem* [120] ([91], Chap. 2). The Higgs mass term receives quadratic radiative corrections which are divergent contributions (see Appendix A.3). Such radiative corrections, within the SM, can be reabsorbed as in any renormalisable theories. However, in the case a physical energy scale Λ_{UV} below the Planck scale exists, the Higgs mass would shift from $O(10^2 \text{ GeV})$ to $O(\Lambda_{UV})$, unless ad hoc cancellations are present. Such shift would be in tension with the value of the mass of the Higgs boson (125.10 ± 0.14 [54]) [121]. SUSY solves the *hierarchy problem* introducing a symmetry between bosons and fermions which cancels such radiative corrections, as better explained in Appendix A.3. In addition, SUSY found further support because among the variety of particles introduced in the spectrum, it provides neutral, massive and stable candidates which can play the role of DM, such as the neutralino, $\tilde{\chi}_1$ [122, 123]. The combination of *superfields* which enter in the definition of $\tilde{\chi}_1$ and few properties of the neutralino are briefly presented. For a list of SUSY particles added to the spectrum of SM particles, refer to Appendix A.3.

The mass term for the spin- $\frac{1}{2}$ neutral superfields $\psi^0 = (\tilde{B}^0, \tilde{W}^0, \tilde{H}_u^0, \tilde{H}_d^0)$ is [120],

$$\mathcal{L} = -\frac{1}{2}(\psi_i^{0T} M_{ij} \psi_j^0 + c.c) \quad (2.16)$$

where M_{ij} is a mass-matrix. The fields in ψ^0 are gauge-eigenstates. The spin-1/2 mass-eigenstates obtained by diagonalising M_{ij} are the neutralinos, $\tilde{\chi}_i^0$, with $i = 1, \dots, 4$,

$$\tilde{\chi}_i^0 = N_{ij} \psi_j^0 = N_{i1} \tilde{B}^0 + N_{i2} \tilde{W}^0 + N_{i3} \tilde{H}_u^0 + N_{i4} \tilde{H}_d^0 \quad (2.17)$$

where N_{ij} is the unitary diagonalisation matrix. By convention, the four neutralinos masses are ordered as follows: $m_{\tilde{\chi}_1} < m_{\tilde{\chi}_2} < m_{\tilde{\chi}_3} < m_{\tilde{\chi}_4}$. If the lightest neutralino is also the lightest supersymmetric particle, then it can be a WIMP candidate as the stability is assured by imposing a new discrete conserved symmetry named R -parity, which prevents neutralino decay into lighter SM particles; in fact, opposite R -parity is imposed to SM and SUSY particles.

SUSY models, although even in its more minimal realisation introduces a huge number of free parameters, strongly motivated the experimental search for SUSY-particles at accelerators and boosted DM particle search in general. For recent reviews of experimental constraints see [124] and Sec. 26 of [54].

Chapter 3

Generalities of dark matter direct detection

In the previous chapter we reviewed the three (very) well motivated DM particle candidates. Most of the currently operating DM experiments search for WIMPs/WIMPs-like using the methods sketched in Fig. 3.0.1, which consist in (i) the production of DM-particles at accelerators, (ii) the indirect search for DM-particles based on the detection of SM annihilation products originated in high DM-density astrophysical regions and (iii) the direct search for DM-particles scattering off target nuclei in ultra-low background environments.

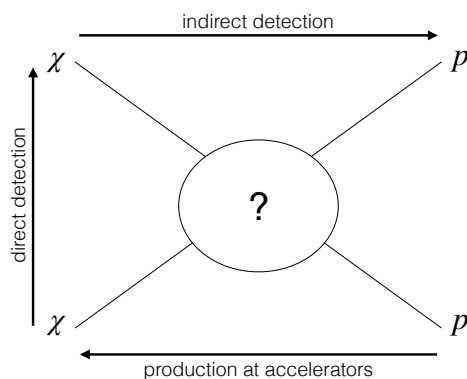


Figure 3.0.1: Schematic representation of the three complementary detection techniques for DM particles.

Since this thesis explores phenomenological aspects of the direct detection (DD) technique for the search of DM-particles scattering off nuclei, in this chapter we review the elements which enter in the description of the DD observables. We introduce in Sec. 3.1 the characteristics of the galactic DM halo, in particular the DM-density profile and the DM-velocity distribution function, in Sec. 3.2 the DD observables which are of interest for this work, in Sec. 3.3 the DM-nucleus interactions and cross-sections which

are commonly adopted by the DD experimental community to show results on the cross-section versus DM-mass parameter space, and in Sec. 3.4 a discussion on DD techniques.

3.1 Dark matter galactic halo

3.1.1 Dark matter density profile

The shape and mass density distribution of galactic-dark halos depend on the galaxy formation history [68]. The simplest model which was used to approximate the DM-halo density-distribution, $\rho(r)$, as a function of the distance from the center, r , is a truncated singular isothermal sphere with $\rho(r) \propto r^{-2}$, for $r < r_h$, where r_h is defined as the distance at which $\rho_h = \rho(r_h) \sim 200\bar{\rho}$, with $\bar{\rho}$ the mean density of the Universe. When N-body simulations started to be employed as support to theoretical calculations, the effort was dedicated to find a universally-valid formulation for the DM-halo density distribution at equilibrium. One of the best agreement between observations and simulations was achieved by C. S. Frank, J. F. Navarro and S. D. M. White [68, 125], who described the DM-halo density distribution as,

$$\rho(r) = \rho_c \frac{\delta_{char}}{\left(\frac{r}{r_s}\right)\left(1 + \frac{r}{r_s}\right)^2} \quad (3.1)$$

where ρ_c is the critical density, Eq 1.2, δ_{char} is the characteristic (dimensionless) density of the halo and r_s is the scale radius. Equation 3.1 is commonly know as NFW model. Despite of the success of the NFW model, subsequently it was found that DM-halo profiles, on average, were more accurately described by an Einasto profile [68, 126],

$$\rho(r) = \rho_{-2} \exp \left\{ -\frac{2}{\alpha} \left[\left(\frac{r}{r_{-2}} \right)^\alpha - 1 \right] \right\} \quad (3.2)$$

where r_{-2} is the radius at which the logarithmic slope of the profile density, $d \ln \rho(r) / d \ln r$, is equal to -2. The index α is obtained as a best-fit parameter.

Today, high-resolution-hydrodynamic-simulations of Milky Way (MW)-like galaxies, including both DM and baryons, are available. The agreement between simulation results and observations is improved with respect to the past, when the role of baryons was neglected and DM-only simulations were possible [127]. DD DM search, which depends on the DM density in the Solar neighbourhood, is supported by recent works, *e.g* [128] and [129], where the parameters used by the community to draw and compare their sensitivity plots are compared with the parameters obtained by using the high-resolution-hydrodynamic-simulations of MW-like galaxies (EAGLE and APOSTLE in the case of the cited references). The inclusion of the baryons in the recent simulations has shown to be one of the possible solutions of the small-scale structure problems of the Λ CDM model [130].

In recent years, Gaia Data Release 2 [131] enriched the knowledge about the structure of the Galaxy and stimulated the development of more accurate models for the galactic DM halo and substructures [132–139].

3.1.2 Dark matter velocity distribution

In first approximation, the assumption of a spherical and isothermal DM-halo, inserted in the equation of hydrodynamical equilibrium, lead to a velocity distribution of DM which follows a Maxwell-Boltzmann distribution function [16]. Although this was the first attempt to describe the DM-halo, the most recent high-resolution-hydrodynamic-simulations show that such simplified model, which is known as Standard Halo Model (SHM), is a reasonable representation of the DM-halo, more appropriate than it was thought in the past when the role of baryons in the galaxy formation was neglected [127, 140, 141]. Below we address the details of the SHM, the phenomenology of the gravitational focusing effect which affects the isotropy of the SHM and the recent refinements of the model based on the analysis of Gaia Data Release 2 [131].

Standard Halo Model. DM-particles are assumed to be on average at rest, distributed according to a thermal distribution in the galaxy and forming an isothermal and spherical halo [16]. The kinematics of DM particles in the galactic frame¹, within the SHM, is described by an isotropic Maxwell-Boltzmann velocity distribution [18, 142] truncated at the escape velocity v_{esc}^{gal} (value usually adopted is 544 km/s). In DD search, the observables depend on the kinematical parameters defined in the laboratory reference frame. The galactic center and the laboratory reference frame are not inertial frames with respect to each other, because of the circular motion of the Solar system around the galactic center. However, given the time scale of the period of rotation, we assume a linear-motion and we use galilean transformation to get the DM kinematical parameters in the laboratory frame. A notation remark: we indicate with \mathbf{v}_b^a the velocity of a in the reference frame b , therefore $\mathbf{v}_b^a = -\mathbf{v}_a^b$. The relation between the DM velocity in the galactic center frame, \mathbf{v}_χ^{gal} , the DM velocity in the detector frame, \mathbf{v}_χ^{det} , and the detector velocity in the galactic center frame, \mathbf{v}_{det}^{gal} , is,

$$\mathbf{v}_\chi^{gal} = \mathbf{v}_\chi^{det} + \mathbf{v}_{det}^{gal} \quad (3.3)$$

The Maxwell-Boltzmann DM velocity distribution in the galactic frame reads,

$$f(\mathbf{v}_\chi^{gal}) \equiv f(\mathbf{v}_\chi^{det} - \mathbf{v}_{gal}^{det}) = \begin{cases} \frac{1}{N_{esc}} \left(\frac{1}{\pi v_0^2} \right)^{3/2} e^{-(\mathbf{v}_\chi^{det} - \mathbf{v}_{gal}^{det})^2 / v_0^2}, & \text{for } |\mathbf{v}_\chi^{det} - \mathbf{v}_{gal}^{det}| < v_{esc}^{gal} \\ 0, & \text{otherwise} \end{cases} \quad (3.4)$$

¹We define galactic frame a reference system with its origin in the galactic center and not co-rotating axes with the stellar disk.

where $N_{esc} = \text{erf}[z] - (2/\sqrt{\pi})ze^{-z^2}$, with $z = v_{esc}^{gal}/v_0$, $v_0 \simeq 220\text{km/s}$ is the most probable speed, which equals the circular speed, and \mathbf{v}_{gal}^{det} is the velocity of the galactic center seen from the laboratory. The velocity \mathbf{v}_{gal}^{det} is a function of time, which can be written using the reference frame of the Sun in the following manner,

$$\mathbf{v}_{gal}^{det}(t) = \mathbf{v}_{gal}^{\odot} + \mathbf{v}_{\odot}^{det}(t) \quad (3.5)$$

where $\mathbf{v}_{gal}^{\odot} \simeq (11, 232, 7)\text{km/s}$ is the velocity of the center of the galaxy seen from the Sun, and \mathbf{v}_{\odot}^{det} is the velocity of the Sun seen from the Earth [18], which is a function of time. At zero order in the eccentricity of the Earth orbit \mathbf{v}_{\odot}^{det} can be approximated as,

$$\mathbf{v}_{\odot}^{det}(t) = -\mathbf{v}_{det}^{\odot}(t) \approx -|\mathbf{v}_{det}^{\odot}|(\hat{\epsilon}_1 \cos(t - t_1) + \hat{\epsilon}_2 \sin\omega(t - t_1)), \quad (3.6)$$

where $|\mathbf{v}_{det}^{\odot}| = 29.79\text{km/s}$ is the mean speed of the Earth, $\hat{\epsilon}_1$ and $\hat{\epsilon}_2$ are the orthonormal unit vectors which span the ecliptic plane, $\omega = 2\pi/1\text{year}$ and t_1 is the vernal equinox (March, 20th) [18]. As a consequence of the time dependence of $\mathbf{v}_{det}^{\odot}(t)$, the flux of DM-particles on Earth is a periodic function of time with period 1 year.

Anisotropies: Gravitational focusing. The gravitational potential of the Sun perturbs the velocity distribution of the dark matter particles, causing a distortion which spoils the velocity distribution isotropy assumed within the SHM. This effect is called gravitational focusing. It occurs because particles on average at rest and nearby the Sun feel its gravitational attraction and tend to focus behind the Sun during their motion around the galactic center, as shown in Fig. 3.1.1 [143]. As a consequence, the period of the year which corresponds to the point behind the Sun along the revolution of the Earth, *i.e.* around March, is expected to be characterised by a larger flux of DM-particles.

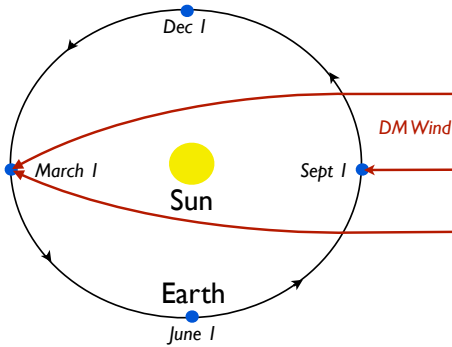


Figure 3.1.1: Scheme of the gravitational focusing effect [143]. The period of larger density of dark matter particles expected as consequence of the gravitational focusing is March.

Following [34], we account for the gravitational focusing effect substituting the velocity distribution-function in Eq. 3.4 with,

$$\tilde{f}(\mathbf{v}_{\chi}^{gal}) = f(\mathbf{v}_{\odot}^{gal} + \mathbf{v}_{\infty}[\mathbf{v}_{\chi}^{det} + \mathbf{v}_{det}^{\odot}]) = f(\mathbf{v}_{\odot}^{gal} + \mathbf{v}_{\infty}[\mathbf{v}_s]), \quad (3.7)$$

where v_{∞} is the DM-particle velocity with respect to the Sun at infinity,

$$\mathbf{v}_\infty = \frac{v_\infty^2 \mathbf{v}_s + v_\infty (G_N M / r) \hat{\mathbf{r}} - v_\infty \mathbf{v}_s (\mathbf{v}_s \cdot \hat{\mathbf{r}})}{v_\infty^2 + G_N M / r - v_\infty (\mathbf{v}_s \cdot \hat{\mathbf{r}})} \quad (3.8)$$

G_N is the gravitational constant, M is the mass of the Sun and \mathbf{r} is the Earth trajectory during the year in the Galactic Coordinate system [18]. For practicalities for the implementation of the gravitational focusing, which enter in some of the results of the next sections, see Appendix B.1.

Other anisotropies. As said, the SHM assumes that DM is isotropically distributed. However, anisotropies both in space and velocity can be present, on analogy with the stellar distribution in the galaxy, which today is probed with unprecedented accuracy by the *Gaia* satellite.

Gaia is a space observatory whose mission is to provide a three-dimensional map of our galaxy and to provide catalogues of the position and radial velocity of millions of stars. These data can be processed to study properties and formation history of the Milky Way².

- *Gaia Sausage and SHM++* In the view of these results, in [20], a second version of the SHM, named SHM++, has been proposed as update of the SHM parameters, in particular in view of the new stellar substructure - ‘the sausage’ - which has been identified by the *Gaia* satellite and is likely to be accompanied by similar DM-substructure. The implementation of this method showed that the sensitivity limits drawn by DD experiments (see Sec. 3.4) are found to be rather accurate regardless of the use of SHM or SHM++.

- *Anisotropies: S1 DM-Hurricane* Streams are localised halo substructures with velocity distribution $f_{stream}(\mathbf{v}) = \delta^3(\mathbf{v})$. Higher impact on DD was expected from the S1 stream, discovered by the Sloan Digital Sky Survey (SDSS) and the *Gaia* satellite. However, it was proven [145] that the discrimination between the event rates due to the stream and the SHM, respectively, is not feasible, even using the annual modulation information, since the phase of modulation is the same for the two components. More interesting phenomenology is found, instead, for directional DD [145].

3.2 Two direct detection observables

This section described two key observables of the DD-technique based on DM-scattering off nuclei³: first the nuclear recoil energy spectrum, which is a one-dimensional spectrum and it is distributed only in energy, and second the annual modulation of the energy spectrum, a two-dimensional observable, which requires to monitor both the energy deposited in the target material and the time of the event.

²Gaia Data Release 2 [144] has been renamed the *Gaia Revolution*, as it provided celestial positions for about 1.7 million stars, radial velocities for more than seven million stars and many other measurements.

³A third observable is the number of target-recoiling-events in a certain direction. The differential rate in energy and solid angle is discussed in Sec. 4.3.1.

3.2.1 Expected energy spectrum

Given the DM velocity distribution function $f(\mathbf{v}_\chi^{det} + \mathbf{v}_{det}^{gal})$ and the DM-nuclei cross section $\frac{d\sigma}{dE_R}(E_R, \mathbf{v}_\chi^{det})$, where E_R is the nuclear recoil energy, the energy-spectrum of nuclear recoil events, expected in the $\mathcal{O}(\text{keV})$ energy range, is,

$$\frac{dR}{dE_R} = \frac{\rho_\chi}{m_\chi m_T} \int_{|\mathbf{v}_\chi^{det}| > v_{min}}^{|\mathbf{v}_\chi^{det} + \mathbf{v}_{det}^{gal}| < v_{esc}} d\mathbf{v}_\chi^{det} |\mathbf{v}_\chi^{det}| f(\mathbf{v}_\chi^{det} + \mathbf{v}_{det}^{gal}) \frac{d\sigma}{dE_R}(E_R, \mathbf{v}_\chi^{det}) \quad (3.9)$$

where ρ_χ is the DM mass density at the position of the Sun, m_χ the DM-mass, m_T the target nucleus mass, v_{min} the minimal velocity required to produce the recoil energy E_R , v_{esc} the maximum velocity for particles trapped in the gravitational field of the galaxy, $f(\mathbf{v}_\chi^{det} + \mathbf{v}_{det}^{gal})$ and \mathbf{v}_{det}^{gal} are defined in Eqs. 3.4 and 3.5, and $\frac{d\sigma}{dE_R}(E_R, \mathbf{v}_\chi^{det})$ is defined in the next section.

The differential rate in Eq. 3.9 is defined as the *true* energy spectrum, because it is the count rate of an ideal detector. Indeed, the *detected* energy spectrum is the result of the convolution of the differential rate, computed at the deposited energy, with the efficiency and the energy resolution of the detector. To account for these experimental effects, Eq. 3.9 is written as,

$$\frac{dR}{dE'_R} = \int dE_R \epsilon(E_R) \phi(E_R, E'_R) \frac{dR}{dE_R} \quad (3.10)$$

where E'_R is the detected recoil energy, $\epsilon(E_R)$ is the detector efficiency and $\phi(E_R, E'_R)$ the detector resolution.

3.2.2 Annual modulating event rate

The expected direct-detection-event-rate is a function of \mathbf{v}_χ^{det} , that is the DM-particle-velocity in the laboratory reference-frame. As a consequence of the composition of velocities in Eq. 3.5, \mathbf{v}_χ^{det} acquires a periodic time dependence which is inherited by the differential rate, with a period of one year [16]. The Fourier expansion of the differential event rate is,

$$\frac{dR(t)}{dE_R} = A_0 + \sum_{n=1}^{\infty} A_n \cos n\omega(t - t_0) + \sum_{n=1}^{\infty} B_n \sin n\omega(t - t_0), \quad (3.11)$$

where A_n and B_n are Fourier coefficients,

$$\begin{aligned} A_n &= \frac{2}{T} \int_0^T dt \frac{dR(t)}{dE_R} [\cos(n\omega t) \cos(n\omega t_0) + \sin(n\omega t) \sin(n\omega t_0)] \\ B_n &= \frac{2}{T} \int_0^T dt \frac{dR(t)}{dE_R} [\cos(n\omega t) (-\sin(n\omega t_0)) + \sin(n\omega t) \cos(n\omega t_0)] \end{aligned} \quad (3.12)$$

where $\omega = 2\pi/T$, with $T = 1$ year, and t_0 is a reference time. If t_0 is the time of maximum rate in the energy interval of interest and the velocity distribution is isotropic, in particular $f(\mathbf{v}) = f(-\mathbf{v})$, the coefficients B_n are null [17]. Furthermore, a usual approximation in the literature is,

$$\frac{dR}{dE_R} \approx A_0 + A_1 \cos \omega(t - t_0) \quad (3.13)$$

because higher order harmonics decrease as ϵ^n , where ϵ is the ratio between $|\mathbf{v}_{det}^\odot|$ and $|\mathbf{v}_\odot^{gal}|$ [18]. In the approximation of Eq. 3.13, the modulation amplitude is conventionally defined as the difference between the differential rate in June and in December, respectively [17],

$$A_1(v_{min}) = \frac{1}{2} \left[\frac{dR}{dE}(v_{min}, \text{Jun } 1) - \frac{dR}{dE}(v_{min}, \text{Dec } 1) \right], \quad (3.14)$$

where v_{min} is the minimal velocity required to get a specific recoil energy E_R . The reason for this convention is the following. In June the velocity of the Earth is antiparallel to the velocity of the Sun, therefore the relative velocity is larger with respect to the time of the year when the two velocities are parallel, which is in December. DD experiments are limited by a certain energy threshold, below which the deposited energy in the target material is not visible, therefore commonly the larger the deposited energy, *i.e.* the relative DM-target velocity, the easier the detection of the event⁴.

However, it has been shown that,

1. the velocity distribution function is not isotropic (see *e.g.* Sec. 3.1.2 and [18]);
2. the time of maximum of the rate depends on the minimal velocity and on the type of interaction [22];
3. the hierarchy among higher order harmonics depends not trivially on the minimal velocity v_{min} [17];
4. the hierarchy among higher order harmonics depends also on the type of interaction, as we discussed in Sec. 4.2

For these reasons Eq. 3.13 is considered a rough approximation; one of the first studies developed in this work was dedicated to a refinement of the annual modulation phenomenology and it is presented in the next chapter.

3.3 DM-nucleus scattering cross section

From the particle physics point of view, the most interesting input entering in the description of the DM-observables is the differential cross-section.

⁴The story is different for low threshold experiments, which can probe the left tail of the DM-velocity distribution, as is discussed in the next chapter.

The scattering cross-section in the relativistic regime is defined as (Eq.4.9 of [146]),

$$d\sigma = \frac{|\mathcal{M}|^2}{F} dQ = \frac{1}{v} \frac{1}{4E_p^i E_k^i} |\mathcal{M}|^2 (2\pi)^4 \delta^{(4)}(p_N + k_\chi - p'_N - k'_\chi) \frac{d^3 p'_N}{(2\pi)^3 E_{p'}} \frac{d^3 k'_\chi}{(2\pi)^3 E_{k'}} \quad (3.15)$$

where $|\mathcal{M}|$ is the relativistic transition amplitude, F the incoming flux, dQ the Lorentz invariant phase space factor, v the relative velocity between incoming particles, $E_{\chi,N}^{i,f}$ the initial or final DM/nucleon energies and p_N, k_χ, p'_N and k'_χ the initial and final DM/nucleon quadri-momenta. By integrating Eq. 4.7, the differential cross-section with respect to the nuclear recoil energy, E_R , is [147],

$$\frac{d\sigma}{dE_R} = \frac{1}{32 m_\chi^2 m_T \pi v^2} |\mathcal{M}|^2 \quad (3.16)$$

Since the typical DM-velocity is $v \sim \mathcal{O}(10^{-3}c) \ll c$, the DM-nuclei interaction can be described in NR approximation. The relation between the relativistic, \mathcal{M} , and non-relativistic, \mathcal{M}_{NR} , transition amplitudes is [15],

$$\mathcal{M}_{NR} = \frac{\mathcal{M}}{4 m_\chi m_T} \quad (3.17)$$

Furthermore, the cross-section on non-polarised nuclei is the average over initial spins and the sum over the final spins. Using this information, the NR cross section is (see *e.g.* [148]),

$$\frac{d\sigma}{dE_R} = \frac{2 m_T}{4\pi v^2} \frac{1}{(2 J_\chi + 1)(2 J_T + 1)} \sum_{spins} |\mathcal{M}_{NR}|^2 \quad (3.18)$$

where J_T is the total angular momentum of the target nucleus.

SI and SD interactions. Since the nature of DM is unknown, an explicit expression for the cross-section requires arbitrary assumptions on the DM-nucleus interactions. An assumption widely adopted by the DD community to present experimental results is related to the conventional *spin-independent* (SI) and *spin-dependent* (SD) interactions⁵. SI and SD-interactions can be derived from the effective interactions,

$$\begin{aligned} \mathcal{O}_{SI} &= \bar{\chi}\chi \bar{N}N \\ \mathcal{O}_{SD} &= \bar{\chi}\gamma^\mu \gamma^5 \chi \bar{N}\gamma_\mu \gamma^5 N \end{aligned} \quad (3.19)$$

where χ is the DM field and N is the nucleon. \mathcal{O}_{SI} and \mathcal{O}_{SD} describe fermionic DM-nucleons couplings mediated by spin-0 and spin-1 mediators heavier than the scale

⁵As discussed in the next chapter, there are many effective interactions which in the NR limit are dependent or independent from the nuclear spin. The origin of the SI/SD-convention is probably related to historical reasons, for example associated to the well known papers by Engel, Pittel and Vogel (1992) [149] describing the physics of WIMP detection in laboratory and by Kamionkowski, Jungman and Griest (1995) [150], both focused on the hypothesis of the lightest neutralino as DM candidate.

of interest in DD searches. By performing a NR expansion of the bilinears in Eq. 3.19, which can be found for example in Eqs. 46 and 47 of [147], the interactions in Eq. 3.19 in the low energy limit are,

$$\begin{aligned}\mathcal{O}_{SI} &\simeq 4m_\chi m_T \mathbf{1}_{\chi N} \equiv 4m_\chi m_T \mathcal{O}_{SI}^{NR} \\ \mathcal{O}_{SD} &\simeq 4m_\chi m_T \mathbf{S}_\chi \cdot \mathbf{S}_N \equiv 4m_\chi m_T \mathcal{O}_{SD}^{NR}\end{aligned}\quad (3.20)$$

In agreement with Eq. 3.17.

SI and SD cross sections. The typical DM de Broglie wavelength is $\lambda_\chi = h/q > 1$ fm, where h is the Planck constant ($h \simeq 4.136 \times 10^{-15}$ eV · s) and $q \lesssim \mathcal{O}(10^2)$ MeV/c. For small q , λ_χ is larger than the typical nuclear size, $r_N \simeq 1$ fm, and therefore it is reasonable in a first approximation to describe the DM-nucleus scattering treating the nucleus as a point like object. The SI and SD DM-nuclei cross-sections, σ_{SI} and σ_{SD} , related to the NR interactions in Eqs. 3.20, and obtained using Eq. 3.18 with $|\mathcal{M}_{NR}|^2 = |\langle \mathcal{O}_{SI/SD}^{NR} \rangle|^2$, are [150],

$$\frac{d\sigma_{SI}}{dE_R} = \frac{2 m_T}{\pi v^2} [Z f_p + (A - Z) f_n]^2 \quad (3.21)$$

$$\frac{d\sigma_{SD}}{dE_R} = 2 m_T \frac{8G_F^2}{(2J_T + 1)v^2} S_A(0) \quad (3.22)$$

where v is the DM-nucleus relative velocity, Z is the atomic number, A is the atomic mass number, $f_{p,n}$ are the effective DM-nucleon-couplings for SI-interactions, G_F is the Fermi constant, J_T is the total angular momentum of the nucleus and $S_A(0)$ is the axial nuclear structure function at zero transferred momentum, defined as,

$$S_A(0) = \frac{(2J_T + 1)(J_T + 1)}{4\pi J_T} \times |(a_0 + a_1)\langle S_p \rangle + (a_0 - a_1)\langle S_n \rangle|^2 \quad (3.23)$$

In Equation 3.23, $a_0 = a_p + a_n$ and $a_1 = a_p - a_n$ are effective DM-nucleons couplings for SD-interactions and $\langle S_{p,n} \rangle = \langle T | S_{p,n} | T \rangle$ are the expectation values of the spin content of the proton and neutron groups in the nucleus (T).

For heavier nuclei and large DM-nuclei relative velocity, the point-like approximation for the nucleus worsens since the DM de Broglie wavelength can be smaller than the size of the nucleus and the DM-scattering off nuclei can be sensitive to the nuclear structure. Such scattering decoherence can be described by multiplying the point-like cross-sections by the so called *form factors*, $F(q)$, suppressing the scattering cross-sections for large q .

Helm form factor. For SI-interactions the form factor commonly used is the Helm form factor [151], which is the Fourier transform of a specific nuclear charge density distribution, proposed by Helm, which allows to write down the analytical expression for $F(q)$ [152],

$$F(q) = 3 \frac{j_1(q r_n)}{q r_n} e^{-\frac{(q s)^2}{2}} \quad (3.24)$$

where j_1 is the Bessel function of first kind, $j_1(x) = (\sin(q r_n) - q r_n \cos(q r_n))/(q r_n)^2$, $r_n = c^2 + \frac{7}{3} \pi a^2 - 5 s^2$ is the effective nuclear radius and c, a, s are nuclear parameters related to the charge density distribution. Using $c = 1.23 A^{1/3} - 0.60$ fm, $s = 0.9$ and $a = 0.52$, the Helm form factors for some nuclear targets are shown in Fig. 3.3.1.

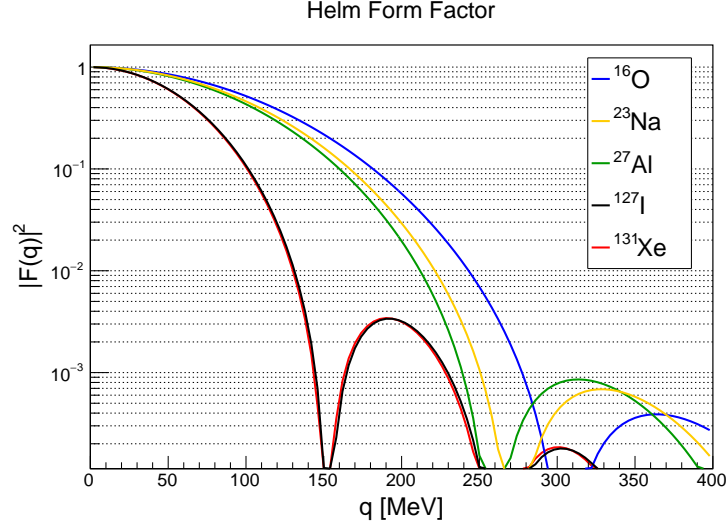


Figure 3.3.1: Helm form factors for O, Na, Al, I and Xe.

Axial structure function. For large q , the nuclear structure function⁶, related to the nucleons spin is,

$$S_A(q) = a_0^2 S_{00}(q) + a_0 a_1 S_{01}(q) + a_1^2 S_{11}(q) \quad (3.25)$$

which reduces to Eq. 3.23 for zero transferred momentum. The functions $S_{ij}(q)$ can be computed from the matrix elements of the nuclear axial currents [149].

3.4 Direct detection experiments and latest results

The first proposal for a DM DD experiment published by Goodman and Witten in 1985 [153], can be considered as the priming which motivated the tremendous engagement of the scientific community in the DM DD search. Since then, a huge effort was put in developing very sophisticated DM detection techniques which within the last decade made enormous progress and arrived at unprecedented sensitivities.

⁶Not called form factors because it is not normalised to 1. The common form factor is $F(q) = \frac{S_T(q)}{S_T(0)}$.

A concise overview of the DD experiments based on the detection of DM-nucleon scattering events, which probe DM masses in the range of hundreds of MeV to hundreds of GeV, is provided in the following⁷ (see [155] for an extensive review).

Experiments based on DM-scattering off nuclei. Experiments currently in operation can be classified according to their detection principle. Any particle interacting inside the detector volume deposits a certain amount of energy which is partially converted and measured as scintillation light if occurring in scintillators at room temperature (*e.g.* DAMA [25], ANAIS [26], COSINE [27], SABRE [43]), as scintillation light and lattice vibrations if the target material is made of scintillating cryogenic calorimeters (*e.g.* CRESST [4], COSINUS [156]), as charge and lattice vibrations if the detector is a cryogenic semiconductor (*e.g.* EDELWEISS [28], SuperCDMS [157], CDMSlite [158]), as ionisation signal or scintillation light if the experiments employ noble liquid single phase time projection chambers (TPCs) (*e.g.* NEWS-G [159], DEAP-3600 [160], XMASS [161]) or CCDs (*e.g.* DAMIC [162]) and as ionisation signal plus scintillation light in the case of dual phase TPCs (*e.g.* XENON1T [29], LUX [30], PandaX [31], LZ [32], DarkSide [33]). Finally, the energy is converted into bubbles in superheated liquids mainly containing fluorine if the experiment employs bubble chambers or superheated droplet detectors (*e.g.* PICO-60 [163], PICASSO [164]).

These classes of experiments push their limits towards different goals: room temperature scintillators are mainly dedicated to annual modulation search as they offer good time stability and large exposures, cryogenic detectors are suited for reaching low energy thresholds, $\sim \mathcal{O}(10 \text{ eV})$, therefore the focus is nowadays mainly on low mass DM search, while noble liquid TPC-based searches to-date arrive at ton-scale fiducial mass and place most stringent limits at $\mathcal{O}(10 \text{ GeV})$ DM-mass. However, this distinction is only valid if results are compared using the standard framework reviewed in Sec. 3.3. New methods have been proposed to lower the energy thresholds of conventional detectors which are based on the prediction of the Migdal effect [165, 166] and the bremsstrahlung [167], as applied, for instance, by the LUX [168] and XENON1T [169] collaborations.

The presence of fluorine nuclei in the atomic composition of superheated liquids, makes bubble chambers particular suited for SD DM-nuclei interactions. In particular, PICO-60, which employs C_3F_6 , provided the most stringent constraint on the DM-proton SD cross section in the DM-mass range $\sim [10 - 100] \text{ GeV}$ [163]. A further class of detectors was conceived to detect the angular differential rate of DM-nucleon scattering events (*e.g.* MIMAC [49], DRIFT [50], CYGNUS project [51]), to exploit the anisotropy of the nuclear recoil spatial distribution caused by the motion of the Solar system around the galactic center and towards the Cygnus constellation.

Current SI and SD experimental limits are shown in Figs. 3.4.1 and 3.4.2, respectively [155].

⁷The keV-MeV DM mass range can be probed by considering DM-electron interactions, as discussed in Ref. [154] and following literature. Refer to [155] and to <http://ddldm.physics.sunysb.edu/ddlDM/> for a collection of papers and tools related to DM-electron scatterings.

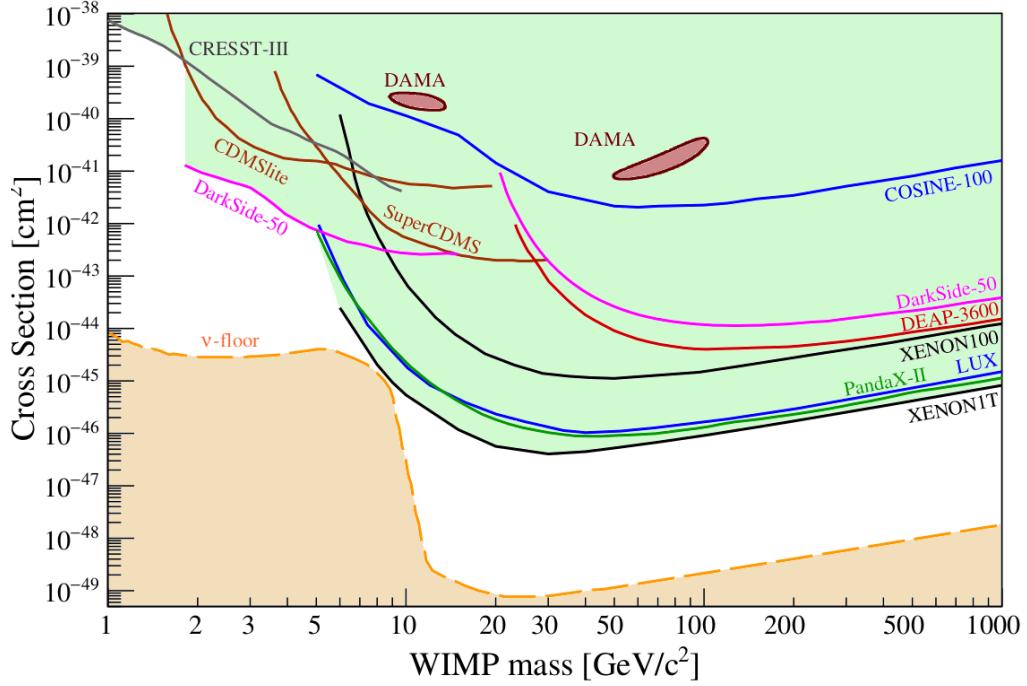


Figure 3.4.1: Experimental limits on elastic SI DM-nucleon interactions in the cross section versus DM mass plane [155]. The color coding is: black curves XENON1T [29] and XENON100 [170], blue LUX [30], at lower cross-sections, and COSINE-100 [27] below the two brown-shaded areas which represent the interpretation of the DAMA/LIBRA results performed in 2009 in [24] (the Na and I labels on the DAMA islands present on the original plot in [155] are inverted, as the island around $m_\chi = 10$ GeV is for Na and the one around $m_\chi = 80$ GeV is for I; for this reason the labels are removed here), green PandaX [31], red DEAP-3600 [160], magenta DarkSide-50 [33], brown lines SuperCDMS [157] and CDMSlite [158], gray CRESST-III [4]. The orange dashed line marks the DM parameter space which is limited by the irreducible background from coherent neutrino-nucleus scattering (CNNS), known as ‘neutrino-floor’, computed in [46] for Xe-based experiments.

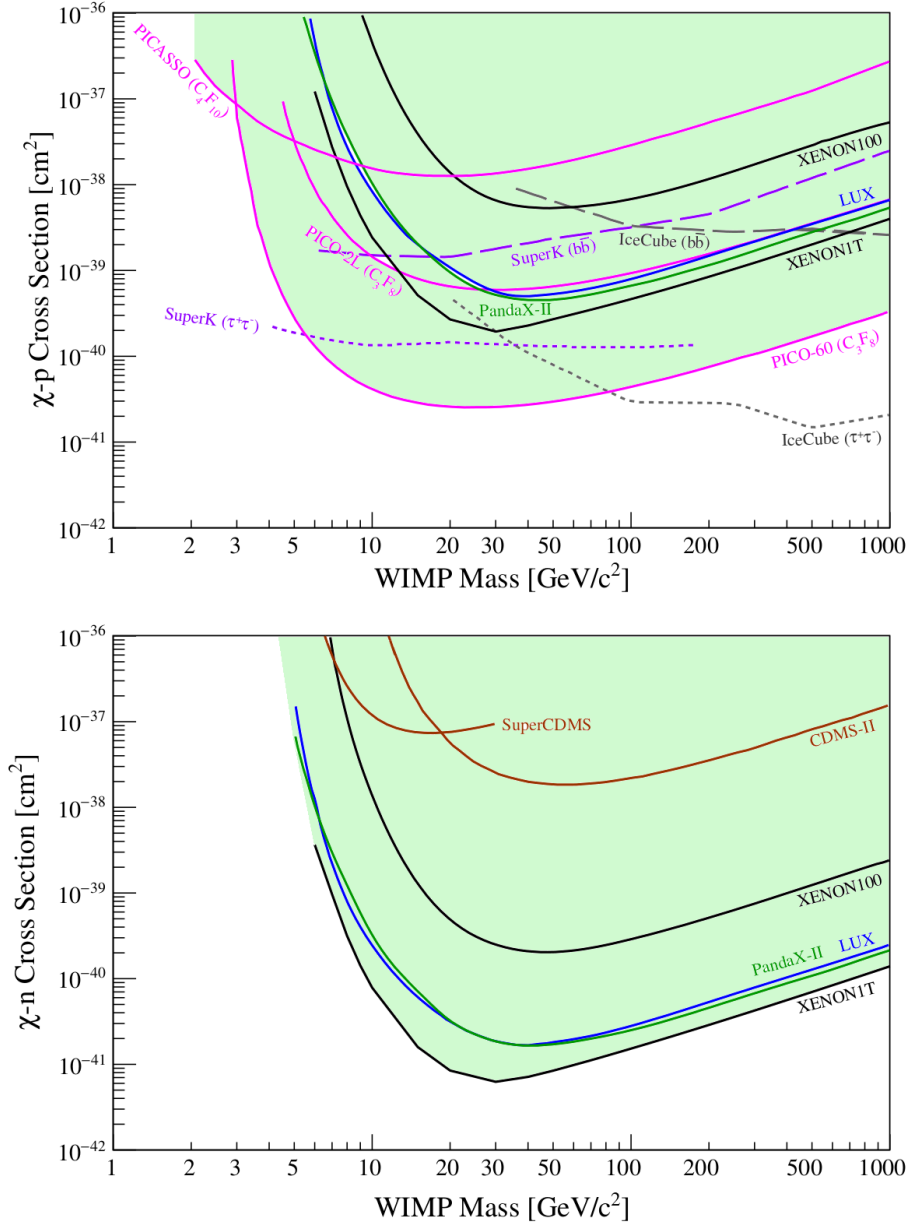


Figure 3.4.2: Experimental limits on elastic SD DM-nucleon interactions in the cross section versus DM mass plane [155]. **Top:** *proton-only* SD interactions. Color coding is: solid magenta PICO-60 [163] and PICASSO [164], solid black XENON1T [171] and XENON100 [170], solid blue LUX [172], solid green is PandaX [31], dashed black Icecube [173] and violet [174], for DM annihilation into $\tau\bar{\tau}$ (small dashed) and into $b\bar{b}$. **Bottom:** *neutron-only* SD interactions. In addition to color coding for top panel, solid brown limits indicate SuperCDMS [175] and CDMSlite [176].

The case of DAMA. The DAMA/LIBRA experiment is a room temperature NaI(Tl) scintillator, consisting of an array of 25 crystals, about 10 kg each, located in Gran Sasso National Laboratory (LNGS), Italy. The large mass exposure and the time stability of the setup [177] make it suitable for a continuous data taking which allows for a time dependent analysis of collected data. Although the single channel readout of scintillation light prevent from distinguishing nuclear recoils from e^-/γ events, the experiment can perform a background discrimination searching for the DM annual modulation signal discussed in Sec. 3.2.2.

Table 3.1: Combination of DAMA/LIBRA Phase-I and Phase-II results, in the energy range [2-6] keV. In the third column also DAMA/NaI data are included. In the analysis here reported, the period is left as free parameter. For the complete discussion of the results see [25].

	Phase-I+Phase-II	DAMA/NaI+Phase-I+Phase-II
Total exposure (ton \times yr):	2.17	2.46
Statistical significance:	12.0 σ	12.9 σ
Period (yr):	0.9987 \pm 0.0008	0.9987 \pm 0.0008
Phase (days):	145 \pm 5	145 \pm 5
Amplitude ([day kg keV] $^{-1}$):	0.0096 \pm 0.0008	0.0103 \pm 0.0008

During the first stage of the experiment, DAMA/NaI, an annual modulating signal was detected [178], which was confirmed by the results of the two phases, Phase-I [23] and Phase-II [25], of the subsequent stage, DAMA/LIBRA. In Fig. 3.4.1, the interpretation of the results of DAMA/NaI and DAMA/LIBRA Phase-I, performed in [24] in terms of the SI DM-nucleon scattering, is shown as two brown-shaded areas, while Tab. 3.1 contains an example of the combination of DAMA/NaI and DAMA/LIBRA results, including results from Phase-II, taken from [25].

For a discussion on the tension between the DAMA/LIBRA claim for the detection of the DM annual modulation signal and the null-results from the other experiments, see Sec. 6.1.

Chapter 4

Dark matter direct detection effective theory: two applications

The lack of evidence for the existence of DM beyond the cosmological and gravitational effects focuses the attention of the astroparticle physics community on the detection of the particles forming the DM cosmological component. In the desirable case a DM particle signal is detected, extracting information on the nature of the DM particle, such as mass, couplings and spin, is a priority. Motivated by this consideration, this chapter presents two studies which aim at identifying DM properties from the detection of DM particles at DD experiments. Common to these two studies is the application of effective theory methods to the theoretical modelling of the DD observables.

In Sec. 4.1 the non-relativistic effective theory of DD DM (NREFT) is reviewed. This is applied in Sec. 4.2 to model the expected annual modulation in the rate of DM-nucleus scattering events at DD experiments. In Sec. 4.3 the effective field theory methods are applied to study the scattering of DM particles by polarised nuclei.

4.1 Non-relativistic effective theory of DM direct detection (NREFT)

While the existence of DM particles is a well motivated hypothesis supported by large part of the scientific community, the understanding of the dynamics underlying the interaction of DM with SM-particles is currently far from our reach. As a consequence the community has adopted the agnostic approach to model in a common framework all the interactions which are compatible with the symmetries of the DM-nucleus system. This approach is known as the non-relativistic effective theory of direct detection (DD) (or of DM-nucleon interactions), or simply NREFT [14, 15]. In general, the effective theory approach to the description of a physical system starts from an analysis of the following aspects¹,

¹When describing a scene, like two people talking in a bar, you are likely to describe their position, their movements, the environment. I doubt you would start talking about their atomic composition.

1. the energy scale of interest,
2. the degrees of freedom involved,
3. the symmetry of the system.

One example of EFT is the one used in the past to describe physics processes probed at accelerators². This EFT is characterised by an energy scale $\Lambda \leq \mathcal{O}(10 \text{ TeV})$. The degrees of freedom involved are the ones with masses $m \leq \Lambda$ and the symmetry describing the system (*i.e.* the set of interacting particles) is Lorentz invariance. The effect of a potential higher energy scale is incorporated in unspecified coefficients, known as *Wilson coefficients*. The building blocks of this EFT are Lorentz invariant combinations of the fermionic and/or bosonic fields which are introduced for each degree of freedom .

EFT have also been applied to model DM-nucleus scattering events in DD experiments. NREFT is the most prominent example of an EFT approach to DD. In the case of DM DD, the energy scale of DM-nucleus scattering is $\mathcal{O}(\text{keV})$, as derived in Appendix B.2, therefore the DM-nucleus system is studied in non-relativistic (NR) approximation. The NREFT expresses the NR transition amplitude $|\langle \mathcal{M}_{NR} \rangle|$ as a power series in $|\mathbf{q}|/m_N$ and \mathbf{v}/c , where \mathbf{q} is the transferred momentum, m_N is the nucleon mass, \mathbf{v} is the relative DM-nucleus velocity and c is the speed of light. It is based on the assumption that DM-nucleon interactions are mediated by bosons heavier than $\sim 200 \text{ MeV}$, which is the order of typical transferred momentum (see Appendix B.2). Another assumption is that DM-nucleon currents are one-body currents, that is interactions with two or more nucleons mediated by pions are neglected³. Under such assumptions, the degrees of freedom of the system are DM and nucleons; their interactions are constrained by rotational and Galilean invariance, the symmetries of the DM-nucleon system.

NREFT building blocks

The building blocks of the NREFT of DM-nucleon interactions are Galilean invariant combinations of low-energy operators, which are the DM and the nucleon three vector spin, $\hat{\mathbf{S}}_\chi$ and $\hat{\mathbf{S}}_N$, and two combinations of their momenta, namely the transferred momentum, $i\hat{\mathbf{q}}$ and the transversal velocity, $\hat{\mathbf{v}}^\perp$,

$$\hat{\mathbf{v}}^\perp = \mathbf{v} + \frac{\mathbf{q}}{2\mu} = \frac{\mathbf{k} + \mathbf{k}'}{2m_\chi} - \frac{\mathbf{p} + \mathbf{p}'}{2m_N} \quad (4.1)$$

where \mathbf{v} is the DM-nucleon relative velocity, μ is the DM-nucleon reduced mass, \mathbf{k} , \mathbf{k}' , \mathbf{p} and \mathbf{p}' are the DM and nucleon initial and final momenta, m_χ and m_N their mass and $\hat{\mathbf{v}}^\perp$ is the transversal velocity, as $\hat{\mathbf{v}}^\perp \cdot \hat{\mathbf{q}} = 0$. The low energy-operators $\hat{\mathbf{S}}_\chi$, $\hat{\mathbf{S}}_N$, $i\hat{\mathbf{q}}$ and

An effective theory is a representation of reality which reproduces the phenomenology at the scale of interest.

²The validity of the EFT approach for the DM search at LHC has been investigated in [179]. For a review on the more recent approach based on the so-called ‘simplified models’ see [180]

³The implication of such simplification is discussed at the end of this section.

$\hat{\mathcal{O}}_1 = \mathbf{1}_\chi \mathbf{1}_N$	$\hat{\mathcal{O}}_{11} = i \hat{\mathbf{S}}_\chi \cdot \frac{\hat{\mathbf{q}}}{m_N} \mathbf{1}_N$
$\hat{\mathcal{O}}_3 = i \hat{\mathbf{S}}_N \cdot \left(\frac{\hat{\mathbf{q}}}{m_N} \times \hat{\mathbf{v}}^\perp \right) \mathbf{1}_\chi$	$\hat{\mathcal{O}}_{12} = \hat{\mathbf{S}}_\chi \cdot \left(\hat{\mathbf{S}}_N \times \hat{\mathbf{v}}^\perp \right)$
$\hat{\mathcal{O}}_4 = \hat{\mathbf{S}}_\chi \cdot \hat{\mathbf{S}}_N$	$\hat{\mathcal{O}}_{13} = i \left(\hat{\mathbf{S}}_\chi \cdot \hat{\mathbf{v}}^\perp \right) \left(\hat{\mathbf{S}}_N \cdot \frac{\hat{\mathbf{q}}}{m_N} \right)$
$\hat{\mathcal{O}}_5 = i \hat{\mathbf{S}}_\chi \cdot \left(\frac{\hat{\mathbf{q}}}{m_N} \times \hat{\mathbf{v}}^\perp \right) \mathbf{1}_N$	$\hat{\mathcal{O}}_{14} = i \left(\hat{\mathbf{S}}_\chi \cdot \frac{\hat{\mathbf{q}}}{m_N} \right) \left(\hat{\mathbf{S}}_N \cdot \hat{\mathbf{v}}^\perp \right)$
$\hat{\mathcal{O}}_6 = \left(\hat{\mathbf{S}}_\chi \cdot \frac{\hat{\mathbf{q}}}{m_N} \right) \left(\hat{\mathbf{S}}_N \cdot \frac{\hat{\mathbf{q}}}{m_N} \right)$	$\hat{\mathcal{O}}_{15} = - \left(\hat{\mathbf{S}}_\chi \cdot \frac{\hat{\mathbf{q}}}{m_N} \right) \left[\left(\hat{\mathbf{S}}_N \times \hat{\mathbf{v}}^\perp \right) \cdot \frac{\hat{\mathbf{q}}}{m_N} \right]$
$\hat{\mathcal{O}}_7 = \hat{\mathbf{S}}_N \cdot \hat{\mathbf{v}}^\perp \mathbf{1}_\chi$	$\hat{\mathcal{O}}_{17} = i \frac{\hat{\mathbf{q}}}{m_N} \cdot \mathcal{S} \cdot \hat{\mathbf{v}}^\perp \mathbf{1}_N$
$\hat{\mathcal{O}}_8 = \hat{\mathbf{S}}_\chi \cdot \hat{\mathbf{v}}^\perp \mathbf{1}_N$	$\hat{\mathcal{O}}_{18} = i \frac{\hat{\mathbf{q}}}{m_N} \cdot \mathcal{S} \cdot \hat{\mathbf{S}}_N$
$\hat{\mathcal{O}}_9 = i \hat{\mathbf{S}}_\chi \cdot \left(\hat{\mathbf{S}}_N \times \frac{\hat{\mathbf{q}}}{m_N} \right)$	$\hat{\mathcal{O}}_{19} = \frac{\hat{\mathbf{q}}}{m_N} \cdot \mathcal{S} \cdot \frac{\hat{\mathbf{q}}}{m_N}$
$\hat{\mathcal{O}}_{10} = i \hat{\mathbf{S}}_N \cdot \frac{\hat{\mathbf{q}}}{m_N} \mathbf{1}_\chi$	$\hat{\mathcal{O}}_{20} = \left(\hat{\mathbf{S}}_N \times \frac{\hat{\mathbf{q}}}{m_N} \right) \cdot \mathcal{S} \cdot \frac{\hat{\mathbf{q}}}{m_N}$

Table 4.1: List of the NREFT building blocks [14, 182, 183].

$\hat{\mathbf{v}}^\perp$ are all hermitian as well as their combinations. All the independent contributions to the NR amplitude, \mathcal{M}_{NR} , are obtained by contraction of the low-energy operators with Kronecker deltas δ_{ij} and ϵ_{ijk} -tensors [181]. The resulting set of building blocks, $\hat{\mathcal{O}}_i$, up to first order in $\hat{\mathbf{v}}^\perp$ and second order in $\hat{\mathbf{q}}$, are listed in Tab. 4.1 [14, 182].

$\hat{\mathcal{O}}_1$ and $\hat{\mathcal{O}}_4$ are the two interactions which are separately adopted to show the experimental limits on the cross-section versus DM-mass parameter space, the conventional spin-independent (SI) and spin-dependent (SD) interactions discussed in Sec. 3.3. The operator $\hat{\mathcal{O}}_2 = v^\perp \hat{\mathcal{O}}_1$ was initially included among the possible interesting operators but removed afterwards, as quadratic in $\hat{\mathbf{v}}^\perp$ and $\propto \hat{\mathcal{O}}_1$. The same is true for $\hat{\mathcal{O}}_{16}$ which is a linear combination of $\hat{\mathcal{O}}_{12}$ and $\hat{\mathcal{O}}_{15}$ [148].

For spin = 1/2, the operator $S_i = \sigma_i/2$, where σ_i is the Pauli matrix (S_i stays both for S_χ and S_N). The two additional operators in this list, $\hat{\mathcal{O}}_{17}$ and $\hat{\mathcal{O}}_{18}$, with respect to the sixteen appearing in [14], extend the list to DM-spin = 1 [184] and the other two further operators, $\hat{\mathcal{O}}_{19}$ and $\hat{\mathcal{O}}_{20}$, for spin-1 DM are found in [183]. \mathcal{S} is a symmetric combination of DM-polarization vectors, $S_{ij} = i(\epsilon_i^\dagger \epsilon_j + \epsilon_j^\dagger \epsilon_i)$. In the reference frame where the z-axis is aligned to the DM particle momentum, \mathbf{k} , the polarisation vector is defined as,

$$\epsilon_s^\mu(\mathbf{k}) = \left(\frac{|\mathbf{k}|}{m_\chi}, \frac{|\mathbf{k}_0|}{m_\chi} \mathbf{e}_s(\mathbf{k}) \right) \quad (4.2)$$

where $s = 1, 2, 3$, $\mathbf{e}_{1,2}(\mathbf{k})$ are two orthonormal unit vectors and $\mathbf{e}_3(\mathbf{k}) = \mathbf{k}/|\mathbf{k}|$ [185]. The $\hat{\mathcal{O}}_i$ combinations are defined as the *building blocks* of the NREFT, they are at most quadratic in the momentum transfer, and linear in the transverse relative velocity [14, 184].

DM-nucleon interaction hamiltonian

The interaction hamiltonian density written as a combination of the *building-blocks* is [186],

$$\hat{\mathcal{H}} = 2 \sum_i \left[c_i^p \left(\frac{\mathbf{1} + \tau_3}{2} \right) + c_i^n \left(\frac{\mathbf{1} - \tau_3}{2} \right) \right] f_{\hat{\mathcal{O}}_i}(q^2, v^{\perp 2}) \hat{\mathcal{O}}_i \quad (4.3)$$

where i runs over the non-zero coefficients in Tab. 4.1, c_i^p and c_i^n are the coupling constants for DM-proton and DM-neutron interactions, respectively, $\mathbf{1}$ is the 2×2 identity matrix, τ_3 is the diagonal Pauli matrix and f_i are coefficients which can depend on $q^2, v^{\perp 2}$ and on the non-dynamical parameters, such as m_χ, m_N and coupling coefficients. The structure of $\hat{\mathcal{H}}$ in Eq. 4.3 is thought to project the nucleon state into an eigenstate of isospin. It can be equally written as,

$$\hat{\mathcal{H}} = \sum_i f_{\hat{\mathcal{O}}_i}(q^2, v^{\perp 2}) (c_i^0 \hat{\mathcal{O}}_i \mathbf{1} + c_i^1 \hat{\mathcal{O}}_i \tau_3) \quad (4.4)$$

where $c_i^p = (c_i^0 + c_i^1)/2$ and $c_i^n = (c_i^0 - c_i^1)/2$.

DM-nucleus interaction hamiltonian

In the one-body current approximation, the effective hamiltonian density for DM interactions with the whole nucleus is obtained by summing the DM-nucleon hamiltonian density in Eq. 4.4 over all the nucleons,

$$\hat{\mathcal{H}}_T = \sum_{k=1}^A \sum_i f_{\hat{\mathcal{O}}_i^k}(q^2, v^{\perp 2}) (c_i^0 \hat{\mathcal{O}}_i^k \mathbf{1} + c_i^1 \hat{\mathcal{O}}_i^k \tau_3^k) \quad (4.5)$$

In order to calculate the amplitude, \mathcal{M}_{NR} , the matrix element of the DM-nucleus interaction hamiltonian between initial and final states is evaluated, where initial and final states are tensor products of the DM and nuclear states, $|\mathbf{k}, j_\chi\rangle$ and $|\mathbf{p}_T, J_T\rangle$, where T indicates the target nucleus. The non-relativistic amplitude for DM-nucleus interactions is related to $\hat{\mathcal{H}}_T$ by,

$$\langle f | \int d^3\mathbf{r} \hat{\mathcal{H}}_T | i \rangle = (2\pi)^3 \delta(\mathbf{k}'_T + \mathbf{p}' - \mathbf{k}_T - \mathbf{p}) i \mathcal{M}_{NR} \quad (4.6)$$

The NR amplitude \mathcal{M}_{NR} in Eq. 4.6 is the same as the NR amplitude in Eq. 2.1 of [15].

The calculation involved in Eq. 4.6 is not reviewed here and it can be found in [14, 186]. However, it is important to stress one point, *i.e.* that the NR amplitude can be simplified in a sum of five terms, each one presenting two factors: a function of the kinematics parameters and DM-nucleon coupling coefficients and one which only depends on the properties of the nucleus, that is the *nuclear matrix elements*. The module squared of the NR amplitude in Eq. 4.6 containing the five terms, provides the NREFT DM-nucleus differential cross-section described in the following, which results equal to the sum of eight independent terms, as explained below.

DM-nucleus cross-section

The differential cross-section, $d\sigma/dE_R$, in Eq. 3.18 can be expressed as follows (see, e.g., [148])

$$\frac{d\sigma_T}{dE_R} = \frac{2m_T}{4\pi v^2} \frac{4\pi}{(2J_T + 1)} \sum_{\tau, \tau', k} \left(\frac{q^2}{m_N^2} \right)^{\ell(k)} R_k^{\tau\tau'} \left(v_T^{\perp 2}, \frac{q^2}{m_N^2}, \{c_i^\tau, c_j^{\tau'}\} \right) W_k^{\tau\tau'}(y), \quad (4.7)$$

m_T is the target mass, $v = |\mathbf{v}_\chi^{det}|$, J_T is the target nucleus total angular momentum, m_N the nucleon mass, $v_T^{\perp 2} = v^2 - q^2/(4\mu_T^2)$ is the nucleus transversal velocity squared, with $q = \sqrt{2m_T E_R}$ the momentum transfer, and μ_T the DM-nucleus reduced mass. The $R_k^{\tau\tau'} \left(v_T^{\perp 2}, \frac{q^2}{m_N^2}, \{c_i^\tau, c_j^{\tau'}\} \right)$ are eight DM response functions, which depend on the NR effective coefficients, c_i , where i runs over the DM-nucleon interactions for spin 0-1/2 listed in Tab. 4.1 [14]. The index $k = M, \Sigma', \Sigma'', \Phi'', \Phi''M, \tilde{\Phi}', \Delta, \Delta\Sigma'$ refer to the nuclear response functions $W_k^{\tau\tau'}(y)$, where $y = (qb/2)^2$ and b is the harmonic oscillator size parameter, $b = (41.467/(45 \cdot A^{-1/3} - 25 \cdot A^{-2/3}))^{1/2}$, where A is the atomic mass number. The index $\ell(k)$ is 0 for $k = M, \Sigma', \Sigma''$ and 1 for the other responses. The $R_k^{\tau\tau'}$ for spin 1/2 DM were first derived in [14] and are listed in Appendix C.1, where J_χ is the DM particle spin. The $R_k^{\tau\tau'}$ for vector DM are listed in Appendix B of [184]. The eight nuclear response functions, $W_k^{\tau\tau'}$, in Eq. (4.7) are quadratic in reduced matrix elements of nuclear charges and currents, and must be computed numerically. Since they are independent from DM assumptions, they are the same for spin 0, 1/2, and 1-DM. The computation of $W_k^{\tau\tau'}$ can be done at different levels of accuracy and it is a rich field of research in nuclear physics. The simplest approach is to use shell model calculations, as developed for example in [14] and [186]. Since their computation is independent from DM assumptions, in the next section the nuclear response functions will be employed as a black box, while referring to the Appendix of [148] for computation details.

4.1.1 NREFT application, limitations and subsequent developments

In recent years, the NREFT framework described in this section was adopted by some DD experimental collaborations [187, 188], as well as by the CRESST collaboration [7], to present their experimental results. The method was to draw limits on single NR coefficients, c_i , as function of the DM-mass, assuming all the other $c_j = 0$, with $j \neq i$. The framework was also applied to compare the limits on the Wilson coefficients in a ‘model independent’ manner [189], to highlight the target dependence of the DM-observables and, ideally, identify the source of tension which afflicts the comparison of the DD results since long time. Such tension is due to the claim of the DAMA/LIBRA collaboration of the detection of the DM annual modulation signal [25], which has not been confirmed by any other experiment so far.

However, the NREFT framework and its application has been criticised and discussed extensively both from the nuclear and the particle physics points of view. In fact, the NREFT has been improved by using more sophisticated nuclear calculations, together

with more advanced DM-nucleon EFTs, as discussed in the following. This paragraph summarises, at the best of our knowledge, developments and refinements of [14, 15].

The efforts to improve the NREFT were stimulated by three limitations of the NREFT proposal and application, which we list in the following and discuss subsequently.

1. The exclusion of light mesons from the theory, which motivated the application of chiral effective field theories (ChEFT) to model DM-nucleon and DM-meson interactions,
2. the use of the shell model for the calculation of the nuclear structure functions, which pushed the community to apply more recent and already available nuclear physics calculations to obtain improved nuclear response functions and uncertainty estimations,
3. From the application point of view, the tendency to use single building blocks to derive experimental constraints or phenomenological conclusions, neglecting the matching with the UV-energy-scale.

Let us discuss the first point. Already in [190] long-distance QCD corrections to the DM-nucleon interactions were discussed, within the framework of ChEFT. In QCD, the spontaneous symmetry breaking of $SU(2)_A$ produces pseudo Nambu Goldstone bosons, the pions. These latter mediate nucleon-nucleon interactions in the nucleus and can give rise to two-body currents which give relevant contributions to the DM-nucleon cross-sections, as extensively studied in [191–194]. All these works stress that the ChEFT predicts pion-poles which increase the contribution of operators which would, otherwise, be suppressed by factors $\mathcal{O}(q^2)$.

For what concerns nuclear response functions, one-body shell model calculations [14, 186], have been improved by including two-body currents [191, 195]. One or two-body shell model calculations are currently the best approximation for some heavy nuclei. For light nuclei, very accurate ab initio nuclear calculations are starting to be available, accompanied by uncertainties estimations - see *e.g.* [196–198].

The third and last point is a criticism to NREFT application which arise if one wants to draw physical conclusions from DD-results. NR-interactions are the low-energy version of some unknown UV theory. To extract physical insights from low energy experimental results, a specific UV-theory must be considered. The reason is that the NR-reduction of UV-interactions typically is a combination of the building blocks in Tab. 4.1. The combination is weighted by NR-coefficients c_i whose functional form (and potential dependence on kinematical parameters) is derived by using the matching procedure typical of the EFT method. An example is the well known case of the pion-pole; it appears in the NR coefficient c_6 and enhances the contribution of $\hat{\mathcal{O}}_6$ in the NR reduction of fermionic DM-quark axial current, which combines $\hat{\mathcal{O}}_4$ and $\hat{\mathcal{O}}_6$. Recipes to map all the possible Lorentz invariant currents into the NR regime have been proposed [147, 181, 184, 193, 194]. Furthermore, the connection of specific UV models with

effective currents at the electroweak scale was studied in [199] and [200]. They showed that the running of the coupling constants between these two scales introduces relations among effective currents at the electroweak scale, which further complicate the construction of a general framework at low energy univocally connected with the above UV theory.

4.2 Annual modulation in NREFT

The NREFT framework is now applied to model the time-dependence of the expected rate of nuclear recoil events in DD experiments. If DM couples to SM particles in the nucleus, regardless of the DM-nature, time-dependent analyses of data provided by DD experiments could reveal a DM signal in terms of an annual modulating energy spectrum (see Sec. 3.2.2). For this reason the search for the annual modulation in DD experiment is a powerful tool to investigate the existence of DM particles in our galaxy.

In 2018, the DAMA/LIBRA collaboration released updated results on the search for the annual modulated signal from DM scattering in radio-pure NaI(Tl) crystals [25]. Based on analysis of such data [201], it has been argued that if the new results by the DAMA/LIBRA collaboration are interpreted in terms of DM, these disfavour the canonical spin-independent DM-nucleon interaction [201–203] with a statistical significance of 5.2 (2.5) standard deviations for DM masses around 8 (54) GeV [201]. The results in [201–203], motivated an exploration of alternative DM-nucleon interactions which could better fit the updated DAMA/LIBRA data [203]. S. Kang *et al* found that DM-nucleon interactions leading to DM-nucleus scattering cross-sections independent of the DM-nucleus relative velocity can fit the new DAMA/LIBRA data for a broad range of DM masses (in contrast to the canonical spin-independent interaction), and that a different coupling to protons and neutrons is necessary to achieve an acceptable fit (in terms of chi squared per degree of freedom) of the new DAMA/LIBRA data (see Tab. 1 in [203]).

As highlighted by these findings, the reconstruction of the parameters of the annual modulation probed by DM direct detection experiments depends upon the assumed DM-nucleon interaction. In this work we systematically explore the dependence of,

1. The modulation amplitude A_1 ;
2. The time at which the predicted rate of nuclear recoil events is maximum, $t_{\max}(v_{\min})$;
3. The target dependence of $t_{\max}(v_{\min})$, inspired by previous works [21, 22], effect related to the combination of *building-blocks* in Tab. 4.1 with different dependence on the dark-matter-nucleus relative velocity (see Sec. 4.2.2);
4. The validity of the single cosine approximation for the rate of nuclear recoil events ($A_1/A_{n \geq 2} \gg 1$ in Eq. 28 of [17]).

on the nature of the underlying DM-nucleon interaction, within the NREFT of DM-nucleon interactions [14, 15].

4.2.1 Theoretical Framework

The foundations of the phenomenology of DM DD are reviewed in Chap. 3. The computation of the differential rate of DM-nucleus scattering events per unit detector mass in a DD experiment is described in Eq. 3.9 [17]. In this equation, $f(\mathbf{v}_\chi^{det} + \mathbf{v}_{det}^{gal})$ denotes the DM velocity distribution in the detector rest frame, where \mathbf{v}_χ^{det} is in general a function of time, t , and $d\sigma/dE_R$ is the differential cross-section for DM-nucleus scattering. For $d\sigma/dE_R$ three cases are considered, separately. In the first one the DM-nucleus interactions are mediated by individual NREFT operators. In the second and third one a linear combination of NREFT operators is considered, corresponding to the magnetic dipole and anapole DM model, respectively.

Cross-section

Individual NREFT operators. This part is focused on four operators, or *building-blocks*, $\hat{O}_1, \hat{O}_7, \hat{O}_8$ and \hat{O}_{11} . Below the explicit equations for $d\sigma/dE_R$ for these four cases are provided, starting from the NREFT cross-section in Eq. 4.7,

$$\begin{aligned}
\left. \frac{d\sigma}{dE_R} \right|_{\hat{O}_1} &= \frac{m_T}{2\pi v^2} \sum_{\tau, \tau'} c_1^{(\tau)} c_1^{(\tau')} \tilde{W}_M^{\tau\tau'}(q^2), \\
\left. \frac{d\sigma}{dE_R} \right|_{\hat{O}_7} &= \frac{m_T}{2\pi v^2} \sum_{\tau, \tau'} c_7^{(\tau)} c_7^{(\tau')} \frac{(v^2 - v_{min}^2)}{8} \tilde{W}_{\Sigma'}^{\tau\tau'}(q^2), \\
\left. \frac{d\sigma}{dE_R} \right|_{\hat{O}_8} &= \frac{m_T}{2\pi v^2} \sum_{\tau, \tau'} c_8^{(\tau)} c_8^{(\tau')} \frac{J_\chi(J_\chi + 1)}{3} \left[v^2 \tilde{W}_M^{\tau\tau'}(q^2) - v_{min}^2 \left(\tilde{W}_M^{\tau\tau'}(q^2) - \frac{4\mu^2}{m_N^2} \tilde{W}_\Delta^{\tau\tau'}(q^2) \right) \right], \\
\left. \frac{d\sigma}{dE_R} \right|_{\hat{O}_{11}} &= \frac{m_T}{2\pi v^2} \sum_{\tau, \tau'} c_{11}^{(\tau)} c_{11}^{(\tau')} \frac{J_\chi(J_\chi + 1)}{3} \times \left[\frac{q^2}{m_N^2} \tilde{W}_M^{\tau\tau'}(q^2) \right], \tag{4.8}
\end{aligned}$$

where E_R is the recoil energy, m_T the target mass, $v = |\mathbf{v}_\chi^{det}|$, $c_i^\tau = (c_p \pm c_n)$ the NR Wilson coefficients, with $\tau = 0, 1$ and p, n for protons and neutrons, $\tilde{W}_k^{\tau\tau'}$ are the nuclear response functions times $4\pi/(2J_T + 1)$, where J_T is the nuclear angular momentum, $v_{min} = q/(2\mu_T)$ (see Appendix B.2), with μ_T the DM-nucleus reduced mass, J_χ is the DM-spin and m_N the nucleon mass. These are used as representative of four classes of *building-blocks* with specific dependence of $d\sigma/dE_R$ on relative velocity, $v = |\mathbf{v}_\chi^{det}|$, and transferred momentum, $q = |\mathbf{q}|$. The four classes are (i) $\propto 1/v^2$, (ii) $\propto q^2/v^2$, (iii) $\propto (1 - q^2/v^2)$ and (iv) combinations of $O(1)$ and $O(q^2/v^2)$ terms.

Magnetic dipole DM - As anticipated, here the NREFT operators are used to treat specific relativistic interactions. In particular, the magnetic dipole DM interaction

(MDDM) is considered [21], which couples the DM-spin with the electromagnetic (EM) field of the nucleus⁴. It is null for Majorana particles, therefore Dirac fermions must be considered. The interaction Lagrangian is [206],

$$\mathcal{L} = -\lambda_\chi \bar{\chi} \sigma^{\mu\nu} \chi F_{\mu\nu} \quad (4.9)$$

where λ_χ is the dipole coupling constant, χ the DM-field and $F_{\mu\nu}$ the EM strength tensor. The Lagrangian in Eq. 4.9 is a dim-5 operator, therefore $[\lambda_\chi] = \text{GeV}^{-1}$. The DM-nucleus scattering cross-section for MDDM expressed in terms of $\tilde{W}_k^{NN'}$ [14] and c_i^N , with $N, N' = p, n$, is derived in Appendix C.2 and it is,

$$\begin{aligned} \frac{d\sigma}{dE_R} = \frac{m_T}{2\pi v^2} \alpha \pi \lambda_\chi^2 \left[\left(\frac{1}{m_\chi^2} - \frac{1}{\mu_T^2} + \frac{1}{\mu_T^2} \frac{v^2}{v_{min}^2} \right) \tilde{W}_M^{pp} + \frac{1}{m_N^2} \left(\tilde{\mu}_p^2 \tilde{W}_{\Sigma'}^{pp} + 2\tilde{\mu}_p \tilde{\mu}_n \tilde{W}_{\Sigma'}^{np} + \tilde{\mu}_n^2 \tilde{W}_{\Sigma'}^{nn} \right) \right. \\ \left. + 4\tilde{W}_\Delta^{pp} - 4\tilde{\mu}_p \tilde{W}_{\Delta\Sigma'}^{pp} - 4\tilde{\mu}_n \tilde{W}_{\Delta\Sigma'}^{pn} \right] \quad (4.10) \end{aligned}$$

where m_T is the target nucleus mass, $v = |\mathbf{v}_\chi^{det}|$, α the fine structure constant, μ_T the DM-nucleus reduced mass, $\tilde{\mu}_{p,n}$ the nucleon magnetic moments.

Anapole DM The anapole DM interaction (ADM) consists in the coupling of the DM-spin with the EM-current, \mathcal{J}_μ^{EM} , and it is non-null both for Majorana and Dirac DM-particles [206, 207],

$$\mathcal{L} = -a_\chi \bar{\chi} \gamma^\mu \gamma^5 \chi \mathcal{J}_\mu^{EM} \quad (4.11)$$

where a_χ is the anapole coupling constant⁵ and $\mathcal{J}_\mu^{EM} = \partial^\nu F_{\mu\nu}$. The Lagrangian in Eq. 4.11 is a dim-6 operator⁶, therefore $[a_\chi] = \text{GeV}^{-2}$. The DM-nucleus scattering cross-section for ADM expressed in terms of nuclear response functions $\tilde{W}_k^{NN'}$ [14] and c_i^N , with $N, N' = p, n$, is [208],

$$\begin{aligned} \frac{d\sigma_T}{dE_R} = \frac{m_T}{2\pi v^2} a_\chi^2 \left[v^2 \tilde{W}_M^{pp} - v_{min}^2 \tilde{W}_M^{pp} + \frac{4\mu_T^2}{m_N^2} v_{min}^2 \left[\tilde{W}_\Delta^{pp} - \tilde{\mu}_n \tilde{W}_{\Delta\Sigma'}^{pn} - \tilde{\mu}_p \tilde{W}_{\Delta\Sigma'}^{pp} + \right. \right. \\ \left. \left. + \frac{1}{4} \left(\tilde{\mu}_p^2 \tilde{W}_{\Sigma'}^{pp} + 2\tilde{\mu}_p \tilde{\mu}_n \tilde{W}_{\Sigma'}^{np} + \tilde{\mu}_n^2 \tilde{W}_{\Sigma'}^{nn} \right) \right] \right] \quad (4.12) \end{aligned}$$

where m_T is the target nucleus mass, $v = |\mathbf{v}_\chi^{det}|$, μ_T the DM-nucleus reduced mass, $v_{min} = q/2\mu_T$, $\tilde{\mu}_{p,n}$ the nucleon magnetic moments.

⁴A recent paper [204] shows that thermal DM with EM form factors in the sub-GeV regime is ruled out if it is required to make 100% of DM. Thermal DM with MDDM interaction and $m_\chi > 10$ GeV was already ruled out in the past [205]. DM-particle with EM form factors, produced by different cosmological mechanisms are not constrained and can be still DM [204].

⁵See Fig. 4 of [207] for the curve $a_\chi(m_\chi)$ needed to account for the DM relic density.

⁶The dim-4 operator coupling the DM-anapole to the standard photon field, $\bar{\chi} \gamma^\mu \gamma^5 \chi A_\mu$, would be not gauge invariant, that is why a dim-6 operator is considered [207].

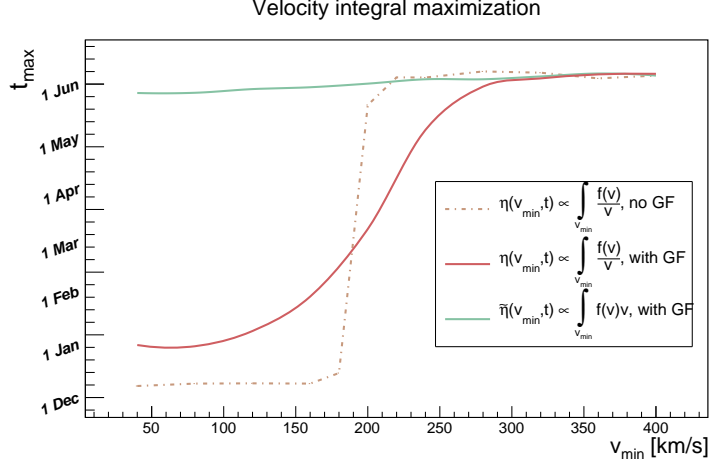


Figure 4.2.1: Time of maximum of the velocity distribution integral during the year: $\eta(v_{min}, t)$ in absence of the gravitational focusing (GF) effect (point-dashed brown curve), $\eta(v_{min}, t)$ (solid red curve) including GF and $\tilde{\eta}(v_{min}, t)$ (light green curve), where the plots including and not including GF are overlapped.

Velocity distribution integrals

In order to convolve the NREFT differential cross-sections with the velocity distribution in Eq. 3.4, two velocity distribution integrals must be computed,

$$\begin{aligned} \eta(v_{min}, t) &= \int_{v_{min}}^{|\mathbf{v}_\chi^{det} + \mathbf{v}_{det}^{gal}| < v_{esc}} d\mathbf{v}_\chi^{det} \frac{f(\mathbf{v}_\chi^{det}(t) + \mathbf{v}_{det}^{gal})}{v} \\ \tilde{\eta}(v_{min}, t) &= \int_{v_{min}}^{|\mathbf{v}_\chi^{det} + \mathbf{v}_{det}^{gal}| < v_{esc}} d\mathbf{v}_\chi^{det} v f(\mathbf{v}_\chi^{det}(t) + \mathbf{v}_{det}^{gal}), \end{aligned} \quad (4.13)$$

where $v = |\mathbf{v}_\chi^{det}(t)|$. For this reason, a C++/ROOT code was written which computes the three-dimensional and time dependent velocity distribution integrals, $\eta(v_{min}, t)$ and $\tilde{\eta}(v_{min}, t)$. The effect of the gravitational focusing (GF), discussed in Sec. 3.1.2, is taken into account following the approach developed in [143] and [34] and implemented using the convenient change in the integration variable discussed in Appendix B.1. The curves $t_{max}(v_{min})$ for $\eta(v_{min}, t)$ (point-dashed brown line) and $\tilde{\eta}(v_{min}, t)$ (light green solid line) are shown in Fig. 4.2.1, which reproduces Fig. 3 of [22]. The agreement between this result with [22] is a validation of the reliability of the velocity distribution integrals computed in this work. Figure 4.2.1 shows that the GF influences the time of maximal $\eta(v_{min}, t)$ at low v_{min} (solid red line), causing a shift of about one month with respect to the SHM, while $\tilde{\eta}(v_{min}, t)$ is not influenced.

4.2.2 Systematic study of the annual modulation signal properties in NREFT

Amplitude of modulation

The definition of the amplitude of modulation, A_1 , is given in Eq. 3.14. In Fig. 4.2.2 the behaviour of A_1 for the four cross-sections in Eq. 4.8 is shown as a function of the minimal velocity, v_{min} , for $m_\chi = 10$ GeV (top four panels) and $m_\chi = 100$ GeV (bottom four panels), for several targets with the same exposure (1 kg \times day). A_1 is computed using a modified version of the Mathematica Package `DMFormFactor` [148, 186]. The isotopic abundances of the different targets are taken into account and the Wilson coefficients are set to $c_0^i = 1/246$ GeV² and $c_1^i = 0$, for $i = 1, 7, 8, 11$, separately. The amplitudes of modulation for the operators $\hat{\mathcal{O}}_1$ and $\hat{\mathcal{O}}_{11}$, which represent the classes (i) and (ii), show an inversion of phase⁷, well-known in the case of $\hat{\mathcal{O}}_1$. The modulation amplitude for the interaction class (ii) tends to zero for small v_{min} because the cross-section is $\propto v_{min}^2$. For classes (iii) and (iv), represented by $\hat{\mathcal{O}}_7$ and $\hat{\mathcal{O}}_8$, the modulation amplitude is positive for all v_{min} . The modulation amplitude for $\hat{\mathcal{O}}_1$, $\hat{\mathcal{O}}_8$ and $\hat{\mathcal{O}}_{11}$ are in general dominated by the heaviest targets because these three interactions depend on $\tilde{W}_M^{00}(q^2 \rightarrow 0) \sim A^2$, where A is the atomic mass number. $\hat{\mathcal{O}}_7$ is a spin-dependent interaction that involves $\tilde{W}_{\Sigma'}^{00}(q^2)$. At equal exposure, aluminium shows the largest modulation amplitude both for $m_\chi = 10$ GeV and $m_\chi = 100$ GeV.

Time of maximal rate

The differential rate $\frac{dR}{dE}(v_{min}, t)$ in Eq. 3.9 within the NREFT is a linear combination of the two velocity integrals $\eta(v_{min}, t)$ and $\tilde{\eta}(v_{min}, t)$ in Eqs. 4.13,

$$\frac{dR}{dE}(v_{min}, t) \propto [A(v_{min}) \eta(v_{min}, t) + B(v_{min}) \tilde{\eta}(v_{min}, t)] \quad (4.14)$$

since the DM nuclear responses $R_k^{\tau\tau'}\left(v_T^{\perp 2}, \frac{q^2}{m_N^2}, \{c_i^\tau, c_j^{\tau'}\}\right)$ in the differential cross-section in Eq. 4.7 contain up to $\mathcal{O}(v^2)$ terms (see Appendix C.1). Equation 4.14 is evaluated using a code written for this work which interfaces two tools: a Mathematica package [186] based on a modified version of the package `DMFormFactors` [148], which computes the coefficients $A(v_{min})$ and $B(v_{min})$, and a C++/ROOT code which combines such coefficients with the three-dimensional velocity distribution integrals in Eqs. 4.13. For the purpose of this section, the resulting differential rate is further processed to be maximised over the year. The differential rate calculated taking GF into account is expected to show a similar phenomenology as the velocity distribution integrals in Fig. 4.2.1.

In Fig. 4.2.3 the result of the differential rate maximisation obtained with this procedure is shown. In particular it is shown the example of two NR effective operators $\hat{\mathcal{O}}_1$ and $\hat{\mathcal{O}}_5$, for $m_\chi = 10$ GeV and for ²⁷Al. The two operators considered are $\hat{\mathcal{O}}_1$,

⁷It is common to refer to the change of sign of A_1 as an ‘inversion of phase’ because using the approximation in Eq. 3.13, if A_1 is taken positive, inverting the time of maximal and minimal differential rate corresponds to invert the phase of the modulation.

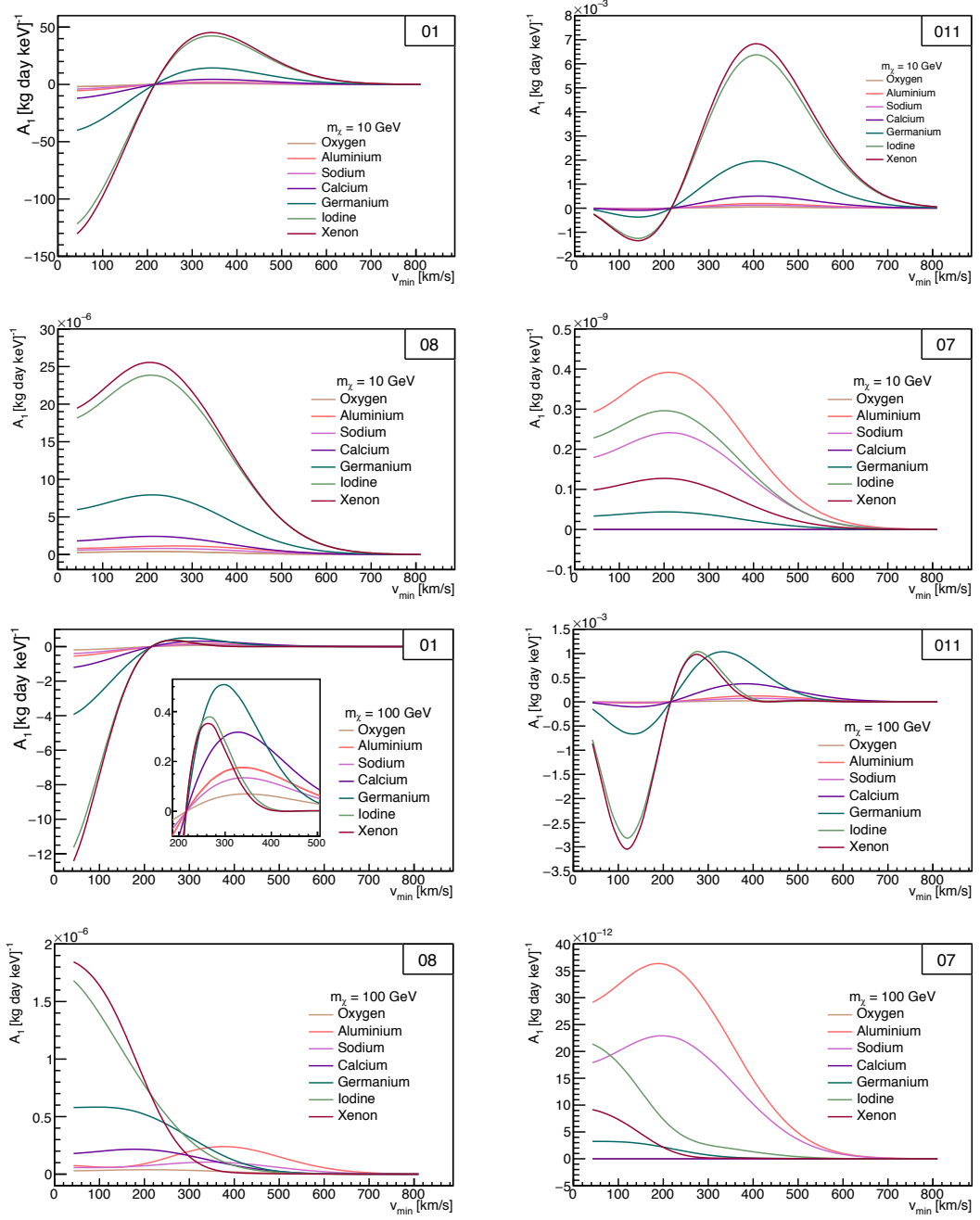


Figure 4.2.2: **Top:** Amplitude of modulation for the four non-relativistic effective operators $\hat{\mathcal{O}}_1$, $\hat{\mathcal{O}}_7$, $\hat{\mathcal{O}}_8$, $\hat{\mathcal{O}}_{11}$ and $m_\chi = 10$ GeV. Different colours correspond to different targets. The effective coupling constants are fixed at $c_0^i = 1/246$ GeV². **Bottom:** Same as on top plot, but with $m_\chi = 100$ GeV. This selection of operators includes interactions with different dependency on the relative DM-nucleon velocity.

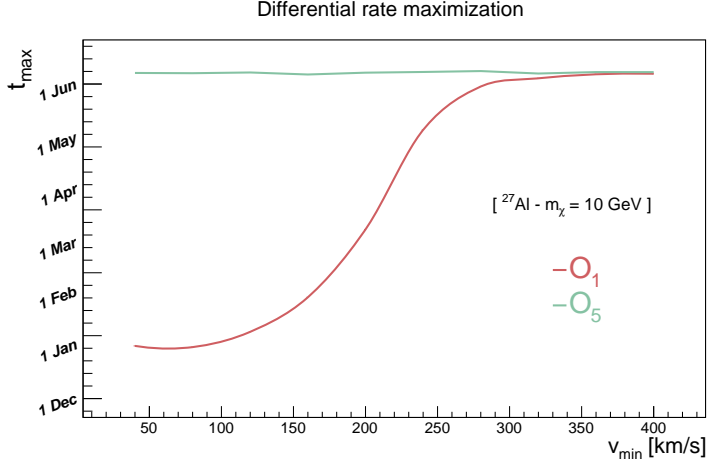


Figure 4.2.3: Time of maximal rate during the year plotted as function of the minimal velocity, for the effective operators $\hat{\mathcal{O}}_1$ and $\hat{\mathcal{O}}_5$, for aluminium and $m_\chi = 10 \text{ GeV}$.

as it corresponds to the usual SI-interaction, and $\hat{\mathcal{O}}_5$, as it belongs to the (iv) class of *building-blocks*, which depend on v^2 . Since for the operator $\hat{\mathcal{O}}_1$ the coefficients B is null, the time of maximal rate follows the time of maximum of the function $\eta(v_{min}, t)$, hence it shows an inversion of phase at low minimal velocities. The cross-section for $\hat{\mathcal{O}}_5$ is instead a combination of $\eta(v_{min}, t)$ and $\tilde{\eta}(v_{min}, t)$, similarly to the operator $\hat{\mathcal{O}}_8$, as they differ just by a factor of q^2/m_N^2 . The flat trend up to low minimal velocities visible in Fig. 4.2.3 implies that the cross-section for $\hat{\mathcal{O}}_5$, as well as for all the interactions falling in the (iv) class, is dominated by the $\tilde{\eta}(v_{min}, t)$ contribution. To conclusion the four classes of *building-blocks* investigated here can be classified in two groups as a function of their $t_{max}(v_{min})$ curve: (a) the ones with inversion of phase, which are previous categories (i) and (ii), and (b) the ones without inversion of phase, which are previous categories (iii) and (iv), since no other peculiar features were identified.

Target dependence

For MDDM and for specific DM masses, it has been found that the curve $t_{max}(v_{min})$ depends on the target material [21, 22]. The required differential rate for this effect to occur is a linear combination of the two velocity integrals $\eta(v_{min}, t)$ and $\tilde{\eta}(v_{min}, t)$, such as in Eq. 4.14, but with target dependent weights,

$$\frac{dR}{dE_R} \propto [A_i(v_{min}, m_T) \eta(v_{min}, t) + B_i(v_{min}, m_T) \tilde{\eta}(v_{min}, t)] \quad (4.15)$$

Within NREFT, the (iv) class of *building-blocks* which $\hat{\mathcal{O}}_5$ and $\hat{\mathcal{O}}_8$ belong to, at a first glance fulfils the conditions for target dependence. In the case of $\hat{\mathcal{O}}_{5,8}$ explicitly given in Eq. 4.8 the coefficients A and B are,

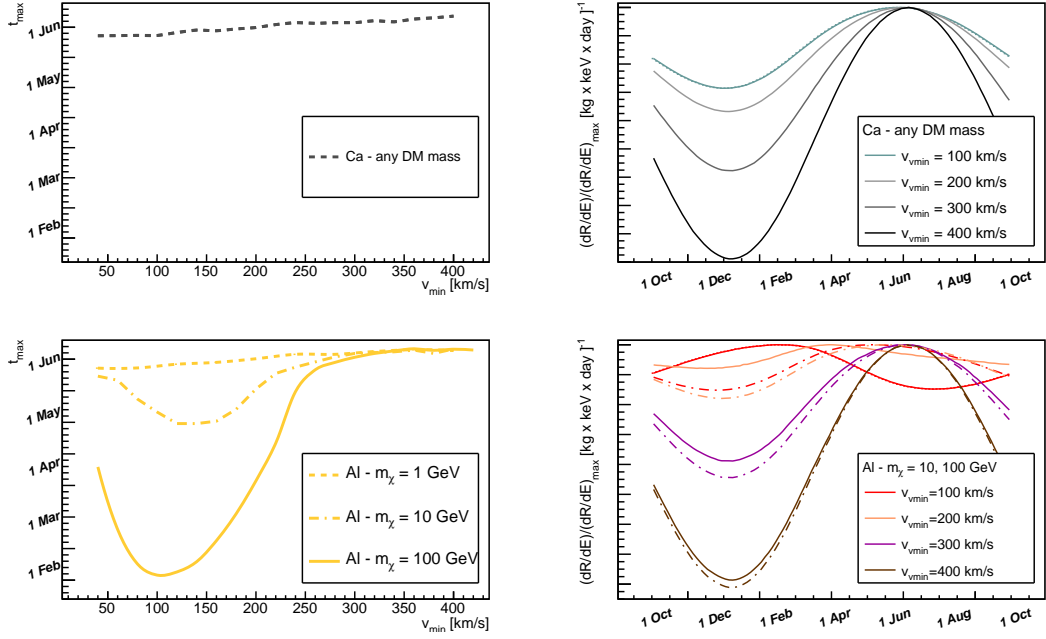


Figure 4.2.4: Target dependence of the annual modulation for the MDDM interaction, for ^{40}Ca , ^{16}O and ^{27}Al . **Top left:** $t_{\max}(v_{\min})$ for ^{40}Ca . The curve is constant along the whole range of v_{\min} , for any dark matter mass. The same holds for ^{16}O . **Top right:** Annual modulation of the normalised differential rate for ^{40}Ca , for different v_{\min} . The maximum differential rate is reached around June for any v_{\min} and the same is true for ^{16}O . **Bottom left:** $t_{\max}(v_{\min})$ for ^{27}Al for $m_{\chi} = 100$ GeV (solid line), 10 GeV (pointed-dashed line), 1 GeV (dashed line). **Bottom right:** annual modulation of the normalised differential rate for ^{27}Al for different v_{\min} : The time of maximum of the differential rate is function both of v_{\min} and m_{χ} .

$$\begin{cases} A(v_{min}, m_T) &= v_{min}^2 \left(\tilde{W}_M^{\tau\tau'}(q^2) - \frac{4\mu^2}{m_N^2} \tilde{W}_\Delta^{\tau\tau'}(q^2) \right) \\ B(v_{min}, m_T) &= \tilde{W}_M^{\tau\tau'}(q^2) \end{cases} \quad (4.16)$$

but since the effect appears at low v_{min} and the weight $A(v_{min}, m_T)$ is suppressed by the factor v_{min}^2 , the *building blocks* belonging to the (iv) class do not present target dependence, regardless of the DM-mass used as input.

In the light of a future time dependent analysis of the CRESST experiment (see Chap. 5), the results in [21, 22] concerning the time of maximum rate for the MDDM interaction, have been extended to ^{40}Ca , ^{16}O and ^{27}Al , using the nuclear response functions computed in [186].

^{40}Ca and ^{16}O are spin-0 nuclei. This is relevant as the nuclear spin plays an important role for the appearance of the target dependence in the differential rate produced by MDDM interactions. In Eq. 4.10, the coefficients $A(v_{min}, m_T)$ and $B(v_{min}, m_T)$ for spin-0 nuclei, read,

$$\begin{cases} A(v_{min}, m_T) &= \left(\frac{1}{m_\chi^2} - \frac{1}{\mu_T^2} \right) \tilde{W}_M^{pp} \\ B(v_{min}, m_T) &= \left(\frac{1}{\mu_T^2 v_{min}^2} \right) \tilde{W}_M^{pp} \end{cases} \quad (4.17)$$

being $\tilde{W}_{\Sigma'}$, $\tilde{W}_{\Delta\Sigma'}$ and \tilde{W}_Δ null. Since $B(v_{min}, m_T) \propto 1/v_{min}^2$, it is enhanced at low v_{min} and in Fig. 4.2.4, top left panel, it dominates the behaviour of the differential rate for ^{40}Ca , whose maximum is found around June along the whole minimal velocity range and for any m_χ ⁸. The nuclear spin of ^{27}Al is instead $J_T = 5/2$, therefore its spin-dependent nuclear response function, \tilde{W}_Δ included, are non-null. For this target, the differential rate is maximum in different months of the year as function of both the minimal velocity and the DM-mass: The heavier m_χ , the deeper the curvature for some ranges of minimal velocities, the larger the difference with respect to the ‘flat’ scenario, as shown in Fig. 4.2.4, bottom left panel.

Once clarified the requirements needed for the effect of target dependence to occur, unsurprising the ADM model, presented in the theoretical overview of this section, exhibits the same phenomenology as the MDDM (Fig. 4.2.5). The coefficients $A(v_{min}, m_T)$ and $B(v_{min}, m_T)$ for spin-0 nuclei, for the ADM interaction cross-section in Eq. 4.12, are,

$$\begin{cases} A(v_{min}, m_T) &= -v_{min}^2 \tilde{W}_M^{pp} \\ B(v_{min}, m_T) &= \tilde{W}_M^{pp} \end{cases} \quad (4.18)$$

At small v_{min}^2 the coefficient $A(v_{min}, m_T)$ decreases and the $B(v_{min}, m_T)$ term dominates, as evident in Fig. 4.2.5, top panels, while for the case of ^{27}Al , the $t_{max}(v_{min})$

⁸In Fig. 4.2.3 bottom panel, the plot for \hat{O}_5 shows a null slope along all the range. The “flat” plots resulting in the magnetic dipole or the anapole dark matter interactions for specific choice of the parameters (Fig. 4.2.4) instead show a slight positive slope. The discrimination of this two trends would require an accurate estimation of the day of maximum differential rate.

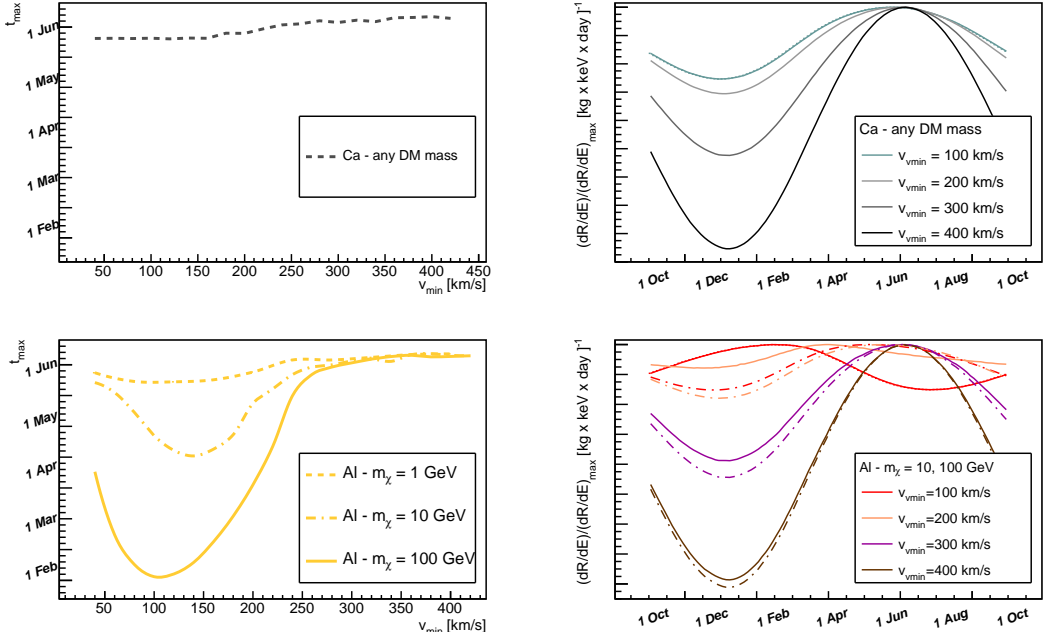


Figure 4.2.5: Similar as Fig. 4.2.4, but for the ADM interaction.

curves are more or less deep as a function of the DM mass considered, as shown in Fig. 4.2.5, bottom panels.

Single cosine approximation

A further aspect of the DM-signal time dependence concerns its Fourier expansion and the hierarchy between the higher order harmonics in Eqs. 3.12. This last part consists in a comment on the phenomenology of the first three harmonics, $A_{0,1,2}$, studied for the two classes of operators identified in the previous sections, which exhibit (a) an inversion of phase and (b) no inversion of phase. In Fig. 4.2.6, the dashed-dot purple curve shows the ratios $|A_1|/|A_0|$ and $|A_2|/|A_1|$ for \hat{O}_1 , class (a), computed for Xe and $m_\chi = 50$ GeV. This curve reproduces the result shown in Fig. 5 of [18], used as a cross-check for the calculation performed in this work. The black solid line represents the same ratios of harmonics but for \hat{O}_7 , class (b), for Al and $m_\chi = 10$ GeV. On the left panel, the spike at around $v_{min} \approx 200$ km/s for \hat{O}_1 is expected as a consequence of the inversion of phase occurring at this value, that in Fig. 4.2.2 appears as the change of sign of A_1 . Since the black curve refers to the operator \hat{O}_7 , which belongs to the (b)-class, no spikes are expected. $|A_2|$ is also different for the two classes. For the operator \hat{O}_7 it shows two zeros at [415-420] km/s and [690-700] km/s, while the operator \hat{O}_1 shows two zeros at [160-180] km/s and [500-540] km/s. For what concerns the hierarchy among the first three harmonics, for the (a)-class the approximation in Eq. 3.13 is not fulfilled around the point of phase-inversion, while for the (b)-class it is a better approximation.

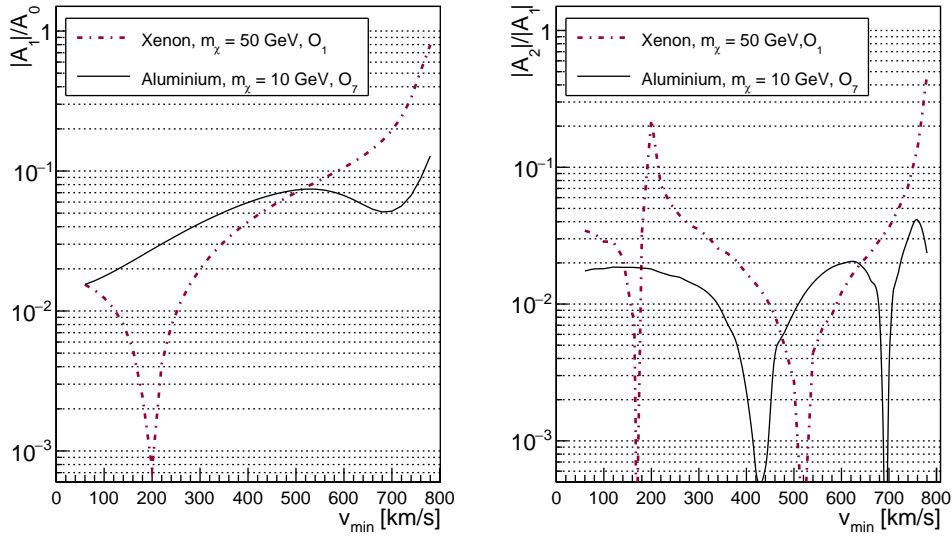


Figure 4.2.6: Hierarchy among the first three higher order harmonics for the two classes of NREFT *building blocks*. **Left:** Ratio $|A_1|/|A_0|$ versus v_{min} , for $\hat{\mathcal{O}}_1$, class (a), computed for Xe and $m_\chi = 50$ GeV (dashed-dot purple curve) and for $\hat{\mathcal{O}}_7$, class (b), for Al and $m_\chi = 10$ GeV (solid black curve). **Right:** Same as left panel, but for the ratio $|A_2|/|A_1|$.

Summary

In this work the properties of the DM annual modulation are explored using the NREFT tool. The amplitude of modulation for several targets and for $m_\chi = 10$ and 100 GeV is shown for four categories of cross-sections, classified as a function of their dependence on the momentum transfer and relative DM-nuclear velocity, identified among the list of NREFT *building-blocks*. For the same categories, the $t_{max}(v_{min})$ curves for the differential rate is studied and the number of classes of operators is reduced to two, with and without inversion of phase. The peculiar features of the $t_{max}(v_{min})$ curve underlined in [21, 22] and related to its target dependence are not present when single *building-blocks* are assumed as possible interactions. The calculations of [21, 22] is extended to ^{40}Ca , ^{16}O and ^{27}Al , which are targets of interest for the CRESST experiment.

This systematic work put in evidence that in case of signal, low threshold experiments would be suitable to discriminate models whose $t_{max}(v_{min})$ curve differs at low v_{min} . This observation motivated further investigations, which are discussed in Sec. 5.3.

4.3 Search for dark matter with polarised nuclei

In the context of DM DD, recently it was found that the polarisation of target nuclei in antiparallel direction with respect to the direction of the neutrino flux from the Sun, can

reduce the count rate of such flux up to 98% if ${}^3\text{He}$ detectors are employed [209]⁹. In a previous work [35], the rate of fermionic DM scattering events off point-like spin-1/2 polarised nuclei, assuming interactions mediated by a vector or pseudo-vector boson, was computed for the first time. In the following, an extension of this work to spin-1 DM particles is presented [2]. The case of scalar DM is neglected since the effect of the nuclear polarisation is extremely velocity suppressed [35] and smaller than for the case of spin-1/2 and 1 DM. The explicit expression of the transition amplitude module squared for fermionic and vector DM scattering off point-like spin-1/2 nuclei is provided, using a generic set of simplified models [182, 184]. In simplified models, the SM of particle physics is extended by the DM particle and one additional particle that mediates the DM interactions with quarks and leptons (see *e.g.* [180]). In contrast to EFTs, this allows to describe processes where the momentum transfer is comparable with the mediator mass.

If DM-nucleon interactions depend on parity violating operators and the target nucleus is polarised, the probability of DM-nucleon interaction can depend on the orientation of the nuclear spin [35]. This implies that the cross-section presents an angular anisotropy which can be taken into account by computing the double differential cross-section, and therefore rate, in energy and solid angle, as described in the following.

4.3.1 Double differential DM-nucleus scattering rate

The differential cross-section in terms of both the recoil energy and the solid angle is given in Eq. 15 of [210], and can be obtained using,

$$\frac{d\sigma}{dq^2}(q^2, \Omega(q^2)) = \int d\Omega \frac{d\sigma}{dq^2}(q^2, \Omega) \delta(\Omega - \Omega(q^2)) \quad (4.19)$$

$$\frac{d\sigma}{dq^2 d\Omega}(q^2, \Omega(q^2)) = \frac{d\sigma}{dq^2}(q^2, \Omega) \delta(\Omega - \Omega(q^2)) \quad (4.20)$$

$$= \frac{d\sigma}{dq^2}(q^2, \Omega) \frac{v}{2\pi} \delta(\mathbf{v}_\chi^{det} \cdot \hat{q} - v_q) \quad (4.21)$$

where $v = |\mathbf{v}_\chi^{det}|$, $v_q = q/(2\mu) = v_{min}$ and $\mathbf{v}_\chi^{det} \cdot \hat{q} = v \cos \theta$. The DM rate in Eq. 3.9, differentiated also with respect to the solid angle, can be written using Eq. 4.20,

$$\frac{dR}{dE_R d\Omega} = \frac{\rho_0}{m_\chi m_T} \int_{|\mathbf{v}_\chi^{det}| > v_{min}}^{|\mathbf{v}_\chi^{det} + \mathbf{v}_{det}^{gal}| < v_{esc}} d\mathbf{v}_\chi^{det} |\mathbf{v}_\chi^{det}| f(\mathbf{v}_\chi^{det} + \mathbf{v}_{det}^{gal}) 2m_T \frac{d\sigma}{dq^2 d\Omega} \quad (4.22)$$

⁹The direction of the nuclear polarisation which reduces the count rate due to the solar neutrinos flux is established by computing the neutrino-nucleus cross-section for polarised nuclei and by minimising the probability of interaction as a function of the angle between the incoming neutrino flux and the direction of the polarised nuclear spin (see Eq. 3 of [209] and details therein).

The three-dimensional integral over the velocity distribution is equal to,

$$\int_{|\mathbf{v}_\chi^{det}| > v_{min}}^{|\mathbf{v}_\chi^{det} + \mathbf{v}_{det}^{gal}| < v_{esc}} d\mathbf{v}_\chi^{det} = \int_{v_{min}}^{v_{esc} - v_e} dv v^2 \int_{-1}^1 d\cos\theta \int_0^{2\pi} d\phi + \int_{v_{esc} - v_e}^{v_{esc} + v_e} dv v^2 \int_{-1}^{\frac{v_{esc}^2 - v^2 - v_e^2}{2vv_e}} d\cos\theta \int_0^{2\pi} d\phi \quad (4.23)$$

where $v_e = |\mathbf{v}_{det}^{gal}|$, $\cos\theta = (\mathbf{v}_\chi^{det} \cdot \mathbf{v}_{det}^{gal})/(v v_e)$. The integral intervals derive from the condition $|\mathbf{v}_\chi^{det} + \mathbf{v}_{det}^{gal}|^2 < v_{esc}^2$ and $v > v_{min}$ ¹⁰.

A compact expression for the double differential rate in Eq. 4.22, using the relation $\delta(g(v)) = \delta(v - \bar{v})/|g'(\bar{v})|$, where $g(\bar{v}) = 0$, is,

$$\frac{dR}{dE_R d\Omega} = \frac{\rho_0}{64\pi^2 m_\chi^3 m_T^2 N_{esc}} \sum_{\ell=1}^2 \int_{-1}^{\alpha_\ell} d\cos\theta \int_0^{2\pi} d\phi \frac{\bar{v}^2}{|\hat{v} \cdot \hat{q}|} e^{(\bar{v}^2 + v_e^2 + 2\bar{v}v_e \cos\theta)/v_0^2} |\overline{\mathcal{M}}|^2 \Theta_\ell \quad (4.26)$$

where $\alpha_1 = +1$, $\alpha_2 = (v_{esc}^2 - \bar{v}^2 - v_e^2)/(2\bar{v}v_e)$, $\Theta_1 = \Theta(\bar{v} - v_{min})\Theta((v_{esc} - v_e) - \bar{v})$ and $\Theta_2 = \Theta(\bar{v} - (v_{esc} - v_e))\Theta((v_{esc} + v_e) - \bar{v})$, $\bar{v} = v_q/\cos\theta = q/[2\mu(\hat{v} \cdot \hat{q})]$. The term $|\overline{\mathcal{M}}|^2$ is the transition amplitude averaged over DM initial spin (j_χ) and summed over DM and nuclear final spin,

$$|\overline{\mathcal{M}}|^2 = \frac{1}{(2j_\chi + 1)} \sum_{ss'} \sum_r |\mathcal{M}|^2 \quad (4.27)$$

4.3.2 DM-nucleus effective Lagrangian

The first step to calculate $|\overline{\mathcal{M}}|^2$ is to compute the effective Lagrangian for DM-nucleus interactions within the assumed simplified model. This calculation is performed here by “integrating out” the mediator by using its equation of motion. The DM interactions with the nucleus, which is considered here as an elementary particle with spin 1/2 denoted by N , are assumed mediated by a heavy spin-1 boson. The mediator mass term is assumed to be described by Proca Lagrangians¹¹. We will show below the steps to compute the effective Lagrangian for the the case of fermionic DM and, omitting the calculation, we show the effective Lagrangian for vector DM.

¹⁰In particular, using,

$$\begin{cases} \cos\theta < (v_{esc}^2 - v_e^2 - v^2)/(2vv_e) \\ v > v_{min} \end{cases} \quad (4.24)$$

the integral intervals in Eq. 4.23 derive from,

$$\begin{cases} (v_{esc}^2 - v_e^2 - v^2)/(2vv_e) > 1, \text{ implies } -1 < \cos\theta < 1 \\ (v_{esc}^2 - v_e^2 - v^2)/(2vv_e) < 1 \text{ implies } -1 < \cos\theta < (v_{esc}^2 - v_e^2 - v^2)/(2vv_e) \end{cases} \quad (4.25)$$

¹¹It is known that Proca Lagrangians are not gauge invariant and in order to compute the effective action and solve the equation of motion one can use an analogy to electromagnetism (similarly to Fermi’s effective theory), using a photon-like propagator with mass.

Effective Lagrangian for fermionic DM

The presence of the nuclear spin vector in the final expression of the counting rate requires to start from parity violating Lagrangian. For a system with DM fields, χ , nucleus, N , and a vector mediator, G_μ , the most general Lorentz invariant and parity violating Lagrangian is [182, 184],

$$\begin{aligned} \mathcal{L}_{\chi GN} = & i\bar{\chi}\not{D}\chi - m_\chi\bar{\chi}\chi - \frac{1}{4}G_{\mu\nu}G^{\mu\nu} + \frac{1}{2}m_G^2G_\mu G^\mu + \\ & + i\bar{N}\not{D}N - m_T\bar{N}N - \lambda_3\bar{\chi}\gamma^\mu\chi G_\mu - \lambda_4\bar{\chi}\gamma^\mu\gamma^5\chi G_\mu + \\ & - h_3\bar{N}\gamma^\mu N G_\mu - h_4\bar{N}\gamma^\mu\gamma^5 N G_\mu \end{aligned} \quad (4.28)$$

where $G_{\mu\nu}$ is the mediator field strength tensor, m_χ , m_G and m_T are the DM, mediator and nucleus mass, and $\lambda_3, \lambda_4, h_3$ and h_4 are real coupling constants. The equation of motion for the free mediator is,

$$\frac{\partial\mathcal{L}_G}{\partial G^\alpha} - \partial_\beta \frac{\partial\mathcal{L}_G}{\partial(\partial_\beta G^\alpha)} = 0 \quad (4.29)$$

where,

$$\frac{\partial\mathcal{L}_G}{\partial G^\alpha} = m_G^2 G_\alpha - J_\alpha \quad (4.30)$$

with,

$$J_\alpha = \lambda_3\bar{\chi}\gamma_\alpha\chi - \lambda_4\bar{\chi}\gamma_\alpha\gamma^5\chi - h_3\bar{N}\gamma_\alpha N - h_4\bar{N}\gamma_\alpha\gamma^5 N \quad (4.31)$$

The second part of the equation of motion is,

$$\partial_\beta \frac{\partial\mathcal{L}_G}{\partial(\partial_\beta G^\alpha)} = -\square G_\alpha + \partial_\beta \partial_\alpha G^\beta \quad (4.32)$$

Since the vector field G^ν is equal to,

$$G^\nu = \sum_s \int \frac{d^3q}{(2\pi)^{3/2}} \frac{1}{\sqrt{2E_q}} \left(\epsilon_q^\nu a_{q,s} e^{-iqx} + \epsilon_q^{*\nu} a_{q,s}^\dagger e^{iqx} \right) \quad (4.33)$$

the two terms in Eq. 4.32 transform as,

$$\partial_\beta \partial_\alpha G^\beta \rightarrow -q_\beta q_\alpha \tilde{G}^\beta \quad (4.34)$$

$$-\square G_\alpha \rightarrow q^2 \tilde{G}_\alpha \quad (4.35)$$

where \tilde{G} is the Fourier transform of G_α and q^2 is the module squared of the quadri-momentum in this context. Therefore,

$$(m_G^2 g_{\alpha\beta} - q^2 g_{\alpha\beta} + q_\alpha q_\beta) \tilde{G}^\beta = \tilde{J}_\alpha \quad (4.36)$$

where $g_{\alpha\beta}$ is the metric tensor. The Green function of this equation of motion is,

$$iD^{\mu\nu} = i \frac{-g^{\mu\nu} + q^\mu q^\nu / m^2}{q^2 - m_G^2 + i\epsilon} \quad (4.37)$$

It follows,

$$G^\nu = \frac{-g^{\mu\nu} + q^\mu q^\nu / m_G^2}{q^2 - m_G^2 + i\epsilon} J_\mu \quad (4.38)$$

In the hypothesis that $m_G^2 \gg q^2$, the expansion in q^2/m_G^2 , at first order is,

$$G^\nu \approx -\frac{1}{m_G^2} \left(-g^{\mu\nu} + \frac{q^\mu q^\nu}{m_G^2} \right) (1 + \mathcal{O}((q/m_G)^2)) J_\mu \quad (4.39)$$

$$G^\nu \approx \frac{1}{m_G^2} (\lambda_3 \bar{\chi} \gamma^\nu \chi + \lambda_4 \bar{\chi} \gamma^\nu \gamma^5 \chi + h_3 \bar{N} \gamma^\nu N + h_4 \bar{N} \gamma^\nu \gamma^5 N) + \mathcal{O}(q^2/m_G^4). \quad (4.40)$$

Then we can substitute into the Lagrangian,

$$\begin{aligned} \mathcal{L}_{\text{eff},\chi N} &= \mathcal{L}_{0,\chi} + \mathcal{L}_{0,N} - \frac{1}{2} (\partial_\nu G_\mu \partial^\nu G^\mu - \partial_\mu G_\nu \partial^\nu G^\mu) + \frac{1}{2} m_G^2 \frac{J^\mu}{m_G^2} \frac{J_\mu}{m_G^2} - J^\mu \frac{J_\mu}{m_G^2} + \mathcal{O}(q^2/m_G^4) \\ &= \mathcal{L}_{0,\chi} + \mathcal{L}_{0,N} - \frac{1}{2} m_G^2 \frac{J^\mu}{m_G^2} \frac{J_\mu}{m_G^2} + \mathcal{O}(q^2/m_G^4) \end{aligned} \quad (4.41)$$

where $\mathcal{L}_{0,\chi}$ and $\mathcal{L}_{0,N}$ are the free DM and nucleus Lagrangian, and,

$$\frac{1}{2} (\partial_\nu G_\mu \partial^\nu G^\mu - \partial_\mu G_\nu \partial^\nu G^\mu) \simeq \mathcal{O}(q^2/m_G^4). \quad (4.42)$$

Finally, the fermionic DM-nucleus interaction terms of the effective Lagrangian in Eq. 4.41 are,

$$\begin{aligned} \mathcal{L}_{\text{eff},\chi N}^I &= -\frac{\lambda_3 h_3}{m_G^2} \bar{\chi} \gamma^\mu \chi \bar{N} \gamma_\mu N - \frac{\lambda_3 h_4}{m_G^2} \bar{\chi} \gamma^\mu \chi \bar{N} \gamma_\mu \gamma^5 N - \frac{\lambda_4 h_3}{m_G^2} \bar{\chi} \gamma^\mu \gamma^5 \chi \bar{N} \gamma_\mu N + \\ &\quad - \frac{\lambda_4 h_4}{m_G^2} \bar{\chi} \gamma^\mu \gamma^5 \chi \bar{N} \gamma_\mu \gamma^5 N. \end{aligned} \quad (4.43)$$

Effective Lagrangian for vector DM

The Proca Lagrangian for vector DM and uncharge vector mediator is [182, 184],

$$\begin{aligned} \mathcal{L}_{XGN} &= -\frac{1}{2} \chi_{\mu\nu}^\dagger \chi^{\mu\nu} + m_X^2 X_\mu^\dagger X^\mu - \frac{\lambda_X}{2} (X_\mu^\dagger X^\mu)^2 + i\bar{N} \not{D} N - m_N \bar{N} N + \\ &\quad - \frac{1}{4} \mathcal{G}_{\mu\nu} G^{\mu\nu} + \frac{1}{2} m_G^2 G_\mu^2 - \frac{\lambda_4}{4} (G_\mu G^\mu)^2 - \frac{b_3}{2} G_\mu^2 (X_\nu^\dagger X^\nu) - \frac{b_4}{2} (G^\mu G^\nu) (X_\mu^\dagger X_\nu) + \\ &\quad - [i b_5 X_\nu^\dagger (\partial_\mu X^\nu) G^\mu + b_6 X_\mu^\dagger (\partial^\mu X_\nu) G^\nu + b_7 \epsilon_{\mu\nu\rho\sigma} (X^{\dagger\mu} \partial^\nu X^\rho) G^\sigma + h.c.] + \\ &\quad - h_3 G_\mu \bar{N} \gamma^\mu N - h_4 G_\mu \bar{N} \gamma^\mu \gamma^5 N \end{aligned} \quad (4.44)$$

where X_μ , $\chi_{\mu\nu}^\dagger$, m_X are the DM field, field strength tensor and mass, N and m_N are the nucleus field and mass, G^μ , $\mathcal{G}_{\mu\nu}$ and m_G are the mediator field, field strength tensor and mass, b_5 , b_6 and b_7 are coupling constants, b_5 is real and b_6 , b_7 are complex

because of the structure of the indexes of the DM fields, which are contracted for b_5 , not contracted for b_6, b_7 . By analogy with the calculation of the previous section, the DM-nucleus interaction terms of the effective Lagrangian are,

$$\begin{aligned} \mathcal{L}_{\text{eff},XN}^I &= -\frac{ib_5h_3}{m_G^2}X_\nu^\dagger\partial_\mu X^\nu\bar{N}\gamma^\mu N - \frac{ib_5h_4}{m_G^2}X_\nu^\dagger\partial_\mu X^\nu\bar{N}\gamma^\mu\gamma^5 N + \\ &\quad - \frac{b_6h_3}{m_G^2}X_\nu^\dagger\partial^\nu X_\mu\bar{N}\gamma^\mu N - \frac{b_6h_4}{m_G^2}X_\nu^\dagger\partial^\nu X_\mu\bar{N}\gamma^\mu\gamma^5 N + \\ &\quad - \frac{b_7h_3}{m_G^2}\epsilon_{\sigma\nu\rho\mu}(X^{\dagger\sigma}\partial^\nu X^\rho)\bar{N}\gamma^\mu N - \frac{b_7h_4}{m_G^2}\epsilon_{\sigma\nu\rho\mu}(X^{\dagger\sigma}\partial^\nu X^\rho)\bar{N}\gamma^\mu\gamma^5 N + h.c. \end{aligned} \quad (4.45)$$

4.3.3 Polarised scattering amplitude

Here the modulus square of the transition amplitude for fermionic and vector DM is computed and the nucleus is assumed polarised in the initial state, thus it is performed an average on the DM spin and a sum over the DM and nucleus final spins.

Modulus square of the scattering amplitude for fermionic DM

To sum over the final nuclear spin the following relations are used, where no implicit sum over r is assumed, as the nucleus polarisation is fixed in the initial state,

1. $\sum_{r'}\delta^{r'r}\delta^{rr'} = 1$
2. $\sum_{r'}\delta^{r'r}S_N^{rr'} = S_N^{rr}$
3. $\sum_{r'}S_N^{r'r} \cdot S_N^{rr'} = \frac{3}{4}$ (see footnote¹²)
4. $\sum_{r'}S^{rr} = 2S^{rr}$
5. $\sum_{r'}(\mathbf{S}_N^{r'r} \times \mathbf{S}_N^{rr'}) = -i\mathbf{S}_N^{rr}$
6. $\sum_{ij}\sum_{ss'}a^ib^jS_\chi^{s's,i}S_\chi^{ss',j} = \frac{1}{2}a \cdot b$
7. $\sigma^i\sigma^j = \delta^{ij} + i\epsilon^{ijk}\sigma_k$

where $\mathbf{S}_N^{r'r} = \xi^{r'\dagger}\frac{\sigma_i}{2}\xi^r$, $r, r' = 1, 2$ are the nuclear polarisation states, ξ^r is the bi-dimensional unit spinor, $\mathbf{S}_\chi^{s's} = \xi^{s'\dagger}\frac{\sigma_i}{2}\xi^s$, $s, s' = 1, 2$ are the DM polarisation states, $\sigma = (\sigma_1, \sigma_2, \sigma_3)$ is a vector whose components are the three Pauli matrices.

¹²Explicit calculation for $\sum_{r'}S_N^{r'r} \cdot S_N^{rr'} = \frac{3}{4}$,

$$\begin{aligned} \sum_{r'}S_N^{r'r} \cdot S_N^{rr'} &= \sum_{r'}S_N^{rr'} \cdot S_N^{r'r} = \sum_{r'}\xi^{\dagger r}\frac{\sigma_i}{2}\xi^{r'}\xi^{\dagger r'}\frac{\sigma_i}{2}\xi^r = \\ &= \xi^{\dagger r}\frac{\delta_i^i}{4}\xi^r = \frac{3}{4}\xi^{\dagger r}\xi^r = \frac{3}{4} \end{aligned}$$

In this work, since the DM-polarisation index are summed over, the relativistic DM-currents are first contracted with themselves using the Dirac matrix trace properties which follows,

1. $Tr(\gamma^\rho \gamma^\mu \gamma^\sigma \gamma^\nu \gamma^5) = -4i\epsilon^{\rho\mu\sigma\nu}$
2. $Tr(\gamma^\mu \gamma^\nu) = 2g^{\mu\nu}$
3. $Tr(\gamma^\mu \gamma^\nu \gamma^\rho) = Tr(\gamma^\mu \gamma^\nu \gamma^5) = Tr(\gamma^\mu \gamma^\nu \gamma^\rho \gamma^5) = 0$

and then the non-relativistic approximation for the initial and final DM quadrimomenta, $k = (m_\chi, \mathbf{k})$ and $k' = (m_\chi, \mathbf{k}')$, is performed. For the nuclear part, it is used the non-relativistic expansion of the Dirac bilinear given in Eqs. 46 and 47 of [147], after cross-checking.

The final result for the module square of the transition amplitude for fermionic DM is,

$$\begin{aligned} |\overline{\mathcal{M}}|^2 = & (16m_\chi^2 m_T^2) [(A^2 + 3D^2) + \\ & - 2(\mathbf{v} \cdot \mathbf{S}_N^{rr}) \left(AB \left(1 - \frac{m_\chi}{m_T} \right) + 2BD + CD \left(1 + \frac{m_\chi}{m_T} \right) \right) + \\ & - 2(\mathbf{v}' \cdot \mathbf{S}_N^{rr}) \left(AB \left(1 + \frac{m_\chi}{m_T} \right) - 2BD + CD \left(1 - \frac{m_\chi}{m_T} \right) \right)] \end{aligned} \quad (4.46)$$

where $A = \lambda_3 h_3$, $B = \lambda_3 h_4$, $C = \lambda_4 h_3$ and $D = \lambda_4 h_4$. Equation 4.46 differs for two signs from the same equation presented in [35].

Modulus square of the scattering amplitude for vector DM

The vector DM field is,

$$X^\nu(x) = \sum_{\tilde{s}} \int \frac{d^3 \tilde{k}}{(2\pi)^3} \frac{1}{\sqrt{2E_{\tilde{k}}}} (a_{\tilde{k}} \epsilon_{\tilde{k}, \tilde{s}}^\nu e^{-i\tilde{k}x} + b_{\tilde{k}}^\dagger \epsilon_{\tilde{k}, \tilde{s}}^{*\nu} e^{i\tilde{k}x}) \quad (4.47)$$

where $\epsilon_{\tilde{k}, \tilde{s}}^\nu$ are the polarisation vectors, which satisfy the relation,

$$\sum_r \epsilon_{k r}^{*\mu} \epsilon_{k r}^\nu \equiv \sum_r \epsilon_{k r}^\mu \epsilon_{k r}^{*\nu} \equiv \left(-g^{\mu\nu} + \frac{k^\mu k^\nu}{m_\chi^2} \right) \quad (4.48)$$

The final result of calculation of the modulus square of the transition amplitude is,

$$\frac{1}{3} \sum_{r'} \sum_{ss'} |M_{fi}|^2 = \left(\frac{4}{m_G^4} \right) \cdot 16 m_\chi^2 m_N^2 [\mathcal{I} - \mathcal{J}(\mathbf{v} \cdot 2\mathbf{S}_N^{rr}) - \mathcal{K}(\mathbf{v}' \cdot 2\mathbf{S}_N^{rr})] \quad (4.49)$$

where,

$$\mathcal{I} = b_5^2 h_3^2 + 2\text{Re}(b_7)^2 h_4^2 \quad (4.50)$$

$$\mathcal{J} = b_5^2 h_3 h_4 \left(1 - \frac{m_\chi}{m_N}\right) + \frac{2}{3}\text{Re}^2(b_7) h_3 h_4 \left(1 + \frac{m_\chi}{m_N}\right) - \frac{4}{3}\text{Re}\{b_7\}\text{Im}(b_6) h_4^2 \quad (4.51)$$

$$\mathcal{K} = b_5^2 h_3 h_4 \left(1 + \frac{m_\chi}{m_N}\right) + \frac{2}{3}\text{Re}^2(b_7) h_3 h_4 \left(1 - \frac{m_\chi}{m_N}\right) + \frac{4}{3}\text{Re}\{b_7\}\text{Im}(b_6) h_4^2 \quad (4.52)$$

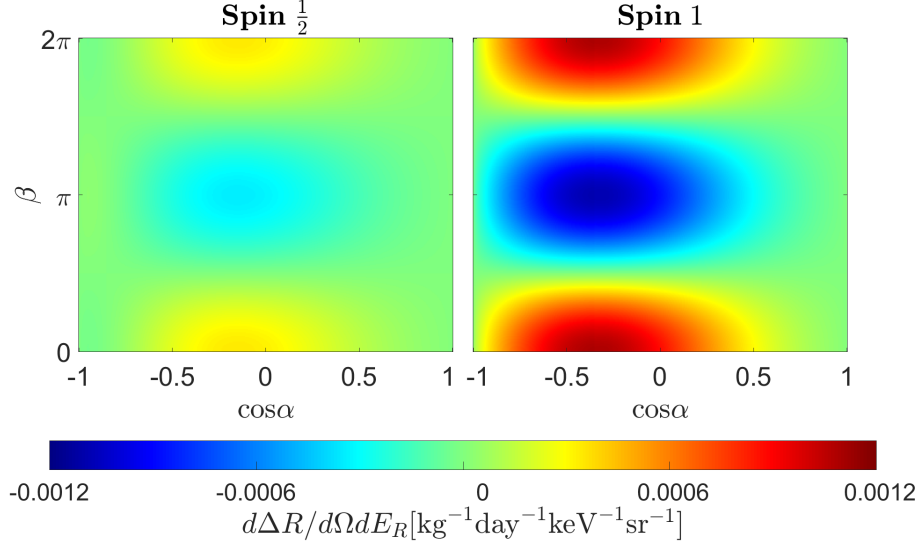


Figure 4.3.1: Purely polarisation dependent double differential rate distribution as a function of the spherical coordinates of the momentum transfer. The recoil energy is fixed at $E_R = 20$ keV and the nuclear spin is fixed to $\vartheta = \pi/2$. In this conditions, the maximal absolute value of the spin modulation, $\frac{d\Delta R}{dE_R d\Omega}$, is predicted at $\beta = 0(2\pi)$ or $\beta = \pi$ and $\alpha > \pi/2$ [2].

4.3.4 Discussion

The results for the modulus square of the transition amplitude in Eqs. 4.46 and 4.49 computed here allow to compute the double differential rate in Eq. 4.26. Since both expressions present a term which is independent from the nuclear spin, a convenient observable is,

$$\frac{d\Delta R}{dE_R d\Omega} \equiv \frac{1}{2} \left(\frac{dR(\mathbf{S}_N)}{dE_R d\Omega} - \frac{dR(-\mathbf{S}_N)}{dE_R d\Omega} \right) \quad (4.53)$$

which is a purely polarisation dependent differential scattering rate. In order to compute $\frac{d\Delta R}{dE_R d\Omega}$, masses and coupling constants are set to the following values,

- $m_T = m_\chi = m_G = 100$ GeV,

- the spin independent terms in the fermionic and vector transition amplitude in Eqs. 4.46 and 4.49 are fixed at an equal value, $A^2 + 3D^2 = I$,
- $h_3 = -h_4 = \lambda_3 = -\lambda_4 = \text{I}(b_6) = -\text{Re}(b_7) = \frac{1}{2}$, $b_5 = \frac{1}{\sqrt{2}}$, $\text{Re}(b_6) = \text{Im}(b_7) = 0$. This choice makes parity conserving and parity violating terms of the same order and fixes γ -combinations in nuclear currents to be left-handed projectors.

Using this benchmark, the purely polarisation dependent differential rate can be studied by fixing couples of parameters and varying the other two in the set $(\cos \alpha, \beta, \vartheta, E_R)$, on analogy with [35], where α and β are the spherical coordinate angles of the momentum transfer, \mathbf{q} , and ϑ is the angle between the direction of polarisation of the nuclear spin and the direction of motion of the Earth in the galaxy, \mathbf{v}_{det}^{gal} .

The results obtained under these conditions are shown in Fig. 2 and 3 of [2]. An example is reported in Fig. 4.3.1, which shows the angular distribution of the differential rate as a function of $\cos \alpha$ and β , for $E_R = 20$ keV and $\vartheta = 0$. The difference between spin-1/2 DM (left panel) and spin-1 DM (right panel) is highlighted by the different color of the two panels, while the maximal absolute value of the purely polarisation dependent differential rate is predicted at $\beta = 0(2\pi)$ or $\beta = \pi$ and $\alpha > \pi/2$ for both cases. The order of magnitude of the “spin modulation”, $\frac{d\Delta R}{dE_R d\Omega}$, in the coloured legend implies that $\sim 10^5$ [kg day] of exposure is necessary to obtain about 200/(day sr) counts of difference between the maximum and the minimum of the spin modulation.

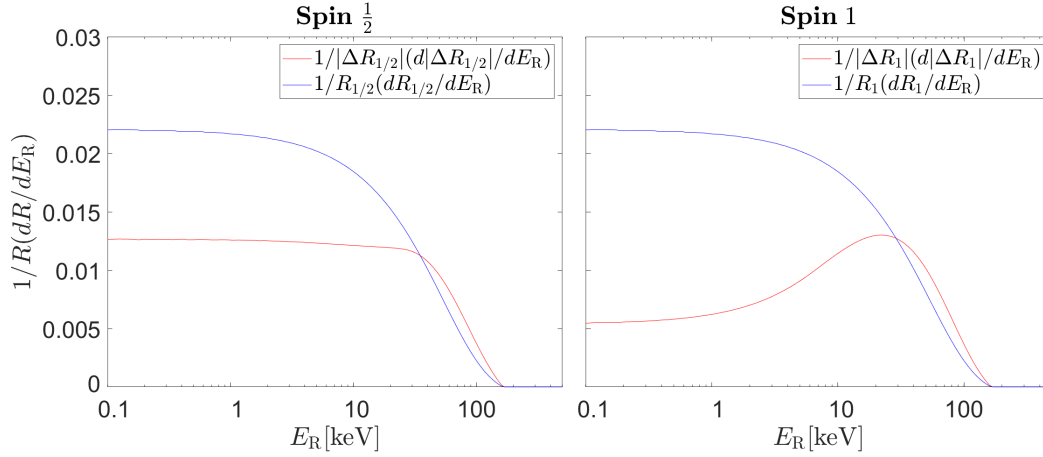


Figure 4.3.2: Energy spectrum for spin-1/2 DM (left panel) and spin-1 DM (right panel), normalised to the total rate. The blue curve shows the total differential rate, the red curve the purely spin dependent polarisation rate. At low recoil energy the spectrum present different feature for spin-1/2 and spin-1 DM, while the total energy spectrum is the same, as expected for construction [2].

Figure 4 of [2], reported in Fig. 4.3.2, shows in blue the total differential rate and in red the purely polarisation dependent differential rate, both integrated over the solid

angle and normalised to the total rate, similarly to Fig. 5 of [35]. At low recoil energy the behaviour of the red curves is different, which implies that using polarised nuclei for DM DD detection could be used to discriminate between different DM models also without the directional information. If from one side this result can be important, very large exposure are required to measure the polarisation dependent effects in the rate of DM-nucleus scattering, of the order of the one reached by the DAMA collaboration([25]) [35]. On the other hand, the required number of signal events is expected to decrease when directional information is available. To evaluate the experimental application of this method a statistical approach would be required, including in the estimations the experimental parameters, *e.g.* efficiencies, resolutions and exposures, and the experimental background, which is not included in this work.

Chapter 5

Dark matter search with the CRESST experiment

Part of the work described in this thesis was developed in close collaboration with the CRESST experiment: Section 5.1 describes the experimental concept and last DM results obtained by CRESST-III [4], Sec. 5.2 presents the derivation of the SD cross-section commonly used to show experimental limits, with a focus on lithium nuclei, as first CRESST results on SD interactions are based on this calculation, and in Sec. 5.3 a basic statistical approach is applied to simulated data inspired by CRESST-III data release to provide a first evaluation of the impact of a time dependent analysis on the signal discrimination power in low threshold experiments. This last work, which is a starting point and not a conclusive result, was motivated by the potential phenomenology of the DM annual modulation phase described in Sec. 4.2 together with the low-energy excess detected by CRESST-III and discussed in the following

5.1 CRESST-III experiment

CRESST (Cryogenic Rare Event Search with Superconducting Thermometers) operates scintillating cryogenic calorimeters working at mK temperature, realised for the DD of DM particles in a low background environment. It is located in the underground laboratory Laboratori Nazionali del Gran Sasso (LNGS), Italy. The last stage of the CRESST experiment, called CRESST-III, is an upgrade of the detector-setup with focus on the search for light DM-particles, thus detectors are optimised to reach low-energy-thresholds. The recent CRESST-III Data Release [4] collects the outcome of almost two years of data-taking: in the following we describe the CRESST-III detector module design and the results obtained with the most performant detector, called detector A, which showed an energy threshold of 30.1 eV.

Experimental concept

In CRESST-III phase 1 CaWO_4 crystals were operated, with dimensions (20 x 20 x 10) mm^3 and weight ~ 24 g. A detector module (Fig. 5.1.1) consists of two main parts: the phonon detector and the light detector. An energy deposition in the crystal produces vibrations of the crystal lattice, whose energy, E_p , flows through the crystal surface and cause an increase of temperature, ΔT , in the TES (Transition Edge Sensor), which is proportional to the amount of deposited energy. The CaWO_4 crystal equipped with a sensitive superconducting thermometer, the TES, is the phonon detector. By employing scintillating crystals, part of the deposited energy is converted into light, E_l , which propagates outside the crystal. A thin squared wafer of silicon-on-sapphire (SOS), 0.4 mm thick and 20 mm long, is interfaced to the crystal and works as light absorber. The SOS wafer is also equipped with a TES, which measures the ΔT caused by the absorbed scintillation light¹. Both components of the detector module are fixed in position by CaWO_4 -sticks of 12 mm length, 2.5 mm of diameter and with a rounded edge of about 2-3 mm of radius. The sticks holding the crystal are also instrumented with TESs in order to tag and reject possible events which occur in these holding sticks itself. The use of the same target material for the sticks reduces the stress due to thermal expansion in the target crystal. Instead the sticks holding the light absorber are not instrumented since any event there would be light-only and rejected anyways. To achieve a fully active coverage, the detector module is encapsulated in a reflective and scintillating housing foil, which allows to reject surface back-to-back α -events occurring in the target crystal, which otherwise could mimic nuclear recoils events.

Light yield and energy spectrum

The energy deposited by any particle scattering off a scintillating crystal is partially converted into lattice vibrations (phonons) and light. The amount of energy converted into lattice vibrations and detected by the phonon detector is almost independent from the type of recoiling particle. By comparing such energy with the results obtained in calibration runs, this channel is used to reconstruct the total energy of the event. The amount of energy which is converted in light follows, instead, the Birks' law [211] - the lighter the recoiling particle, the larger the amount of scintillation light emitted. The *light-yield* (LY), which is defined as the ratio between the energy detected in light and the energy detected in phonons, E_l/E_p , is a powerful tool for particle discrimination and background rejection. The events which survived the selection criteria and were used for CRESST-III DM data analysis [4] are shown in Fig. 5.1.2, top panel, in the light-yield versus energy plot. These results refer to detector A, which is the module which reached the lowest energy threshold. The solid lines mark the regions where 80% of β/γ events (blue) and recoils off oxygen (red) and tungsten (green) are expected. The events populate different bands as function of the emitted light, which is proportional to the light quenching factors. The distortion of the band at low energy for the β/γ -band

¹The light detector works as calorimeter: the light absorbed in the SOS produces phonons, whose thermal signal is measured by a TES.

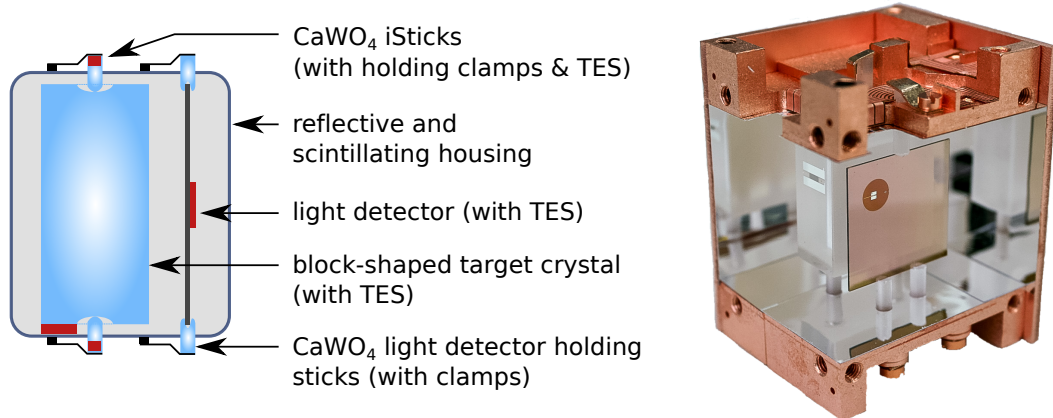
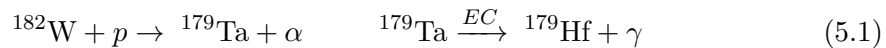


Figure 5.1.1: Left: Scheme of a CRESST-III detector module. The CaWO₄-crystal, (20 x 20 x 10) mm³ and ~ 24 g, instrumented with a TES, is the phonon detector. The three CaWO₄-sticks, with holding clamps and also instrumented with TESs, keep the target crystal in position. The thin wafer of silicon-on-sapphire (SOS), 20 mm long and 0.4 mm thick, equipped with a TES, is the light detector, and also held by two CaWO₄-sticks [4]. The stick holding system, in combination with the reflective and scintillating foil, provide a fully active surface coverage. Right: picture of CRESST-III detector module. Credit M. Willers (Technical University Munich).

is known as the *non-proportionality effect*, studied in [212]. The description of the bands follows [213], where measurements of the nuclear-quenching factors for CaWO₄ at mK temperature were performed. Two dense regions of points are visible in the β/γ -band at around 2.6 keV and 11.27 keV. These are the Auger electrons and X-rays emitted as consequence of the ¹⁷⁹Hf relaxation, following the cosmogenic activation,



where EC stays for electron capture. The dashed red line marks the center of the oxygen band, which is also the upper contour of the *acceptance region*. The acceptance region corresponds to the events in the light-yield plot which are *accepted* as dark matter events and are used to draw the sensitivity limit. The lower contour of the acceptance region is defined to contain 99.5% of the tungsten events. The energy range of the acceptance-region is identified from below by the condition that the detection efficiency, ϵ , is larger than 50%, which occurs for energies $E > 30.1$ eV, and from above by saturation effects which limit the energy range to 16 keV. Such saturation effects are connected with the use of the *optimum-filter-method* [214], used to collect CRESST-III data to the energy-resolution, thus the energy threshold. See CRESST-III Data Release paper for all the details [4].

Figure 5.1.2, bottom panel, shows the one-dimensional energy spectrum of the events in the LY plot, events of the acceptance region are marked in red. Above threshold and below 200 eV an excess of events is clearly visible over the flat background. These events cannot be associated to a specific class of events (β/γ or nuclear recoils) since they fall

in the region where the bands overlap. The same excess is visible in other detectors which were installed together with detector A in the CRESST-III setup and which also have energy thresholds below 100 eV. Distributions are not compatible among crystals, thus a DM origin is highly unlikely, but further investigations are necessary. In order to identify the nature of this excess, modifications on the detector-side were made and implemented in the present scientific run of the CRESST-III phase 1 programme. At present the experimental campaign is stopped due to the COVID-19 pandemic.

CRESST-III DM results

In Fig. 5.1.3, CRESST-III sensitivity curve is compared to the sensitivity of other experiments in the conventional SI cross-section versus DM mass parameter space. CRESST-III probes an unexplored region in the DM-mass range $(0.16 - 1.8) \text{ GeV}/c^2$ and pushed its lower mass limit from $500 \text{ GeV}/c^2$ [215] to $160 \text{ MeV}/c^2$ [4].

5.2 Spin-dependent search in ${}^7\text{Li}$ target

CRESST technology is constantly refined and developed to push experimental limits towards new frontiers of research. Different target materials, detector geometries, temperature sensor layout, data acquisition systems are contemplated and tested to eventually improve the employed technology and enlarge the DM parameter space which can be probed. An example is the R&D of the prototype detector module based on Li_2MoO_4 material. It showed good cryogenic performances and the presence of lithium, which is one of the lightest elements and it has a nuclear angular momentum $J_T \neq 0$, motivated further investigations. Such properties make lithium in fact suitable for SD DM search in the low DM mass region. Although SI interactions are expected to give the larger contribution to the cross-section, since the corresponding event rate is $\propto A^2$, where A is the atomic mass number, scenarios where the SD interactions dominate the event rate can be conjectured, see *e.g* [228].

The analysis of data collected operating 2.66 g of Li_2MoO_4 in an above ground laboratory, for a short effective time of 9.68 hours and interpreted using only the percentage of ${}^7\text{Li}$ as target material (corresponding to $7.91 \cdot 10^{-5} \text{ kg} \times \text{day}$ of exposure), showed sensitivity to SD interaction cross section for masses below 1.5 GeV [3], a region so far explored only by [225] among the DD experiments².

Lithium target nucleus. Lithium nuclear parameters are summarised in Tab. 5.1. The role of the expectation value of the nucleon spin in the DM-nucleus SD cross-section is shown in Eqs. 3.22 and 3.23. The spin matrix elements for ${}^6\text{Li}$ in Tab. 5.1, were not available at the time this studies were done and they have been requested to the authors of [198] only motivated by the findings of this work. The nucleon spin expectation values

²The comparison with the search at LHC and the indirect DM search is not straightforward, for this reason we refer just to DD search.

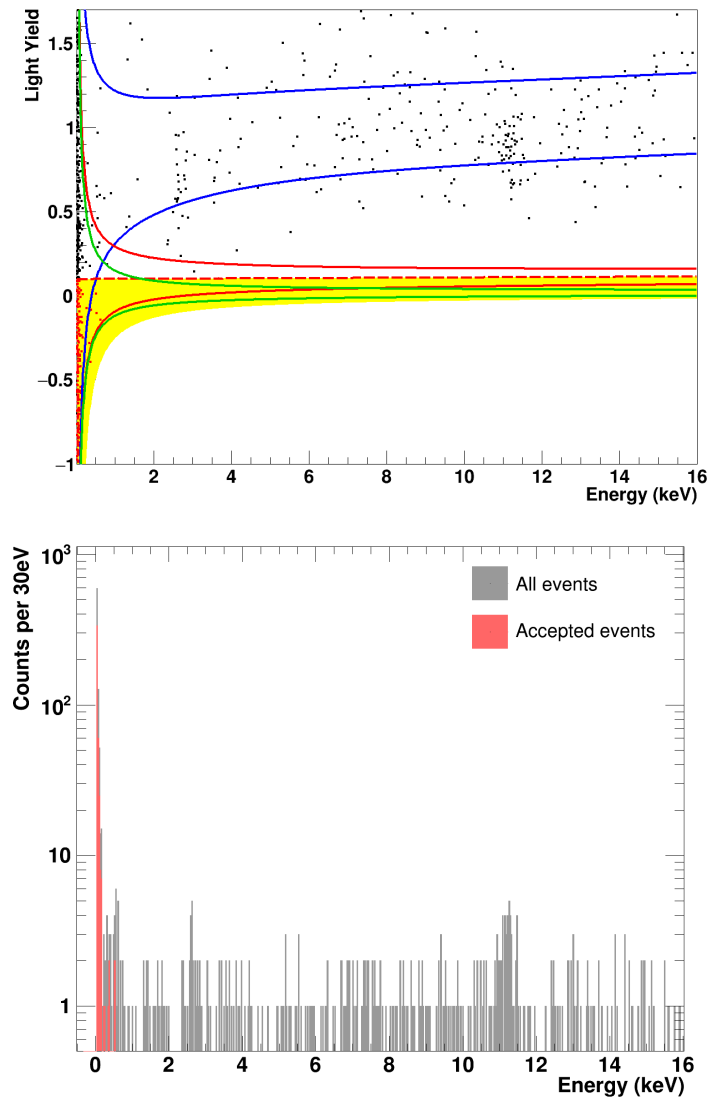


Figure 5.1.2: **Top:** Light yield versus energy plane for the events in the DM data set and surviving the selection criteria, CRESST-III Data release [4]. The light-yield plot is normalised to the light-yield of K_{α_1} and K_{α_2} escape lines of tungsten, with a weighted mean energy of 63.2 keV. Events result distributed along bands, as function of the relative light quenching, which is larger as heavier is the recoiling particle. Band fit is shown in blue for β/γ events, red for oxygen recoils, green for tungsten (calcium band fit is not shown for graph-clearness). Upper and lower boundaries include 80% of the events in the band. Shaded yellow band identifies the *acceptance region*. **Bottom:** The energy spectrum detected during the first campaign of CRESST-III [4]. Gray are all the events, red are the events devoted to the acceptance region. The peaks at around 2.6 keV and 11.23 keV are the relaxation emission events following the cosmogenic activation of ^{182}W . Below 200 eV, an excess of events over the flat background is observed.

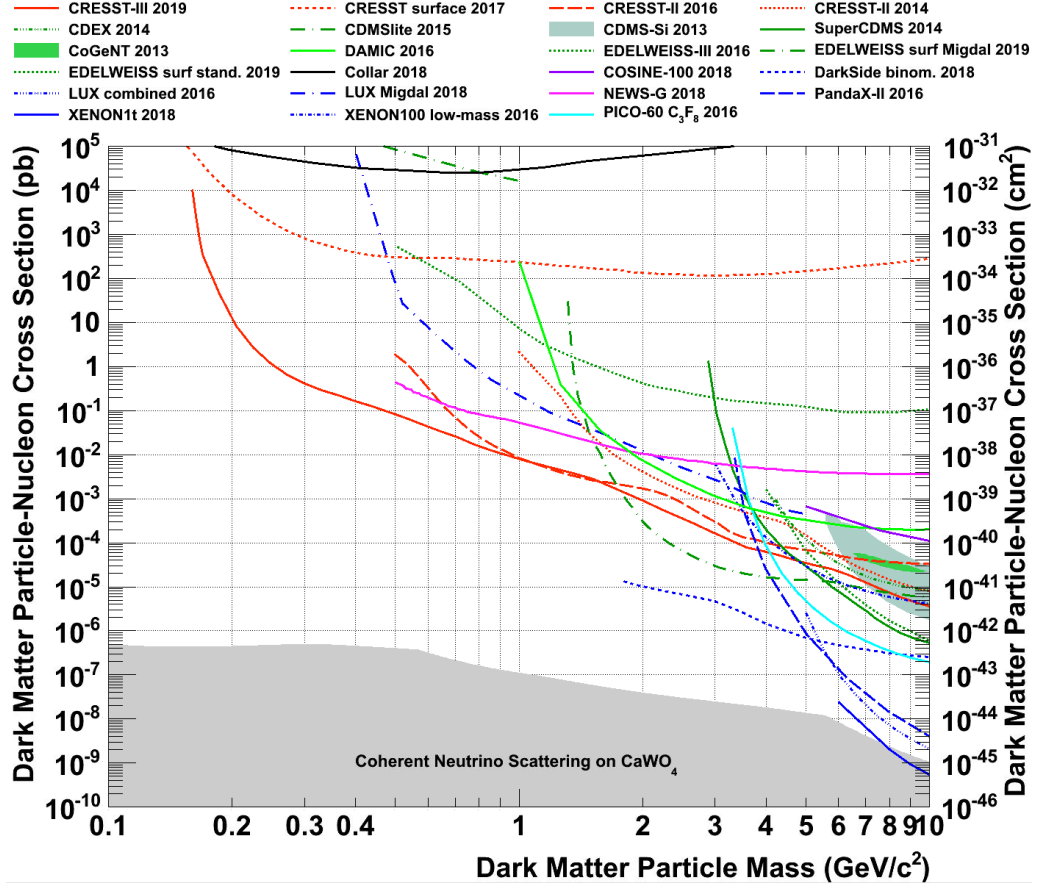


Figure 5.1.3: Experimental results on elastic, SI DM nucleus scattering presented in the cross-section versus DM particle mass plane [4]. CRESST-III result [4], shown in solid red, extends previous constraints for the mass range of $(0.16 - 1.8) \text{ GeV}/c^2$. For comparison, previous experimental results are shown: the dashed red is CRESST-II [215], the red dotted line is the CRESST surface measurement with a gram-scale Al_2O_3 detector [216], green curves indicate exclusion limits (CDEX [217], CDMSlite [218], DAMIC [162], EDELWEISS [219, 220], SuperCDMS [221]) and positive evidence (CDMS-Si (90% C.L.) [221], CoGeNT (99% C.L.) [222]) obtained with Si and Ge semiconductor, blue for liquid noble gas experiments based on argon or xenon (DarkSide [33], LUX [30, 168], Panda-X [31], Xenon100 [223], Xenon1t [29]), violet for COSINE-100 (NaI) [224], black for Collar (H) [225], magenta for the gaseous spherical proportional counter NEWS-G (Ne + CH₄) [159] and cyan for the superheated bubble chamber experiment PICO (C₃F₈) [226]. The gray region marks the so-called neutrino floor calculated for CaWO₄ in [227]. (Caption taken from [4]).

for ${}^7\text{Li}$ are taken from [229], since, among the literature cited in [230], applies the most advanced method³.

Isotope	Z	Abundance	J_T^P	$\langle S_p \rangle$	$\langle S_n \rangle$	Ref. for $\langle S_N \rangle$
${}^6\text{Li}$	3	0.0759(4)	1+	0.464(3)	0.464(3)	[198]
${}^7\text{Li}$	3	0.9241(4)	3/2-	0.497	0.004	[229, 230]

Table 5.1: Lithium stable isotopes nuclear properties. Abundances and J_t taken from <https://www.nndc.bnl.gov/nudat2/reCenter.jsp?z=3&n=3>.

Detector module design and properties. The Li_2MoO_4 crystal employed in this measurement is a small cube of 10 mm of side length and 2.66 g of weight, incapsulated in a copper housing and held by bronze clamps. It is equipped with a Neutron Transmutation Doped (NTD) temperature sensor, which is glued on its surface. The combination Li_2MoO_4 crystal and NTD constitutes the phonon detector (PD). The crystal is enclosed in a reflective foil which optimises the scintillation light collection which is measured by a CRESST-III light detector (LD), a $(20 \times 20 \times 0.3)$ mm³ wafer of Silicon-On-Sapphire (SOS) interfaced to the target crystal and equipped with a TES. A ${}^{55}\text{Fe}$ X-ray source with 0.055 Bq of activity is placed at 5 mm from the LD and is used to calibrate the LD energy response. The combination of PD and LD constitutes the detector module.

Data taking. The measurement was performed at the Max Planck Institute (MPP) for Physics in Munich, Germany, using a dilution refrigerator not shielded against environmental background and cosmic radiation (see [216] for the facility description). After two calibration runs, performed with a ${}^{57}\text{Co}$ γ -source and an AmBe neutron source, both placed outside the cryostat, 14.77 hours of background data were collected⁴.

Despite of the good performance of the LD whose energy resolution is $\sigma_{\text{baseline}}^{LD} = (5.90 \pm 0.13)$ eV, the module showed a poor light yield (LY) equal to (0.32 ± 0.01) keV/MeV, which prevented from applying particle identification according to the light-yield method described in the previous section. The LD was therefore only used as veto for muons and for backgrounds from the surrounding materials. The light-yield plot was substituted by a two dimensional plot where the events are distributed according to the portion of energy converted in scintillation light (y-axis) detected in coincidence with the portion of energy released in the Li_2MoO_4 target crystal (x-axis), as shown in Fig. 5.2.1, top panel. In this way, the anti-coincidence cut can reject events occurring both in the LD and in the PD, as DM is not expected to make multiple interactions. On the x-axis, the acceptance region is confined between the energy threshold, set at 0.932 ± 0.012 keV [214], and 50 keV. On the y-axis, the borders of the acceptance region

³More recent and accurate nuclear calculations are available at the present day, as discussed at the end of Sec. 4.1, therefore we expect the expectation values for the nucleon spin of ${}^7\text{Li}$ to be soon released, as it was the case for ${}^6\text{Li}$.

⁴The background run is not defined a DM run since the experimental setup was not optimised for the DM search.

are set between two values, $\pm C$, where $C = LY \times 50 \text{ keV} + 2\sigma_\gamma^{LD}$. σ_γ^{LD} is the energy resolution of the LD computed using the events which populate the peak of the X-ray line at 122 keV observed during the ^{57}Co calibration campaign. All the events in the acceptance region, that is the region between the two red horizontal lines in Fig. 5.2.1, are considered as DM events.

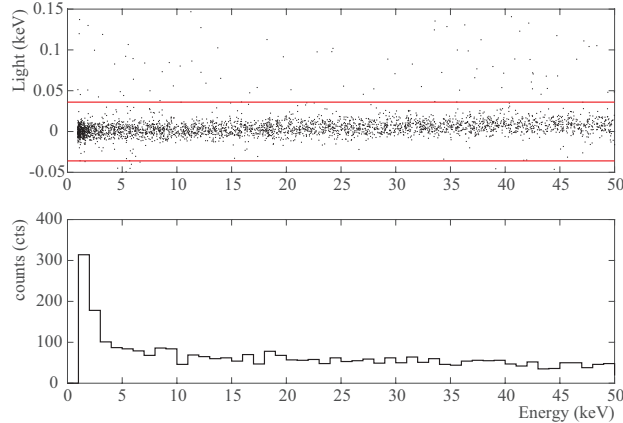


Figure 5.2.1: **Top:** Two dimensional plot where the events are distributed according to the portion of energy converted in scintillation light (y-axis) detected in coincidence with the portion of energy released in the Li_2MoO_4 target crystal. The two red horizontal lines confine the acceptance region (see text). **Bottom:** Energy spectrum for the Li target crystal.

5.2.1 Expected SD differential scattering rate off lithium

The scenario typically assumed to calculate the sensitivity of a given DD experiment to SI/SD interactions was introduced in Sec. 3.3. For the calculation of the SD cross-section off lithium we consider a point-like approximation for the nucleus, according to the following consideration. The momentum transferred to the nucleus in the laboratory reference frame is larger as larger is the incoming DM velocity. The maximal relative velocity is expected for a DM flux which points towards the Solar system (SS) along the same direction of the SS motion around the galactic center. The module of the maximal relative velocity is expected to be roughly $v_{max} \simeq 533 + 220 < 760 \text{ km/s}$. The maximal momentum transfer, which is obtained for $m_\chi = m_T$, for lithium is (see Appendix B.2),

$$q = \mu_T v (1 - \cos \theta) < 2m_T v_{max} \simeq 36 \text{ MeV} \quad (5.2)$$

in natural units. For the maximal momentum transfer, the DM wavelength is $\lambda_\chi \simeq 34 \text{ fm} \gg r_n(\text{Li})$, where $r_n(\text{Li}) \simeq 1 \text{ fm}$ is the effective nuclear radius defined in Sec. 3.3. Since $\lambda_\chi \gg r_n(^7\text{Li})$, the point-like approximation for the nucleus is appropriate and $S_A(q) \simeq S_A(0)$ for any possible momentum transfer, where $S_A(q)$ is defined in Eq. 3.25. Therefore we assume the $q^2 \rightarrow 0$ limit, that is equivalent to assume a form factor $F(q) = S_A(q)/S_A(0) = 1$.

The values of the couplings a_0 and a_1 in Eq. 3.23 are commonly fixed for convenience at $a_0 = a_1 = 1$ or $a_0 = -a_1 = 1$ and labeled as *proton-only* and *neutron-only* interactions, respectively.

Taking into account all the numerical coefficients, the number of counts per ($\text{kg} \times \text{keV} \times \text{day}$) for DM SD interactions is derived in Appendix D.1 and it is equal to,

$$\frac{dR}{dE_R} = \left[\frac{dR}{dE_R} \right] \xi \frac{2m_T[\text{GeV}]}{m_\chi[\text{GeV}]} \left(\frac{J_T + 1}{3J_T} \right) \left(\frac{\mu_T}{\mu_{p/n}} \right)^2 (2\langle S_{p/n} \rangle)^2 \frac{\sigma_{SD}^{p/n}[\text{cm}^2]}{4\mu_T^2[\text{GeV}^2]} \mathcal{I}_{halo} \left[\frac{\text{GeV cm}}{\text{cm}^3 \text{ s}} \right] \quad (5.3)$$

where E_R is the recoil energy, $\left[\frac{dR}{dE_R} \right]$ is the numerical factor derived in Appendix D.1, ξ accounts for the isotopic abundance and for the quantity of target nucleus of interest in 1 kg of material, m_T is the target nucleus mass, m_χ the DM mass; J_T is the total nuclear angular momentum, μ_T the DM-nucleus reduced mass and $\mu_{p/n}$ the DM-nucleon reduced mass; $\langle S_{p/n} \rangle$ is the expectation value of the spin content of the nucleons in the nucleus (see Tab. 5.1) and $\sigma_{p/n}^{SD}$ is the SD DM-nucleon cross-section, that is the parameter the sensitivity curves in Fig. 5.2.2 refer to. Finally, \mathcal{I}_{halo} is $\mathcal{I}_{halo} = \rho_\chi \eta(v_{min}, t)$, where ρ_χ is the DM mass density and $\eta(v_{min}, t)$ is the mean inverse velocity calculated in the standard halo model (SHM) defined in Eq. 4.13 [18], with v_{min} the minimal velocity required to produce a recoil energy E_R .

The differential rate of DM scattering off ${}^7\text{Li}$ as a function of the DM mass and the DM-nucleon SD cross-section $\sigma_{p/n}^{SD}$, used to interpret the experimental data of Sec 5.2, thus for the exclusion plots in Fig. 5.2.2, is given in the following equations.

- Differential rate for SD *proton-only* interactions in ${}^7\text{Li}$, ($a_0 = a_1$),

$$\frac{dR}{dE_R} \left[\frac{1}{\text{kg} \times \text{keV} \times \text{day}} \right] = 1.3701 \cdot 10^{41} \frac{(0.938 + m_\chi)^2}{m_\chi^3} \mathcal{I}_{halo} \left[\frac{\text{km}}{\text{s}} \right] \sigma_p^{SD}[\text{cm}^2] \quad (5.4)$$

- Differential rate for SD *neutron-only* interactions in ${}^7\text{Li}$, ($a_0 = -a_1$),

$$\frac{dR}{dE_R} \left[\frac{1}{\text{kg} \times \text{keV} \times \text{day}} \right] = 8.8751 \cdot 10^{36} \frac{(0.938 + m_\chi)^2}{m_\chi^3} \mathcal{I}_{halo} \left[\frac{\text{km}}{\text{s}} \right] \sigma_n^{SD}[\text{cm}^2] \quad (5.5)$$

where m_χ is in GeV, and the units of the other terms are in squared brackets. The values of the ${}^7\text{Li}$ spin structure function both for protons and neutrons are taken from [230], while we neglected ${}^6\text{Li}$ for because its spin structure functions were not yet available, as explained above.

5.2.2 DM result with CRESST Li_2MoO_4 prototype

After applying selection cuts, the effective background run time reduced from 14.77 hours to 9.68 hours, corresponding to $7.91 \cdot 10^{-5} \text{ kg} \times \text{day}$ of ${}^7\text{Li}$ exposure. The exclusion

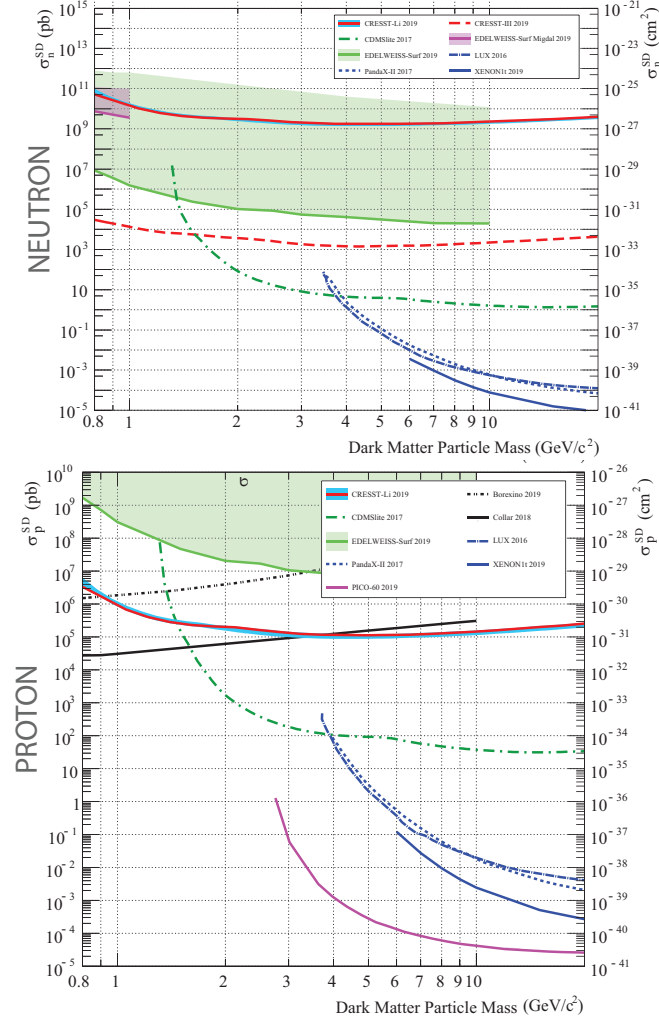


Figure 5.2.2: **Top:** Exclusion limit obtained for *neutron-only* spin-dependent interactions of dark matter particles with Standard Model particles. The cross section for this kind of interactions is shown on the y-axis (pb on the left, cm^2 on the right), while the dark matter particle mass is on the x-axis. The result of this work with ${}^7\text{Li}$ is drawn in solid red with the two-sigma band resulting from statistical uncertainty in solid blue: we reach $1.06 \cdot 10^{-26} \text{ cm}^2$ at $1 \text{ GeV}/c^2$. In dashed red we show the CRESST-III [4] limit using ${}^{17}\text{O}$. For comparison, we show limits derived by other direct detection experiments: EDELWEISS [220] and CDMSlite [175] using ${}^{73}\text{Ge}$; LUX [172], PandaX-II [231], and XENON1T [232] using ${}^{129}\text{Xe}+{}^{131}\text{Xe}$ (see legend). **Bottom:** Same, but for *proton-only* spin-dependent interactions. Our result with ${}^7\text{Li}$ is depicted in solid red with with the two-sigma band in solid blue, reaching $6.88 \cdot 10^{-31} \text{ cm}^2$ at $1 \text{ GeV}/c^2$. Additionally, we plot limits from other experiments: CDMSlite [175] and EDELWEISS [220] with ${}^{73}\text{Ge}$; LUX [172], XENON1T [231], and PandaX-II [231] with ${}^{129}\text{Xe}+{}^{131}\text{Xe}$; PICO-60 with ${}^{19}\text{F}$ [163]; Collar [225] with ${}^1\text{H}$. Finally, we plot in dotted black a constraint from Borexino data derived in [233]. Plot and caption taken from [3].

limits on the SD *proton-only* and *neutron-only* interactions were computed using the conservative Yellin method [234, 235]. The standard DM halo parameters entering in \mathcal{I}_{halo} (see Eq. 5.3 and Eq. 3.4) and which are used to draw the exclusion limits, are $\rho_\chi = 0.3 \text{ GeV/cm}^3$, $v_{esc} = 544 \text{ km/s}$ and $v_0 = 220 \text{ km/s}$. The SD cross-section versus DM mass sensitivity curve obtained with the preliminary measurement described in this section, contributes to constrain the DM parameter space for $m_\chi < 1.5 \text{ GeV}$, Fig. 5.2.2. This result motivated further tests using Li-based crystals, which later brought to decide to employ Li-based target crystals in the CRESST-III experiment. Modules constituted by Li-based absorbers are currently mounted in the CRESST cryostat for the next run.

CRESST-III SD limits using ^{17}O . In Fig. 5.2.2, the dashed-red line shows the exclusion limit derived by CRESST-III [4] using ^{17}O . The expectation values of the nucleon spin content of ^{17}O are taken from [230] and are $\langle S_n \rangle = 0.5$ and $\langle S_p \rangle = 0$. More updated results for these parameters are highly recommended to provide more accurate results.

5.3 Annual modulation phenomenology in CRESST-III

The very low thresholds reached by CRESST-III (30.1 eV), poses the challenge of the yet unexplained exponential background at low energies (*i.e.* $E < 200$ eV) discussed in Sec. 5.1. In this energy region the discrimination power between β/γ -events and nuclear recoils is lost because the bands overlaps because at such low energies the detection of the very few emitted photons is not feasible anymore. In the view of this background limitation, a study to establish if a 2-dimensional (2D) analysis in time and energy is of advantage for signal discovery or model discrimination is performed considering certain conditions. After a preliminary cross-check of the energy spectrum of signal events simulated in this work with previous literature, in Sec. 5.3.2 a rough estimation of the background is obtained by fitting a parametric model to CRESST-III energy-spectrum, in Sec. 5.3.3 the statistical theory which the analysis is based on is presented, in Sec. 5.3.4 technical details for data-simulation and data-fit are discussed and, finally, in Secs. 5.3.5 and 5.3.6 results are presented.

5.3.1 Dark matter signal calculation: Cross-check with previous literature

As a first step, the DM energy spectrum that is computed with the computer code developed in this work is compared with the examples illustrated in the public repository of the dmdd package⁵, which is the code used by the authors of Ref. [236]. For a DM mass of 50 GeV, a cross-section $\sigma_{SI} = 7 \cdot 10^{-46}$ cm², in the assumption of the SHM, using Xenon as target material with form factors taken from [148], the total number of events N per second and kilogram in the energy range [5 – 40] keV is,

- dmdd code: $N \simeq 4.9 \cdot 10^{-9}$ events/sec/kg,
- this work: $N \simeq 4.9 \cdot 10^{-9}$ events/sec/kg.

The total number of events calculated with the dmdd package and with the code used for this work, agree at the precision of the example given in the dmdd tutorial⁵⁶. In Tab. 5.2, the comparison between the differential rate computed for 5 energy values, from 1 to 100 keV, is provided. It is evident that there is a large discrepancy at recoil energies larger than about 50 keV. A possible reason is the use of different nuclear form factors. Although it is interesting to pin down the source of this discrepancy, it is expected to not have impact on the results presented in the following since the larger energy involved here is 16 keV.

⁵https://github.com/veragluscevic/dmdd/blob/master/dmdd_tutorial.ipynb

⁶As reference for later, the same number of counts is computed using the Helm form factor described in Sec. 3.3. The result is : $N \simeq 5.1 \cdot 10^{-9}$ events/sec/kg, about 5% of discrepancy.

Energy (keV)	dmdd (counts/sec/kg/keV)	This work (counts/sec/kg/keV)	Error
1	$7.32 \cdot 10^{-10}$	$7.29 \cdot 10^{-10}$	$\simeq 0.4\%$
25.75	$5.9967 \cdot 10^{-11}$	$5.9967 \cdot 10^{-11}$	$< 10^{-4}\%$
50.5	$2.9 \cdot 10^{-12}$	$3.1 \cdot 10^{-12}$	$\simeq 7\%$
75.25	$6.5 \cdot 10^{-14}$	$7.7 \cdot 10^{-14}$	$\simeq 18\%$
100	$2.5 \cdot 10^{-17}$	$1.0 \cdot 10^{-16}$	$\simeq 96\%$

Table 5.2: Comparison between the energy spectrum computed with the dmdd package and the computer code developed in this work. For energies larger than about 50 keV, the two calculations probably differ because of the use of different nuclear form factors.

5.3.2 CRESST background

The CRESST-III energy-spectrum [4] shown in Fig. 5.3.1, can be described by the following energy function,

$$\frac{dN_b}{dE} = p_0 + p_1 E + p_2 e^{-E/p_3} + N_K \text{Gauss}(E, E_K, \sigma_K) + N_L \text{Gauss}(E, E_L, \sigma_L) \quad (5.6)$$

where p_0 and p_1 are the parameters of the linear part of the energy spectrum, while p_2 and p_3 are the parameters of the exponential part. The two gaussian functions are inserted to describe the X-ray and Auger-electron emissions following the ^{179}Ta electron capture (see Sec. 5.1). N_K and N_L are the intensities, E_K and E_L the mean energies and σ_K and σ_L the standard deviations of the K-shell and L-shell, respectively. Equation 5.6 is fitted to the CRESST-III data in the acceptance region, as shown in Fig. 5.1.2. Data were collected using 23.6 g of CaWO_4 for a total exposure of 3.64 kg days. For details on data refer to [4] and [237]. CRESST-III data are available on the arXiv database (at the link <https://arxiv.org/abs/1905.07335>).

To fit data and to estimate parameters given in Eq. 5.6, the ROOT Data Analysis Framework [238] is used. Data are binned using ROOT TH1 Class. The TH1::Fit function is used to fit the model in Eq. 5.6 to data. In general, the TH1::Fit function requires two arguments, which are the fit-function and the fit-options. The fit-function is Eq. 5.6, while the fit-options are ‘**LIR**’. According to the ROOT User Guide: **L** sets the use of the likelihood method, **I** imposes the use of the integral of the function in the bin instead of its value at the bin center and **R** implies that the range of values of the variable which data are distributed according to, is equal to the range of values specified in the fit-function definition.

A combined fit procedure is performed in order to find reasonable starting values for the parameters. First the linear part of Eq. 5.6 is fitted to the flat background in the energy range [1 – 16] keV. Then the two additional terms in Eq. 5.6 are added, that are two gaussian functions which approximate the X-ray/Auger-lines and data are then fitted in the same energy-range [1 – 16] keV with the linear-function-parameters fixed;

in this way the parameters of the gaussian functions are estimated. Finally, the energy-range is extended to $[0.02 - 16]$ keV, introducing the exponential term. The starting values of the linear term and of the two gaussian functions instead are fixed at the values found in the previous steps. Then the final fit is performed with all parameters left free and starting values chosen as described above. At this stage, the only fixed parameter is the bin width which is multiplied to Eq. 5.6, as required by the **I** option in the TH1 class. The plot of the fit to data is shown in Fig. 5.3.1. The fit-parameters are listed in Table 5.3. The value for σ_L reported in the table is the one obtained by fixing the parameter, E_L , since otherwise the fit provides a value with a too large error and different from the previous steps, while all the other parameter values are very stable. Since the ratio between N_K and N_L is in agreement with the K/L-branching ratio shown in Fig. 5.3.1, the fit-result is considered reasonable.

N	Parameter	Value	Error (\pm)
1	p_0	28.0	1.0
2	p_1	-0.80	0.10
3	p_2	19776	610
4	p_3	0.0423	0.0012
5	E_K	11.196	0.035
6	σ_K	0.165	0.029
7	E_L	2.70	0.41
8	σ_L	0.033	0.023
9	N_K	42.5	7.6
10	N_L	13.7	4.5
11	bin size	0.16	fixed

Table 5.3: Fit parameters of Eq. 5.6 to the CRESST-III energy spectrum data [4].

The number of events in the CRESST-III acceptance region⁷ is 441, with ~ 158 days of exposure [4]. These events which survive the selection cut, are in the nuclear recoil bands or in the region where particle discrimination is lost. In the next sections, the rate of 500 counts in 158 days is used as a reference number for the background level in a CRESST-like detector and Eq. 5.6 is used to model the functional form of the background, neglecting the two X-ray emission lines at about 2.7 keV and 11.3 keV as they are easily identified and rejected.

⁷CRESST-III acceptance region is described in Sec. 5.1.

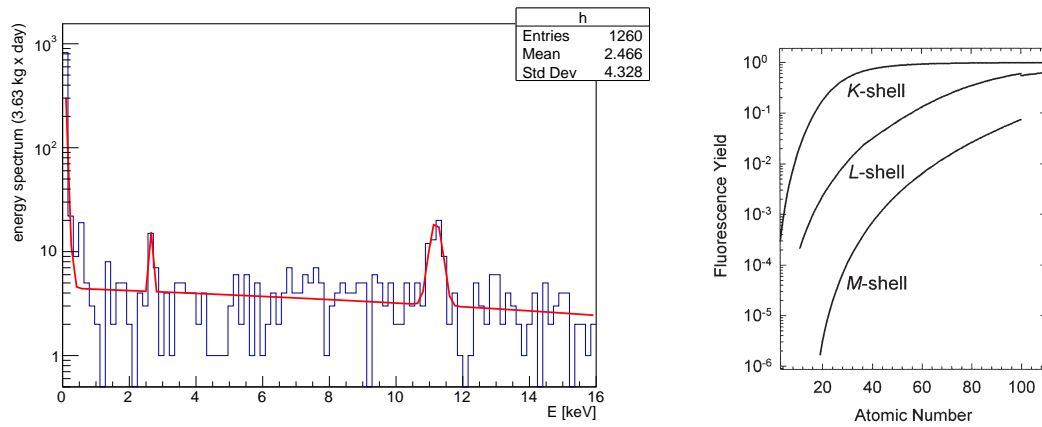


Figure 5.3.1: **Left:** CRESST-III energy spectrum as taken from [4]. The fit of Eq. 5.6 to data is shown as red solid line. **Right:** K and L-shell emission line intensities as a function of the atomic number. The K/L branching ratio can be easily calculated from this plot taken from the X-Ray Data Booklet [239].

5.3.3 Statistical theory

In this section the statistical methods used to perform the 1D (energy-only) and 2D (time and energy) analyses are introduced. The treatment is divided into two parts,

1. The problem of signal discovery
2. The problem of model discrimination

Signal discovery. The test statistics with higher significance power for signal versus background discrimination⁸ is the likelihood ratio, according to the Neyman-Pearson (NP) lemma and as explained by Glen Cowan in [240]. If the presence of a signal is not certain and data analysis goal is the signal-plus-background versus background-only-hypothesis discrimination, the likelihood ratio takes the following form,

$$q = -2 \log \left(\frac{\mathcal{L}(\mathcal{H}|b)}{\mathcal{L}(\mathcal{H}|\mu s + b)} \right) \quad (5.7)$$

where \mathcal{H} is the hypothesis which mock data are simulated according to, s stays for signal and μ is the signal strength parameter which takes values from 0 to 1 used for fitting. Its role is to ‘weight the quantity of signal’ in the data and it is left as free parameter when the fit of the model to data is performed. In order to establish the compatibility of the alternative-hypothesis with data, the test statistics q is randomly generated N times simulating the data under the null-hypothesis (background-only), \mathcal{H}_0 , and N times under the alternative hypothesis (signal-plus-background), \mathcal{H}_1 , such that two test statistics distributions are constructed. The critical region is then defined as the ensemble of q -values larger than q_{med} , where q_{med} is the median of the distribution of test statistics computed under the alternative-hypothesis or, in other words, is the most probable value under \mathcal{H}_1 . The p-value is the area under the null-hypothesis distribution curve, $f(q_0)$, in the range $[q_{med}, \infty]$,

$$\text{p-value} = \int_{q_{med}}^{\infty} dq_0 f(q_0) \quad (5.8)$$

If the p-value is low, the data are more compatible with \mathcal{H}_1 , that is data favour \mathcal{H}_1 .

When nuisance parameters are present, for instance in the case some background parameters are not known, the NP lemma does not hold, *i.e.* the likelihood-ratio in Eq. 5.7 is not the test statistics with the highest probability of null-hypothesis rejection. Since there is not an optimal choice for the test statistics indicator, different equivalent methods can be applied. Statistical results depend on the method used. The test-statistics commonly adopted for the problem of signal discovery involving nuisance parameters is

⁸The *power* of a test statistics is the probability of rejecting the null-hypothesis if the alternative-hypothesis is true.

the profile likelihood (PL) ratio. If θ is the vector of nuisance parameters, the PL ratio reads,

$$q = -2 \log \left(\frac{\mathcal{L}(\mathcal{H}|\mu s + b(\hat{\theta}))}{\mathcal{L}(\mathcal{H}|\hat{\mu} s + b(\hat{\theta}))} \right) \quad (5.9)$$

where $\hat{\theta}$ represents the nuisance parameters which maximise the likelihood-function, \mathcal{L} , for μ fixed at the value under test and $\hat{\mu}$ and $\hat{\theta}$ are the parameters which maximise $\mathcal{L}(\mu, \theta)$. For the purpose of signal discovery, which is the case of interest of this section, μ at the numerator is fixed at $\mu = 0$.

Model discrimination. Assuming that the signal discovery is already assessed, the goal to identify the model which better describes data is referred to as model discrimination. If there are two possible models and data contain also background events, the two hypotheses to compare consist in (i) first model plus background and (ii) second model plus background. The statistical method used in this analysis follows the one explained in [182], which considers the test statistics,

$$\begin{aligned} q_0 &= -2 \log \frac{\mathcal{L}(\mathcal{H}_0|\mu s_0 + b(\hat{\theta}))}{\mathcal{L}(\mathcal{H}_0|\mu s_a + b(\hat{\theta}))} \\ q_a &= -2 \log \frac{\mathcal{L}(\mathcal{H}_a|\mu s_0 + b(\hat{\theta}))}{\mathcal{L}(\mathcal{H}_a|\mu s_a + b(\hat{\theta}))} \end{aligned} \quad (5.10)$$

where q_0 and q_a are test statistics indicators computed on data simulated according to the first model (the null-hypothesis, \mathcal{H}_0) and to the second model (the alternative-hypothesis, \mathcal{H}_a), respectively. The terms s_i , with $i = 0$ or a , indicate the model used for fitting data, while θ represent the vector of nuisance parameters, which is just the background-normalisation in the analysis proposed below. The procedure for the p-value calculation is the following,

1. Generate N mock data samples and for each generation, compute the test-statistics q_0 ;
2. Build the distribution $f(q_0)$;
3. Repeat the procedure using q_a and build the distribution $f(q_a)$;
4. Compute the median of $f(q_a)$, that is q_{med} .
5. Compute the p-value, which is defined as in Eq. 5.8.

5.3.4 Methodology for p-value computation

In this section the procedure followed to compute the p-value of the hypothesis under test is explained. The procedures for different problems slightly differ from each other,

but basics steps are the same: data are simulated and the two distributions of the test-statistics computed under the null-hypothesis and the alternative-hypothesis are built using N -Monte Carlo generations. The two distributions are normalised to 1. The p-value of the null-hypothesis is computed at the median of the alternative-hypothesis. If the p-value is equal to or lower than a chosen value α in the range $[0, 1]$, data favours the alternative-hypothesis with $(1 - \alpha) \cdot 100\%$ of confidence level. In the following the simulation and fitting procedure are addressed.

Details on data simulation

The probability density function (p.d.f.) used to simulate the background energy spectrum reads,

$$(\text{p.d.f.})_b = \frac{dN_b}{dE} \left(\int_{\Delta E} dE \frac{dN_b}{dE} \right)^{-1} \quad (5.11)$$

where dN_b/dE is taken from Eq. 5.6. The p.d.f. used for signal simulation is,

$$(\text{p.d.f.})_s = \frac{dN_s}{dE} \left(\int_{\Delta E} dE \int_{\Delta t} dt \frac{dR_s}{dE} \right)^{-1} \quad (5.12)$$

where $dN_s/dE = \int_{\Delta t} dt (dR_s/dE)$ and Δt is the time-window of data-taking (data-simulation in our case). If data are distributed both in time and energy, the p.d.fs. used for background and signal simulation are,

$$(\text{p.d.f.})_b = \frac{1}{\Delta t} \frac{dN_b}{dE} \left(\int_{\Delta E} dE \frac{dN_b}{dE} \right)^{-1} \quad (5.13)$$

$$(\text{p.d.f.})_s = \frac{dR_s}{dE} \left(\int_{\Delta E} dE \int_{\Delta t} dt \frac{dR_s}{dE} \right)^{-1} \quad (5.14)$$

Using Eqs. 5.11 and 5.12, the p.d.fs used for simulating data can be constructed according to the null and the alternative-hypotheses. Since the hypotheses are different for the two problems addressed in this work, that are signal discovery and model discrimination, they are treated and discussed separately.

Signal discovery: The null-hypothesis consists in data containing background-only events and it is tested against the alternative-hypothesis which is data containing both signal and background events. In particular,

- *null-hypothesis* (\mathcal{H}_0): A 1D (2D) histogram is randomly filled with a certain number of counts $\tilde{\lambda}_b$ distributed according to Eq. 5.11 (Eq. 5.13), being background-only data,

$$(\text{p.d.f.})_{\mathcal{H}_0} \equiv (\text{p.d.f.})_b \quad (5.15)$$

The number $\tilde{\lambda}_b$ is randomly generated from a Poisson probability function with mean λ_b , which is the expected number of background events injected as input for

the simulation. This method is used to impose a CRESST-like background energy spectrum, while the total number of background counts is fixed as a function of the chosen total exposure (target mass times time exposure) considered.

- *alternative-hypothesis* (\mathcal{H}_a): A 1D or 2D histogram is filled with $\tilde{\lambda}_{s+b} = \tilde{\lambda}_b + \tilde{\lambda}_s$ number of counts, according to the following p.d.f,

$$(\text{p.d.f})_{\mathcal{H}_a} = \frac{1}{\lambda_b + \lambda_s} (\lambda_b \cdot (\text{p.d.f})_b + \lambda_s \cdot (\text{p.d.f})_s) \quad (5.16)$$

where,

$$\lambda_s = \epsilon \cdot \left(\int_{\Delta E} dE \int_{\Delta t} dt \frac{dR}{dE}(v_{min}, t) \right) \quad (5.17)$$

and ϵ is total exposure (target mass times time exposure). The numbers $\tilde{\lambda}_b$ and $\tilde{\lambda}_s$ are generated from Poisson distributions with mean λ_b and λ_s , respectively. The two functions $(\text{p.d.f})_b$ and $(\text{p.d.f})_s$ are taken from Eqs. 5.11 and 5.12 for the 1D case, and Eqs. 5.13 and 5.14 for the 2D case.

Model selection: If the aim is to pin down the theory which better reproduces experimental results, both the null-hypothesis and the alternative-hypothesis consider data containing both background events and signal events. The difference is in the model assumed to describe the signal. Usually one of the models is the one accepted by the community or the simpler hypothesis, which is treated as the hypothesis to reject. The other model is then the alternative scenario, which is proposed as substitution of the standard one. The p.d.fs used to simulate data according to the null and alternative-hypotheses are,

- *null-hypothesis* (\mathcal{H}_0):

$$(\text{p.d.f})_{\mathcal{H}_0} = \frac{1}{\lambda_b + \lambda_{s_0}} (\lambda_b \cdot (\text{p.d.f})_b + \lambda_{s_0} \cdot (\text{p.d.f})_{s_0}) \quad (5.18)$$

- *alternative-hypothesis* (\mathcal{H}_a):

$$(\text{p.d.f})_{\mathcal{H}_a} = \frac{1}{\lambda_b + \lambda_{s_a}} (\lambda_b \cdot (\text{p.d.f})_b + \lambda_{s_a} \cdot (\text{p.d.f})_{s_a}) \quad (5.19)$$

where λ_b is the expected number of background events, λ_{s_0} and λ_{s_a} are the number of signal events for the null and the alternative-hypotheses, respectively, $(\text{p.d.f})_b$ is defined in Eq. 5.11 or Eq. 5.13, and the $(\text{p.d.f})_{s_0}$ and $(\text{p.d.f})_{s_a}$ can be both parametrised using Eq. 5.12, with the differential rate computed according to the corresponding models.

Details on fit functions

Once simulated data are available, the likelihood-ratios in Eqs. 5.7, 5.9 or 5.10 are computed. The fitting functions used in the actual calculations are equal to the p.d.fs defined in Eqs. 5.15-5.19, not normalised, that is not divided by $(\lambda_b + \lambda_s)$. These fitting functions are then implemented in the code by using the TF1 (TF2) Class in the ROOT Data Analysis framework (TF1/TF2 for 1D and 2D analyses respectively). For an analytical treatment of the likelihood-ratios we refer the reader to Appendix D.2⁹.

Test statistics distributions and p-value calculation

The procedure explained so far allows to compute one realisation of the test-statistics, q . It is, therefore, repeated for each Monte Carlo generation and the likelihood-ratios obtained in this way are distributed in two 1D histograms, one for data simulated according to the null-hypothesis, $f_0(q)$, and one for data simulated according to the alternative-hypothesis, $f_a(q)$. To simplify the calculation of the p-value, the cumulative of the two distributions, $\Phi(f_0)$ and $\Phi(f_a)$, is computed, so that the median of $f_a(q)$ corresponds to $\Phi(f_a|_{q_{med}}) = 0.5$. Finally the p-value is computed using Eq. 5.8.

All results are obtained using $N = 10^3$ Monte Carlo generations, the p-value considered as a reference is 0.1 (90% of C.L.) and, for the precision on the p-value, an upper limit equal to $1/\sqrt{4N} \simeq 0.016$ is considered, according to the following reasoning. The p-value can be interpreted as the number of times that the test statistics, q , falls on one side of the alternative-hypothesis distribution median, case which will be defined as a ‘success’. In other words, q can be considered as a binomial variable and the p-value as the number of successes of q . The variance of the number of successes is equal to $\sigma^2 = Np(1-p)$, where N in our case is the number of Monte Carlo generations and p , that is the probability of success, depends on the relative position of the two distributions $f_0(q)$ and $f_a(q)$. Since the probability, p , can take values between 0 and 1 and the variance is symmetric for $p < 1/2$ and $p > 1/2$, with maximum at $p = 1/2$, for an upper limit on the variance $p = 1/2$ can be used. The error on the p-value can then be estimated as the square root of the variance, normalised with respect to the total number of Monte Carlo generations. Using these indications, the upper limit on the error for the p-value, $\sigma/N = \sqrt{Np(1-p)}/N < 1/\sqrt{4N} \simeq 0.016$, is estimated¹⁰.

5.3.5 Results on signal discovery

The results of the analysis outlined in the previous sections are described below. Following the structure of the previous sections, the discussion is divided into two parts:

⁹*Technicality*: The minimisation algorithm implemented in ROOT is Minuit. According to Minuit manual <https://root.cern.ch/download/minuit.pdf>, Sec. 1.4.3, when the fitting function is highly non-linear, as in the case treated here, MINOS program is needed. In Sec. 5.3.2 the options used in the argument of the ROOT function ‘TH1:Fit’ to fit CRESST-III energy spectrum are explained. MINOS is selected by adding the option ‘E’.

¹⁰I thank S. Di Lorenzo for this interpretation.

the results concerning the signal discovery (this section) and the results concerning the possibility of model selection (sec. 5.3.6), both cases applied to CRESST-like detectors.

1D versus 2D analysis for DAMA-like signal

The first result concerns the statistical test of signal-plus-background hypothesis against the background-only hypothesis, in the assumption the true signal is the one described by the best-fit parameters of DAMA/LIBRA (see Sec. 3.4) data. The approach is to interpret the annual modulation detected by DAMA/LIBRA [25] as a signature of DM and simulate the same signal in CRESST-like detectors. The final purpose is to verify if and under which conditions analysing data distributed both in time and energy (2D analysis) is statistically advantageous with respect to analysing just energy-spectra (1D analysis). Since the properties of the signal are assumed already established, the test statistics in Eq. 5.7 is used, with the strength parameter fixed to $\mu = 1$.

The DM scenario assumed for this part of the analysis is the common SI DM-nucleon elastic-scattering (see Sec. 3.3), with DM mass and cross-section fixed at the best-fit values of DAMA/LIBRA-data reported in [241]¹¹,

$$m_\chi = 11.17 \text{ GeV}/c^2, \quad \sigma_0^p = 2.67 \cdot 10^{-38} \text{ cm}^2 \quad \text{and} \quad r = c_1^n/c_1^p = -0.76 \quad (5.20)$$

The simulation of the signal described by these parameters and expected in 23 g of sapphire Al_2O_3 and 1 yr exposure is shown in Fig. 5.3.2, where the left panel is the number of counts distributed in energy and the right panel is the number of counts distributed in time (y-axis) and energy (x-axis). The signal is simulated using the modified version Mathematica package *DMFormFactor* [148] which includes nuclear responses for *O* and *Al* from [186] to compute the cross-section (see Sec. 4.1) and the velocity distribution is computed using the isotropic standard halo model (SHM) [18], (see Sec. 3.1.2). As stated already above the target material considered here is sapphire, a crystal also employed in the CRESST-III phase 1 low-mass DM campaign. Sapphire contains two light nuclei which together with a low-energy threshold make such crystal a good choice for low-mass DM detection. Furthermore sapphire contains aluminium which has a nuclear angular momentum equal to $J_N = 5/2$ and therefore is also sensitive to SD DM-nucleon interactions. The spin property is not relevant for this analysis but is, besides the before mentioned advantages, another argument for its employment in DD DM experiments.

Neyman-Pearson method: known background scenario. A graphical example of $f(q_0)$ and $f(q_a)$ for the 1D case, is shown in Figs. 5.3.3. The parameters used for these examples are 23 g of Al_2O_3 , 1 yr exposure and $[\sim 0.105 - 16]$ keV as energy range. The lower energy limit is the lowest energy which is kinematically accessible, the upper limit is taken equal to the CRESST-III acceptance region. Data are distributed in 10 energy bins and three background-normalisations are considered: $\lambda_b = 10^3, 10^4$ and 10^5 .

¹¹See [201] for updated fits on the $c_p = c_n$ case.

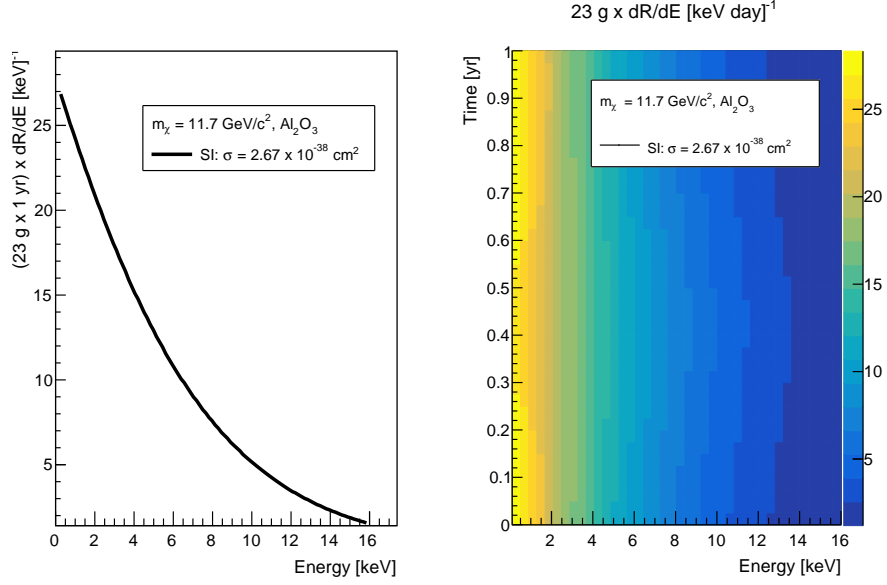


Figure 5.3.2: Differential rate for a DM signal simulated according to DAMA best-fit parameters and scattering off a sapphire target. The exposure is 23 g sapphire crystal for 1 yr. **Left:** 1D spectrum, distributed as a function of energy. **Right:** 2D spectrum, distributed in time and energy. From the color-map it becomes evident that at low energy the maximum of the rate is around January/December, while at high energy the maximum of the rate is around June, as expected according to the change of the time of maximal rate during the year as a function of the energy range considered (see discussion and curves $t_{max}(v_{min})$ in Sec. 4.2).

Efficiency and resolution are not taken into account¹². The background is assumed to be known, thus the background normalisations are fixed parameters. Results for the 1D and 2D analyses are given in Tab. 5.4. For an ideal detector (efficiency and resolution are not taken into account) constituted by 23 g of Al_2O_3 , with an acceptance energy region equal to $[0.105 - 16]$ keV and for 1 yr exposure, the p-value for background-only-hypothesis rejection is approximately zero (zero within the precision of the MC used in this work) for a background level $\lambda_b = 10^3$ counts, 0.046 (0.045 for 2D analysis) for $\lambda_b = 10^4$. According to these results, if the background-normalisation is known, an ideal CRESST detector affected by a factor 10 more background-counts with respect to current CRESST-III counts in the acceptance region (which are about 500 in 158 days) would be still sufficient to exclude the background-only-hypothesis with $\sim 2\sigma$ if a DM signal described by DAMA best fit parameters was the true model. By increasing the background level, the p-value becomes larger, while increasing the exposure the p-value

¹²The 2D analysis is favoured when larger number of counts are available, because of the small fraction of counts which modulate during the year around the central value of the differential rate. According to this observation, the assumption of ideal detectors, with efficiency equal to one and perfect energy resolution, favours the 2D analysis. For this reason, detector-dependent terms will be considered only if the 2D-analysis results useful to lower the p-value.

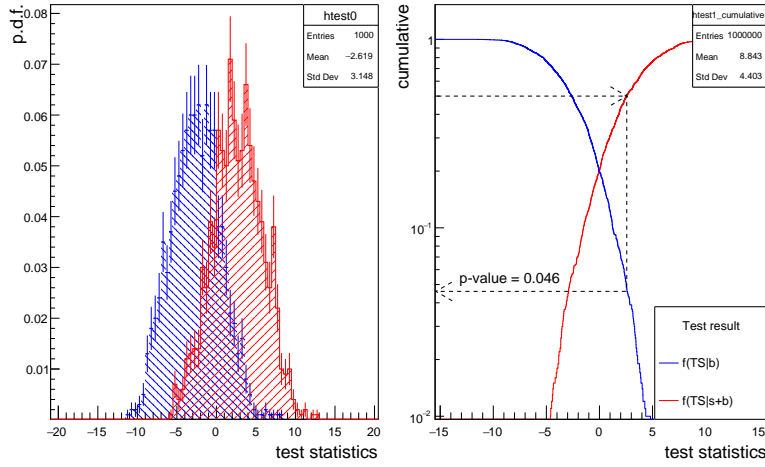


Figure 5.3.3: **Left:** 1D test statistics distributions for the null (blue) and alternative (red) hypotheses. **Right:** Cumulative of the test statistics distributions. Mass exposure = 23 g of Al_2O_3 , time exposure = 1 yr, $\lambda_s \simeq 141$ counts, number of iteration = 10^3 . $\lambda_b = 10^4$, p-value $\simeq 0.046$.

gets smaller and the significance for B-rejection improves, as expected. This behaviour is common to 1D and 2D analyses and the comparison shows that the introduction of a time dependent analysis is not advantageous with respect to the analysis based just on the energy-spectrum. Since results are probabilistic, the p-values should be sampled and then compared. However, since this analysis is seeking for an evident advantage of the 2D analysis, such comparison is not further explored.

m_T	time	λ_b	λ_s	N inter	p-value 1D	p-value 2D
23 g	1 yr	10^3	$\simeq 141$	10^3	$\simeq 0$	$\simeq 0$
"	"	10^4	"	"	0.046	0.045
"	"	10^5	"	"	0.284	0.247
2 x 23g	"	"	283	"	0.161	0.163
3 x 23g	"	"	424	"	0.055	0.077

Table 5.4: Neyman-Pearson: Results for the case of DAMA-like signal, known background and no nuisance parameters. The number of bins is fixed to 10 both for energy and time.

PL-method: background normalisation as nuisance parameter. If the number of background events is unknown, as it is the case for CRESST-III, the problem of signal discovery can be treated using the PL-method explained in Sec. 5.3.3, based on the test-statistics in Eq. 5.9. The signal is simulated under the same assumptions made in the previous section (SI DM scatterings off 23 g of Al_2O_3 , for the DM model described by DAMA signal best-fit parameters). Three configurations for three different background

normalisations are simulated: 10^3 , 10^4 and 10^5 counts. The background normalisation is treated as a nuisance parameter.

Note on signal simulation: When the likelihood function is maximised over one or more parameters, test statistics computation gets slower, especially for the 2D case. 2D analysis takes around 10 seconds to compute one profile likelihood-ratio. For this reason, in this part of the analysis the signal is simulated by replacing the nuclear form factors computed using the package *DMFormFactor* [14] with the general Helm form factors [151], described in Sec. 3.3. Helm form factors, although less accurate, allow to write down the analytical equation for the differential rate which fastens the simulation. The cost is a difference of about 16 counts in the total rate. In fact, in Tab. 5.4 the total number of counts for 23 g of Al_2O_3 and for 1 yr exposure is $\simeq 141$, while in Tab. 5.5 is $\simeq 159$. If the Helm form factors are replaced in the calculations which lead to the results in Tab. 5.4, the p-values obtained are similar to the ones in Tab. 5.4.

Results are summarised in Tab. 5.5, both for 1D and 2D analysis. When the background-normalisation is not known and the PL-method is used, the p-value is larger than the p-value found for the case of known background (Tab. 5.4), as expected according to Neyman-Pearson's lemma. An example of the profile-likelihood distributions obtained in this section is shown in Fig. 5.3.4.

m_T	time	λ_b	λ_s	N inter	p-value 1D	p-value 2D
23 g	158 days	500	$\simeq 69$	10^3	0.086	0.083
"	1 yr	10^3	$\simeq 159$	"	$\simeq 0$	$\simeq 0$
"	"	10^4	"	"	0.21	0.212
"	"	10^5	"	"	0.398	0.415
23 g	2 yr	$2 \cdot 10^3$	$\simeq 319$	"	$\simeq 0$	$\simeq 0$
"	"	$2 \cdot 10^4$	"	"	0.127	0.14
"	"	$2 \cdot 10^5$	"	"	0.34	0.362

Table 5.5: PL-method for DAMA-like signal and for the case of background normalisation considered as nuisance parameters. $m_\chi = 11.7 \text{ GeV}/c^2$.

The comparison of the results in Tab. 5.5 for the 1D and 2D analysis, shows that using the PL-method for an unknown background normalisation, for a signal compatible with the DAMA/LIBRA best-fit results and for the given exposures, a 2D analysis does not bring advantages to the signal from background discrimination in CRESST-like detectors.

1D versus 2D analysis for signal with $m_\chi = 3 \text{ GeV}/c^2$

In this section different DM parameters to the DAMA best fit are assumed and the problem of signal discovery is investigated for a different benchmark of DM mass and cross-section. The benchmark is fixed at the DarkSide-50 upper limit at $m_\chi = 3 \text{ GeV}/c^2$ ($\sigma_p \simeq 4 \cdot 10^{-42} \text{ cm}^2$) [33] and the PL-method described in Eq. 5.9 is used.

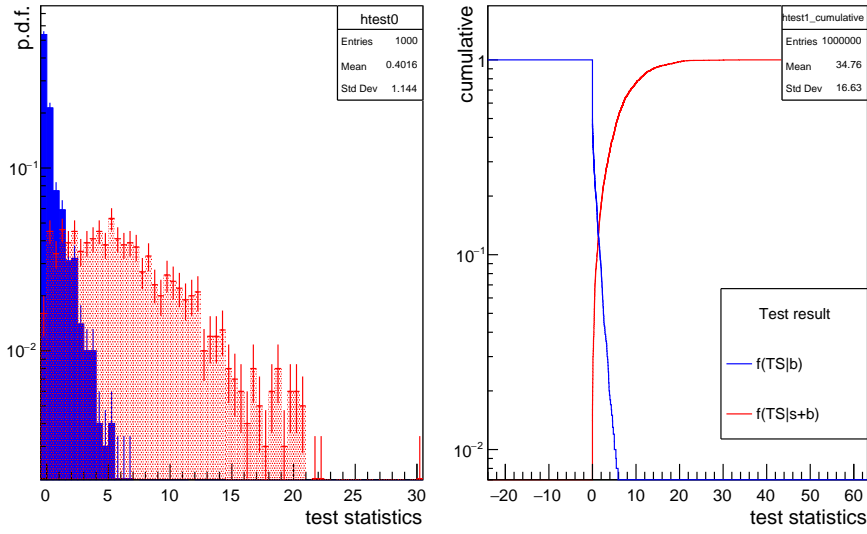


Figure 5.3.4: Example for the PL-ratio test statistics distributions.

Why $m_\chi = 3 \text{ GeV}/c^2$? In the region of low DM-mass, exclusion limits on the DM-nucleon couplings strongly depend on the energy threshold of the experiments. For this reason, low-temperature experiments despite of their small mass exposure, are more suitable. Currently, TPCs experiments are all sensitive to $m_\chi > 3 \text{ GeV}/c^2$ [242], if the new limits which use the Migdal effect and Bremsstrahlung processes [243] are not considered. The benchmark is fixed at $m_\chi = 3 \text{ GeV}/c^2$ because it is the lowest DM mass which would cause a minimum recoil velocity below $\sim 200 \text{ km/s}$. If minimum recoil velocities below $\sim 200 \text{ km/s}$ are included, it is possible to establish if sensitivity to the energy region where the inversion of phase occurs (see Fig. 4.2.1) is statistically beneficial when the 2D-dimensional analysis is used. The largest energy range compatible with kinematics for scattering of $3 \text{ GeV}/c^2$ DM particles off Al_2O_3 is considered, which is $\simeq [0.012 - 5.4] \text{ keV}$. To fasten the simulation, the Helm form factors are used, as in the previous section.

Results of the 1D vs 2D comparison are summarised in Table 5.6. Similarly to previous sections, the comparison between the 1D and 2D analyses shows that, under the conditions described in this work (using PL-method for the unknown background normalisation, a signal with a DM mass of $3 \text{ GeV}/c^2$ and $\sigma_p = 4 \cdot 10^{-42} \text{ cm}^2$ and the exposures listed in Tab. 5.6), the 2D analysis does not bring any statistical improvements to the problem of signal discovery with respect to the 1D analysis. In Fig. 5.1.3, the sensitivity curve of CRESST-III is almost two orders of magnitude higher than the benchmark used for this analysis. The result in Tab. 5.6 is in agreement with observations, as the 90% of CL for signal discovery is found for an exposure which is between 100 and 500 times larger than the current CRESST-III exposure ($23 \text{ g} \times 158 \text{ days}$). In

target mass	time	λ_s	λ_b	N iter	p-value 1D	p-value 2d
23 g	158 days	$\simeq 1$	500	10^3	0.436	0.482
230 g	"	$\simeq 22$	10^4	"	0.323	0.346
"	2 yr	$\simeq 45$	$2 \cdot 10^4$	"	0.223	0.263
"	5 yr	$\simeq 112$	$5 \cdot 10^4$	"	0.151	0.151
1 kg	"	$\simeq 491$	"	"	$\simeq 0$	$\simeq 0$
"	"	"	$5 \cdot 10^5$	"	0.065	0.094

Table 5.6: PL-ratio method, with background normalisation as the only nuisance parameter. Energy window is $\simeq [0.012 - 5.4]$ keV, $m_\chi = 3$ GeV/ c^2 , target is Al₂O₃.

particular, for the exposure 230 g \times 5 yr, which corresponds to about 100 times the exposure of CRESST-III, the p-value is equal to 0.151, while for an exposure of 1 kg \times 5 yr, which corresponds to about 500 times the exposure of CRESST-III, the p-value is below 0.1. Therefore, the results in Tab. 5.6 are consistent with the two orders of magnitude which separate current CRESST-III sensitivity limit from the benchmark used in this work.

5.3.6 Results on model selection

If a DM signal was detected, the challenge would be to identify the type of DM-nucleon interaction. Based on the statistical method discussed in Sec. 5.3.3, Eq. 5.10, the following analysis aims at establishing if the monitoring of the count rate time dependence in CRESST-like detectors increases the statistical significance for model selection. A similar analysis was presented in [236] for thresholds up to 300 MeV (for Germanium), DM masses larger than 20 GeV/ c^2 and under the assumption of zero-background. The study performed in this work focuses on low-energy-threshold (down to 10 eV) experiments, low DM masses (*e.g.* 3 GeV/ c^2 , but lighter particles can be considered as well) and takes into account the effect of non-zero background. To simplify the treatment, the DM mass is assumed as known.

Discrimination between SI and magnetic dipole DM interactions. The benchmark used in the previous section, ($m_\chi = 3$ GeV/ c^2 and $\sigma_p^{SI} = 4 \cdot 10^{-42}$ cm²), is used to simulate the signal under the null-hypothesis, that is SI DM-nucleon interactions, and to extract the corresponding benchmark for the alternative-hypothesis, that is MDDM interactions (see Appendix C.2). The total number of expected signal counts for the SI-interaction can be in fact computed for the exposure and target of interest and it can be used as the starting point to extract the value of the corresponding cross-section for any other interactions at the same DM mass, which is assumed as known. For example, using 23 g of sapphire and 1 yr exposure, the number of counts expected for the SI-interaction hypothesis is $\simeq 2.2$ counts. The MDDM cross-section corresponding to this number of counts (for the same DM-mass $m_\chi = 3$ GeV/ c^2) is equal to $\sigma_{MD} \simeq 4.72 \cdot 10^{-41}$ cm². To summarise, the test-statistics for the null-hypothesis is built by using,

$$\sigma_p^{SI} = 4 \cdot 10^{-42} \text{ cm}^2 \quad \text{and} \quad m_\chi = 3 \text{ GeV}/c^2 \quad (5.21)$$

while the alternative-hypothesis is constructed assuming,

$$\sigma_{MD} = 4.72 \cdot 10^{-41} \text{ cm}^2 \quad \text{and} \quad m_\chi = 3 \text{ GeV}/c^2 \quad (5.22)$$

An example of energy spectrum simulation is shown in Fig. 5.3.5. These energy spectra, as well as the analysis which follows are derived using the nuclear form factors computed with a modified version of the software *DMFormFactor* [14] given in [186] and the three-dimensional DM velocity distribution integrals computed with a computer code developed during this thesis and mentioned in Sec. 4.2, which includes the Sun gravitational focusing effect.

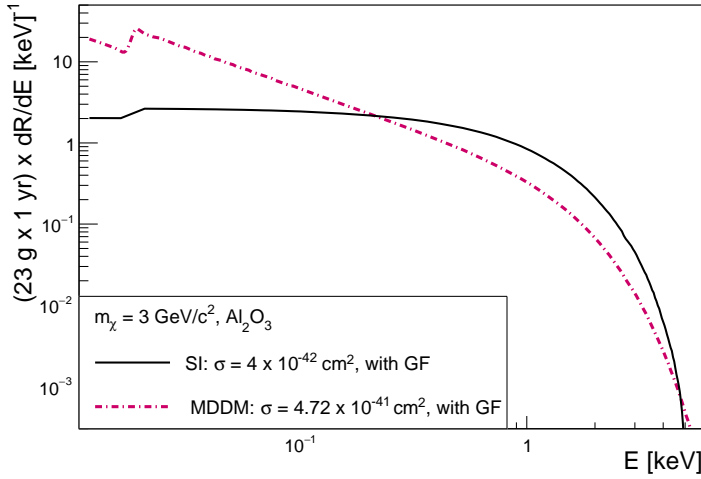


Figure 5.3.5: Energy spectra for SI (black) and MDDM (purple) interactions for $m_\chi = 3 \text{ GeV}/c^2$, scattering off Al_2O_3 , with $\sigma_p^{SI} = 4 \cdot 10^{-42} \text{ cm}^2$ and $\sigma_{MD} = 4.72 \cdot 10^{-41} \text{ cm}^2$, respectively. The Sun gravitational focusing (GF) effect is included. Exposure = $23 \text{ g} \times 1 \text{ yr}$, energy range = $\sim [0.01 - 5.4] \text{ keV}$. The total number of counts is $\simeq 2.2$.

Motivation for assuming the MDDM model as alternative-hypothesis. In Sec. 4.2, Fig. 4.2.4, the curve describing the time of the year of maximal rate as function of the minimal velocity, $t_{max}(v_{min})$, is drawn for the MDDM interaction with ^{27}Al and ^{40}Ca . In that context, it was explained that since both ^{40}Ca and ^{16}O are spin-0 nuclei, their $t_{max}(v_{min})$ curve for MDDM interaction is the same for any DM mass considered, therefore the plot can describe both the nuclei which constitute sapphire crystals. If DM consists of light particles ($m_\chi < 10 \text{ GeV}/c^2$) and interacts via its magnetic dipole with the electromagnetic field of the nucleus, the $t_{max}(v_{min})$ curve in Fig. 4.2.4 is flat and fixed in June along the whole range of minimal velocities both for ^{27}Al and ^{16}O . Since, instead, for SI-interactions an inversion of phase is expected for $v_{min} \leq 200 \text{ km/s}$ (see Fig. 4.2.3, Sec. 4.2), it was natural to explore the possibility of discriminating the two models (SI and MDDM) on the basis of their time-dependence in the low-energy-region.

m_χ	m_T	time	λ_b	λ_s	N inter	p-value 1D	p-value 2D
3 GeV/c ²	23 g	1 yr	10 ³	$\simeq 2.2$	10 ³	0.467	0.338
"	230 g	2 yr	$2 \cdot 10^3$	$\simeq 44$	"	0.101	0.145
"	"	5 yr	$5 \cdot 10^3$	$\simeq 110$	"	0.056 (0.02, 0.021)	0.024 (0.025)
"	1 kg	"	$2 \cdot 10^4$	$\simeq 478$	"	$\simeq 0$	$\simeq 0$

Table 5.7: Model selection: Comparison between 1D and 2D analyses (SI-interaction vs MD-interaction). In parenthesis, additional computations under same conditions are provided as a cross-check of the first result.

Results. The results of the comparison between p-values computed using 1D (energy-only) or 2D (energy and time) analyses are collected in Table 5.7.

Similarly to the results obtained for the problem of signal discovery, under the assumptions considered, the conclusion is that the 2D analysis is not advantageous with respect to the 1D analysis.

The prospects for model selection using annual modulation for DD Generation 2 (G2) experiments which are currently taking data or will take data in the future (*e.g.* XENON1T¹³, SuperCDMS¹⁴ and LZ¹⁵) are presented in [236]. Three benchmarks of DM mass (20 GeV, 125 GeV and 500 GeV) and corresponding cross-sections taken from the most constraining DD upper limits ($\sigma = 2 \cdot 10^{-46}$ cm², $\sigma = 1.8 \cdot 10^{-46}$ cm² and $\sigma = 6.94 \cdot 10^{-46}$ cm²) are considered for signal simulation; detectors are assumed as ideal (unitary efficiency, infinite energy resolution and null-background) and a statistical bayesian approach is used. Their conclusion is that introducing the time information in G2 experiments does not improve the prospects for model selection (the two models there considered are the conventional SI-interaction and the anapole DM model), while it is promising for Generation 3 (G3) experiments. For the case of G3-experiments the focus is mainly on Xe-based DD experiments, and the assumptions are an exposure of 40000 kg \times yr and an energy threshold of 5 keV (see Tab. 2 of [236]).

In general, the lower the energy threshold, the lower the detectable DM mass, and, consequently, the larger the cross-sections not yet excluded and which can be probed. The reason is that low energy thresholds are typically achieved by small size experiments, which therefore put weaker constraints on the DM-nucleon cross-section because of the limited exposure. The idea of the work discussed in this section is to establish, using a statistical frequentist approach, if introducing the timing information in the analysis of low threshold experiments (more specifically, CRESST-III) helps the discrimination of models when an exponential background rate is considered. The benchmark used for the signal simulation is a DM mass of 3 GeV and a cross-section of $4 \cdot 10^{-42}$ cm², the target considered is Al₂O₃ and the energy threshold is about 10 eV. Comparing the conventional SI-interactions with the MDDM model, the 2D-analysis based on time

¹³<http://www.xenon1t.org>

¹⁴<https://supercdms.slac.stanford.edu>

¹⁵<https://lz.lbl.gov>

and energy does not improve the significance for model selection with respect to the 1D energy-only analysis.

This analysis, however, highlights the potential of current CRESST-III setup to make model selection using the 1D analysis: Tab. 5.7 shows that if a total exposure larger than $230 \text{ g} \times 2 \text{ yr}$ was available, the MDDM model could be discriminated from the SI-interaction model at 90% of C.L.. For a final statement about this prediction, detector efficiency and energy resolution must be included in the estimations.

Chapter 6

COSINUS phenomenology

- Section taken from [5] and [6].

COSINUS (Cryogenic Observatory for Signatures seen in Next-generation Underground Searches) is an experiment employing scintillating cryogenic calorimeters dedicated to the direct DM search in underground laboratories. Its goal is to cross-check the annual modulation signal the DAMA collaboration has been detecting for about 20 years [244] and which has been ruled out by other experiments in certain DM scenarios. COSINUS can provide a model-independent test by the use of the same target material (NaI), with the additional chance of discriminating β/γ events from nuclear recoils on an event-by-event basis, by the application of a well-established temperature-sensor-technology developed within the CRESST collaboration (see Sec. 5.1). This technology had so far never been applied to NaI crystals because of several well-known obstacles, and COSINUS is the first experiment which succeeded to operate NaI crystals as cryogenic calorimeters. In Sec. 6.1 COSINUS scientific case is motivated, Sec. 6.2 describes COSINUS prototype design and development status, Sec 6.3 is dedicated to COSINUS pulse shape model, which was developed within this thesis and it is an extension of the generic model for cryogenic particle detectors with superconducting phase transition thermometers published in 1995 [245], in order to describe the COSINUS detector response. Section 6.4 contains preliminary studies on phonon propagation in NaI, conducted in collaboration with the theoretical solid state group of the University of L'Aquila.

6.1 COSINUS scientific motivation

Any scientific result requires severe tests before being accepted as a new contribution to knowledge. More than 20 years ago, the experiment DARKMATTER (DAMA) [177] was realised for the search of hypothetic particles supposed to be the content of the dark halo surrounding the galaxy [246]. After a brief period of data taking, during the TAUP conference held in 1997 at the Gran Sasso National Laboratory (L'Aquila, Italy) the collaboration released data showing the detection of a signal compatible with the

expectations for DM [247]. The experiment has been running since that time and also the most recent data release confirms the detection [25]. Experiments exploiting different techniques probed the DM parameter space and, according to the DAMA result, the claim of a positive signal looked right around the corner and would have provided an unambiguous proof of the detection of DM. Despite of the extraordinary effort and the development of cutting edge technologies, the DAMA detection has not been confirmed by any experiment (see Fig. 3.4.1) and has been excluded in some scenarios [189, 248]. At the same time, all attempts for alternative explanations of the signal are excluded according to the DAMA collaboration (*e.g.* [249, 250]). The exigency of testing this result has motivated the construction of numerous experiments based on the same technology as the DAMA setup for a completely model independent check [26, 27, 43, 251]. COSINUS participates to this campaign and, employing NaI crystals at milli-Kelvin temperature, it aims at developing a dual channel detector, which collects both the light and the heat produced by a particle interaction in the crystal. The discrimination of e^-/γ events from nuclear recoils can provide a powerful test of the nature of the DAMA signal.

COSINUS time scale is very competitive, since the measurement time to reach the required sensitivity is with roughly two years significantly shorter compared to modulation-only searches.

6.2 Experimental concept

The COSINUS prototype is a scintillating cryogenic calorimeter operated at milli-Kelvin temperature [252]. The target material is a small cubic NaI crystal installed in a copper housing (Fig. 6.2.1, left panel). The detection principle relies on the measurement of the temperature increase caused by an energy deposition in the target material. For this measurement, a temperature sensor is required. COSINUS applies Transition-Edge-Sensors (TES), a technology developed within the CRESST collaboration (Sec. 5.1). These highly sensitive temperature sensors consists of tungsten thin films (W-TES), whose specifics are described below. If evaporated directly onto the absorber, a good thermal contact can be achieved [253]. However, since NaI is hygroscopic, the evaporation directly on its surface is not feasible¹. Therefore, the small cube is interfaced to another crystal (*e.g.* CdWO_4), named carrier, of about 40 mm in diameter and $\sim 1 - 2$ mm of thickness, which is instrumented with a TES instead. The interface between NaI and carrier is made by amorphous materials, like epoxy resin or silicone oil. Energy depositions in the target material cause lattice vibrations whose energy flux is transmitted to the carrier and measured by the TES as an increase of temperature. The NaI crystal, interfaced to the carrier and the TES, is the phonon-detector. The detected scintillation light, which accounts for about 10% with respect to the energy converted in heat, is measured by a beaker-shaped light-absorber made from silicon and enclosing the NaI target. The silicon beaker dimensions are: 40 mm in diameter, 39 mm in height

¹Photolithography and handling NaI in electron-beam evaporation-systems and sputter-machines is not feasible both for guaranteeing a controlled humidity-free atmosphere and temperature far away from the melting point.

and a wall-thickness of about $420\ \mu\text{m}$. Its mass is about $9\ \text{grams}^2$. The silicon beaker is also instrumented with a TES (Fig. 6.2.1, central panel). The silicon beaker and the carrier disk are designed to optimise the active surrounding coverage of the target material, in order to fight the surface α -induced background, whose back-to-back emission can produce a nuclear recoil analogous to the expected DM-signal. The silicon beaker, equipped with the TES, is the light detector.

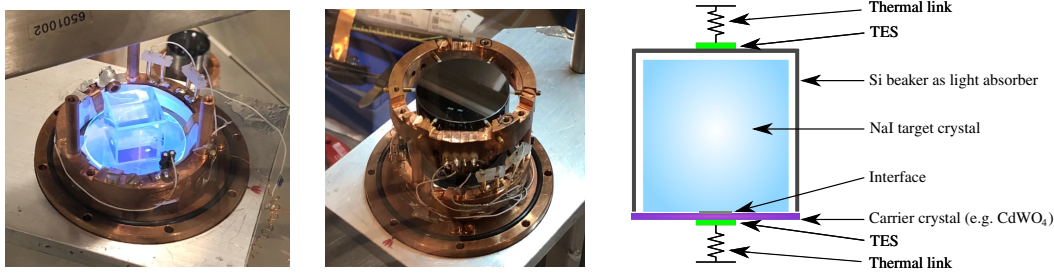


Figure 6.2.1: COSINUS module prototype. **Left:** Photograph of a NaI crystal and a carrier crystal installed in a copper housing and exposed to UV-radiation to show the luminescence effect. **Center:** Silicon beaker enclosing the NaI crystal, equipped with a Transition-Edge-Sensor (TES), visible on top of the beaker surface. **Right:** Schematic drawing of the complete module.

The W-TES (thickness of $200\ \text{nm}$) is evaporated on the carrier and operated in its transition from normal to superconducting state, commonly around $15\text{-}20\ \text{mK}$. An energy deposition results in a temperature increase, which can be measured by the resistance change of the TES - the steeper the transition, the more sensitive the TES. The TES resistance works as electric component of a read-out circuit and the output voltage is finally registered by SQUID (Superconducting Quantum Interference Device) amplifiers. The W-TES technology used here was pushed within CRESST to a sensitivity level of about $4.6\ \text{eV}$ baseline resolution ($\sigma_{baseline}$) for a $24\ \text{g}$ CaWO_4 crystal (CRESST-III) [4] (Sec. 5.1).

The dual-channel read-out of heat and light is a powerful tool for particle discrimination, since the amount of deposited energy going into the production of light depends on the type of event. The suppression expected for nuclear scatterings and α -events with respect to β/γ -events is called light-quenching. The ratio between the amount of energy going into light and the amount of energy converted in heat allows for particle discrimination.

²It is produced by Optec(<https://www.optec-muenchen.de/>) and is machined from bulk silicon, by using a hole saw cutter drill. The surfaces are polished to optical quality.

Status of the prototype development

The first and second COSINUS prototypes have been tested in the cryogenic test facility of the Max Planck Institute installed deep underground in the Gran Sasso National Laboratory (Italy). The dimension and the performance parameters of the second COSINUS prototype are summarised in Tab. 6.1. The light yield (LY) versus energy plane in Fig. 6.2.2 shows data distributed according to two populations: an e^-/γ band centered around $LY \simeq 1$ and a population of events around $LY \simeq 0$, attributed to the carrier. This second population is mainly attributed to stress in the materials, which showed cracks during the unmounting [254], and also to particle events which released energy directly in the carrier. In the e^-/γ band the discrimination of the atomic radiation from ^{40}K is evidently confirmed, together with the 60 keV line from an ^{241}Am source. A relevant result is the discrimination of another atomic spectral line, that is the iodine escape line at around 30 keV, resulting from the photoelectric interaction of the 60 keV X-rays of the ^{241}Am source with the iodine K-shell electrons. The iodine K-shell binding energy is $\simeq 33$ keV. This result has a noteworthy implication. The most abundant isotope of iodine is ^{127}I and it has a non-null cross section ($\sigma \simeq 10$ barns for thermal neutrons (<https://www.oecd-nea.org/janisweb/>) for the (n, γ) process which leads to ^{128}I production. ^{128}I is unstable and decays to ^{128}Xe via β^- decay ($\sim 93.1\%$) and to ^{128}Te via electron capture (EC) ($\sim 6.9\%$) or via β^+ decay ($\sim 0.0026\%$), with half-life $\tau_{1/2} = 24.99$ min [255]. ^{128}Te is left on its first nuclear excited state or on its ground state. In the first case, an X-ray emission at $\simeq 743.22$ keV is expected for nuclear de-excitation. The electron capture is followed by an atomic relaxation occurring through X-ray and Auger emissions, which are likely to be detected as the binding energies of the atomic shells (*e.g.* $\simeq 32$ keV and $\simeq 4.3$ keV, for K and L_3 -shells respectively [255]), whose intensities can be found in <https://www-nds.iaea.org/exfor/endl.htm>. Single atomic spectral lines could emerge if the ^{128}I production process occurs on the crystal surface. COSINUS has proven to have the chance for discriminating also this background.

Mass:	$\simeq 66$ g
Exposure:	1.32 kg days
Crystal dimension:	$(20 \times 20 \times 30)$ mm ³
Interface:	Epoxy resin
Phonon detector threshold:	$[8.26 \pm 0.02$ (stat.) keV ($\sigma_{baseline} = 1.01$ keV)
Light detector threshold:	0.6 keV _{ee} ($\sigma_{baseline} = 0.015$ keV _{ee})
Energy detected in light:	$\simeq 13\%$

Table 6.1: COSINUS 2nd prototype parameters [156].

Improving the radio-purity of NaI crystals is an important step of the COSINUS prototype development. For what concerns potassium concentration, achieving high radio-purity is crucial because of the ^{40}K -decay-emission, which is a source of background in the region of interest of DAMA. In collaboration with SICCAS (Shanghai Institute of Ceramics, Chinese Academy of Science), COSINUS achieved the result of

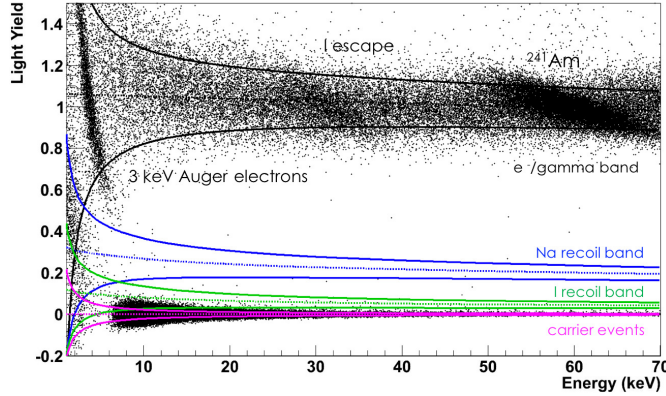


Figure 6.2.2: COSINUS 2nd prototype data, shown in the light yield versus energy plane. From top to bottom: e^-/γ band (black), the sodium recoil band (blue), the iodine recoil band (green) and the carrier band (magenta). ^{40}Ar K-shell line and the ^{128}I escape line are visible at $\simeq 3.2$ keV and $\simeq 30$ keV, respectively. More details are in the text. At 60 keV the line from ^{241}Am source is visible. The carrier band is populated by particles interacting with the carrier volume itself and, mainly, by lattice vibrations due to micro-fracturing that in this measurement occurred in the NaI and the carrier due to thermal stress induced by the Epoxy resin-based interface.

growing NaI-crystals with potassium concentrations of 5-9 ppb at crystals' nose and 22-35 ppb at crystals' tail [256]. COSINUS crystals' potassium concentration at the crystals' nose is below the one of DAMA crystals.

In Tab. 6.1 the characteristics of COSINUS 2nd prototype are summarised. With the beaker-shaped light-absorber design, $\sim 13\%$ ($\sim 10\%$) of the energy deposited in pure (doped)³ NaI crystals is measured in the light detector [156]. The light-energy threshold achieved is ~ 0.6 keV_{ee} (ee = electron-equivalent). The phonon-energy threshold is still far from the COSINUS goal of 1 keV⁴, although it has been improved with respect to the threshold reached in [156] that was ~ 8.26 keV (this was the 2nd prototype, described above, the best recent prototypes arrive at 5-6 keV). The challenging phonon-threshold optimisation is attributed to the vibrational properties of NaI, which require an accurate choice of the temperature sensor (*e.g.* TES/NTD and geometry) and of the general detector design (*e.g.* carrier material).

³The employment of Tl-doped crystals in COSINUS could provide a better discrimination between nuclear recoils and beta/gamma events. However, to establish if the Tl-dopant, apart from changing the LY for beta/gamma events, also changes the light quenching factor (QF), the results from the already planned measurements at the Triangle Universities Nuclear Laboratory (TUNL) facility are necessary. In general, Tl-doped crystals have a lower light output than the pure ones, thus if their QF is the same, pure NaI crystals will be employed. The argument that the DAMA/LIBRA signal is due to inelastic DM scattering off Tl-nuclei is investigated in [257] and largely constrained by [4].

⁴Note that in the phonon-channel, the energy-threshold is already a nuclear-recoil energy-threshold. As comparison, in DAMA/LIBRA the threshold of ~ 1 keV_{ee} corresponds to ~ 3 keV in a recoil off Na, for a light-quenching factor of ~ 0.3 , and to ~ 10 keV in a recoil off I, for a light-quenching factor of ~ 0.1 .

6.3 COSINUS pulse-shape model

The general model for cryogenic particle detectors using superconducting phase transition thermometers was published by F. Pröbst *et al.* in 1995 and it is the starting point for the characterisation of this class of detectors. The working principle of CRESST detector modules is well described by this original model, which assumes a module setup as reported in Fig. 6.3.1. Since COSINUS temperature sensors are based on the technology developed within the CRESST collaboration, the general model by F. Pröbst *et al.* is applied to COSINUS data as well. However, results from the first COSINUS prototype [37] challenged the direct application of the model: in this section the original model by F. Pröbst *et al.* is reviewed, COSINUS experimental findings are discussed and the extension of the original model which was developed in this thesis to better reproduce the phenomenology of the COSINUS setup is presented, followed by its validation using experimental data.

6.3.1 Original pulse shape model (PSM)

The model presented in [36] by Pröbst *et al.* is based on the detector scheme in Fig. 6.3.1. It represents a standard detector module constituted by the ‘absorber’ (the target crystal) thermally coupled to the temperature sensor, both thermally coupled to a thermal bath. In Fig. 6.3.1, T_a , T_e and T_b are the temperatures of the phonon system in the absorber, of the electron system in the TES and of the thermal bath, respectively. C_a and C_e are the absorber and TES heat capacities. G_{ij} are the thermal conductances between system i and system j . G_K is the Kapitza thermal conductance, that is a thermal boundary conductance. The parallel between G_K and the electron-phonon thermal-coupling, G_{ep} , is the absorber-TES thermal conductance, G_{ea} .

Any particle interacting in the absorber deposits a certain amount of energy, which is partially converted into optical phonons (see Sec. 6.4). Optical phonons are non-thermal phonons, with higher frequency with respect to the thermal (or acoustical) phonons. The transmission probability of non-thermal phonons through the interface depends on many factors, which can be parametrised considering that only a certain fraction of the initial deposited energy is injected into the TES. The coupling between non-thermal phonons and electrons in the thermometer perturbs the electron system, which then thermalises at higher temperature with respect to T_b . The same happens to the phonon system in the absorber as a consequence of the thermalisation of optical phonons in the absorber. However, since the whole system is coupled to the thermal bath, the equilibrium is reached once the temperature in all the components goes back to the ‘bath temperature’, T_b .

The phenomenology just described, is mathematically formalised in [36] as a system of differential equations whose solution provides the behaviour of the temperature of the TES, $T_e(t)$, and of the absorber, $T_a(t)$, as a function of time. The model for an ideal sensor ⁵, is the following (Eqs. 8 and 9 of [36]),

⁵Equation 6.1 neglects the finite thermal conductance along the film, that is why the sensor is ‘ideal’. In [36] also the realistic case which considers the finite thermal conductance along the film is discussed

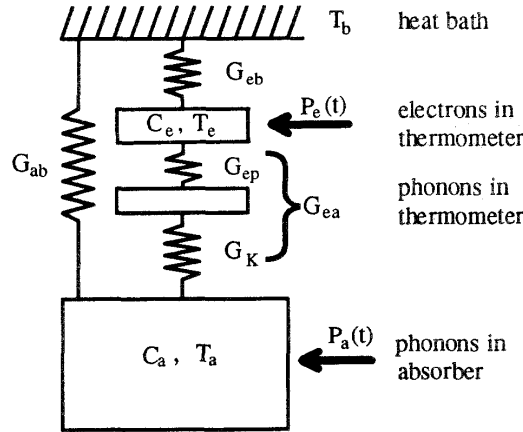


Figure 6.3.1: Scheme of thermal couplings in a cryogenic detector: T_a , T_e and T_b are the temperatures of i) phonon system in the absorber (crystal), ii) electron system in the TES and iii) the thermal bath, respectively. C_a and C_e are the absorber and TES heat capacities. G_{ij} are the thermal conductances between system i and system j . G_K is the Kapitza thermal conductance, that is a thermal boundary conductance. G_K combined with the electron-thermal-phonon thermal-coupling, G_{ep} , is the absorber-TES thermal conductance, G_{ea} . Fig. 6 of [36].

$$\begin{cases} C_e \frac{dT_e}{dt} + G_{ea}(T_e - T_a) + G_{eb}(T_e - T_b) & = P_e(t) \\ C_a \frac{dT_a}{dt} + G_{ea}(T_a - T_e) + G_{ab}(T_a - T_b) & = P_a(t) \end{cases} \quad (6.1)$$

where $P_e(t)$ and $P_a(t)$ are the power inputs in the thermometer and in the absorber, respectively, which are defined as (Eq. 2 of [36]),

$$\begin{cases} P_e(t) & = \Theta(t)P_0 e^{-t/\tau_n} \\ P_a(t) & = \frac{(1-\epsilon)}{\epsilon} P_e(t) \end{cases} \quad (6.2)$$

where $P_0 = \epsilon \frac{\Delta E}{\tau_n}$ is the power input at $t = 0$ into the thermometer (Eq. 3 of [36]), τ_n is the relaxation-time constant of non-thermal phonons, ϵ is the fraction of non-thermal phonons which thermalise in the TES and ΔE is the deposited energy. The time constant τ_n is a function of the relaxation-time of non-thermal phonons in the crystal, τ_a , and in the film, τ_{film} , (Eq. 4 of [36]),

$$\tau_n = \left(\frac{1}{\tau_a} + \frac{1}{\tau_{film}} \right)^{-1} \quad (6.3)$$

The system of differential equations 6.1 has the structure,

$$\begin{cases} \dot{\mathbf{x}}(t) & = \mathbf{A} \mathbf{x} + \mathbf{f}(t) \\ \mathbf{x}(t=0) & = \begin{pmatrix} T_b \\ T_b \end{pmatrix} \end{cases} \quad (6.4)$$

and solved.

where,

$$\mathbf{x}(t) = (T_e(t) \quad T_a(t)) \quad (6.5)$$

$$\mathbf{A} = \begin{pmatrix} -\frac{G_{eb}+G_{ea}}{C_e} & \frac{G_{ea}}{C_e} \\ \frac{G_{ea}}{C_a} & -\frac{G_{ab}+G_{ea}}{C_a} \end{pmatrix} \quad (6.6)$$

$$\mathbf{f}(t) = \begin{pmatrix} \frac{G_{eb}T_b}{C_e} + \frac{P_e(t)}{C_e} \\ \frac{G_{ab}T_b}{C_a} + \frac{P_a(t)}{C_a} \end{pmatrix} \quad (6.7)$$

The system in 6.4 is a 2-dimensional non-homogenous first order differential system, with constant coefficients. Its solution [258]⁶, is,

$$\mathbf{x}(t) = e^{\mathbf{A} t} \mathbf{c} + \int_0^t ds e^{\mathbf{A}(t-s)} \mathbf{f}(s) \quad (6.8)$$

where \mathbf{c} is a vector of coefficients fixed by initial conditions. If A -matrix is diagonalisable, then,

$$e^{\mathbf{A} t} = \mathbf{P} e^{\mathbf{D} t} \mathbf{P}^{-1} \quad (6.9)$$

where \mathbf{P} is the matrix which has as columns A -eigenvectors and \mathbf{D} is the diagonal-matrix which has as elements A -eigenvalues. All the integrals needed to find the solution are of the type,

$$\int_0^t ds e^{a(t-s)} = \frac{e^{at} - 1}{a} \quad (6.10)$$

The solution of Eq. 6.4 is,

$$T_e(t) = T_b + \Theta(t)[A_n (e^{-t/\tau_n} - e^{\lambda_1 t}) + A_t (e^{\lambda_2 t} - e^{-t/\tau_n})] \quad (6.11)$$

where λ_1 and λ_2 are the eigenvalues of the matrix in Eq. C.10, the amplitude A_n is the one defined in Eq. 12 of [36] corrected by a multiplicative additional minus and the amplitude A_t is exactly the one defined in Eq. 13 of [36],

$$A_n = -\frac{P_0(s_{in} - (G_{ab}/C_a))}{\epsilon(s_{in} - s_t)(s_{in} - s_n)} \left(\frac{s_t - (G_{ab}/C_a)}{G_{eb} - (C_e/C_a)G_{ab}} - \frac{\epsilon}{C_e} \right) \quad (6.12)$$

$$A_t = \frac{P_0(s_t - (G_{ab}/C_a))}{\epsilon(s_t - s_{in})(s_t - s_n)} \left(\frac{s_{in} - (G_{ab}/C_a)}{G_{eb} - (C_e/C_a)G_{ab}} - \frac{\epsilon}{C_e} \right) \quad (6.13)$$

where $s_{in} = -\lambda_1$, $s_t = -\lambda_2$ and $s_n = 1/\tau_n$. The model in Eq. 6.11 is interpreted as a two component pulse model: the pulse of amplitude A_n is considered as the non-thermal component and its rise time constant is assumed as the intrinsic response of the temperature sensor, while the pulse of amplitude A_t is considered as the thermal component, written so that the rise time constant is equal to the relaxation time of non-thermal phonons.

⁶See <http://people.dm.unipi.it/acquistp/analisi2.pdf>

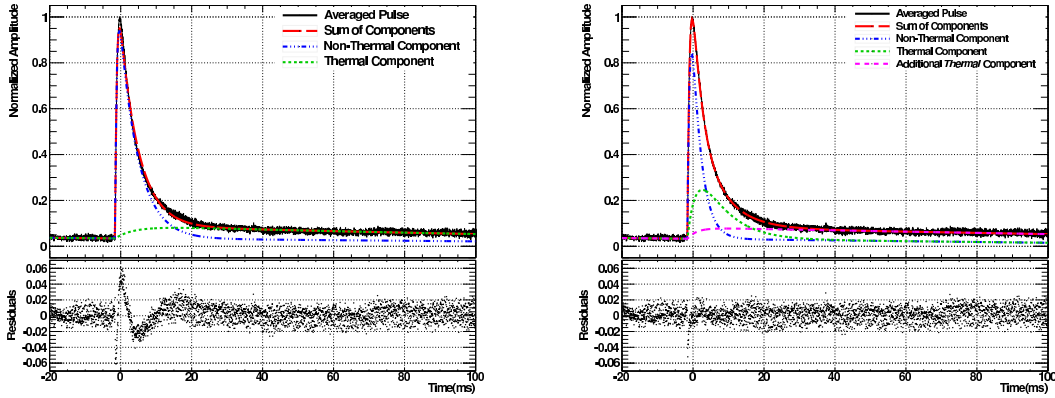


Figure 6.3.2: Fit of a standard event obtained by averaging a large number of 60 keV X-ray events from ^{241}Am source, performed with the two component function in Eq. 6.11 (left panel) and with an additional 2nd thermal component (right panel). On the bottom, the residuals are shown.

COSINUS experimental findings

Since the results obtained with the 1st COSINUS prototype [37], the COSINUS detector signal showed a peculiar pulse shape, which is not well-described by the model in Eq. 6.11. In Fig. 6.3.2, left panel, the fit of the original model to the standard event obtained by averaging a large number of pulses produced at 60 keV from a ^{241}Am source is shown together with the distribution of residuals. The larger residuals of the order of 6% and the observation of a longer tail of the pulse⁷ with respect to expectations based on the CRESST experience, motivated the attempt of introducing a third term in Eq. 6.11, empirically interpreted as an additional thermal component. This finding is interesting as the model in Eq. 6.11 provides a good fit to data collected using other crystals, such as CaWO_4 , CdWO_4 and Al_2O_3 . Same phenomenology is confirmed by data obtained with all subsequent COSINUS prototypes.

A second finding is obtained from neutron calibrations. All the prototypes built according to the design explained in Sec. 6.2 (or slightly different for the light detector geometry which at the beginning was a wafer instead of a beaker) when calibrated with neutron sources provide data which do not allow to identify nuclear recoil events if the LY method explained in Sec. 5.1 is used. More intriguing is the measurement performed with a module constituted by NaI as absorber, sapphire as carrier crystal and a Neutron Transmutation Doped (NTD) temperature sensor for the phonon channel⁸: its data analysis clearly shows the neutron band in the LY plot.

⁷A longer tail of the pulse implies a longer thermalisation time of the film with the bath temperature.

⁸The main difference between the TES and the NTD is that the second has a slower intrinsic response, which makes it mainly insensitive to the temperature rise caused by non-thermal phonons, but suitable to measure (integrating in time) the amount of deposited energy converted in heat.

These two observations pushed for further investigations, which finally focused on three hypotheses:

- NaI crystals are characterised by peculiar phonon propagation properties, which differentiate this material from others,
- The presence of the carrier between the absorber and the TES cannot be neglected in the model if absorber and carrier are not of the same material, as for COSINUS, where the absorber is constituted by NaI and the carrier by *e.g.* CaWO₄, CdWO₄ or Al₂O₃,
- The NaI scintillation light is absorbed by the carrier, which then behaves as a light detector.

These three aspects, which are related and influence each other⁹, are addressed in the following, where a possible explanation to the two findings described above is proposed. For studies on the phonon propagation in NaI see Sec. 6.4.

The first hypothesis, which is that the phonon propagation in NaI is different from the phonon propagation in other materials which COSINUS employs for the carrier (such as CaWO₄, CdWO₄ and Al₂O₃) motivates to consider the absorber and the carrier as two separate systems (second hypothesis), each one with its own non-thermal phonon relaxation time constant, τ_a for the absorber (NaI) and τ_c for the carrier. In this case, the total non-thermal phonon relaxation constant in Eq. 6.3, would be,

$$\tau'_n = \left(\frac{1}{\tau_{film}} + \frac{1}{\tau_c} + \frac{1}{\tau_a} \right)^{-1} \quad (6.14)$$

The third hypothesis was formulated during a brainstorming which was organised at the Max Planck Institute for Physics in Munich (Germany) to discuss with COSINUS and CRESST cryogenic experts the ideas of this proposal, M. Mancuso arose the question on the possible NaI scintillation light absorption in the carrier crystal. Following this idea, in Fig. 6.3.3 the transmission curves of several crystals as a function of the emission wavelength have been collected [260–262].

The scintillation light emission depends on many factors, such as the level of doping, the temperature and the type of particle interacting in the target material [263]. Using as reference $\lambda(\text{NaI}) \simeq 300$ nm and $\lambda(\text{NaI (Tl)}) \simeq 430$ nm, a portion the scintillation light is clearly absorbed by the carriers, which can therefore be considered as a sort of ‘light detector’.

⁹This would explain why CRESST-II modules which also have a carrier crystal did not show the same phenomenology [259].

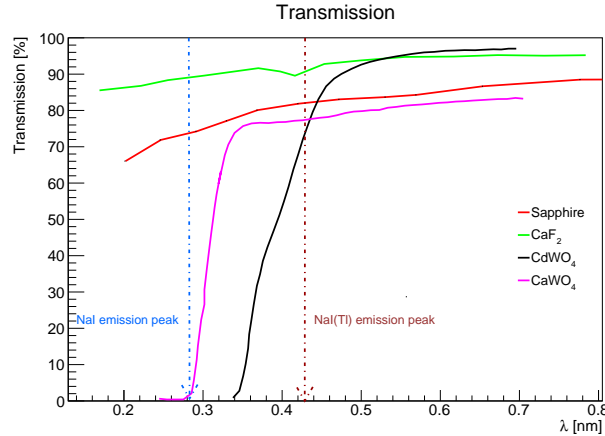


Figure 6.3.3: Crystal light transmission as a function of the wavelength for CdWO_4 (black) [260], sapphire (red), Ca_2F (green) [261] and CaWO_4 (magenta) [262]. For pure NaI and NaI(Tl) in addition the peaks of the scintillation light emission are shown, see [263].

6.3.2 Extended Pulse-Shape Model (EPSM)

The implications of the three hypotheses just discussed have been mathematically formalised by extending the original model in Eq. 6.1 by introducing a third differential equation which takes the carrier into account. The scheme of the cryogenic detectors including a carrier is depicted in Fig. 6.3.4.

The new differential system is,

$$\begin{cases} C_e \frac{dT_e}{dt} + G_{ea}(T_e - T_c) + G_{eb}(T_e - T_b) & = \tilde{P}_e(t) \\ C_c \frac{dT_c}{dt} + G_{ec}(T_c - T_e) + G_{ac}(T_c - T_a) + (T_c - T_b)G_{cb} & = \tilde{P}_c(t) \\ C_a \frac{dT_a}{dt} + G_{ac}(T_a - T_c) + G_{ab}(T_a - T_b) & = \tilde{P}_a(t) \end{cases} \quad (6.15)$$

where the power input is,

$$\begin{cases} \tilde{P}_e(t) & = P_0 e^{-t/\tau'_n} + P_\ell e^{-t/\tau_\ell} \\ \tilde{P}_c(t) & = \frac{1-\epsilon}{\epsilon} P_0 e^{-t/\tau'_n} + \frac{1-\xi}{\xi} P_\ell e^{-t/\tau_\ell} \\ \tilde{P}_a(t) & = \frac{(1-\eta)}{\epsilon\eta} P_0 e^{-t/\tau'_n} \end{cases} \quad (6.16)$$

where $P_0 = \epsilon\eta \frac{\Delta E}{\tau'_n}$, ϵ is the fraction of power input from the carrier to the TES, η is the fraction of power input from the absorber to the carrier, τ'_n is defined in Eq. 6.14, P_ℓ is the power input of non-thermal phonons produced in the carrier by the NaI-scintillation light absorption and transmitted to the TES, and τ_ℓ ,

$$\tau_\ell = \left(\frac{1}{\tau_{film}} + \frac{1}{\tau_c} \right)^{-1} \quad (6.17)$$

is the relaxation time constant of non-thermal phonons produced in the carrier by the NaI-scintillation light absorption. Note that, if the NaI was not present, the system

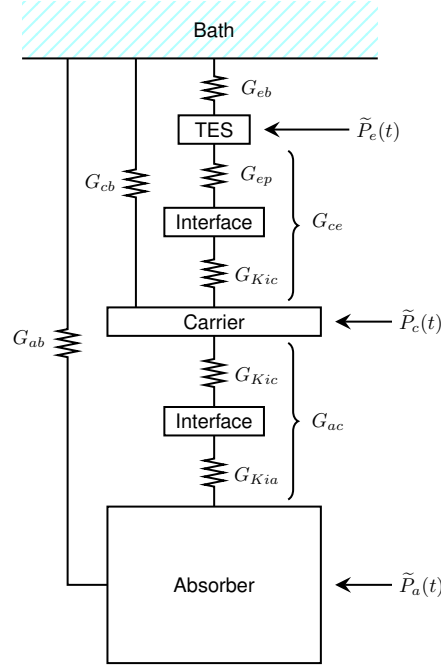


Figure 6.3.4: Scheme of the thermal couplings of a cryogenic particle detector constituted by absorber, carrier and TES. The G_{ij} are the thermal conductances between the systems i and j , G_{Kij} are the Kapitza conductances between the systems i and j , *i.e.* thermal boundary conductances, and G_{ep} is the electron-phonon thermal-coupling. $\tilde{P}_a(t)$, $\tilde{P}_c(t)$ and $\tilde{P}_e(t)$ are the power inputs in the absorber, the carrier and the thermometer, respectively.

constituted by the carrier and the film would be described by the two component original model (the system in Eq.6.1 and its solution in Eq. 6.11).

The exact solution of the system in 6.15 can be parametrised to simplify the calculation. If λ_1, λ_2 and λ_3 are the three eigenvalues of the 3×3 matrix, A , the three eigenvectors \mathbf{v}_i can be found solving the system of three equations in three variables as function of λ_i ,

$$\mathbf{v}_i = (1, \alpha(\lambda_i), \beta(\lambda_i)) \equiv (1, \alpha_i, \beta_i) \quad (6.18)$$

where,

$$\begin{cases} \alpha_i &= \frac{C_e}{G_{ec}} (-) \left(-\frac{G_{ec}}{C_e} - \frac{G_{eb}}{C_e} - \lambda_i \right) \\ \beta_i &= \frac{1}{\left(-\frac{G_{ac}}{C_a} - \frac{G_{ab}}{C_a} - \lambda_i \right)} \frac{G_{ac}}{C_a} \frac{C_e}{G_{ec}} \left(-\frac{G_{ec}}{C_e} - \frac{G_{eb}}{C_e} - \lambda_i \right) \end{cases} \quad (6.19)$$

The exponential matrix $e^{\mathbf{A}t}$ can be parametrised as,

$$\begin{aligned}
 e^{\mathbf{A}t} &= \begin{pmatrix} 1 & 1 & 1 \\ \alpha_1 & \alpha_2 & \alpha_3 \\ \beta_1 & \beta_2 & \beta_3 \end{pmatrix} \cdot e^{\mathbf{J}t} \cdot \begin{pmatrix} 1 & 1 & 1 \\ \alpha_1 & \alpha_2 & \alpha_3 \\ \beta_1 & \beta_2 & \beta_3 \end{pmatrix}^{-1} = \\
 &= \begin{pmatrix} 1 & 1 & 1 \\ \alpha_1 & \alpha_2 & \alpha_3 \\ \beta_1 & \beta_2 & \beta_3 \end{pmatrix} \cdot e^{\mathbf{J}t} \cdot \begin{pmatrix} m_1 & \ell_1 & k_1 \\ m_2 & \ell_2 & k_2 \\ m_3 & \ell_3 & k_3 \end{pmatrix} = \\
 &= \begin{pmatrix} \sum_i e^{\lambda_i t} m_i & \sum_i e^{\lambda_i t} \ell_i & \sum_i e^{\lambda_i t} k_i \\ \sum_i \alpha_i e^{\lambda_i t} m_i & \sum_i \alpha_i e^{\lambda_i t} \ell_i & \sum_i \alpha_i e^{\lambda_i t} k_i \\ \sum_i \beta_i e^{\lambda_i t} m_i & \sum_i \beta_i e^{\lambda_i t} \ell_i & \sum_i \beta_i e^{\lambda_i t} k_i \end{pmatrix}
 \end{aligned} \tag{6.20}$$

with $\mathbf{J} = \text{diag}(\lambda_1, \lambda_2, \lambda_3)$ and $e^{\mathbf{J}t} = \text{diag}(e^{\lambda_1 t}, e^{\lambda_2 t}, e^{\lambda_3 t})$.

With this trick the final solution for the temperature of the electrons in the thermometer can be computed,

$$\Delta T_e(t) = \sum_{i=1}^3 A_i [e^{\lambda_i t} - e^{-t/\tau'_n}] + \sum_{i=1}^3 B_i [e^{\lambda_i t} - e^{-t/\tau_\ell}] \tag{6.21}$$

with,

$$\begin{cases} A_i = \frac{P_0}{\lambda_i + \frac{1}{\tau'_n}} \left(\frac{m_i}{C_e} + \frac{\ell_i}{C_c} \frac{1-\epsilon}{\epsilon} + \frac{k_i}{C_a} \frac{1-\eta}{\eta\epsilon} \right) \\ B_i = \frac{P_\ell}{\lambda_i + \frac{1}{\tau_\ell}} \left(\frac{m_i}{C_e} + \frac{\ell_i}{C_c} \frac{1-\xi}{\xi} \right) \end{cases} \tag{6.22}$$

The explicit expressions of the amplitudes A_i and B_i show that the A_i are related to the power input, P_0 , injected by non-thermal phonons produced in the absorber and transmitted to the TES, while the B_i are related to the power input injected to the TES as a consequence of the scintillation light absorption in the carrier.

Four check-points are used through the solution of the system to compare it with the original model in [36]:

1. Initial conditions require that coefficients \mathbf{c} are equal to T_b , as in the original model;
2. The terms which do not depend on time simplify to T_b . We can calculate $\Delta T_e(t) = T_e(t) - T_b$;
3. The final solution of the differential system shows terms which multiply $e^{\lambda_i t}$ but not e^{-t/τ'_n} or e^{-t/τ_ℓ} . These terms would not describe a pulse component in the form of differences of exponentials and, in fact, these terms simplify to zero as in the original model;
4. The original model is recovered with $\eta = 1$, $\tau_a \rightarrow \infty$ and $P_\ell = 0$.

Physical interpretation

Equation 6.21 can be rewritten to simplify physical interpretation. In the following, each combination of difference of exponentials times the amplitude is defined ‘component’,

$$\Delta T_e(t) = \sum_{i=1}^3 \underbrace{A_i [e^{\lambda_i t} - e^{-t/\tau'_n}]}_{\text{A-components}} + \sum_{i=1}^3 \underbrace{B_i [e^{\lambda_i t} - e^{-t/\tau_\ell}]}_{\text{B-components}} \quad (6.23)$$

Two non-thermal components (one for the A-part and one for the B-part), and four thermal components, (two for the A-part and two for the B-part) can be identified. τ'_n , as well as τ_ℓ , can be considered as decay time constants of the non-thermal components and rise time constants of the thermal components. One of the three $-\tau_i = (\lambda_i)^{-1}$ can work as the intrinsic response time of the TES (rise time constant of the non-thermal component) and the other two τ_i as the decay time constants of the two thermal components. If τ_1 is assumed as the intrinsic response time of the TES, on analogy with the original model, Eq. 6.21 can be written as,

$$\begin{aligned} \Delta T_e(t) = & A'_1 [e^{-t/\tau'_n} - e^{\lambda_1 t}] + A_2 [e^{\lambda_2 t} - e^{-t/\tau'_n}] + A_3 [e^{\lambda_3 t} - e^{-t/\tau'_n}] + \\ & + B'_1 [e^{-t/\tau_\ell} - e^{\lambda_1 t}] + B_2 [e^{\lambda_2 t} - e^{-t/\tau_\ell}] + B_3 [e^{\lambda_3 t} - e^{-t/\tau_\ell}] \end{aligned} \quad (6.24)$$

with,

$$\begin{cases} A'_1 &= -A_1 \\ B'_1 &= -B_1 \end{cases} \quad (6.25)$$

where A_i and B_i are in Eqs. 6.22, or also,

$$\begin{aligned} \Delta T_e(t) = & A'_1 [e^{-t/\tau'_n} - e^{-t/\tau_{in}}] + A_2 [e^{-t/\tau_{t1}} - e^{-t/\tau'_n}] + A_3 [e^{-t/\tau_{t2}} - e^{-t/\tau'_n}] + \\ & + B'_1 [e^{-t/\tau_\ell} - e^{-t/\tau_{in}}] + B_2 [e^{-t/\tau_{t1}} - e^{-t/\tau_\ell}] + B_3 [e^{-t/\tau_{t2}} - e^{-t/\tau_\ell}] \end{aligned} \quad (6.26)$$

where $\tau_{in} = \tau_1$, $\tau_{t1} = \tau_2$ and $\tau_{t2} = \tau_3$.

Why the EPSM could explain COSINUS experimental findings

So far, no approximations or restrictive assumptions have been done. The EPSM presented in the previous section describes the whole COSINUS system including additional phenomenology related to the presence of the carrier.

The solution in Eq. 6.24 contains additional thermal components which could play the role of the empirical 2nd thermal component which was introduced in [37], hence it can explain the first COSINUS finding related to the NaI pulse shape. Such second thermal component is predicted by the new model also if 100% transmittance of the scintillation light from the carrier is assumed (that is $P_\ell = 0$ and $B_i = 0$). Second COSINUS finding is related to the absence of a nuclear recoil band in the LY plot, when neutron calibration data collected by TES sensors are displayed. As explained in Sec. 5.1, the LY ratio used to make particle discrimination is equal to,

$$LY = \frac{E_\ell}{E_p} \quad (6.27)$$

where E_ℓ is the energy detected by the light detector (silicon beaker plus TES for COSINUS) and E_p is the energy detected by the phonon detector (main absorber and TES). According to the discussion on the NaI-scintillation light absorption in the carriers, in addition to E_p , the TES of the phonon-channel is expected to measure also the energy converted in scintillation light of the NaI absorber and re-absorber in the carrier in form of light, which is E_ℓ in first approximation (without considering *e.g.* geometrical effects or the difference in the material between the silicon beaker and the carriers). In this case, the LY in Eq. 6.27 is,

$$LY = \frac{E_\ell}{E_p + E_\ell} \quad (6.28)$$

It is known that the energy converted into heat is quasi independent from the type of interacting particles, while the energy converted in light follows the Birks' law [211]. Furthermore, the measurement of the energy in CRESST, and in COSINUS so far as well, is based on the pulse height (PH) and not on the area of the pulse. In this way, part of the information is lost, as the PH is not a proper "measure" for the energy of an event. The development of reconstruction methods for NaI phonon pulses are urgently necessary as this is the basis for COSINUS raw data analysis. This method is, in fact, reliable if the pulse is fast and large in height, less accurate if the pulse is slow and short in height¹⁰. For the latter case the LY for e^-/γ events, LY_e , and neutron events, LY_n would be,

$$LY_e = \frac{E_{\ell e}}{E_p + E_{\ell e}} \approx \frac{E_{\ell e}}{E_{\ell e}} = 1 \quad (6.29)$$

$$LY_n = \frac{E_{\ell n}}{E_p + E_{\ell n}} \approx \frac{E_{\ell n}}{E_{\ell n}} = 1 \quad (6.30)$$

According to this hypothesis, the neutron induced events distributed in the LY plot are populating the e^-/γ - band.

The EPSM includes this effect and can be used to setup a different type of analysis of the events. The basic idea is to integrate in time the temperature of the electron in the TES, that is Eq. 6.26, separately for the A_i and B_i terms. If the two integrals are labelled as \mathcal{I}_p and \mathcal{I}_ℓ , respectively, the particle discrimination with the present COSINUS detector design could be still done using the Birks' law, as follows,

$$LY = \frac{\mathcal{I}_\ell}{\mathcal{I}_p} \quad (6.31)$$

In the assumption that the method works as expected, the integral \mathcal{I}_p is now the right measurement of the energy deposited in the absorber and converted into heat, while \mathcal{I}_ℓ is the measurement of the amount of deposited energy converted in light and absorbed by the carrier. Nuclear recoils are expected to produce less scintillation light than e^-/γ

¹⁰The original model proposed in [36] was done for calorimeters where the non-thermal part is the dominant signal, thus PH is a very good measure.

events, therefore events shown in the LY-versus- \mathcal{I}_p plot, are expected to distribute along ideally horizontal¹¹ bands similarly to the typical CRESST LY-plot (see Fig. 5.1.2, left panel), as a function of the light quenching factors.

6.3.3 Validation of the EPSM with experimental data

The EPSM and the energy reconstruction method just discussed have been applied to experimental data for validation (work done by the COSINUS data analyst, M. Stahlberg). For comparison with the results of [37] shown in Fig. 6.3.2, the EPSM is applied to the data collected with the first COSINUS prototype, NaIce1. The fit to the standard event of the original model in Eq. 6.11 and of the EPSM given in Eq. 6.26 are shown in Fig. 6.3.5, top and bottom panel, respectively. The comparison between residuals proves that the EPSM provides a better fit to data both on the peak and on the tail of the standard event.

The data chosen for this test are collected with the NaIce6 detector module, whose design scheme is shown in Fig. 6.3.6. It is the same scheme as in Fig. 6.2.1 (right panel), with in addition a NTD thermistor placed on the Al_2O_3 carrier crystal and working as second phonon detectors. The NaI-crystal is a small cube of 20 mm side length and 30 g of weight. The detector response is calibrated using a γ -source of ^{57}Co and the standard event of the TES, shown in Fig. 6.3.6 (black solid line), is constructed by averaging the pulses of the events populating its 122 keV-peak.

In Fig. 6.3.7 the result of the fit of the EPSM in Eq. 6.26 to data is depicted as a red solid curve. The other two curves, *i.e.* the A-Part (blue-dashed-line) and B-Part (green-dashed-line) correspond respectively to,

$$\text{A-Part} = A'_1 [e^{-t/\tau'_n} - e^{-t/\tau_{in}}] + A_2 [e^{-t/\tau_{t1}} - e^{-t/\tau'_n}] + A_3 [e^{-t/\tau_{t2}} - e^{-t/\tau'_n}] \quad (6.32)$$

$$\text{B-Part} = B'_1 [e^{-t/\tau_\ell} - e^{-t/\tau_{in}}] + B_2 [e^{-t/\tau_{t1}} - e^{-t/\tau_\ell}] + B_3 [e^{-t/\tau_{t2}} - e^{-t/\tau_\ell}] \quad (6.33)$$

where all the parameters have been introduced above. The A-Part is proportional to the power input related to the phonons transmitted from the NaI-absorber to the TES (see Eq. 6.16), therefore it is expected to be shorter in height and with a longer decay time with respect to the B-Part. This latter is proportional to the power input related to the phonons produced in the Al_2O_3 -carrier by the NaI-scintillation light absorption. It is known that sapphire crystals are performant cryogenic detectors, with very good non-thermal phonon transmission to the TES, corresponding to large pulse height amplitudes and fast decay time. The shape of the A- and B-parts are, therefore, in agreement with expectations. The bottom of Fig. 6.3.7 shows the residuals of the difference between the fit function and the data. Since this measurement is characterised by very small pulses, it is not optimal to test the goodness of the fit, however it is very suitable to test the energy reconstruction method discussed in the previous section.

The top panel of Fig. 6.3.8 shows NaIce6 events detected by the TES, distributed according to the new version of the LY versus energy plot proposed in Eq. 6.31. On the

¹¹Since in CaWO_4 non-proportionality effects are present [212], the same could be true for NaI.

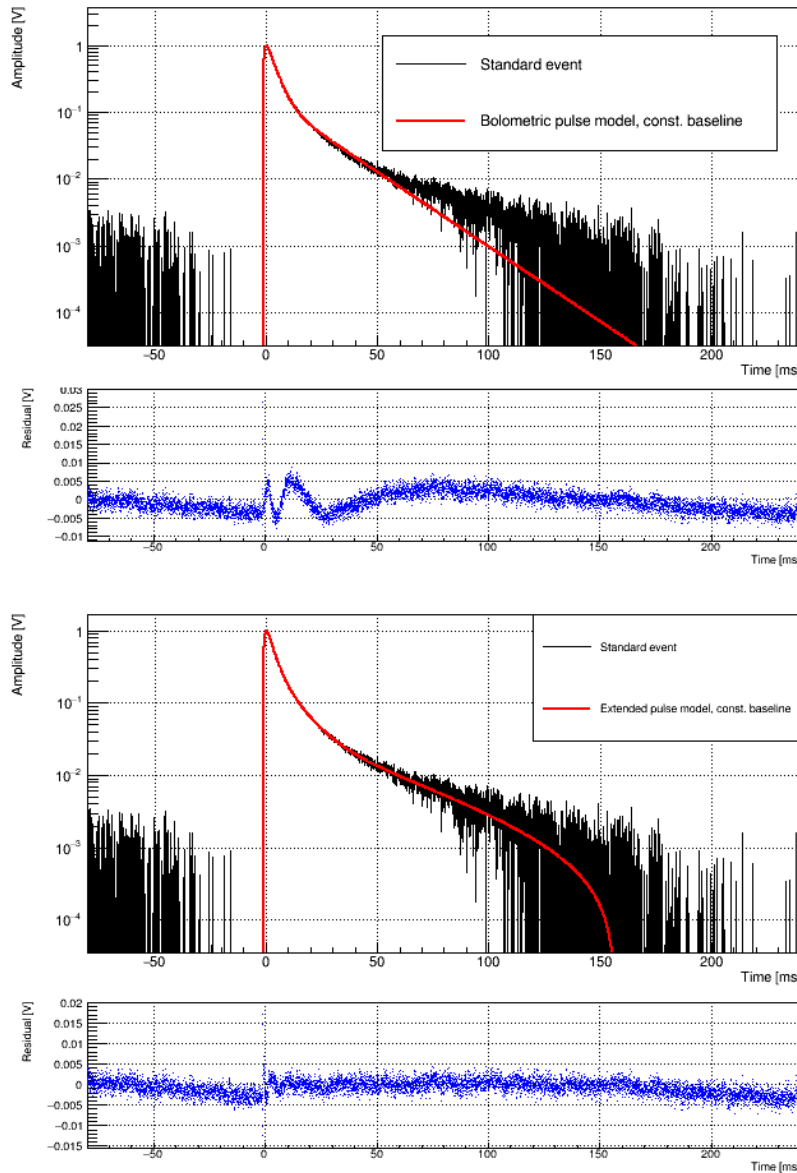


Figure 6.3.5: NaIcel standard event obtained averaging the pulses of the events in the peak at 122 keV produced by a ^{57}Co γ -source. **Top:** the model fitted to data is the original pulse model in Eq. 6.11. **Bottom:** The model fitted to data is the EPSM, given in Eq. 6.26. The blue dots on the bottom of both panels show the residuals of the difference between the fit function and the data.

y-axis it is reported the amplitude ratio B_1/A_1 instead of $\mathcal{I}_\ell/\mathcal{I}_p$, because the final fit of the data set is performed factorising B_1 and A_1 in Eq. 6.26 and fixing the four ratios $A_2/A_1, A_3/A_1, B_2/B_1, B_3/B_1$ and all the time constants, $\tau'_n, \tau_\ell, \tau_{in}, \tau_{t1}, \tau_{t2}$. In this case,

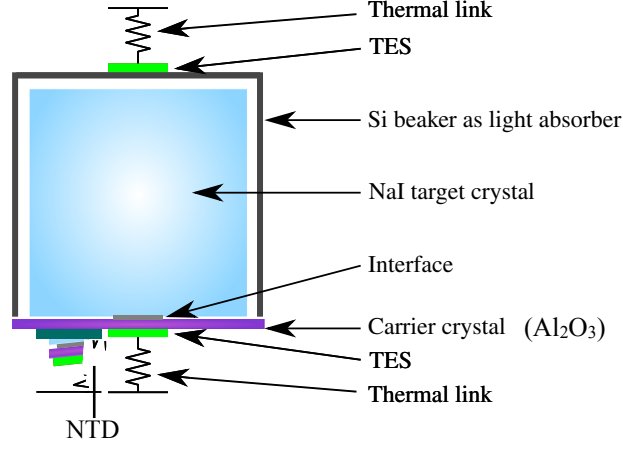


Figure 6.3.6: NaIce6 detector design scheme. The setup is the same as shown in Fig. 6.2.1, right panel, with in addition a NTD on the carrier crystal. NaIce6 carrier crystal is made of sapphire.

the two integrals \mathcal{I}_ℓ and \mathcal{I}_p are simply,

$$\mathcal{I}_\ell = B'_1 \int dt f_B(t) = B'_1 \mathcal{I}_B \quad (6.34)$$

$$\mathcal{I}_p = A'_1 \int dt f_A(t) = A'_1 \mathcal{I}_A \quad (6.35)$$

where \mathcal{I}_B and \mathcal{I}_A are the same for all the events. From this it follows that,

$$LY = \frac{\mathcal{I}_\ell}{\mathcal{I}_p} = \frac{B'_1 \mathcal{I}_B}{A'_1 \mathcal{I}_A} \equiv \frac{B_1}{A_1} C \quad (6.36)$$

where C is just a scaling factor. The black dots in Fig. 6.3.8 correspond to e^-/γ events, while the red dots are identified as neutron induced events as detected in coincidence with the NTD, which allows to discriminate between different types of particle events. The neutron events are found at small or zero B_1 , which is in agreement with the prediction of the EPSM: B_1 is an indicator of the amount of deposited energy converted in scintillation light and absorbed by the carrier, which is expected to be small for neutron events, while it is found to be quite large for e^-/γ events. This finding is further validated using the information coming from the actual light detector, which is translated into a further version of the LY versus energy plot shown in Fig. 6.3.8, bottom panel. On the y-axis it is reported the ratio between the energy converted in light and measured by the light detector (silicon beaker plus TES) and the A_1 component. The rectangular section includes the events which are tagged as neutron events using the NTD data: a clear neutron band is identified below the e^-/γ -band, in agreement with the neutron distribution highlighted with red dots in the top panel.

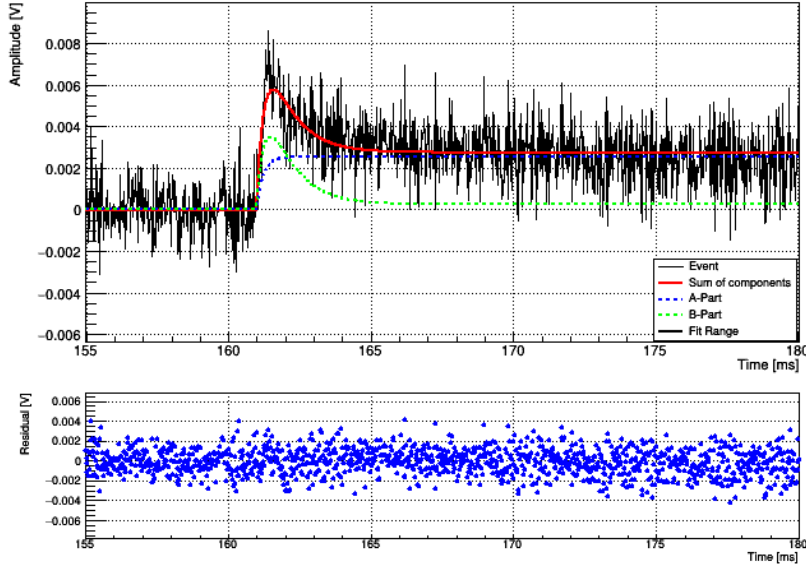


Figure 6.3.7: The standard event of the COSINUS NaIc6 detector, obtained by averaging the pulses of the events in the peak at 122 keV produced by a ^{57}Co γ -source.

The results obtained by the application of the EPSM reads the following conclusion: 1) the implementation of the EPSM in COSINUS data analysis is feasible and 2) the method proposed for the energy reconstruction based on the EPSM and aiming at the neutron identification provide results in agreement with expectations. As a conclusion of this analysis, it is possible to affirm that the EPSM proposal passed the first tests.

The EPSM is a new energy estimator to account for the peculiar shape of NaI particle events and to allow for a difference in pulse shape between e^-/γ -events and nuclear recoils as shown by the ratio of the A and B parts. At first glance, the re-absorbed light in the carrier crystal might seem to be problematic for the overall detector response reconstruction. However, as preliminary shown by the application of the EPSM to experimental data, particle discrimination on event-by-event basis may be achieved with the phonon detector only. This opens the possibility for simplified detector designs relying on one signal detector channel only. This might be of advantage in the light of COSINUS- 2π , an envisioned phase of COSINUS with increased detector mass to allow for a modulation search.

6.4 Outlook of studies on phonon propagation in NaI

A better understanding of the physics at the microscopic level of COSINUS detectors, not only would provide a theoretical background to the phenomenology of COSINUS discussed in previous section, but also would offer the opportunity for a precise charac-

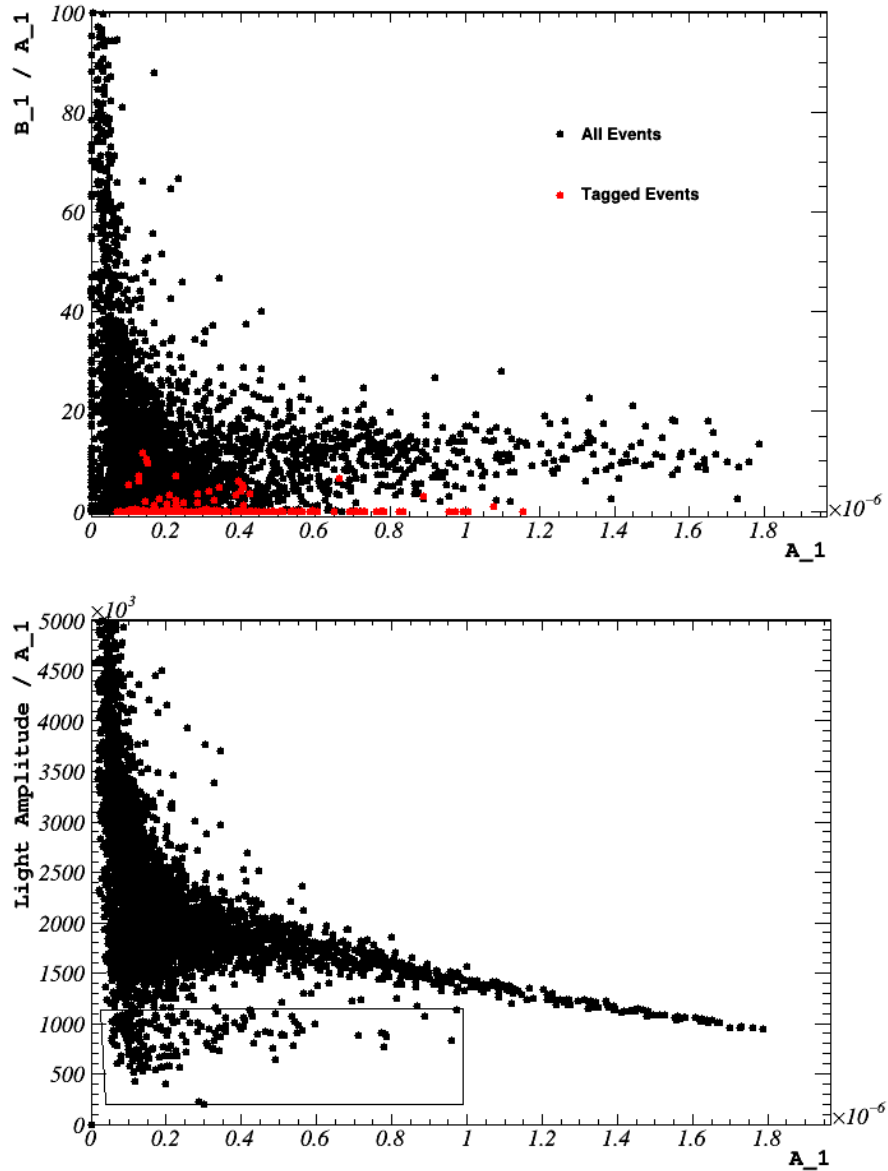


Figure 6.3.8: **Top:** Validation of the proposal for a new 2D-plane/plot to demonstrate particle discrimination, based on the EPSM. Since the four ratios A_2/A_1 , A_3/A_1 , B_2/B_1 and B_3/B_1 and all the time constants are fixed when the EPSM is fitted to data, the LY in Eq. 6.31 is equivalent to the A_1 over B_1 ratio times a constant which is equal for all the events (see text for more details). The black dots correspond to e^-/γ -events, while the red dots are the events tagged as neutron events as identified by the NTD. **Bottom:** LY versus energy plot, based on the ratio between the amount of energy converted in light and detected by the light detector and the amplitude A_1 . The rectangular selection includes the neutron events identified because in coincidence with the neutron events detected by the NTD.

terisation and optimisation of the COSINUS detector design. The hypothesis implied in the elaboration of the EPSM consists in peculiar properties of the phonon propagation in NaI which differentiate this material from the ones typically employed by CRESST. In this section, studies based on solid state physics, developed thanks to the collaboration with the solid state group of L'Aquila University, are presented. Basic solid state properties of NaI are provided, derived within the Debye model and the elastic theory of lattice dynamics [264] and some attempts to simulate transient vibrational excitations, known as discrete breathers or intrinsic localised modes (ILM) [38], which can play a role in COSINUS phenomenology, are discussed. Finally, first experimental and theoretical results obtained by the solid state group of L'Aquila University on the structural properties on NaI(Tl) are presented.

6.4.1 Thermal properties of crystals: Debye model

The theory of heat in solids has been built by analogy with the black body theory of radiation, which opened the road to quantum mechanics. Any crystal at non-zero temperature microscopically can be imagined as a box of vibrating ions, packed in an ordered lattice. The model describing this type of system as an ensemble of bosonic particles, named phonons, was elaborated by P. J. W. Debye in 1912, *The theory of specific heat*[265]. By analogy with the Planck theory of electromagnetic radiation, the random interactions establish a thermal distribution inside the box, whose most probable number of particles in a particular energy state is [266],

$$n_\omega = \frac{1}{e^{\hbar\omega/k_B T} - 1} \quad (6.37)$$

where ω is the phonon frequency, k_B the Boltzmann constant and T the temperature. The quantum statistics for bosons takes into account that any state can be occupied by an arbitrary number of particles, $n = 1, \dots$ (for fermions, $n = 0, 1$). From this distribution the internal energy U and the heat capacity C_V of the crystal can be computed, as follows. The number density of vibration-modes at a particular energy (degeneracy), $D(\omega)d\omega$, is computed by Debye using classical boundary conditions for the propagation of waves in a confined box of volume V , and it is [264],

$$D(\omega) d\omega = \frac{dN_\omega}{d\omega} = \frac{\omega^2 V}{2\pi^2 v_p^3} d\omega \quad (6.38)$$

where v_p is the phase velocity.

Combining Eqs. 6.37 and 6.38, the frequency distribution of the number of thermal phonons in a crystal lattice is,

$$n_\omega D(\omega) d\omega = \left(\frac{V \omega^2}{2\pi^2 v_p^3} \right) \frac{1}{e^{\hbar\omega/k_B T} - 1} d\omega \quad (6.39)$$

The internal energy U is equal to,

$$U = \int_0^{\omega_D} \hbar\omega n_\omega D(\omega) d\omega \underset{\lim_{\omega_D \rightarrow \infty}}{=} \frac{3\pi^4}{5} N k_B T \left(\frac{T}{\theta_D} \right)^3 \quad (6.40)$$

For $T \rightarrow 0$, the long wavelength limit improves, therefore ω_D , which is the cutoff of the Debye approximation, can be taken as infinite. θ_D is a measure of the temperature above which all the modes are excited. In the low temperature limit, the heat capacity is,

$$C_V = \frac{dU}{dT} = \frac{12\pi^4}{5} N k_B \left(\frac{T}{\theta_D} \right)^3 \quad (6.41)$$

At fixed temperature, the lower the Debye temperature, the larger the heat capacity. In Tab. 6.4.1 the Debye temperature of some materials containing sodium are shown [264].

	NaF	NaCl	NaI
Θ_D (K)	492	321	164
ν_D (THz)	64.4	42	21.5

Table 6.2: Debye temperature and frequency for NaF, NaCl and NaI [264]

6.4.2 Elastic theory of lattice dynamics

On top of the thermal phonon distribution, any particle interaction on the surface of the crystal produces shells of non spherical wave fronts starting from the interaction point and developing along the crystal. The excited vibrational modes are populated by non-equilibrium phonons. In the assumption of an ideal isotropic crystal, without defects or surface effects, the non-thermal phonons can propagate freely in all the directions, with non-dispersive motion. One can think about this motion as a system of strings in 3-dimensions. The macroscopic elastic theory of crystals is just a generalisation of the classic coupled oscillator to a multi-body system.

Harmonic approximation. For small displacements of the atoms from their equilibrium position, the interatomic potential can be approximated as harmonic. The expansion of the potential energy around the equilibrium position, \mathbf{r}_{lk} , is [267],

$$U = U_0 + \sum_{lk\alpha} \Phi_{lk\alpha} u_{lk\alpha} + \frac{1}{2} \sum_{lk\alpha} \sum_{l'k'\beta} \Phi_{lk\alpha, l'k'\beta} u_{lk\alpha} u_{l'k'\beta} + \dots \quad (6.42)$$

where U_0 is a constant, which can be neglected, l is the unit-cell-label, k is the atom-label, $u_{lk\alpha(\beta)}$ is the $\alpha(\beta)$ -component of the displacement from the equilibrium position, Φ_{lk} is the potential and $\Phi_{lk\alpha}$ and $\Phi_{lk\alpha, l'k'\beta}$ are the first and second derivatives of the potential along the α and β directions, evaluated at the equilibrium position \mathbf{r}_{lk} . Since \mathbf{r}_{lk} is a minimum of the potential, $\Phi_{lk\alpha} = 0$.

The solution of the equation of motion, \mathbf{u}_{lk} , is wavelike and can be expressed as,

$$\mathbf{u}_{lk} = \frac{1}{\sqrt{m_k}} \Lambda(\mathbf{k}) e_{k\alpha}(\mathbf{k}) \exp\{i[\mathbf{k}\mathbf{r}_l - \omega(\mathbf{k})t]\} \quad (6.43)$$

where m_k is the mass of k th-atom, $\Lambda(\mathbf{k})$ is the amplitude of the wave, $e_{k\alpha}$ is the α -component of the polarisation vector, \mathbf{k} is the wavevector and \mathbf{r}_l is the position of the l th cell. If $\Delta\mathbf{r}_k$ is the distance of the k -atom from the origin of its unit cell and \mathbf{r}_{lk} its distance from the origin of the lattice, the instantaneous position of the k th-atom is,

$$\mathbf{R}_{lk} = \mathbf{r}_{lk} + \mathbf{u}_{lk} \quad (6.44)$$

Taking into account the acoustic sum rule¹² (see [267]), the equation of motion reads,

$$m_k \ddot{u}_{lk\alpha} = - \sum_{l'k'\beta} \Phi_{lk\alpha, l'k'\beta} u_{l'k'\beta} \quad (6.45)$$

The dispersion relation $\omega(\mathbf{k})$ can be obtained by substituting Eq. 6.43 into Eq. 6.45,

$$\omega^2(\mathbf{k}) e_{k\alpha} = \sum_{k',\beta} D_{k\alpha, k'\beta}(\mathbf{k}) e_{k'\beta} \quad (6.46)$$

as the eigenvalues of the dynamical matrix, \mathbf{D} ,

$$D_{k\alpha, k'\beta}(\mathbf{k}) = \frac{1}{\sqrt{m_k m_{k'}}} \sum_{l'} \Phi_{lk\alpha, l'k'\beta} \exp[i\mathbf{k} \cdot (\mathbf{r}'_l - \mathbf{r}_l)] \quad (6.47)$$

The NaI dispersion relations as a function of the direction in the wave-vector space and computed using density functional theory calculations [268], are shown in Fig. 6.4.1, left panel, taken from <https://materialsproject.org>. The gap between the optical band and the acoustical band ($80 \lesssim \nu \lesssim 110 \text{ cm}^{-1}$, or $2.4 \lesssim \nu \lesssim 3.1 \text{ THz}^{-1}$) expected for diatomic materials is evident both in the dispersion relations and in the phonon density of states.

6.4.3 Molecular Dynamics Simulations

The simulation of realistic lattice dynamics can be performed using LAMMPS (Large-scale Atomic/Molecular Massively Parallel Simulator)¹³. It is distributed as an open source code and it is used to model materials according to classical molecular dynamics. Using LAMMPS, the trajectories of all the atoms in the simulated cell, that is positions and velocities at each time step, can be written in data files and analysed afterwards with external codes (common fortran or C++ codes, as the files can be simply setup as columns of numbers). The properties of NaI which are required as input to perform the simulation are given in the following.

¹²The acoustic sum rule is a method to define the second derivatives of the potential, $\Phi_{lk\alpha, l'k'\beta}$, including the case of self interactions, $\Phi_{lk\alpha, lk\beta}$. Refer to [267] for the details.

¹³<https://lammps.sandia.gov>

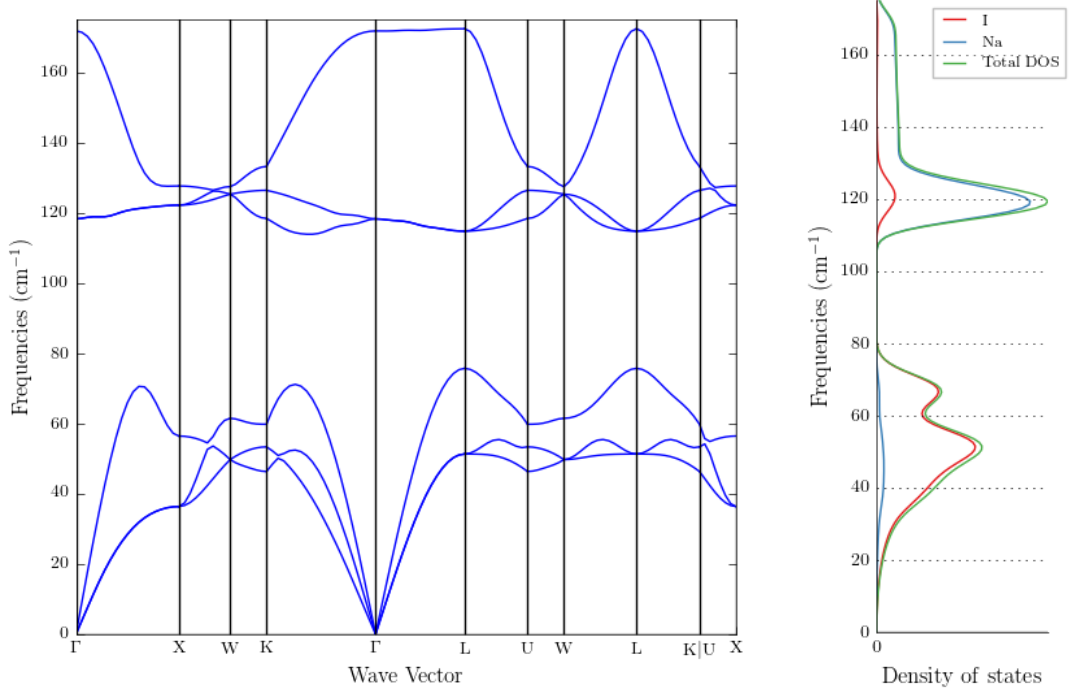


Figure 6.4.1: NaI vibrational properties, computed using density functional theory calculations [268], taken from <https://materialsproject.org>. **Left:** NaI Dispersion relations. **Right:** NaI phonon density of states. ($1 \text{ cm}^{-1} \simeq 0.03 \text{ THz}$)

Crystal Lattice Structure. The NaI crystal structure belongs to the category of the rock-salt (NaCl) crystal-structure [264]. The basis is a Na-ion on the 0 position and I-ion on one half of the main diagonal $a/2(\hat{x} + \hat{y} + \hat{z})$, where $a = 6.47 \text{ \AA}$ [264]. The unit cell resulting by overlapping the basis to the lattice is constituted by two interpenetrating face centred cubic cells. Figure 6.4.2 is the illustration of the NaI ion initial positions obtained with LAMMPS when the NaI structure properties are fixed. The drawing is done with the software Ovito <https://www.ovito.org> used to visualise the trajectories of the atoms in the cell.

NaI realistic interaction potential. The interatomic potential in NaI is fixed to the one used in [269], reported here for completeness,

$$U(\{\mathbf{r}, \mathbf{R}\}) = \sum_{i>j} V_{++}(\mathbf{R}_i - \mathbf{R}_j) + \sum_{i>j} V_{--}(\mathbf{r}_i - \mathbf{r}_j) + \sum_{i,j} V_{+-}(\mathbf{R}_i - \mathbf{r}_j) \quad (6.48)$$

where \mathbf{r} and \mathbf{R} are the positions of I^- and Na^+ ions, respectively, and,

$$V_{\pm\pm}(r) = \frac{Q_{\pm}Q_{\pm}}{4\pi\epsilon_0 r} + W_{\pm\pm}^{LR}(r) + P_{\pm\pm}^{SR}(r) \quad (6.49)$$

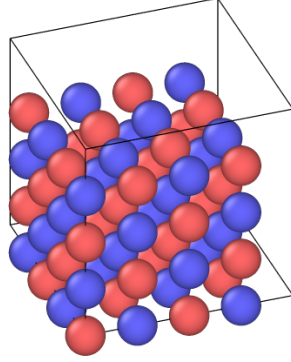


Figure 6.4.2: NaCl structure (same for NaI). Created with the software Ovito <https://www.ovito.org>.

The other terms of Eq. 6.49 are the Lennard-Jones potential,

$$W_{\pm\pm}^{LR}(r) = -\frac{C_{\pm\pm}}{r^6} - \frac{D_{\pm\pm}}{r^8} \quad (6.50)$$

and Buckingham-type potential, which describes the nearest atoms repulsion due to the interpenetration of the electron-shells.

$$P_{\pm\pm}^{SR}(r) = A_{\pm\pm} e^{-r/\rho_{\pm\pm}} \quad (6.51)$$

The parameters A_{\pm} , ρ_{\pm} , C_{\pm} and D_{\pm} are exactly the ones listed in Tab. 1 of [269].

NaI Phonon Density of States

A definition of the phonon density of states (PDOS), which is convenient from a computational point of view, relies on the autocorrelation functions of the atom velocities¹⁴. The theoretical proof of this method can be found in the Appendix of Ref. [270]. The autocorrelation function is defined as,

$$Z(t) = \frac{\sum_i \langle \mathbf{v}_i(t+t_0) \cdot \mathbf{v}_i(t_0) \rangle}{\sum_i \langle \mathbf{v}_i(t_0) \cdot \mathbf{v}_i(t_0) \rangle} \rightarrow \begin{cases} 1, & \text{for } t = 0 \\ 0, & \text{for } t \rightarrow \infty \end{cases} \quad (6.52)$$

where t represents a time delay with respect to the origin t_0 . By studying the frequency spectrum of the autocorrelation function one can infer if atoms are oscillating with the same frequency. In this way phonons can be identified. The Fourier transform

¹⁴The derivation of the PDOS from the atom velocity autocorrelation functions is taken from <http://cacs.usc.edu/education/phys516/VAC.pdf>.

reads,

$$\begin{aligned}
\tilde{Z}(\omega) &= \int_{-\infty}^{\infty} dt Z(t) e^{-i\omega t} = \\
&= \int_{-\infty}^0 dt Z(t) e^{-i\omega t} + \int_0^{\infty} dt Z(t) e^{-i\omega t} = \\
&= - \int_{\infty}^0 dt Z(-t) e^{i\omega t} + \int_0^{\infty} dt Z(t) e^{-i\omega t} \equiv \\
&= \int_0^{\infty} dt Z(t) e^{i\omega t} + \int_0^{\infty} dt Z(t) e^{-i\omega t} = \quad (Z(t) = Z(-t)) \\
&= 2 \int_0^{\infty} dt Z(t) \cos(\omega t)
\end{aligned} \tag{6.53}$$

In Eq. 6.53 the equality $(Z(t) = Z(-t))$ is used which holds since if the origin t_0 in Eq. 6.52 is shifted by $-t$ the result does not change.

This method can be used to compute the spectrum of NaI phonon density of states (NaI-PDOS). The trajectories are generated by using LAMMPS for a cell of 4096 atoms, that is the unit cell of 8 atoms replicated by $(8 \times 8 \times 8)$, and at a temperature of 10 K. The analysis is done by using code provided by G. Profeta (University of L'Aquila). The result is shown in Fig. 6.4.3.

The NaI-PDOS obtained in this work is in agreement with the one found in literature [38] and shown in Fig. 6.4.4. It is also in agreement with the NaI-PDOS in Fig. 6.4.1. This agreement is important as it validates the simulation method which is based on classical molecular dynamics and not on density functional theory. The upper limit of the acoustic-band is $\nu \simeq 10.6$ meV = 2.54 THz ($\omega \simeq 16$ THz rad), the lower limit of the optical band is $\nu \simeq 13.5$ meV = 3.24 THz ($\omega \simeq 20.4$ THz rad). The band gap between acoustical and optical phonon bands is quite large due to the mass difference between the ions Na and I [264]. In the harmonic approximation the frequencies inside the gap are forbidden, while anharmonic oscillations are known to excite vibrations at frequencies inside the gap, which, however, do not propagate through the crystal until they decay into harmonic oscillations (optical or acoustical) [38].

The gap in NaI, thus the ratio between Na and I masses, could be at the origin of the difference between phonon propagation in NaI and phonon propagation in the other crystals, such as CaWO_4 or sapphire. First attempts supporting this speculation are reported in the following.

Intrinsic localised modes in NaI

Intrinsic localised modes (ILM), or discrete breathers, are spatially localised mode which may occur at a frequency above or within the gap of the vibrational spectrum [39]. In [271] S. A. Kiselev and A. J. Sievers state that they ‘demonstrate with molecular dynamics

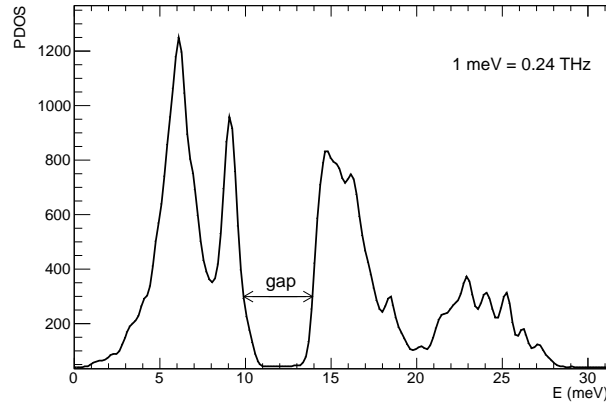


Figure 6.4.3: NaI Phonon Density of States (NaI-PDOS) obtained in this work. The energy $E = h\nu \equiv \nu$, as it is given in natural units.

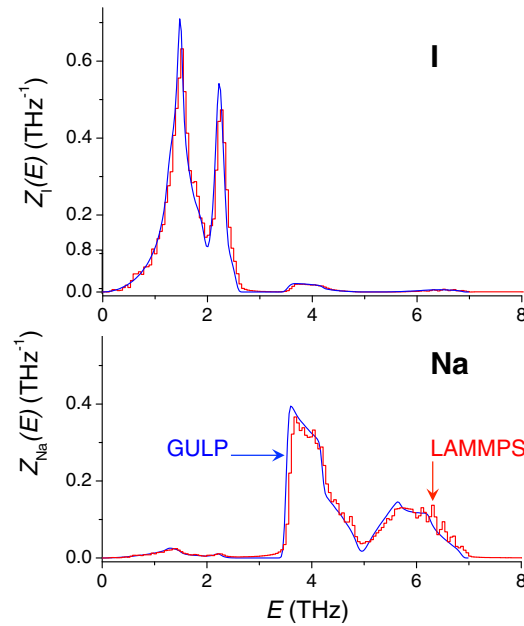


Figure 6.4.4: NaI Phonon Density of States (NaI-PDOS) projected on single ions. The acoustical modes are mainly filled by I vibrations, while optical modes are mainly due to Na vibrations [38]. The energy $E = h\nu \equiv \nu$, as it is given in natural units.

simulations that, for sufficiently large vibrational amplitude, anharmonicity can stabilise an IGM' (intrinsic localised gap mode) 'in a 3D uniform diatomic crystal with rigid ion NaI potential arranged in either the fcc or zinc-blende structure'. In the same paper, they derive a stationary localised mode eigenvector and the frequency of an IGM is

derived as a function of the amplitude of the atomic displacement amplitude α (Fig. 4 in [39]), reported here in Fig. 6.4.5.

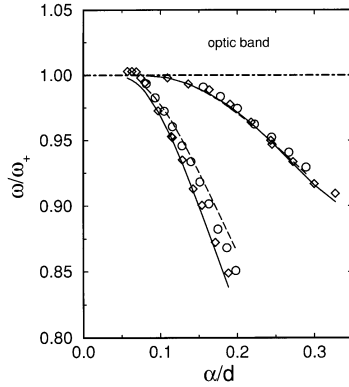


Figure 6.4.5: The frequency of an IGM as a function of the atom displacement amplitude. ω^+ is the lower limit frequency of the optical band and d is the nearest-neighbour distance (half of the lattice parameter). The left set of data are for the zinc-blende and the right set for the fcc lattice [271].

Possible connection between IGMs and COSINUS phenomenology. The NaI interatomic potential introduced in Sec. 6.4.3 is clearly anharmonic. The harmonic approximation in Sec. 6.4.2 is valid for small atomic displacements, but the typical energy involved in DM direct detection, for example the energy deposition of neutrons and beta/gammas from calibration sources inside the target crystal, are expected to even cause permanent defects in the lattice (see *e.g.* [41]). For this reason, such events are expected to cause anharmonic lattice oscillations and, according to the IGM definition given above, to produce IGMs in the NaI band gap. In [272] it is derived that the most stable gap modes in NaI have a lifetime of about $3 \cdot 10^{-9}$ s. If several IGMs excite and decay at different times and positions in the crystal during the whole non-thermal phonon propagation, the IGM localisation of energy could cause a non-thermal phonon transmission delay through the absorber-carrier interface, thus contributing to the unexpected different pulse shape of COSINUS detectors. For example, in the pure speculative assumption that $\tau'_n = \tau_{in}$ in Eq. 6.26, the A'_1 component is null and the pulse forming from the non-thermal phonon signal transmitted from the absorber to the TES would consist just of the thermal components.

Which displacements cause anharmonic oscillations? The goal is to excite vibrations in the gap, as the hypothesis is that such ‘trapped’ excitations (IGMs) can play a role in explaining COSINUS observations. For this reason, it is necessary to identify the order of magnitude of the initial displacement required to produce anharmonic oscillations. The dynamics of a cubic NaI lattice with 1000 atoms is simulated displacing the Na-atom at the vertex by 0.001 Å, 0.1 Å, 0.5 Å, 1 Å and 1.6 Å, respectively. The result is shown in Fig. 6.4.6. The transition between harmonic and anharmonic regime is obtained for an initial displacement between $\simeq 1$ and 1.6 Å.

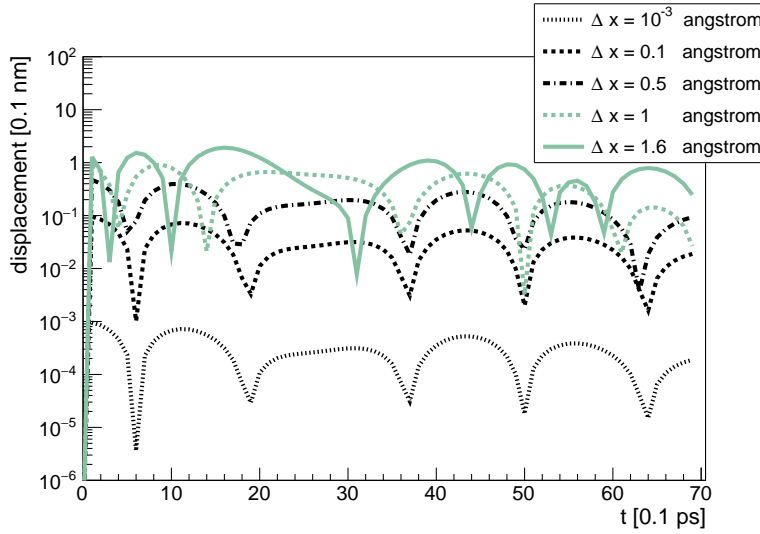


Figure 6.4.6: Displacements of the Na atom at the vertex of the lattice (1000 atoms) as function of time, for 5 different initial displacements: 0.001 Å (black-solid-line), 0.1 Å (black-dashed-line), 0.5 Å (black-dot-dashed-line), 1 Å (green-dashed-line) and 1.6 Å (green-solid-line). We use 0.01 ps for the time step, with 0.1 ps the difference was not clear. For displacements larger than 1 Å, the oscillations are anharmonic.

How to simulate IGMs? Some attempt to simulate IGMs in NaI crystals have been performed, but no positive results have been achieved yet. The approach used is to simulate a NaI cell in LAMMPS, impose an initial perturbation into the lattice (an initial atomic displacement in the anharmonic regime or a random distribution of atomic velocities) and follow the atomic dynamics evolution. The total duration of the simulations done is $\mathcal{O}(10 - 100)$ ps. The excitation of an IGM in this time window must be regarded as a prototype IGM which can be excited at any time after the initial scattering inside the crystal lattice.

Two tests were performed. The first was to impose an initial displacement to one or more ions at the origin of a cell containing 8000 atoms in total. The same test was done for CsI (by just replacing the atomic mass of Na ($\simeq 23$ GeV) with the one of Cs ($\simeq 133$ GeV)) to show the phenomenology in diatomic crystals with different mass splittings.

The distance from the origin of the atoms ¹⁵ with $\pm 10\%$ of the maximum energy versus time is shown in Fig. 6.4.7, top panels. The localisation of the energy in NaI which occurs around the initial displacement and which is visible in Fig. 6.4.7 (top, left panel), could be a hint of IGM. This speculation is supported by the results using CsI which show less localisation (top, right). On the bottom panels, the energy as a function of distance and time is shown: the energy flow propagation velocity (velocity of sound) through the lattice can be computed as the distance over the corresponding time of the

¹⁵When simulating the lattice, is important to take periodic conditions into account. Only results which refer to atoms within the half of the whole cell are reliable.

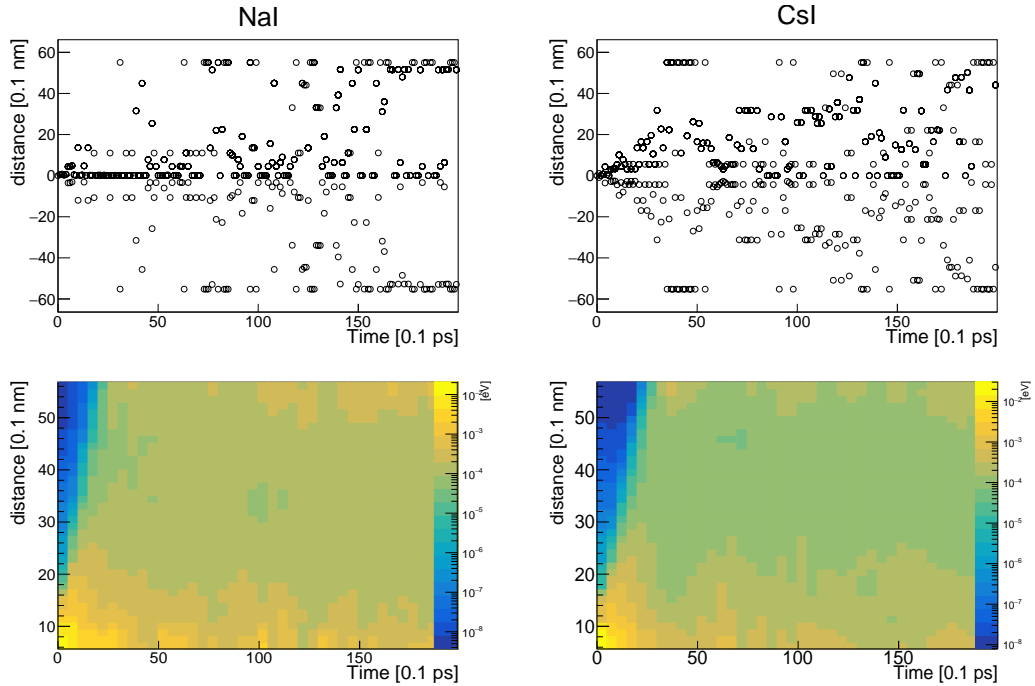


Figure 6.4.7: **Top:** Distance from the origin of the atoms with $\pm 10\%$ of the maximum energy versus time. The localisation of the energy in NaI around the initial displacement (left panel), could point to an IGM, speculation supported by the results in CsI which show less localisation (right). **Bottom:** Energy flow as a function of distance from the origin versus time. The energy flow propagation velocity (velocity of sound) through the lattice can be computed as the distance over the corresponding time of the blue region. The yellow region refers to the maximum energy distribution, more localised around the origin for NaI with respect to CsI.

blue region, the yellow region refers to the maximum energy distribution, more localised around the origin for NaI along the whole time window with respect to CsI.

The second test was to impose an initial displacement with a sinusoidal time dependence, a sort of forcing oscillation at a frequency inside the NaI band gap. The amplitude of the forcing oscillation is the same for the two cases presented in Fig. 6.4.8, while the frequency of the forced oscillation is different: for the top plot, the frequency is $\nu = 2.68$ THz, which is inside the band gap, while for the bottom plot it is $\nu = 3.24$ THz, which is in the optical band. The amplitude is gradually increased and stopped after a certain number of oscillations and the following dynamics of the system is analysed. In Fig. 6.4.8, the initial forcing oscillations is shown in black, coloured lines display all the simulated atoms. No IGMs were observed. However, there is an interesting result which fulfils expectations, that is the system does not oscillate when it is forced at a frequency inside the gap while it keeps vibrating if the frequency is in the harmonic bands (the optical in this case), what is actually called a phonon.

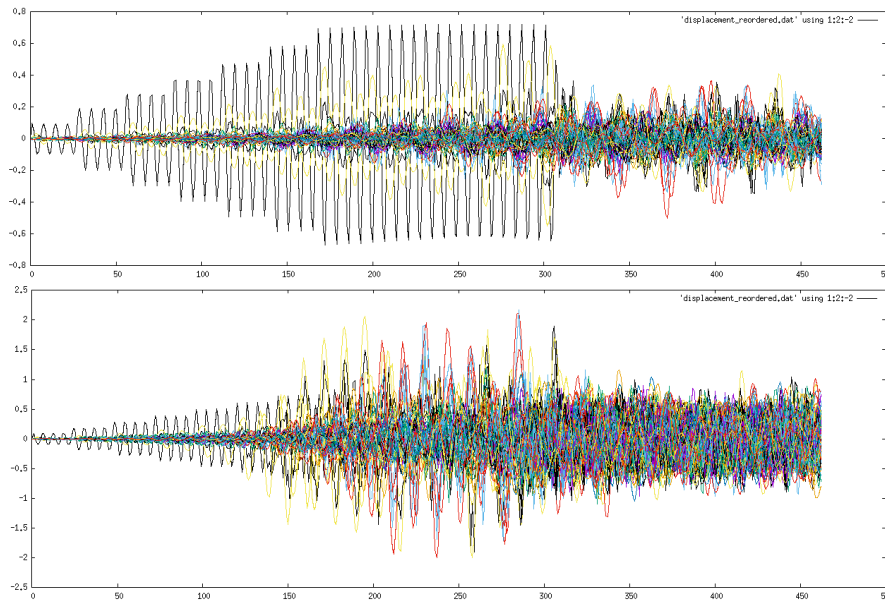


Figure 6.4.8: Oscillation amplitude of a system of atoms as a function of time. The system is perturbed by a forced sinusoidal displacement. The amplitude of the forcing oscillation is the same for the two cases presented, while the frequency of the forced oscillation is different. **Top:** $\nu = 2.68$ THz, inside the band gap. **Bottom:** $\nu = 3.24$ THz, in the optical band.

Summary. NaI is a diatomic crystal whose phonon spectrum is characterised by a large band gap between the optical and the acoustical phonon bands. In solid state literature, the existence of intrinsic gap modes (IGMs) excited by anharmonic oscillations in the crystal lattice are extensively treated and methods to observe them have been proposed. In this section, preliminary studies on the phonon propagation in NaI performed using molecular dynamical simulations have been presented. The NaI phonon density of states (NaI-PDOS) is obtained and compared with density functional theory calculations and found in agreement, therefore LAMMPS can be used as a tool to further explore the details of phonon propagation in NaI. So far, no IGMs have been observed in the simulations performed, however, the method suggested in [271] has not been completely applied yet. It consists in the analysis known as ‘wavelet analysis’, which is used to analyse non-stationary signals in time-frequency and identify transient frequency components which appears for a finite lapse of time. Such method is applied to lattice vibrations induced by high temperature, while the case of interest in this work is related to a perturbation caused by the high energy scattering event in the target crystal, therefore the simulation method requires to be adapted to the present case. Further studies are necessary: the investigation presented in this section is preliminary, as started in the last part of this PhD project, but it shows the great potential that theoretical and experimental analyses based on NaI solid state physics have to provide a better understanding on the physics of COSINUS detectors.

6.4.4 NaI(Tl) structural properties characterisation using the XAS experimental method

Within the project aiming at characterising and optimising COSINUS detectors using theoretical and experimental inputs from solid state physics, a measurement on the impact of Tl⁺ impurities on the structural properties of NaI(Tl) was performed by A. Filipponi and collaborators in October 2019. The measurement is based on the x-ray absorption spectroscopy method and it was conducted at the XAFS-XRF beam-line of the SESAME synchrotron radiation facility.

The ion of Tl⁺ enters in the NaI crystal lattice as a substitutional impurity of Na⁺. The difference in the atomic dimensions between Tl⁺ and Na⁺ is expected to induce lattice structure deformations around the impurity, which affect the characteristics of the localised electronic states and the cross-sections of the events related to them, such as the scintillation light emission. The XAS method applied to study the properties of atomic species present in low concentrations in the sample, is based on the fluorescence effect induced by a monochromatic source, tuned at energies around the edge of an atomic shell. In the case of Tl, the L_3 edge at 12.568 keV is used and the two radiative core-hole emission at 10.2658 keV and 10.1728 keV are measured. The experimental and data analysis details will be published in the forthcoming paper [12]. The conclusive result, in agreement with previous literature, consists in the measurement of a 5% expansion of the average distance of the first shell of I⁻ ions around the Tl⁺ impurities with respect to the bond length of $R_1 = a/2 = 3.237 \text{ \AA}$, where a is the 300 K cubic cell parameter reported in Sec. 6.4.3 [264]. Such result is compared with theoretical predictions based on first-principles density functional theory calculations and found in excellent agreement, as the experimental value is $R_1^{exp} = 3.416(14) \text{ \AA}$ and the theoretical prediction is $R_1^{th} = 3.40 \text{ \AA}$ (corresponding to 5.1% of shell expansion with respect to the NaI value). This work allowed to verify the experimental and data analysis technique to study the impact of the Tl⁺ impurity on the lattice structure and motivated new measurements based on the same method, which will be performed at the UK's national synchrotron, the Diamond Light Source ¹⁶.

¹⁶<https://www.diamond.ac.uk/Home/About.html>

Conclusions

This PhD thesis explores different aspects of the physics of the dark matter (DM) particle search. More specifically, it focuses on the phenomenology of the DM direct detection (DD) experimental technique. The properties of the DM annual modulation signal are studied using the *non-relativistic effective theory* (NREFT) of DM DD [14, 15] (manuscript in preparation). The time of maximal rate as a function of the minimal DM velocity, $t_{max}(v_{min})$, shows that the NREFT operators in Tab. 4.1 can be grouped into two classes: the one corresponding to a flat $t_{max}(v_{min})$ function fixed in June, and the one characterised by the so called ‘inversion of phase’. Such classification holds also for the operators which are eligible for the target dependent annual modulation effect studied in [21, 22]. Neglecting statistical aspects and detector parameters (such as efficiency, energy resolution and background), in the case one of the *building blocks* in Tab. 4.1 gives the largest contribution to the DM-nucleus elastic cross-section, low energy threshold experiments can recognise which class the operator belongs to using the timing information. The results of [21, 22] are then extended to ^{40}Ca , ^{16}O and ^{27}Al , which are targets of interest for the CRESST experiment. Finally, the amplitude of the second order harmonics of the periodic DM signal is found to be dependent on the class of interaction considered.

The cross-sections for fermionic and vector DM scattering off spin-1/2 polarised nuclei are derived, for vectorial and pseudo-vectorial mediators [2]. For fermionic DM, it is provided to refine a previous calculation in [35] and for vector DM as original contribution. The double differential rate in solid angle and energy is computed for both cases and the observed differences between the spin-1/2 and spin-1 DM scenarios can be used to discriminate the two cases from each other and extract information on the DM spin [2]. Very large exposures as available with DAMA/LIBRA [23, 25] are required to significantly separate the part of the event rate depending only on the nuclear spin from the total event rate [35]. This discrimination is also required to make a statement on the DM spin. Detector parameters, such as detector efficiency, energy resolution and background rate, are neglected in these estimations.

In collaboration with the CRESST-III experiment, the potential of Li-based targets, employed as cryogenic scintillating calorimeters working at milli-Kelvin temperature, is shown by calculating the sensitivity limit on the conventional SD-cross-section versus DM-mass plot [3]. The measurement is done using a small Li_2MoO_4 crystal (2.66 g) operated above ground for a very short time exposure (14.77 hours). Despite of the

non-optimal run conditions, a good sensitivity is reached: for example, at $m_\chi = 1$ GeV an upper limit on the cross-section equal to $1.06 \cdot 10^{-26}$ cm² is obtained. This result motivated further tests using Li-based materials, which finally succeeded in promoting such crystals as detector modules for CRESST-III. This SD limit is the first extracted from CRESST data. Along this initiative, CRESST provided a SD-limit also using the percentage of ¹⁷O contained in the best performing CRESST-III module, detector A [4].

In the light of the exponential background observed in the last CRESST-III data release [4], a statistical study is performed to investigate the advantages of using the DM signal time information to analyse low-energy threshold data limited by an exponential background (manuscript in preparation). First the DM signal is simulated according to the best-fit parameters for SI-interactions [203] of DAMA/LIBRA data [23, 25]. The statistical frequentist approach, based on Monte Carlo method, shows that in all the cases considered, the timing information does not improve the significance for signal discovery with respect to the one-dimensional (1D) analysis (energy-only). The same result is obtained when a different benchmark for the signal simulation ($m_\chi = 3$ GeV, $\sigma^{SI} = 4 \cdot 10^{-42}$ cm² [33]) is considered. Using these last DM parameters, a similar analysis as in [236] addressing the problem of DM model selection (between the SI and the magnetic dipole DM model) is repeated for low-threshold experiments with an exponential background rate. The conclusion is that, despite of the phenomenology discussed previously when studying the annual modulation with NREFT, the 2D analysis in time and energy does not improve the prospects for model selection for the configurations considered (the largest exposure assumed is 1 kg \times 5 yr). From the results obtained it emerged that low-threshold experiments, even when limited by an exponential background at low energy, but with an exposure between 230 g \times 2 yr and 1 kg \times 5 yr could provide a 90% CL for model selection.

Last but not least, a possible explanation to the experimental observations of the COSINUS experiment [5, 6], related to its detector response, is provided. The empirical second thermal component which was introduced in [37] to obtain a good description of the data, is derived here within a theoretical model describing the detector setup. Such model is obtained as an extension of the general model published in 1995 [36] which successfully describes CRESST-like detectors, while does not accurately fit to COSINUS data. This distinction can be due to peculiar NaI-phonon propagation properties, hypothesis which COSINUS is currently investigating with solid state physics methods, as discussed in the last part of this thesis. A novel method to reconstruct the amount of energy converted in heat in the NaI-absorber, based on the extended pulse shape model, is proposed, to the aim of efficiently identifying nuclear recoil events using TES-thermometers. The EPSM is based on the hypothesis that the carrier crystal absorbs part of the NaI scintillation light. The model has been already applied to COSINUS data and first results prove that it provides a good description of the pulse shape. The ‘proof-of-principle’ of the possible application of the energy reconstruction method has been successfully done. In fact, the LY plot, using the NTD as sensor, allowed to discover the neutron induced events, observation which is in agreement with the neutron induced events identified using the new extended pulse shape model (EPSM).

Appendix A

A.1 Strong CP-violation

The CP violation of the Lagrangian term in Eq. A.1 is shown in the following.

$$L_{\bar{\theta}} = \bar{\theta} \frac{g^2}{32\pi^2} F_a^{\mu\nu} \tilde{F}^{\mu\nu a} \quad (\text{A.1})$$

Consider first the Abelian case. The QED strength tensor and its dual are:

$$\begin{cases} F^{\mu\nu} &= \partial^\mu A^\nu - \partial^\nu A^\mu \\ \tilde{F}^{\mu\nu} &= \frac{1}{2} \epsilon^{\mu\nu\alpha\beta} F_{\alpha\beta} \end{cases} \quad (\text{A.2})$$

Because of the $F^{\mu\nu}$ antisymmetry, only the off-diagonal terms are non-null, with $F^{0i} = -E^i$ and $F^{ij} = -\epsilon^{ijk} B_k$, therefore,

$$\begin{cases} F^{0i} \tilde{F}_{0i} &= (-E^i) (\frac{1}{2} \epsilon_{0ijk} F^{jk}) = -\frac{1}{2} \epsilon_{0ijk} \epsilon^{jkl} (-E^i) B_l = \delta_i^l E^i B_l = \vec{E} \cdot \vec{B} \\ F^{ij} \tilde{F}_{ij} &= (-\epsilon^{ijl} B_l) (\frac{1}{2} \epsilon_{ijk0} F^{k0}) = -\frac{1}{2} \epsilon^{ijl} \epsilon_{ijk0} B_l (E^k) = -\delta_k^l B_l E^k = -\vec{E} \cdot \vec{B} \end{cases} \quad (\text{A.3})$$

where $\epsilon_{0ijk} \epsilon^{jkl} \equiv \epsilon_{ijk} \epsilon^{jkl} = \epsilon_{ijk} \epsilon^{ljk} = 2\delta_i^l$ and,

$$F^{\mu\nu} \tilde{F}^{\mu\nu} = F^{0i} \tilde{F}_{0i} + F^{i0} \tilde{F}_{i0} + F^{ij} \tilde{F}_{ij} = 2\vec{E} \cdot \vec{B} - \vec{E} \cdot \vec{B} = \vec{E} \cdot \vec{B} \quad (\text{A.4})$$

Given Tab. A.1, the scalar product $\vec{E} \cdot \vec{B}$ product is T-odd (or equivalently CP-odd), therefore the associated Lagrangian term is CP violating.

	P	T	C
E	-	+	-
B	+	-	-

Table A.1: Electric and magnetic field discrete-symmetries-eigenvalues.

Now consider the non-Abelian theory:

$$G_a^{\mu\nu} = \partial^\mu A_a^\nu - \partial^\nu A_a^\mu + ig \epsilon_{abc} A^{\mu b} A^{\nu c} \quad (\text{A.5})$$

$$\tilde{G}_a^{\mu\nu} = \epsilon_{\mu\nu\alpha\beta}(\partial^\alpha A_a^\beta - \partial^\beta A_a^\alpha + ig\epsilon_{abc}A^{\alpha b}A^{\beta c}) \quad (\text{A.6})$$

with $G_a^{\mu\nu}$ antisymmetric and only G^{0i} and G^{ij} ($i \neq j$) non-null (similarly for its dual). At the leading order the non-Abelian field theory reduces to the Abelian one, therefore $G^{\mu\nu a}\tilde{G}_{\mu\nu a}$ ($\vec{E}_a \cdot \vec{B}_a$) violates CP as well.

The electric-dipole-moment connection with the strong CP-problem

The Electric Dipole Moment (EDM) is an observable connected with the Lagrangian term in Eq. 2.2. If EDM was observed, it would be a proof of the strong CP-violation. The non-observation of EDM imposes a fine-tuning for the parameter $\bar{\theta}$.

Maxwell's equations are¹,

$$\begin{aligned} \vec{\nabla} \cdot \vec{E} &= \rho \\ \vec{\nabla} \cdot \vec{B} &= 0 \\ \vec{\nabla} \times \vec{E} + \frac{\partial \vec{B}}{\partial t} &= 0 \\ \vec{\nabla} \times \vec{B} - \frac{\partial \vec{E}}{\partial t} &= j \end{aligned} \quad (\text{A.7})$$

where ρ is the electric charge density and $j = \rho v$ is the electric charge current. Maxwell's equation are invariant under discrete symmetries, as evident from Tab. A.2 [274].

	P	T	C
E	-	+	-
B	+	-	-
ρ	+	+	-
j	-	-	-

Table A.2: Discrete symmetries of observables in Maxwell's equations [274]

Dirac's proposed the existence of a 'magnetic charge', on analogy with the electric one. In 1949 Dirac writes "I do not believe there is any need for physical laws to be invariant under reflections in space and time although all the exact laws of nature so far known do have this invariance" [275] and in effect he proposed the modification of second and third Maxwell's equations,

$$\begin{aligned} \vec{\nabla} \cdot \vec{B} &= \rho_m \\ \vec{\nabla} \times \vec{E} + \frac{\partial \vec{B}}{\partial t} &= j_m \end{aligned} \quad (\text{A.8})$$

where ρ_m and j_m would be the magnetic charge density and the magnetic charge current, with $j_m = \rho_m v$. Note that with Dirac's modification, the electric and magnetic

¹This part refers to [273].

parts of Maxwell's equations are completely symmetric. This idea stimulated the search for EDM d_e on analogy with the magnetic dipole moment, that is as result of the rotation of a 'magnetic charge'. The hamiltonian term relative to the electric dipole moment would be,

$$H_e = -\vec{d}_e \cdot \vec{E} \quad (\text{A.9})$$

The hamiltonian term H_e would be invariant under P if d_e changed sign $\vec{d}_e \rightarrow -\vec{d}_e$. However, \vec{d}_e is projected on the angular momentum direction, because in a rotating system all the orthogonal components of vectors average to zero,

$$\vec{d}_e = \alpha \vec{J} \quad (\text{A.10})$$

where α is some constant, and the \vec{J} eigenvalues under discrete symmetries are,

	P	T	C
J	+	-	+

i.e. \vec{J} is a pseudo-vector. This means that parity conservation is violated and time-reversal reflection is similarly violated. Since under T $\vec{J} \rightarrow -\vec{J}$, then $\vec{d}_e \rightarrow -\vec{d}_e$, while $\vec{E} \rightarrow \vec{E}$ as shown in the previous tables. This implies that H_e is not invariant under time-reversal, or equivalently under CP. The relativistic generalisation of Eq. (A.9) is [276],

$$L_{dim=5} = -d_e \frac{i}{2} \bar{\psi} \sigma_{\mu\nu} \gamma_5 \psi F_{\mu\nu} \quad (\text{A.11})$$

where dim=5 stay for the energy dimension of the Lagrangian density, that implies $[d_e] = E^{-1}$. The connection between the parameter $\bar{\theta}$ and the electric dipole moment d_e is approximated by Eq. 2.24 of [276],

$$d_e \sim e \bar{\theta} \frac{m_*}{\Lambda_{had}^2} \quad (\text{A.12})$$

where m_* is the u and d quark reduced mass and $\Lambda_{had} \sim 4\pi f_\pi$, with $f_\pi = 93$ MeV. Using Eq. A.12 and the experimental constraints on the NEDM, the upper limit on the theta parameter is [277],

$$d_e \leq 2.9 \cdot 10^{-26} e \cdot cm \rightarrow |\bar{\theta}| \leq 10^{-10} \quad (\text{A.13})$$

The small value of $|\bar{\theta}|$ is considered a fine-tuning.

A.2 The role of sterile neutrinos in the neutrino mass term

In this appendix we investigate a bit further the role of a sterile neutrino in the neutrino mass term. Since both Dirac and Majorana mass terms will be introduced, few words on the different fermion representations are spent, following the overview given by P. B. Pal in [278].

Fermion representation

A *Dirac spinor* is the linear combination of plane waves whose positive frequency part annihilates $\pm\frac{1}{2}$ -polarised particles and the negative frequency part creates $\pm\frac{1}{2}$ -polarised antiparticles. It is a generic solution of the Dirac equation of motion for fermionic fields. A Dirac field ψ can be always projected into two-component chiral spinors, ψ_R and ψ_L , where R and L stand for right- and left-handed. In the massless limit, these two-component chiral spinors become independent solutions of the Dirac equation of motion. In this limit, they are called *Weyl spinors*. A *Majorana spinor* is a real solution of the Dirac equation. In the *Majorana-representation* of Dirac matrices γ , where all matrices are pure imaginary, a *Majorana-fermion* is defined as $\psi = \psi^*$. Using the important theorem discussed in Appendix A.1 of [1], if we consider any other representation of Dirac matrices, Majorana-fields are identified by the condition $\psi = \gamma_0 C \psi^*$, where C is a unitary matrix (charge conjugation matrix, see Appendix A.2 of [1]).

Both Dirac and Majorana field can be obtained as a combination of Weyl fields. Consider two Weyl fields, ψ_1, ψ_2 , that can be left or right handed, respectively. Dirac and Majorana are massive fields, therefore both chiralities right and left must be present in the combination. The difference between Dirac and Majorana fields is that the first is complex and the second is real. This implies that the Dirac field ψ^D is the combination of two different Weyl fields with different chirality, while the Majorana field ψ^M is the combination of the same Weyl field with different chiralities,

$$\psi^D = \psi_1^W + \hat{\psi}_2^W \quad (\text{A.14})$$

$$\psi^M = \psi_1^W + \hat{\psi}_1^W \quad (\text{A.15})$$

Why neutrinos are massless in the standard model

The mass term for Dirac neutrinos is described by the Lagrangian density [1],

$$\mathcal{L}_D = - \sum_{\ell, \ell'} \left(\overline{\nu_{\ell R}} \mathcal{M}_{\ell\ell'}^D \nu_{\ell' L} + \overline{\nu_{\ell' L}} (\mathcal{M}_{\ell\ell'}^D)^\dagger \nu_{\ell R} \right) \quad (\text{A.16})$$

with,

$$\mathcal{M}^D = V \text{diag}(m_1, m_2, m_3) U^\dagger \quad (\text{A.17})$$

where $\ell, \ell' = e, \mu, \tau$ and $\nu_{\ell' L} = P_L \nu_{\ell'}$ and $\nu_{\ell R} = P_R \nu_{\ell}$ are the projections of the neutrino field in the left- and right-handed subspaces, with $P_{R,L} = (1 \pm \gamma_5)/2$, U is the neutrino mixing matrix and V is another mixing matrix, that concerns only right handed neutrino fields. The mass term for Majorana neutrinos is, instead [1],

$$\mathcal{L}_M = - \frac{1}{2} \sum_{\ell, \ell'} \left(\overline{\nu_{\ell R}^c} \mathcal{M}_{\ell\ell'}^M \nu_{\ell' L} + \overline{\nu_{\ell' L}} (\mathcal{M}_{\ell\ell'}^M)^\dagger \nu_{\ell R}^c \right) \quad (\text{A.18})$$

with,

$$\mathcal{M}^M = U^* \text{diag}(m_1, m_2, m_3) U^\dagger \quad (\text{A.19})$$

where we can define one right-spinor in terms of the left-spinor by using the charge conjugation matrix as follows, $\nu_R^c \equiv C\overline{\nu_L}^t$. From this definition, $\overline{\nu_R^c} = -\nu_L^t C^{-1}$ (see Appendix A.2 of [1]). Note that for Majorana spinors the mixing matrix U and V coincide since right-spinors are built from left-spinors.

From Eqs. A.16 and A.18, it is possible to conclude that within the standard model of particles, the observation of only one neutrino-helicity (left-handed) implies that neutrinos are massless, since

- a Dirac mass term involves two helicities and therefore it requires the introduction of gauge singlet right handed neutrinos;
- a Majorana mass term involves only one helicity at a time, being $\propto \nu_L^t C^{-1} \nu_L$, therefore it would be favoured by observations. However, it violates the $U(1)_Y$ gauge symmetry: left handed neutrinos have $Y = -\frac{1}{2}$ and the Higgs doublet $\phi^T = (\phi^+ \ \phi^0)$ has $Y = \frac{1}{2}$, therefore any Yukawa-like coupling involving only left handed neutrinos produces a lagrangian term with total hypercharge different from zero.

Dirac and Majorana neutrino mass term

Recent results on neutrino oscillations prove that neutrinos are massive, which definitively implies that physics beyond the standard model is required.

Standard neutrinos can acquire a Dirac mass term if coupled to gauge-singlet right handed neutrino ν_R , which instead have a Majorana mass term $\propto \nu_R^t C^{-1} \nu_R$ [103]. In this way, no additional scalar particles are necessary, the only new ingredient would be the right handed neutrino, as shown in the left diagram in Fig. A.2.1. The ‘see-saw mechanism’ known as ‘type I’ is based on this hypothesis [103].

To allow a Majorana mass term through minimal extensions of the standard model, there are two possibilities which at low energies reduce to the non-renormalizable 5-dimensional operator $\frac{C}{\Lambda}(L\phi)(L\phi)$, where C is a dimensionless constant, Λ a large energy scale and ϕ the standard higgs scalar [103]. The diagram of this effective operator is shown in Fig. A.2.1, on the right. Such two possibilities are listed below and are known as ‘type II- and type III-see-saw mechanisms’, respectively,

1. Introduce an extra heavy fermion $SU(2)_L$ triplet with zero hypercharge which couples to the standard higgs. The integration of the heavy triplet at low energy generates the non-renormalizable operator $\frac{C}{\Lambda}(L\phi)(L\phi)$,
2. Introduce a higgs triplet ϕ^T with hypercharge $Y = 1$, such that when it couples to $\nu_L^t C^{-1} \nu_L$ the gauge invariance is restored - see central diagram in Fig. A.2.1.

The effective term $\frac{C}{\Lambda}(L\phi)(L\phi)$ restores the hypercharge conservation involving only

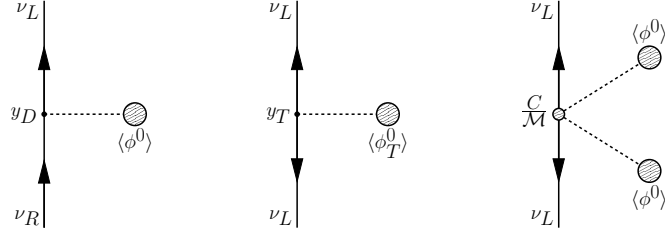


Figure A.2.1: **Left:** Dirac mass term, that involves both neutrino helicities, right (R) and left (L), coupled to the neutral component ϕ^0 of the standard higgs doublet (y_D is the Yukawa coupling). **Center:** Majorana mass term, whose gauge invariance under $U(1)_Y$ is obtained introducing an higgs triplet ϕ^T , coupled to left handed neutrinos (y_T is the Yukawa coupling). **Right:** effective diagram for a Majorana mass term provided by a gauge invariant non renormalizable 5-dimensional operator, in which the two left handed neutrinos are coupled to the neutral components ϕ^0 of two standard higgs doublets (C is a dimensionless constant and M is the large energy scale associated to the unexplored higher energy theory, labeled as Λ in the text.). This figure is taken from [104].

standard model particles² and it provides a Majorana mass term below the electroweak-spontaneous-symmetry-breaking-scale suppressed by the energy scale Λ [103, 104].

Type I see-saw mechanism

‘See-saw mechanism’ is a completion of standard model proposed to explain the hierarchy of mass between neutrinos and other standard model particles. Here as example we discuss type-I see-saw, which introduces sterile neutrinos, ν_R , with a Majorana mass term and involved in the Dirac mass term for standard neutrinos³.

The Dirac-Majorana mass term can be written in compact form using matrix-notation. If one defines a column matrix for left-handed neutrinos [279],

$$N_L = \begin{pmatrix} \nu_L \\ C\bar{\nu}_R^T \end{pmatrix} \quad (\text{A.20})$$

where we consider just one flavor generation for simplicity, the Lagrangian density for Dirac/Majorana (D+M) mass term is,

$$\mathcal{L}_{mass}^{D+M} = \frac{1}{2} N_L^T C^\dagger M N_L + h.c. \quad (\text{A.21})$$

²The Majorana mass terms would violate the lepton number conservation. Since the lepton number is not a gauge quantum number, its violation is admissible.

³This Dirac-Majorana mass term implies that the particle content is enlarged by new particles, whose right handed component is involved in the Dirac mass term. Since these new particles are Majorana-fermions, the total mass term is the sum of (i) Dirac mass term for standard neutrinos, (ii) Majorana mass term for the right-handed-component of sterile neutrinos (iii) Majorana mass term for the left-handed-component of sterile neutrinos.

where \mathcal{M} is the mass-matrix,

$$\mathcal{M} = \begin{pmatrix} m_L & m \\ m & M \end{pmatrix} \quad (\text{A.22})$$

where m is the Dirac mass for standard neutrinos, M is the Majorana mass for the right-handed-component of sterile neutrinos and m_L is the Majorana mass for the left-handed-component of sterile neutrinos. By using Appendix A.2 of [1] it is straightforward to show that Eq. A.21 provides terms with the same structure as the ones in Eqs. A.16 and A.18.

Active-sterile neutrino mixing. Chiral fields are not eigenstates of mass. Since we are interested in a prediction for neutrino mass, we proceed with the diagonalisation process⁴, rotating the neutrino vector in Eq. A.20 of an angle θ . The mass matrix in Eq. A.22 would transform into,

$$O^T \begin{pmatrix} 0 & m \\ m & M \end{pmatrix} O = \begin{pmatrix} M \sin^2\theta + 2m \sin\theta\cos\theta & \frac{M \sin(2\theta)}{2} + m \cos(2\theta) \\ \frac{M \sin(2\theta)}{2} + m \cos(2\theta) & M \cos^2(\theta) - 2m \sin(\theta)\cos(\theta) \end{pmatrix}$$

The off-diagonal terms are null if $\frac{M \sin(2\theta)}{2} + m \cos(2\theta) = 0 \Rightarrow \tan(2\theta) = -2\frac{m}{M}$. Since θ is the mixing angle between standard and sterile neutrinos, which we assume to be small, it is,

$$\theta \approx \frac{m}{M} \quad (\text{A.23})$$

In the $m \ll M$ limit, the mass-matrix is,

$$\begin{pmatrix} -\frac{m^2}{M} & 0 \\ 0 & \sim M \end{pmatrix} \quad (\text{A.24})$$

For a rough estimation, since $m \sim v \sim 100$ GeV as for hypothesis and M is a very large energy scale, *e.g.* $M \sim O(10^{14}$ GeV), the mass of the rotated ‘active’ neutrino, ν_a is,

$$m_a \sim \frac{m^2}{M} \sim 10^{-10}\text{GeV} = 0.1\text{eV}, \quad (\text{A.25})$$

thus of the order of the cosmological experimental limit $\sum_i \nu_{a,i} \lesssim 0.23\text{eV}$ [55]. With this mechanism the hierarchy of mass in the standard model would be explained.

In these conditions, the sterile-neutrino-eigenstate, ν_s , is,

$$\nu_s = -\sin\theta \nu_L + \cos\theta C\bar{\nu}_R^T \approx \frac{m^2}{M}\nu_L + C\bar{\nu}_R^T \quad (\text{A.26})$$

that for $m \ll M$ is purely Majorana-fermion [103]. Under the hypotheses of this section, the active-sterile neutrino mixing in Eq. A.26 opens the important radiative decay channel, $\nu_s \rightarrow \nu_a\gamma$, shown in the Feynman diagrams in Fig. A.2.2, which is relevant for observations. The coupling to the electron and the W boson is made possible by the small left-handed component in the sterile neutrino combination in Eq. A.26.

⁴For a formal treatment see Appendix A of [105].

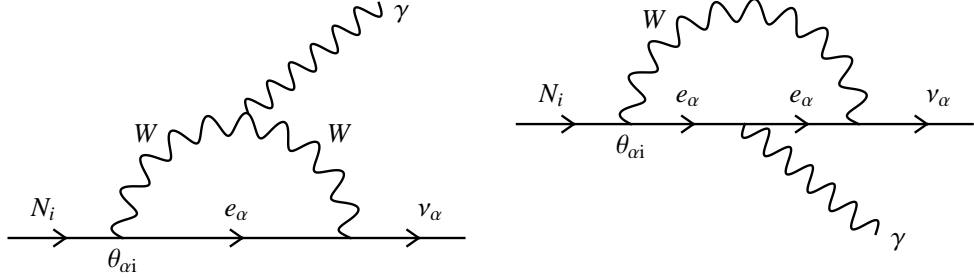


Figure A.2.2: Feynman diagrams of the sterile neutrino radiative decay, allowed by the active-sterile neutrino mixing [105]. N_i and ν on the diagrams correspond to ν_s and ν_α , respectively, in the text.

A.3 SUSY: motivations and consequences

SUPERSymmetry (SUSY) is a mathematical proposal that imagines a symmetry between fermions and bosons [120]. Since SUSY introduces a symmetry between particles with different statistics, it is a more general symmetry group than the Poincarè one⁵. If Q is the supersymmetry generator, such that,

$$Q|\text{fermion}\rangle = |\text{boson}\rangle \quad Q|\text{boson}\rangle = |\text{fermion}\rangle \quad (\text{A.28})$$

the square of the spin generator S^2 cannot be a Casimir for the SUSY group, while P^2 is imposed to be a Casimir adding superpartners for all the elementary particles with the same mass but different statistics. Irreducible multiplets of this extension of the Poincarè group, known as *supermultiplets*, contain fermions and bosons of equal mass.

Hierarchy or naturalness problem. The introduction of superpartners of SM particles degenerate in mass is the SUSY property that solves the tension known as *hierarchy* or *naturalness problem*. It refers to the appearance of quadratic divergences in the radiative corrections of the Higgs mass if an energy scale of new physics exists. Consider

⁵ The Poincarè group counts two Casimir, the length of the Pauli-Lubansky pseudo-vector, W^2 , and the length of the 4-momentum generator, P^2 . The Pauli-Lubansky pseudo-vector is defined as,

$$W_\mu = \frac{1}{2}\epsilon_{\mu\nu\rho\sigma}M^{\nu\rho}P^\mu \equiv \{\mathbf{P} \cdot \mathbf{J}, P_0\mathbf{J} + \mathbf{P} \times \mathbf{K}\} \quad (\text{A.27})$$

where $M^{\nu\rho} = \frac{i}{4}[\gamma^\nu, \gamma^\rho]$ is the rotation generator, P^μ is the spacetime translation generator, J^μ is the total angular momentum generator and \mathbf{K} is the boost generator. For particle with $P^2 = m^2 > 0$, one can define a rest frame such that $\mathbf{P} = 0$ and $W^2 = -m\mathbf{S}^2$, where S is the spin generator. Writing the two Casimir in this way makes clear that elementary particles can be collected according their mass and spin in irreducible multiplets under the Poincarè transformations - irreducible multiplets of the Poincarè group are constituted by the particles with the same mass and spin. Taken from <http://cftp.ist.utl.pt/~gernot.eichmann/2014-hadron-physics/hadron-app-2.pdf>.

the Higgs potential [120],

$$V = m_H^2 |H|^2 + \lambda(|H|)^4 \quad (\text{A.29})$$

where m_H is the Higgs mass and λ is the coupling constant. SM masses are fixed by a unique energy scale, that is the vacuum expectation value of the Higgs field (vev), that is non null if $m_H^2 < 0$ and $\lambda > 0$. The one-loop diagrams involving fermionic or bosonic intermediate states shown in Fig. A.3.1 correct the m_H^2 ,

- The diagram (a) corresponds to the coupling of the Higgs scalar with SM fermion, $-\lambda_f H \bar{f} f$. The radiative correction to m_H^2 is,

$$\Delta m_H^2 = -\frac{|\lambda_f|^2}{8\pi^2} \Lambda_{UV}^2 \quad (\text{A.30})$$

- The diagram (b) corresponds to the coupling of the Higgs scalar to an additional BSM scalar, $-\lambda_S |H|^2 |S|^2$. The radiative correction to the mass would be,

$$\Delta m_H^2 = -\frac{\lambda_S}{16\pi^2} [\Lambda_{UV}^2 - 2m_S^2 \ln(\Lambda_{UV}/m_S) + \dots] \quad (\text{A.31})$$

where m_S is the scalar field mass.

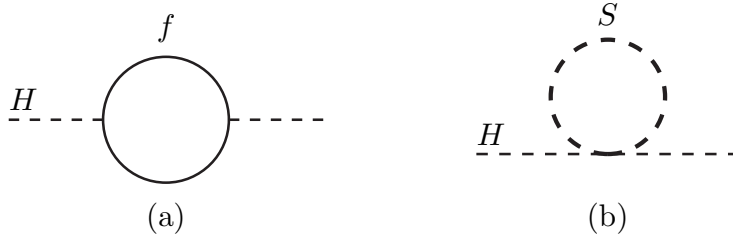


Figure A.3.1: One-loop corrections to the Higgs squared mass m_H^2 due to (a) a fermionic intermediate state and (b) a scalar intermediate state [120]

The quadratic divergence in Eq. A.30 can be reabsorbed by the renormalisation procedure or it can be avoided using the dimensional regularisation. The SM does not present a hierarchical problem. The naturalness problem arises if a physical energy scale BSM is found, such as a heavy scalar field as in Eq. A.31, because in order to provide the cancellation of the term $\propto m_S^2$, fine-tuned conditions are required [120]. In [121] hints for such energy scale BSM are discussed. SUSY succeeds in providing an order by order cancellation of the divergent terms and this is one of the strongest motivations in its favour. The mechanism is based on the existence of superpartners for any SM particles: fermion- and boson-loops have, in fact, opposite signs therefore the mass degeneration combined with the different statistics provide exactly the opposite term for each divergent diagram.

Indeed SUSY does not solve completely the ‘naturalness question’. Taking into account gravity, the complete Lagrangian contains another term, the cosmological constant, Λ , one of the main ingredients of the Λ CDM-model, which we discussed in the first chapter. A specific combination of the cosmological constant with the vacuum energy density is measured to be $\sim 10^{-47}$ GeV⁴, while the vacuum energy density is expected to be $\sim 10^{71}$ GeV⁴, which means that the cosmological constant and the vacuum energy density need a fine-tuning of about 118 decimal numbers. SUSY in its actual shape fails in solving the naturalness problem associated with the cosmological constant [57].

Minimal Supersymmetric Standard Model (MSSM)

The minimal low energy SUSY extension of the SM is known as the Minimal Supersymmetric Standard Model (MSSM). It extends the SM-particle-content introducing superpartners for each SM particle [120, 280]. The notation for superpartners consists in adding the prefix ‘s-’ to fermions to get the bosonic superpartner and the suffix ‘-ino’ to bosons to get the fermionic superpartner, while a tilde is used on top of superpartners symbols. The SUSY-particle content extends the SM with (i) four spin- $\frac{1}{2}$ gauginos, one Bino, \tilde{B} and three Winos, \tilde{W}_i , (ii) a scalar Higgs doublet in addition to the SM Higgs doublet⁶ (iii) the two Higgs doublets spin- $\frac{1}{2}$ superpartners, the higgsinos, $\tilde{H}_{1,2}$ and (iv) scalar superpartners for each SM fermion, squarks and sleptons. The list is shown in Figs. A.3.2 and A.3.3. Despite of the strong motivation for the extension of the SM to right-handed neutrinos, the MSSM does not include them.

Names		spin 0	spin 1/2	$SU(3)_C, SU(2)_L, U(1)_Y$
squarks, quarks ($\times 3$ families)	Q	$(\tilde{u}_L \ \tilde{d}_L)$	$(u_L \ d_L)$	$(\mathbf{3}, \mathbf{2}, \frac{1}{6})$
	\bar{u}	\tilde{u}_R^*	u_R^\dagger	$(\bar{\mathbf{3}}, \mathbf{1}, -\frac{2}{3})$
	\bar{d}	\tilde{d}_R^*	d_R^\dagger	$(\bar{\mathbf{3}}, \mathbf{1}, \frac{1}{3})$
sleptons, leptons ($\times 3$ families)	L	$(\tilde{\nu} \ \tilde{e}_L)$	$(\nu \ e_L)$	$(\mathbf{1}, \mathbf{2}, -\frac{1}{2})$
	\bar{e}	\tilde{e}_R^*	e_R^\dagger	$(\mathbf{1}, \mathbf{1}, 1)$
Higgs, higgsinos	H_u	$(H_u^+ \ H_u^0)$	$(\tilde{H}_u^+ \ \tilde{H}_u^0)$	$(\mathbf{1}, \mathbf{2}, +\frac{1}{2})$
	H_d	$(H_d^0 \ H_d^-)$	$(\tilde{H}_d^0 \ \tilde{H}_d^-)$	$(\mathbf{1}, \mathbf{2}, -\frac{1}{2})$

Figure A.3.2: MSSM spectrum for spin-0 and spin-1/2 matter and Higgs supermultiplets [120].

Soft symmetry breaking. If SUSY-particles had masses equal to their SM-partners, clearly we would have already detected them. In order to comply with the known phenomenology, SUSY is supposed to be a broken symmetry. There is a mechanism widely discussed and applied for the purpose of SUSY symmetry breaking, which is the *soft symmetry breaking* [281]. As for the electroweak theory, SUSY symmetry breaking

⁶MSSM foresees an additional scalar Higgs to not spoil the anomaly cancellations which occurs naturally in the SM.

Names	spin 1/2	spin 1	$SU(3)_C, SU(2)_L, U(1)_Y$
gluino, gluon	\tilde{g}	g	$(\mathbf{8}, \mathbf{1}, 0)$
winos, W bosons	$\tilde{W}^\pm \tilde{W}^0$	$W^\pm W^0$	$(\mathbf{1}, \mathbf{3}, 0)$
bino, B boson	\tilde{B}^0	B^0	$(\mathbf{1}, \mathbf{1}, 0)$

Figure A.3.3: MSSM spectrum for spin-1 and spin-DM1/2 gauge supermultiplets [120].

provides SUSY-particles with masses proportional to a unique mass scale, m_{soft} . This symmetry breaking is said "soft" because it is built ad hoc such that radiative corrections do not spoil the cancellation of potentially dangerous quadratic divergences. However, such mechanism does not provide a prediction of the energy scale of SUSY symmetry breaking [120]. This is the reason of the large arbitrariness in the parameter space, when we talk about supersymmetric DM candidates. Since the main SUSY motivation is the solution of the hierarchy problem, it is used as a guiding principle to decide at which scale to probe SUSY - probably by also making a compromise with experimental sensitivity. However, the numerical value of this corrections is not so relevant because the value of the Higgs bare mass is unknown, therefore SUSY symmetry breaking energy scale is imposed, not derived. In the last decades, m_{soft} was considered to be of $O(\text{TeV})$, to probe an energy scale accessible to experiments.

***R*-parity.** Finally, to consider a supersymmetric DM candidate, it is necessary to introduce an important property, the conservation of *R*-parity. *R*-parity is the discrete symmetry [120],

$$R = (-1)^{3(B-L)+2s} \quad (\text{A.32})$$

where B and L are the baryon and lepton numbers, and s is the spin. For SM particles $R = +1$, while for superpartners $R = -1$. To preserve *R*-parity, SUSY-particles must be always produced in couple. This new discrete symmetry is introduced because the MSSM, although it is the simplest version of SUSY, allows terms that violate the conservation of B and L numbers. This violation is admissible because they are not gauge symmetries, but in these conditions unobserved processes are allowed, such as the proton decay. The *R*-parity conservation is imposed to avoid these processes. From the DM problem point of view, the *R*-parity is the symmetry that allows to isolate SUSY-particles from SM particles, so that the lightest particle of the SUSY-spectrum is stable. The conservation of this additional discrete symmetry imposed by hand is one of the crucial ingredients to obtain supersymmetric DM candidates.

Appendix B

B.1 Gravitational focusing: practical suggestion

The cross-section for direct detection experiments contains the relative velocity between DM and target-nuclei, \mathbf{v}_χ^{det} in our notation. However, the three-dimensional velocity distribution integrals, including the gravitational focusing, can be easily computed with a change of integration variable:

$$\mathbf{v}_\chi^{gal} = \mathbf{v}_\chi^\odot - \mathbf{v}_{gal}^\odot \equiv \mathbf{v}_\chi^\odot + \mathbf{v}_\odot^{gal} \quad (\text{B.1})$$

According to the discussion in Sec. 3.1.2, we decide to integrate over $\mathbf{v}_s \equiv \mathbf{v}_\chi^\odot = \mathbf{v}_\chi^{det} + \mathbf{v}_{det}^\odot$ in spherical coordinates. This implies the two conditions,

$$|\mathbf{v}_s - \mathbf{v}_{det}^\odot| > v_{min}^{det}, \quad (\text{B.2})$$

$$|\mathbf{v}_s + \mathbf{v}_\odot^{gal}| < v_{esc}^{gal} \quad (\text{B.3})$$

The Earth velocity we use here, evaluated considering the corrections due to its orbit eccentricity, follows Eq. B.8 of [18]. The coordinate system we use is the Galactic Coordinate system.

B.2 Elastic scattering kinematics

Consider two reference systems, the laboratory frame (LF) and the center of mass (CM). We indicate with \mathbf{v}_χ^{LF} , \mathbf{v}_T^{LF} , \mathbf{v}_χ^{CM} and \mathbf{v}_T^{CM} the velocity of DM (χ) and of the target (T) in the LF and in the CM, respectively, with \mathbf{v}_{LF}^{CM} the velocity of the LF seen from CM and with $\mathbf{v}_{CM}^{LF} = -\mathbf{v}_{LF}^{CM}$ the velocity of CM seen from LF. With this notation, $\mathbf{v}_{CM}^{LF} = \frac{m_\chi \mathbf{v}_\chi^{LF} + m_T \mathbf{v}_T^{LF}}{m_\chi + m_T}$. We add the prime to all the velocities after diffusion. The galilean transformation from LF to CM is,

$$\begin{cases} \mathbf{v}_\chi^{CM} &= \mathbf{v}_\chi^{LF} + \mathbf{v}_{LF}^{CM} \equiv \mathbf{v}_\chi^{LF} - \mathbf{v}_{CM}^{LF} \\ \mathbf{v}_T^{CM} &= \mathbf{v}_T^{LF} + \mathbf{v}_{LF}^{CM} \equiv \mathbf{v}_T^{LF} - \mathbf{v}_{CM}^{LF} \end{cases} \quad (\text{B.4})$$

Since $\mathbf{v}_\chi^{LF} \neq 0$ and $\mathbf{v}_T^{LF} = 0$,

$$\begin{cases} \mathbf{v}_\chi^{CM} = \frac{m_T}{m_\chi + m_T} \mathbf{v}_\chi^{LF} \\ \mathbf{v}_T^{CM} = -\frac{m_\chi}{m_\chi + m_T} \mathbf{v}_\chi^{LF} \end{cases} \rightarrow \begin{cases} \mathbf{p}_\chi^{CM} = \mu \mathbf{v}_\chi^{LF} \\ \mathbf{p}_T^{CM} = -\mu \mathbf{v}_\chi^{LF} \end{cases} \rightarrow |\mathbf{p}_\chi^{CM}| = |\mathbf{p}_T^{CM}| \quad (\text{B.5})$$

Since in the CM the elastic scattering is a rigid rotation, using the momentum conservation,

$$\mathbf{p}'_T{}^{LF} = \mathbf{p}_\chi^{LF} - \mathbf{p}'_\chi{}^{LF} \equiv \mathbf{p}_\chi^{CM} - \mathbf{p}'_\chi{}^{CM} = |\mathbf{p}_\chi^{CM}|(1 - \cos\theta) = \mu \mathbf{v}_\chi^{LF}(1 - \cos\theta) \quad (\text{B.6})$$

For $\theta = \pi$, $\mathbf{p}'_T{}^{LF} = 2\mu \mathbf{v}_\chi^{LF} \equiv \mathbf{q}_{max}$, where \mathbf{q} is the transferred momentum. Commonly, in literature the label ‘max’ is dropped. The maximum recoil energy for a relative DM-target-velocity in the LF, is, ($c = 1$ and $|\mathbf{v}_\chi^{LF}| = v$),

$$E_{R,max} \equiv \frac{q_{max}^2}{2m_T} = \frac{2\mu^2 v^2}{m_T} \equiv 1 \text{ GeV} \cdot 10^{-6} \cdot 2 \frac{\mu^2}{1 \text{ GeV}^2} \frac{v^2}{(10^{-3})^2} \frac{1 \text{ GeV}}{m_T} \sim \mathcal{O}(\text{keV}) \quad (\text{B.7})$$

The typical recoil energy is $\mathcal{O}(\text{keV})$. For a given energy E_R , the correspondent velocity v in Eq. B.7 is the minimum velocity, v_{min} which can provide a target-recoil of energy E_R . The typical transferred momentum $q_{max} = 2\mu v$ is $\mathcal{O}(1 - 100 \text{ MeV})$, as a function of the DM and target nucleus mass. For instance, assuming $v = 10^{-3} c \equiv 10^{-3}$ in natural units, ($v \approx 300 \text{ km/s}$),

$$\begin{cases} q_{max} = 2 \cdot (100 \text{ GeV}) \cdot (10^{-3}) \approx 200 \text{ MeV}, & m_\chi = m_T = 100 \text{ GeV} \\ q_{max} = 2 \cdot (1 \text{ GeV}) \cdot (10^{-3}) \approx 2 \text{ MeV}, & m_\chi = m_T = 1 \text{ GeV} \\ q_{max} = 2 \cdot (\frac{100}{101} \text{ GeV}) \cdot 10^{-3} \approx 1.98 \text{ MeV}, & m_{\chi(T)} = 1 \text{ GeV}, m_{T(\chi)} = 100 \text{ GeV} \end{cases} \quad (\text{B.8})$$

Appendix C

C.1 NREFT DM-response functions

$$\begin{aligned}
R_M^{\tau\tau'} \left(v_T^{\perp 2}, \frac{q^2}{m_N^2} \right) &= c_1^\tau c_1^{\tau'} + \frac{J_\chi(J_\chi + 1)}{3} \left[\frac{q^2}{m_N^2} v_T^{\perp 2} c_5^\tau c_5^{\tau'} v_T^{\perp 2} c_8^\tau c_8^{\tau'} + \frac{q^2}{m_N^2} c_{11}^\tau c_{11}^{\tau'} \right] \\
R_{\Phi''}^{\tau\tau'} \left(v_T^{\perp 2}, \frac{q^2}{m_N^2} \right) &= \frac{q^2}{4m_N^2} c_3^\tau c_3^{\tau'} + \frac{J_\chi(J_\chi + 1)}{12} \times \left(c_{12}^\tau - \frac{q^2}{m_N^2} c_{15}^\tau \right) \left(c_{12}^{\tau'} - \frac{q^2}{m_N^2} c_{15}^{\tau'} \right) \\
R_{\Phi''M}^{\tau\tau'} \left(v_T^{\perp 2}, \frac{q^2}{m_N^2} \right) &= c_3^\tau c_1^{\tau'} + \frac{J_\chi(J_\chi + 1)}{3} \times \left(c_{12}^\tau - \frac{q^2}{m_N^2} c_{15}^\tau \right) c_{11}^{\tau'} \\
R_{\Phi'}^{\tau\tau'} \left(v_T^{\perp 2}, \frac{q^2}{m_N^2} \right) &= \frac{J_\chi(J_\chi + 1)}{12} \left[c_{12}^\tau c_{12}^{\tau'} + \frac{q^2}{m_N^2} c_{13}^\tau c_{13}^{\tau'} \right] \\
R_{\Sigma''}^{\tau\tau'} \left(v_T^{\perp 2}, \frac{q^2}{m_N^2} \right) &= \frac{q^2}{4m_N^2} c_{10}^\tau c_{10}^{\tau'} + \frac{J_\chi(J_\chi + 1)}{12} \left[c_4^\tau c_4^{\tau'} + \frac{q^2}{m_N^2} (c_4^\tau c_6^{\tau'} + c_6^\tau c_4^{\tau'}) + \frac{q^4}{m_N^4} c_6^\tau c_6^{\tau'} \right. \\
&\quad \left. + v_T^{\perp 2} c_{12}^\tau c_{12}^{\tau'} + \frac{q^2}{m_N^2} v_T^{\perp 2} c_{13}^\tau c_{13}^{\tau'} \right] \\
R_{\Sigma'}^{\tau\tau'} \left(v_T^{\perp 2}, \frac{q^2}{m_N^2} \right) &= \frac{1}{8} \left[\frac{q^2}{m_N^2} v_T^{\perp 2} c_3^\tau c_3^{\tau'} + v_T^{\perp 2} c_7^\tau c_7^{\tau'} \right] + \frac{J_\chi(J_\chi + 1)}{12} \left[c_4^\tau c_4^{\tau'} + \frac{q^2}{m_N^2} c_9^\tau c_9^{\tau'} \right. \\
&\quad \left. + \frac{v_T^{\perp 2}}{2} \left(c_{12}^\tau - \frac{q^2}{m_N^2} c_{15}^\tau \right) \times \left(c_{12}^{\tau'} - \frac{q^2}{m_N^2} c_{15}^{\tau'} \right) + \frac{q^2}{2m_N^2} v_T^{\perp 2} c_{14}^\tau c_{14}^{\tau'} \right] \\
R_\Delta^{\tau\tau'} \left(v_T^{\perp 2}, \frac{q^2}{m_N^2} \right) &= \frac{J_\chi(J_\chi + 1)}{3} \left[\frac{q^2}{m_N^2} c_5^\tau c_5^{\tau'} + c_8^\tau c_8^{\tau'} \right] \\
R_{\Delta\Sigma'}^{\tau\tau'} \left(v_T^{\perp 2}, \frac{q^2}{m_N^2} \right) &= \frac{J_\chi(J_\chi + 1)}{3} \left[c_5^\tau c_4^{\tau'} - c_8^\tau c_9^{\tau'} \right],
\end{aligned} \tag{C.1}$$

C.2 Dark matter magnetic dipole moment

At the relativistic energy scale the interaction is,

$$\mathcal{L}_{MD} = \frac{1}{2} \lambda_\chi \bar{\chi} \sigma^{\mu\nu} \chi F_{\mu\nu} \quad (\text{C.2})$$

where λ_χ is the unknown coupling constant and $F_{\mu\nu} = \partial_\nu A_\mu - \partial_\mu A_\nu$ is the electromagnetic strength tensor. With an integration by parts,

$$\mathcal{L}_{MD} = \frac{1}{2} \lambda_\chi \bar{\chi} \sigma^{\mu\nu} \chi F_{\mu\nu} = -\lambda_\chi J_\nu(x) A^\nu(x) \quad (\text{C.3})$$

with $J^\nu(x) = \lambda_\chi \partial_\mu (\bar{\chi}(x) \sigma^{\mu\nu} \chi(x))$. Note that,

In perturbation theory, the S-matrix element of the underlined interaction is,

$$S_{fi} = \lim_{T \rightarrow \infty(1-\epsilon)} \langle p', k' | \int d^4x \mathcal{H}_I | p, k \rangle_I \quad (\text{C.4})$$

where \mathcal{H}_I and $\langle \rangle_I$ refer to hamiltonian and matrix element in the interaction representation (its evolution is $U^\dagger H_I^S U$ where $U = e^{iH_0 t}$). At the first non trivial order of the theory,

$$S_{fi}^{(1)} = \langle p', k' | \int d^4x \mathcal{H}_I | p, k \rangle_I \quad (\text{C.5})$$

In our case, if λ and k are the nuclear and DM momentum, and we make explicit the time evolution, focusing just on the DM-current, we have,

$$\begin{aligned} \langle p', k' | \int d^4x \mathcal{H}_I | p, k \rangle_I &= \lambda_\chi \langle p', k' | \int d^4x J^\mu(x) A_\mu(x) | p, k \rangle_I = \\ &= \lambda_\chi \int d^4x \langle k' | e^{iH_I t} | e^{iH_0 t} J_0^\mu(x) e^{iH_0 t} | e^{iH_I t} k \rangle \langle p' | A_\mu(x) | p \rangle_I \\ &= \lambda_\chi \int dt e^{i(\epsilon_{k'} - \epsilon_k)t} \int d^3x \langle k' | J_0^\mu(x) | k \rangle \langle p' | A_\mu(x) | p \rangle_I \end{aligned} \quad (\text{C.6})$$

DM current matrix element The matrix element,

$$\begin{aligned} \langle k', s' | J_0^\mu(x) | k, s \rangle &= \langle k', s' | \partial_\mu (\bar{\chi}(x) \sigma^{\mu\nu} \chi(x)) | k, s \rangle = \\ &= \sum_{s', s} \frac{1}{(2\pi)^{\frac{3}{2}}} \frac{1}{(2\pi)^{\frac{3}{2}}} \frac{1}{\sqrt{(2\epsilon_{k'})}} \frac{1}{\sqrt{(2\epsilon_k)}} \bar{u}_{s'}(k') \sigma^{\mu\nu} u_s(k) e^{i(k'-k)x} i(k' - k)_\nu \end{aligned} \quad (\text{C.7})$$

using,

$$\bullet \bar{\chi} = \sum_{\tilde{s}'} \int \frac{d^3 \tilde{k}'}{(2\pi)^{\frac{3}{2}}} \frac{1}{\sqrt{(2\epsilon_{\tilde{k}'})}} a_{\tilde{k}', \tilde{s}'}^\dagger e^{i\tilde{k}'x} \bar{u}_{\tilde{s}'}(\tilde{k}')$$

- $\chi = \sum_{\tilde{s}} \int \frac{d^3\tilde{k}}{(2\pi)^{\frac{3}{2}}} \frac{1}{\sqrt{(2\epsilon_{\tilde{k}})}} a_{\tilde{k},\tilde{s}} e^{-i\tilde{k}x} u_{\tilde{s}}(\tilde{k})$
- $|k, s\rangle = \sqrt{2E_k} a_s^\dagger(k) |0\rangle$, with $\{a_{s'}^\dagger(k'), a_s(k)\} = (2\pi)^3 \delta^{(3)}(k' - k) \delta_{s',s}$
- $u_{s'}^\dagger(k') u_s(k) = 2E_k \delta(k' - k) \delta_{s',s}$
- $\sigma^{\mu\nu} = \frac{i}{2} [\gamma^\mu, \gamma^\nu]$ (the sign in $\sigma^{\mu\nu}$ is irrelevant for our discussion because is over all)

The expression for the fermion DM fields follows from the absence of antiparticles in both the initial and the final state. The normalisation of the spinors follow from the request that $\chi^\dagger \chi$ is normalised to 1.

EM field matrix element Substituting Eq. C.7 in Eq. C.6, we get,

$$\lambda_\chi i(k'-k)_\nu \sum_{s',s} \frac{1}{(2\pi)^3} \frac{1}{\sqrt{(2\epsilon_{k'})}(2\epsilon_k)} \bar{u}_{s'}(k') \sigma^{\mu\nu} u_s(k) \underbrace{\int dt e^{i(\epsilon'_k - \epsilon_k)t} \int d^3x e^{-i\mathbf{q}\cdot\mathbf{x}} \langle p' | A_\mu(x) | p \rangle_I}_{\text{Let us focus on this term, } \int \int \langle A \rangle} \quad (\text{C.8})$$

The equation of motion of the electromagnetic field in external field (the nucleus) is,

$$\square A^\mu(x) = J_{ext}^\mu(x) \quad \rightarrow \quad A^\mu(q) = -\frac{J^\mu(q)}{q^2} \quad (\text{C.9})$$

where we used the Fourier transform in the momentum space. Going back to the coordinate space and substituting in $\int \int \langle A \rangle$,

$$\begin{aligned} \int \int \langle A \rangle &= \int dt e^{i(\epsilon'_k - \epsilon_k)t} \int d^3x e^{-i\mathbf{q}\cdot\mathbf{x}} \langle p' | J_\mu(x) | p \rangle_I \frac{e}{q^2} = \\ &= \int dt e^{i(\epsilon'_k - \epsilon_k)t} \int d^3x e^{-i\mathbf{q}\cdot\mathbf{x}} e^{i(E_{p'} - E_p)t} \langle p' | J_\mu^0(x) | p \rangle \frac{e}{q^2} = \\ &= (2\pi)^3 \delta(\epsilon'_k - \epsilon_k + E_{p'} - E_p) \langle p' | J_\mu^0(q) | p \rangle \frac{e}{q^2} \end{aligned} \quad (\text{C.10})$$

For electrons of momenta p , the EM current for single photon exchange is,

$$\langle p' | J_\mu^0(q) | p \rangle \propto \bar{u}_{r'}(p') \gamma_\mu u_r(p) = \bar{u}_{r'}(p') \left(\frac{(p' + p)_\mu}{2m_N} + i \frac{\sigma_{\mu\nu} q^\nu}{2m_N} \right) u_r(p) \quad (\text{C.11})$$

For the nucleons, considering also the radiative correction to the vertex,

$$\langle p' | J_\mu^0(q) | p \rangle = \bar{u}_{r'}(p') \left(\gamma_\mu F_1(q^2) + i \frac{\sigma_{\mu\nu} q^\nu}{2m_N} F_2(q^2) \right) u_r(p) \quad (\text{C.12})$$

We consider single nucleons, since within the NREFT, the nuclear response is obtained by summing up the DM-nucleon matrix elements over all the nucleons. By substituting Eq. C.7 and Eq. C.10 in Eq. C.6 we obtain,

$$S_{fi}^{(1)} = i\lambda_\chi(2\pi)\delta(\epsilon'_k - \epsilon_k + E_{p'} - E_p) \sum_{s',s} \frac{1}{\sqrt{(4\epsilon_{k'}\epsilon_k)}} q_\nu \bar{u}_{s'}(k') \sigma^{\mu\nu} u_s(k) \langle p' | J_\mu^0(q) | \lambda \rangle \frac{e}{q^2} \quad (\text{C.13})$$

For simplicity we can write,

$$S_{fi}^{(1)} = i(2\pi)\delta(E_{p'} + \epsilon_{k'} - E_p - \epsilon_k) T_{fi} \quad (\text{C.14})$$

In the non-relativistic limit, $k = (m, \mathbf{k})$, $k' = (m, \mathbf{k}')$, and $q^0 = 0$. Using Eqs. (47a-f) of [147] and the following ingredients,

1. Neglect terms $\mathcal{O}(q^2)$,
2. $\mathbf{p}' + \mathbf{p} = 2m_N(\frac{\mathbf{q}}{2m_\chi} - \mathbf{v}^\perp)$,
3. multiply F_1 times Q_N and F_2 times $\mu_N - Q_N$, with $N = p, n$, where $Q_p = 1$ and $Q_n = 0$, and μ_N is the DM-nucleon reduced mass,
4. $S_i^{ss'} = \xi_{s'} \frac{\sigma_i}{2} \xi_s$, with $s, s' = 0, 1$ spin polarisations and $\xi_0 = \begin{pmatrix} 1 \\ 0 \end{pmatrix}$ and $\xi_1 = \begin{pmatrix} 0 \\ 1 \end{pmatrix}$
5. $(\mathbf{a} \times \mathbf{b})(\mathbf{c} \times \mathbf{d}) = (\mathbf{a} \cdot \mathbf{c})(\mathbf{b} \cdot \mathbf{d}) - (\mathbf{a} \cdot \mathbf{b})(\mathbf{c} \cdot \mathbf{d})$
6. $\sqrt{(4\epsilon_{k'}\epsilon_k)} = 2m_\chi$
7. $\mathbf{p}'_N = \mathbf{q}$

we get,

$$T_{fi} \simeq -ie\lambda_\chi \left[\frac{1}{2m_\chi} \langle \mathcal{O}_1 \rangle Q_N + \frac{2m_N}{q^2} \langle \mathcal{O}_5 \rangle Q_N + \frac{2m_N}{q^2} \left(\frac{q^2}{m_N^2} \langle \mathcal{O}_4 \rangle - \langle \mathcal{O}_6 \rangle \right) \mu_N + \mathcal{O}(q^2) \right] \quad (\text{C.15})$$

where we use the classification *building blocks* performed by Haxton et al. [14] and listed in Tab. 4.1. The term proportional to $\langle \mathcal{O}_3 \rangle$ is $\mathcal{O}(q^2)$ therefore we neglect it. The coefficients are,

$$\begin{cases} c_1^N &= \frac{e\lambda_\chi}{2m_\chi} Q_N \\ c_5^N &= \frac{e\lambda_\chi}{q^2} 2m_N Q_N \\ c_4^N &= e\lambda_\chi \frac{2}{m_N} \mu_N \\ c_6^N &= -e\lambda_\chi \frac{2m_N}{q^2} \mu_N \end{cases} \quad (\text{C.16})$$

The NREFT framework provides a straightforward map from the NR transition amplitude to the NR differential cross-section. The final result, reported in Eq. 4.10

$$\begin{aligned} \frac{d\sigma}{dE_R} &= \frac{m_T}{2\pi v^2} \lambda_\chi^2 \alpha \pi \left[\left(\frac{1}{m_\chi^2} - \frac{1}{\mu^2} + \frac{1}{\mu^2} \frac{v^2}{v_{min}^2} \right) \tilde{W}_M^{pp} + \frac{1}{m_N^2} \left(\tilde{\mu}_p^2 \tilde{W}_{\Sigma'}^{pp} + 2\tilde{\mu}_p \tilde{\mu}_n \tilde{W}_{\Sigma'}^{np} + \tilde{\mu}_n^2 \tilde{W}_{\Sigma'}^{nn} + \right. \right. \\ &\quad \left. \left. + 4\tilde{W}_\Delta^{pp} - 4\tilde{\mu}_p \tilde{W}_{\Delta\Sigma'}^{pp} - 4\tilde{\mu}_n \tilde{W}_{\Delta\Sigma'}^{pn} \right) \right] \quad (\text{C.17}) \end{aligned}$$

Appendix D

D.1 Spin-dependent differential rate

The differential number of scattering events on N targets per keV and per second is,

$$\frac{dR}{dE_R} = N \int d\mathbf{v} \phi(\mathbf{v}) \frac{d\sigma}{dE_R} = N \int d\mathbf{v} n v f(\mathbf{v}) \frac{d\sigma}{dE_R} \quad (\text{D.1})$$

where $n = \frac{\rho_\chi}{m_\chi}$ is the number density of DM particles. The differential number of scattering events off 1 kg of detector constituted by nuclei with atomic mass number A , is,

$$\frac{1}{\text{kg}} \frac{dR}{dE_R} = \frac{6.022 \cdot 10^{26}}{A} \frac{\rho_\chi}{m_\chi} \int d\mathbf{v} v f(\mathbf{v}) \frac{d\sigma}{dE_R} \quad (\text{D.2})$$

because the number of diffusors in 1 kg of detector is $N = \frac{6.022 \cdot 10^{26}}{A} \text{kg}^{-1}$. Equation D.2 is usually written as,

$$\frac{dR}{dE_R} = \frac{\rho_\chi}{m_\chi m_T} \int d\mathbf{v} v f(\mathbf{v}) \frac{d\sigma}{dE_R} \quad (\text{D.3})$$

similarly to Eq. 3.9, where m_T is the target mass. The conventional SD differential cross section is, (see Eq. 3.22),

$$\frac{d\sigma_{SD}}{dE_R} = 2m_T \frac{8G_F^2}{(2J_T + 1)v^2} S_A(0) \quad (\text{D.4})$$

If we define,

$$\sigma_0 = 32 \frac{G_F^2}{(2J_T + 1)} \mu_T^2 S_T(0) \quad (\text{D.5})$$

then,

$$\frac{d\sigma_{SD}}{dE_R} = 2m_T \frac{\sigma_0}{4\mu_T^2 v^2} \quad (\text{D.6})$$

The differential rate is,

$$\frac{1}{\text{kg}} \frac{dR}{dE_R} = \frac{6.022 \cdot 10^{26}}{A} \frac{1}{m_\chi} 2m_T \frac{\sigma_0}{4\mu_T^2} \mathcal{I}_{halo} \quad (\text{D.7})$$

where $\mathcal{I}_{halo} = \rho_\chi \eta(v_{min}, t)$ and $\eta(v_{min}, t)$ is defined in Eq. 4.13. Let's write the units,

$$\begin{aligned}
\left[\frac{1}{\text{kg}} \frac{dR}{dE} \right] &= \text{kg}^{-1} \text{keV}^{-1} \text{s}^{-1} = \\
&= \left[\frac{6.022 \cdot 10^{26}}{A} \frac{1}{\text{kg}} \frac{1}{m_\chi} \frac{\sigma_0}{4\mu^2} 2m_T \mathcal{I}_{halo} \right] = \\
&= \frac{6.022 \cdot 10^{26}}{A} \frac{1}{\text{kg}} \frac{1}{\frac{\text{GeV}}{c^2}} \frac{\text{cm}^2}{\frac{\text{GeV}^2}{c^4}} \frac{\text{GeV}}{c^2} \frac{\frac{\text{GeV}}{c^2}}{\text{cm}^3} \frac{1}{\frac{\text{cm}}{\text{s}}} = \\
&= (3 \cdot 10^{10})^2 \frac{6.022 \cdot 10^{26}}{A} \text{s}^{-1} \text{GeV}^{-1} \text{kg}^{-1}
\end{aligned} \tag{D.8}$$

Since $1 \text{ GeV} = 10^6 \text{ keV}$ and $1 \text{ s} = \frac{1}{86400} \text{ day}$, the differential rate units are,

$$\left[\frac{1}{\text{kg}} \frac{dR}{dE} \right] \equiv \underbrace{\left[\frac{dR}{dE} \right]}_{\text{common writing}} = 9 \cdot 10^{20} \frac{6.022 \cdot 10^{26}}{A} (10^{-6}) 86400 [\text{kg} \times \text{day} \times \text{keV}]^{-1} \tag{D.9}$$

The differential rate can be written as,

$$\frac{dR}{dE_R} = \left[\frac{dR}{dE_R} \right] \frac{1}{m_\chi [\text{GeV}]} \frac{\sigma_0 [\text{cm}^2]}{4\mu_T^2 [\text{GeV}^2]} 2m_T [\text{GeV}] \mathcal{I}_{halo} \left[\frac{\text{GeV}}{\text{cm}^3} \frac{\text{cm}}{\text{s}} \right] \tag{D.10}$$

where the units in squared brackets give just the information on the type of numbers to put in each term. Note: If \mathcal{I}_{halo} is computed with velocities in km/s, to use the units in Eq. D.10 an additional factor equal to 10^{-5} must be multiplied to Eq. D.9 ($\text{km}^{-1} = 10^{-5} \text{cm}^{-1}$).

Standard Spin Dependent Expected Rate

The nuclear spin structure function in Eq. 3.25 for low transferred momentum, $q \rightarrow 0$, is (Eq. 3.23),

$$S_T(0) = \frac{(2J_T + 1)(J_T + 1)}{4\pi J_T} \times |(a_0 + a_1)\langle S_p \rangle + (a_0 - a_1)\langle S_n \rangle|^2 \tag{D.11}$$

which applied to nucleons is equal to,

$$S_T^{p/n}(0) = \begin{cases} S_T^p(0) = \frac{(2J_p+1)(J_p+1)}{4\pi J_p} \times |2\langle S_p \rangle|^2 \\ S_T^n(0) = \frac{(2J_T+1)(J_T+1)}{4\pi J_T} \times |2\langle S_n \rangle|^2 \end{cases} \tag{D.12}$$

In Eq. (D.6), σ_0 is,

$$\sigma_0^{SD} = \frac{32G_F^2}{2J_T + 1} \mu_T^2 S_T(0) \tag{D.13}$$

The cross section on single proton or neutron is instead,

$$\sigma_{p/n}^{SD} = \frac{32G_F^2}{2} \mu_{p/n}^2 \frac{(2J_{p/n} + 1)(J_{p/n} + 1)}{4\pi J_{p/n}} \times |2\langle S_{p/n} \rangle|^2 \equiv 32 G_F^2 \mu_{p/n}^2 \frac{3}{4\pi} \times 1 \quad (\text{D.14})$$

If we normalise (D.13) by (D.14), we get,

$$\sigma_0^{SD} = \frac{4\pi}{3} \frac{1}{(2J_T + 1)} \left(\frac{\mu_T}{\mu_{p/n}} \right)^2 S_T(0) \sigma_{p/n}^{SD} \quad (\text{D.15})$$

Using Eq. (D.12), to refer to one nucleon per time, the expected rate is,

$$\frac{dR}{dE_R} = \left[\frac{dR}{dE} \right] \frac{2m_T[\text{GeV}]}{m_\chi[\text{GeV}]} \left(\frac{J_T + 1}{3J_T} \right) \left(\frac{\mu_T}{\mu_{p/n}} \right)^2 (2\langle S_{p/n} \rangle)^2 \frac{\sigma^{p/n}[\text{cm}^2]}{4\mu_T^2[\text{GeV}^2]} \mathcal{I}_{halo} \left[\frac{\text{GeV cm}}{\text{cm}^3 \text{ s}} \right] \quad (\text{D.16})$$

where the units in squared brackets give just the information on the type of numbers to put in each term.

D.2 Analytical derivation of the likelihood ratio

The likelihood function for 2-dimensionally binned-data with expectation ν_{ij} and observed value n_{ij} , where i, j label the time and energy bins, respectively, is,

$$\mathcal{L}(n|\nu) = \prod_{i,j} \frac{(\nu_{ij})^{n_{ij}}}{n_{ij}!} e^{-\nu_{ij}} \quad (\text{D.17})$$

Therefore,

$$\begin{cases} \mathcal{L}(\mathcal{H}_0|s+b) &= \prod_{i,j} \frac{(s+b)_{ij}^{n_{b,ij}}}{n_{b,ij}!} e^{-(s+b)_{ij}} \\ \mathcal{L}(\mathcal{H}_0|b) &= \prod_{i,j} \frac{(b_{ij})^{n_{b,ij}}}{n_{b,ij}!} e^{-b_{ij}} \end{cases} \rightarrow \frac{\mathcal{L}(\mathcal{H}_0|s+b)}{\mathcal{L}(\mathcal{H}_0|b)} = \prod_{i,j} \frac{(s+b)_{ij}^{n_{b,ij}}}{b_{ij}^{n_{b,ij}}} e^{-s_{ij}} \quad (\text{D.18})$$

and finally,

$$q = -2 \log \left(\frac{\mathcal{L}(\mathcal{H}_0|s+b)}{\mathcal{L}(\mathcal{H}_0|b)} \right) = -2 \left(\sum_{i,j} n_{b,ij} \cdot \log \left(1 + \frac{s}{b} \right)_{ij} - s_{ij} \right) \quad (\text{D.19})$$

The likelihood-ratio for data simulated according the alternative-hypothesis has the same structure as Eq. D.19 but with $n_b \leftrightarrow n_{s+b}$. Practically we never use this analytical formula, because we use, instead, the apposite TFitResultPtr function of the ROOT Class TMinuit, which returns the value of the test statistics.

Appendix E

E.1 $^{127}\text{I}(n,\gamma)^{128}\text{I}$ process and following atomic relaxation

The most abundant isotope of iodine is ^{127}I . Its cross section for $^{127}\text{I}(n,\gamma)^{128}\text{I}$ or ^{128}I production, shown in Fig. E.1.1), stimulated deeper investigation on the decay emission of ^{128}I . In the $\text{I}127(n,\gamma)\text{I}128$ neutron capture, prompt- γ s are emitted as a continuous of lines, which cannot be used to tag the following ^{128}I decay.

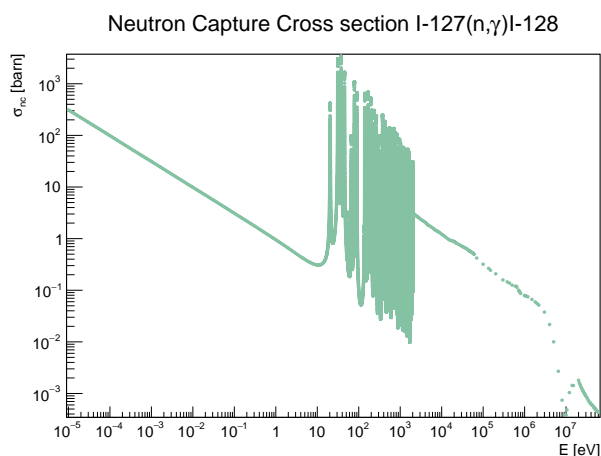
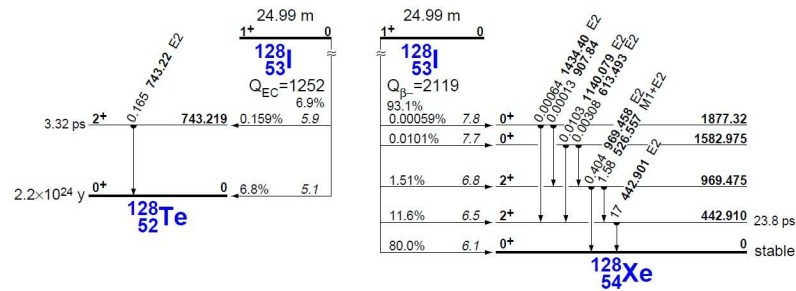


Figure E.1.1: $^{127}\text{I}(n,\gamma)$ or ^{128}I production cross section, taken from <https://www.oecd-neo.org/janisweb/>.

Electron capture in ^{128}I

An excited nucleus has a certain probability to de-excite via the capture of an electron from an atomic shell. A consequence of the electron capture is the conversion of a proton into a neutron (inverse beta decay) and the transmutation of the parent nucleus into the previous one along a period of the table of elements. The daughter nucleus can be produced in the ground state or in the excited state. The following emission depends on this condition.

Figure E.1.2: ^{128}I decay scheme [255]

The decay modes of the isotope ^{128}I is shown in Fig. E.1.2,

The two branches correspond to: electron capture with conversion into ^{128}Te ($\simeq 6.9\%$) and β -decay into ^{128}Xe ($\simeq 93.1\%$), both branches with a half life of 24.99 minutes. The electron is captured from the ^{128}I K-shell (L-shell) with probability $\simeq 84.58\%$ ($12.17(1)\%$) if the final state is the ^{128}Te first excited state, and $\simeq 85.40(2)\%$ ($11.510(2)\%$) if the final state is the ^{128}Te ground state¹. The K-shell intensity is about 7 times larger than the L-shell intensity, being closer to the nucleus.

^{128}I transmutation into ^{128}Te excited or ground state

There is a larger probability that after the electron capture ^{128}I is converted into the ground states of ^{128}Te (intensity $I \simeq 98.3\%$) with respect to the probability of decay into the ^{128}Te excited state ($I \simeq 1.67\%$). Both the excited and the ground states of ^{128}Te are unstable: the more probable (the ground state) has half-life $T_{1/2} = 7.7 \times 10^{24}$ y, the other one has half-life $T_{1/2} = 3.30$ ps. The atomic relaxation from the ground state occurs via X-rays and Auger electron emission. Since the ground state has a long half life, no time-correlation with potential modulating neutron flux is possible. The relaxation from the excited state occurs via the emission of gammas at 743 keV.

^{128}Te ground state atomic relaxation: X-ray and Auger-electron emission

The emission of Auger electrons and X-rays can occur only if the nuclear state is the ground state. The reason is that they are emitted once there is no other way of emitting the energy gained by the electron capture. If the final nuclear state is an excited state, then the emission of a gamma of energy equal to the difference between the two nuclear states or an electron conversion occur.

Auger and X-ray emission are in competition. If one occurs, the other one does not. The sum of K and L line intensities must sum to 6.8%. An observation about the intensities of the K and L shells emission of X-rays and Auger electrons: On the nndc

¹<https://www.nndc.bnl.gov/ensdf/EnsdfDispatcherServlet>

website (<https://www.nndc.bnl.gov>), the page about the ^{128}I ϵ (or also EC)-decay into $^{128}\text{Te}^2$ provides a table of the emission line intensities, separately for X-rays and Auger-electrons, and it shows that the K/L branching ratio for Auger electrons is inverted.

If X-rays and Auger-electrons are emitted in the bulk of a crystal, the total energy detected outside the crystal is likely equal to the the binding energies of the shells involved. The binding energies of ^{128}Te atomic shells are $\simeq 32$ keV and $\simeq 4.3$ keV, for the K and L₃-shells, respectively [255].

²<https://www.nndc.bnl.gov/nudat2/decaysearchdirect.jsp?nuc=128I&unc=nds>

References

- [1] G. Fantini, A. Gallo Rosso, F. Vissani, and V. Zema. Introduction to the Formalism of Neutrino Oscillations. *Adv. Ser. Direct. High Energy Phys.*, 28:37–119, 2018. ix, 1, 136, 137, 139
- [2] R. Catena, K. Fridell, and V. Zema. Direct detection of fermionic and vector dark matter with polarised targets. *JCAP*, 11:018, 2018. ix, 4, 60, 66, 67, 131
- [3] A.H. Abdelhameed et al. First results on sub-GeV spin-dependent dark matter interactions with ${}^7\text{Li}$. *Eur. Phys. J. C*, 79(7):630, 2019. ix, 5, 72, 78, 131
- [4] A.H. Abdelhameed et al. First results from the CRESST-III low-mass dark matter program. *Phys. Rev. D*, 100(10):102002, 2019. ix, 5, 39, 40, 69, 70, 71, 72, 73, 74, 78, 79, 81, 82, 83, 101, 103, 132
- [5] V. Zema. COSINUS: A NaI-based cryogenic calorimeter for direct dark matter search. *Nuovo Cim. C*, 42(5):228, 2020. ix, 5, 99, 132
- [6] G. Angloher et al. COSINUS: Cryogenic Calorimeters for the Direct Dark Matter Search with NaI Crystals. *Journal of Low Temperature Physics*, 2020. ix, 5, 99, 132
- [7] G. Angloher et al. Limits on Dark Matter Effective Field Theory Parameters with CRESST-II. *Eur. Phys. J. C*, 79(1):43, 2019. x, 47
- [8] A.H. Abdelhameed et al. Geant4-based electromagnetic background model for the CRESST dark matter experiment. *Eur. Phys. J. C*, 79(10):881, 2019. [Erratum: *Eur.Phys.J.C* 79, 987 (2019)]. x
- [9] E. Bertoldo et al. Lithium-Containing Crystals for Light Dark Matter Search Experiments. *J. Low Temp. Phys.*, 199(1-2):510–518, 2019. x
- [10] M. Mancuso et al. Searches for Light Dark Matter with the CRESST-III Experiment. *J. Low Temp. Phys.*, 199(1-2):547–555, 2020. x
- [11] H. Kluck et al. Latest results of CRESST-III’s search for sub-GeV/ c^2 dark matter. *J. Phys. Conf. Ser.*, 1468(1):012038, 2020. x

- [12] Filipponi, A. and Profeta, G. and Di Marco, N. and Zema, V. and Schöffner, K. and Reindl, F. and Harfoucheh, M. and Trapananti, A. and Di Cicco, A. Local lattice relaxation around Tl substitutional impurities in a NaI(Tl) scintillator crystal. *Rad. Chem. and Rad. Proc.*, *accepted for publication.* x, 130
- [13] M. Milgrom. A Modification of the Newtonian dynamics as a possible alternative to the hidden mass hypothesis. *Astrophys. J.*, 270:365–370, 1983. 2, 16
- [14] A. Liam Fitzpatrick, Wick Haxton, Emanuel Katz, Nicholas Lubbers, and Yiming Xu. The Effective Field Theory of Dark Matter Direct Detection. *JCAP*, 1302:004, 2013. 3, 43, 45, 46, 47, 48, 50, 51, 92, 95, 131, 150
- [15] JiJi Fan, Matthew Reece, and Lian-Tao Wang. Non-relativistic effective theory of dark matter direct detection. *JCAP*, 11:042, 2010. 3, 36, 43, 46, 48, 50, 131
- [16] A. K. Drukier, Katherine Freese, and D. N. Spergel. Detecting Cold Dark Matter Candidates. *Phys. Rev.*, D33:3495–3508, 1986. 3, 31, 34
- [17] Katherine Freese, Mariangela Lisanti, and Christopher Savage. Colloquium: Annual modulation of dark matter. *Rev. Mod. Phys.*, 85:1561–1581, 2013. 35, 49, 50
- [18] Samuel K. Lee, Mariangela Lisanti, and Benjamin R. Safdi. Dark-Matter Harmonics Beyond Annual Modulation. *JCAP*, 1311:033, 2013. 3, 4, 31, 32, 33, 35, 58, 77, 89, 145
- [19] N. Fornengo and S. Scopel. Temporal distortion of annual modulation at low recoil energies. *Phys. Lett. B*, 576:189–194, 2003. 3
- [20] Evans, N. Wyn and O’Hare, Ciaran A.J. and McCabe, Christopher. Refinement of the standard halo model for dark matter searches in light of the Gaia Sausage. *Phys. Rev. D*, 99(2):023012, 2019. 3, 33
- [21] Eugenio Del Nobile, Graciela B. Gelmini, and Samuel J. Witte. Target dependence of the annual modulation in direct dark matter searches. *Phys. Rev. D*, 91(12):121302, 2015. 4, 49, 51, 55, 57, 59, 131
- [22] Eugenio Del Nobile, Graciela B. Gelmini, and Samuel J. Witte. Prospects for detection of target-dependent annual modulation in direct dark matter searches. *JCAP*, 1602(02):009, 2016. 4, 35, 49, 52, 55, 57, 59, 131
- [23] R. Bernabei et al. First results from DAMA/LIBRA and the combined results with DAMA/NaI. *Eur. Phys. J.*, C56:333–355, 2008. 4, 42, 131, 132
- [24] C. Savage, G. Gelmini, P. Gondolo, and K. Freese. Compatibility of DAMA/LIBRA dark matter detection with other searches. *JCAP*, 04:010, 2009. 40, 42
- [25] R. Bernabei et al. First Model Independent Results from DAMA/LIBRA–Phase2. *Universe*, 4(11):116, 2018. 4, 39, 42, 47, 49, 68, 89, 100, 131, 132

- [26] J. Amar et al. ANAIS-112 status: two years results on annual modulation. *J. Phys. Conf. Ser.*, 1468(1):012014, 2020. 4, 6, 39, 100
- [27] G. Adhikari et al. Search for a Dark Matter-Induced Annual Modulation Signal in NaI(Tl) with the COSINE-100 Experiment. *Phys. Rev. Lett.*, 123(3):031302, 2019. 6, 39, 40, 100
- [28] J. Gascon. Recent results from EDELWEISS Dark Matter searches. *J. Phys. Conf. Ser.*, 1468(1):012018, 2020. 39
- [29] E. Aprile et al. Dark Matter Search Results from a One Ton-Year Exposure of XENON1T. *Phys. Rev. Lett.*, 121(11):111302, 2018. 39, 40, 74
- [30] D.S. Akerib et al. Results from a search for dark matter in the complete LUX exposure. *Phys. Rev. Lett.*, 118(2):021303, 2017. 39, 40, 74
- [31] Xiangyi Cui et al. Dark Matter Results From 54-Ton-Day Exposure of PandaX-II Experiment. *Phys. Rev. Lett.*, 119(18):181302, 2017. 39, 40, 41, 74
- [32] D.S. Akerib et al. Projected WIMP sensitivity of the LUX-ZEPLIN dark matter experiment. *Phys. Rev. D*, 101(5):052002, 2020. 39
- [33] P. Agnes et al. Low-Mass Dark Matter Search with the DarkSide-50 Experiment. *Phys. Rev. Lett.*, 121(8):081307, 2018. 4, 39, 40, 74, 92, 132
- [34] Moqbil S. Alenazi and Paolo Gondolo. Phase-space distribution of unbound dark matter near the Sun. *Phys. Rev.*, D74:083518, 2006. 4, 32, 52
- [35] Chi-Ting Chiang, Marc Kamionkowski, and Gordan Z. Krnjaic. Dark Matter Detection with Polarized Detectors. *Phys. Dark Univ.*, 1:109–115, 2012. 4, 60, 65, 67, 68, 131
- [36] F. Proebst et al. Model for cryogenic particle detectors with superconducting phase transition thermometers. *J. Low. Temp. Phys.*, 100:69–104, 1995. 5, 104, 105, 106, 111, 113, 132
- [37] G. Angloher et al. Results from the first cryogenic NaI detector for the COSINUS project. *JINST*, 12(11):P11007, 2017. 6, 104, 107, 112, 114, 132
- [38] Annise Rivière, Stefano Lepri, Daniele Colognesi, and Francesco Piazza. Wavelet imaging of transient energy localization in nonlinear systems at thermal equilibrium: The case study of nai crystals at high temperature. *Phys. Rev. B*, 99:024307, Jan 2019. 6, 119, 124, 125
- [39] AJ Sievers and S Takeno. Intrinsic localized modes in anharmonic crystals. *Physical Review Letters*, 61(8):970, 1988. 6, 124, 126

- [40] Sinad M. Griffin, Katherine Inzani, Tanner Trickle, Zhengkang Zhang, and Kathryn M. Zurek. Multichannel direct detection of light dark matter: Target comparison. *Phys. Rev. D*, 101(5):055004, 2020. 6
- [41] Fedja Kadribasic, Nader Mirabolfathi, Kai Nordlund, and Flyura Djurabekova. Crystal Defects: A Portal To Dark Matter Detection. 2 2020. 126
- [42] Noah Kurinsky, Daniel Baxter, Yonatan Kahn, and Gordan Krnjaic. A Dark Matter Interpretation of Excesses in Multiple Direct Detection Experiments. 2 2020. 6
- [43] Giulia D’Imperio et al. The SABRE experiment for dark matter search. *PoS, ICHEP2018:653*, 2019. 6, 39, 100
- [44] R. Matthias Geilhufe, Felix Kahlhoefer, and Martin Wolfgang Winkler. Dirac Materials for Sub-MeV Dark Matter Detection: New Targets and Improved Formalism. *Phys. Rev. D*, 101(5):055005, 2020. 6
- [45] Marco Battaglieri et al. US Cosmic Visions: New Ideas in Dark Matter 2017: Community Report. In *U.S. Cosmic Visions: New Ideas in Dark Matter*, 7 2017. 6
- [46] J. Billard, L. Strigari, and E. Figueroa-Feliciano. Implication of neutrino backgrounds on the reach of next generation dark matter direct detection experiments. *Phys. Rev. D*, 89(2):023524, 2014. 6, 40
- [47] Ciaran A.J. O’Hare. Can we overcome the neutrino floor at high masses? 2 2020. 6
- [48] C.E. Aalseth et al. Design and Construction of a New Detector to Measure Ultra-Low Radioactive-Isotope Contamination of Argon. *JINST*, 15(02):P02024, 2020. 6
- [49] Y. Tao et al. Track length measurement of $^{19}\text{F}^+$ ions with the MIMAC Dark Matter directional detector prototype. 3 2019. 6, 39
- [50] J.B.R. Battat et al. Low Threshold Results and Limits from the DRIFT Directional Dark Matter Detector. *Astropart. Phys.*, 91:65–74, 2017. 6, 39
- [51] Kentaro Miuchi, Elisabetta Baracchini, Gregory Lane, Neil J.C. Spooner, and S.E. Vahsen. Cygnus. *J. Phys. Conf. Ser.*, 1468(1):012044, 2020. 6, 39
- [52] Edward W. Kolb and Michael S. Turner. *The Early Universe*, volume 69. 1990. 8, 25, 26
- [53] Giovanni Montani, Marco Valerio Battisti, Riccardo Benini, and Giovanni Imponente. *Primordial cosmology*. World Scientific, Singapore, 2009. 8, 9, 10

- [54] M. Tanabashi et al. Review of Particle Physics. *Phys. Rev.*, D98(3):030001, 2018. 8, 11, 12, 13, 14, 21, 22, 28
- [55] N. Aghanim et al. Planck 2018 results. VI. Cosmological parameters. 2018. 8, 9, 10, 12, 13, 14, 27, 139
- [56] Viatcheslav Mukhanov. *Physical foundations of cosmology*. Cambridge university press, 2005. 9, 11, 13, 14
- [57] Steven Weinberg. The cosmological constant problem. *Reviews of modern physics*, 61(1):1, 1989. 9, 142
- [58] Peter Coles and Francesco Lucchin. *Cosmology: The origin and evolution of cosmic structure*. John Wiley & Sons, 2003. 9
- [59] G. Gamow. Expanding universe and the origin of elements. *Phys. Rev.*, 70:572–573, 1946. 11
- [60] Ralph A. Alpher and Robert C. Herman. On the Relative Abundance of the Elements. *Phys. Rev.*, 74(12):1737–1742, 1948.
- [61] R.A. Alpher, H. Bethe, and G. Gamow. The origin of chemical elements. *Phys. Rev.*, 73:803–804, 1948. 11
- [62] C. Hayashi. Proton-Neutron Concentration Ratio in the Expanding Universe at the Stages preceding the Formation of the Elements. *Prog. Theor. Phys.*, 5(2):224–235, 1950. 11
- [63] Ralph A. Alpher, James W. Follin, and Robert C. Herman. Physical Conditions in the Initial Stages of the Expanding Universe. *Phys. Rev.*, 92:1347–1361, 1953.
- [64] Robert V. Wagoner, William A. Fowler, and Fred Hoyle. On the Synthesis of elements at very high temperatures. *Astrophys. J.*, 148:3–49, 1967. 11
- [65] Richard H Cyburt, Brian D Fields, Keith A Olive, and Tsung-Han Yeh. Big bang nucleosynthesis: Present status. *Reviews of Modern Physics*, 88(1):015004, 2016. 11
- [66] Saul Perlmutter et al. Supernovae, dark energy, and the accelerating universe. *Physics today*, 56(4):53–62, 2003. 14
- [67] Steven Weinberg et al. *Cosmology*. Oxford university press, 2008. 14
- [68] Houjun Mo, Frank Van den Bosch, and Simon White. *Galaxy formation and evolution*. Cambridge University Press, 2010. 14, 24, 30
- [69] Michael Boylan-Kolchin, Volker Springel, Simon D.M. White, Adrian Jenkins, and Gerard Lemson. Resolving Cosmic Structure Formation with the Millennium-II Simulation. *Mon. Not. Roy. Astron. Soc.*, 398:1150, 2009. 15

- [70] Volker Springel, Carlos S. Frenk, and Simon D. M. White. The large-scale structure of the Universe. *Nature*, 440:1137, 2006. 15
- [71] Jess Zavala and Carlos S. Frenk. Dark matter haloes and subhaloes. *Galaxies*, 7(4):81, 2019. 14
- [72] Tommaso Treu. Strong lensing by galaxies. *Annual Review of Astronomy and Astrophysics*, 48:87–125, 2010. 15, 16
- [73] Katherine Freese. Status of dark matter in the universe. *International Journal of Modern Physics D*, 26(06):1730012, 2017. 15
- [74] Gianfranco Bertone. *Particle dark matter: observations, models and searches*. Cambridge University Press, 2010. 15
- [75] Harley Katz et al. Testing feedback-modified dark matter haloes with galaxy rotation curves: estimation of halo parameters and consistency with Λ CDM scaling relations. *Monthly Notices of the Royal Astronomical Society*, 466(2):1648–1668, Dec 2016. 15, 16, 17
- [76] David J Griffiths. Hyperfine splitting in the ground state of hydrogen. *American Journal of physics*, 50(8):698–703, 1982. 15
- [77] Federico Lelli, Stacy S McGaugh, and James M Schombert. Sparc: mass models for 175 disk galaxies with spitzer photometry and accurate rotation curves. *The Astronomical Journal*, 152(6):157, 2016. 16, 17
- [78] Sascha Trippe. The “Missing Mass Problem” in Astronomy and the Need for a Modified Law of Gravity. *Z. Naturforsch.*, A69:173, 2014. 17
- [79] Abbott, B. P. and other (LIGO Scientific Collaboration and Virgo Collaboration). Observation of gravitational waves from a binary black hole merger. *Phys. Rev. Lett.*, 116:061102, Feb 2016. 19
- [80] Miguel Zumalacarregui and Uros Seljak. Limits on stellar-mass compact objects as dark matter from gravitational lensing of type Ia supernovae. *Phys. Rev. Lett.*, 121(14):141101, 2018. 19, 20
- [81] M. Betoule et al. Improved cosmological constraints from a joint analysis of the SDSS-II and SNLS supernova samples. *Astron. Astrophys.*, 568:A22, 2014. 20
- [82] N. Suzuki, D. Rubin, C. Lidman, G. Aldering, R. Amanullah, K. Barbary, L. F. Barrientos, J. Botyanszki, M. Brodwin, N. Connolly, and et al. Thehubble space telescopecluster supernova survey. v. improving the dark-energy constraints abovez_i 1 and building an early-type-hosted supernova sample. *The Astrophysical Journal*, 746(1):85, Jan 2012. 20

- [83] P. Tisserand et al. Limits on the Macho Content of the Galactic Halo from the EROS-2 Survey of the Magellanic Clouds. *Astron. Astrophys.*, 469:387–404, 2007. 20
- [84] Timothy D. Brandt. Constraints on MACHO Dark Matter from Compact Stellar Systems in Ultra-Faint Dwarf Galaxies. *Astrophys. J. Lett.*, 824(2):L31, 2016. 20
- [85] T.S. Li et al. Farthest Neighbor: The Distant Milky Way Satellite Eridanus II. *Astrophys. J.*, 838(1):8, 2017. 20
- [86] Yacine Ali-Hamoud and Marc Kamionkowski. Cosmic microwave background limits on accreting primordial black holes. *Phys. Rev. D*, 95(4):043534, 2017. 20
- [87] Jos Luis Bernal, Nicola Bellomo, Alvise Raccanelli, and Licia Verde. Cosmological implications of Primordial Black Holes. *JCAP*, 10:052, 2017. 20
- [88] Steven Weinberg. A New Light Boson? *Phys. Rev. Lett.*, 40:223–226, 1978. 20, 21
- [89] Frank Wilczek. Problem of Strong P and T Invariance in the Presence of Instantons. *Phys. Rev. Lett.*, 40:279–282, 1978. 20, 21
- [90] R.D. Peccei and Helen R. Quinn. CP Conservation in the Presence of Instantons. *Phys. Rev. Lett.*, 38:1440–1443, 1977. 20, 21
- [91] V Zema. *Comparison between Direct and Indirect Detection of Dark Matter. (Dark matter particles: motivations and observable manifestations, with a focus on the electroweak mass range)*. Master thesis, University of Rome La Sapienza, 2016. 20, 22, 28
- [92] R. D. Peccei. Why PQ? *AIP Conf. Proc.*, 1274(1):7–13, 2010. 20
- [93] Stephen L Adler. Axial-vector vertex in spinor electrodynamics. *Physical Review*, 177(5):2426, 1969. 21
- [94] John S Bell and Roman Jackiw. A PCAC puzzle: $\pi^0 \rightarrow \gamma\gamma$ in the σ -model. *Il Nuovo Cimento A (1965-1970)*, 60(1):47–61, 1969. 21
- [95] R. D. Peccei. QCD, strong CP and axions. *J. Korean Phys. Soc.*, 29:S199–S208, 1996. 21
- [96] R.D. Peccei. The Strong CP problem and axions. *Lect. Notes Phys.*, 741:3–17, 2008. 21
- [97] Gerard 't Hooft. Computation of the Quantum Effects Due to a Four-Dimensional Pseudoparticle. *Phys. Rev. D*, 14:3432–3450, 1976. [Erratum: *Phys.Rev.D* 18, 2199 (1978)]. 21
- [98] Gerard 't Hooft. Symmetry Breaking Through Bell-Jackiw Anomalies. *Phys. Rev. Lett.*, 37:8–11, 1976. 21

- [99] C. A. Baker et al. An Improved experimental limit on the electric dipole moment of the neutron. *Phys. Rev. Lett.*, 97:131801, 2006. 21
- [100] Giovanni Grilli di Cortona, Edward Hardy, Javier Pardo Vega, and Giovanni Villadoro. The QCD axion, precisely. *JHEP*, 01:034, 2016. 21
- [101] Michael S. Turner. Windows on the Axion. *Phys. Rept.*, 197:67–97, 1990. 22
- [102] Rabindra N Mohapatra and Goran Senjanović. Neutrino mass and spontaneous parity nonconservation. *Physical Review Letters*, 44(14):912, 1980. 22
- [103] Alessandro Strumia and Francesco Vissani. Neutrino masses and mixings and... 2006. 22, 23, 137, 138, 139
- [104] Rathin Adhikari, M Agostini, N Anh Ky, T Araki, M Archidiacono, M Bahr, J Baur, J Behrens, F Bezrukov, PS Bhupal Dev, et al. A white paper on keV sterile neutrino dark matter. *Journal of cosmology and astroparticle physics*, 2017(01):025, 2017. 23, 24, 25, 138
- [105] Alexander Merle. keV Neutrino Model Building. *Int. J. Mod. Phys.*, D22:1330020, 2013. 23, 24, 139, 140
- [106] Takehiko Asaka, Steve Blanchet, and Mikhail Shaposhnikov. The ν msm, dark matter and neutrino masses. *Physics Letters B*, 631:151–156, 2005. 23
- [107] Matteo Viel, Julien Lesgourgues, Martin G. Haehnelt, Sabino Matarrese, and Antonio Riotto. Constraining warm dark matter candidates including sterile neutrinos and light gravitinos with WMAP and the Lyman-alpha forest. *Phys. Rev.*, D71:063534, 2005. 24
- [108] Alexander Kusenko, Fuminobu Takahashi, and Tsutomu T Yanagida. Dark matter from split seesaw. *Physics Letters B*, 693(2):144–148, 2010. 24
- [109] Kevork N Abazajian and Alexander Kusenko. Hidden treasures: Sterile neutrinos as dark matter with miraculous abundance, structure formation for different production mechanisms, and a solution to the $\sigma - 8$ problem. *Physical Review D*, 100(10):103513, 2019. 24
- [110] Scott Tremaine and James E. Gunn. Dynamical role of light neutral leptons in cosmology. *Phys. Rev. Lett.*, 42:407–410, Feb 1979. 25
- [111] A. Boyarsky, M. Drewes, T. Lasserre, S. Mertens, and O. Ruchayskiy. Sterile Neutrino Dark Matter. *Prog. Part. Nucl. Phys.*, 104:1–45, 2019. 25
- [112] Yonit Hochberg, Eric Kuflik, Tomer Volansky, and Jay G. Wacker. Mechanism for Thermal Relic Dark Matter of Strongly Interacting Massive Particles. *Phys. Rev. Lett.*, 113:171301, 2014. 25

- [113] Yonit Hochberg, Eric Kuflik, Hitoshi Murayama, Tomer Volansky, and Jay G. Wacker. Model for Thermal Relic Dark Matter of Strongly Interacting Massive Particles. *Phys. Rev. Lett.*, 115(2):021301, 2015. 25
- [114] Gary Steigman, Basudeb Dasgupta, and John F. Beacom. Precise Relic WIMP Abundance and its Impact on Searches for Dark Matter Annihilation. *Phys. Rev.*, D86:023506, 2012. 25, 26, 27
- [115] Robert J Scherrer and Michael S Turner. On the relic, cosmic abundance of stable, weakly interacting massive particles. *Phys. Rev. D*, 33(6):1585, 1986. 26
- [116] Benjamin W Lee and Steven Weinberg. Cosmological lower bound on heavy-neutrino masses. *Physical Review Letters*, 39(4):165, 1977. 27
- [117] Kim Griest and Marc Kamionkowski. Unitarity Limits on the Mass and Radius of Dark Matter Particles. *Phys. Rev. Lett.*, 64:615, 1990. 27
- [118] Maxim Pospelov, Adam Ritz, and Mikhail B. Voloshin. Secluded WIMP Dark Matter. *Phys. Lett. B*, 662:53–61, 2008. 27
- [119] Kyrylo Bondarenko, Alexey Boyarsky, Torsten Bringmann, Marco Hufnagel, Kai Schmidt-Hoberg, and Anastasia Sokolenko. Direct detection and complementary constraints for sub-GeV dark matter. *JHEP*, 20:118, 2020. 27
- [120] Stephen P. Martin. A Supersymmetry primer. pages 1–98, 1997. [Adv. Ser. Direct. High Energy Phys.21,1(2010); Adv. Ser. Direct. High Energy Phys.18,1(1998)]. 28, 140, 141, 142, 143
- [121] Francesco Vissani. Do experiments suggest a hierarchy problem? *Phys. Rev.*, D57:7027–7030, 1998. 28, 141
- [122] Supersymmetric dark matter. *Physics Reports*, 267(5):195 – 373, 1996. 28
- [123] Riccardo Catena and Laura Covi. SUSY dark matter(s). *Eur. Phys. J. C*, 74:2703, 2014. 28
- [124] Giorgio Arcadi, Maíra Dutra, Pradipta Ghosh, Manfred Lindner, Yann Mambrini, Mathias Pierre, Stefano Profumo, and Farinaldo S Queiroz. The waning of the wimp? a review of models, searches, and constraints. *Eur. Phys. J. C*, 78(3):203, 2018. 28
- [125] Julio F Navarro, Carlos S Frenk, and Simon DM White. A universal density profile from hierarchical clustering. *The Astrophysical Journal*, 490(2):493, 1997. 30
- [126] Jaan Einasto. On the construction of a composite model for the galaxy and on the determination of the system of galactic parameters. *Trudy Astrofizicheskogo Instituta Alma-Ata*, 5:87–100, 1965. 30

- [127] Nassim Bozorgnia and Gianfranco Bertone. Implications of hydrodynamical simulations for the interpretation of direct dark matter searches. *Int. J. Mod. Phys.*, A32(21):1730016, 2017. 30, 31
- [128] Nassim Bozorgnia, Francesca Calore, Matthieu Schaller, Mark Lovell, Gianfranco Bertone, Carlos S. Frenk, Robert A. Crain, Julio F. Navarro, Joop Schaye, and Tom Theuns. Simulated Milky Way analogues: implications for dark matter direct searches. *JCAP*, 1605(05):024, 2016. 30
- [129] Nassim Bozorgnia, Francesca Calore, Matthieu Schaller, Mark Lovell, Gianfranco Bertone, Carlos S. Frenk, Robert A. Crain, Julio F. Navarro, Joop Schaye, and Tom Theuns. The Local Dark Matter Distribution from Hydrodynamic Simulations. In *Proceedings, 12th Patras Workshop on Axions, WIMPs and WISPs (PATRAS 2016): Jeju Island, South Korea, June 20-24, 2016*, pages 14–17, 2017. 30
- [130] Antonino Del Popolo, Francesco Pace, Morgan Le Delliou, and Xiguo Lee. Energy transfer from baryons to dark matter as a unified solution to small-scale structure issues of the Λ CDM model. *Phys. Rev. D*, 98(6):063517, 2018. 30
- [131] AGA Brown, A Vallenari, T Prusti, JHJ De Bruijne, C Babusiaux, CAL Bailer-Jones, M Biermann, Dafydd Wyn Evans, L Eyer, Femke Jansen, et al. Gaia data release 2-summary of the contents and survey properties. *Astronomy & astrophysics*, 616:A1, 2018. 31
- [132] Katelin Schutz, Tongyan Lin, Benjamin R Safdi, and Chih-Liang Wu. Constraining a Thin Dark Matter Disk with Gaia. *Phys. Rev. Lett.*, 121(8):081101, 2018. 31
- [133] Lorenzo Posti and Amina Helmi. Mass and shape of the Milky Way’s dark matter halo with globular clusters from Gaia and Hubble. *Astronomy & Astrophysics*, 621:A56, 2019.
- [134] N Wyn Evans, Ciaran AJ O’Hare, and Christopher McCabe. Refinement of the standard halo model for dark matter searches in light of the Gaia Sausage. *Physical Review D*, 99(2):023012, 2019.
- [135] Lina Necib, Mariangela Lisanti, and Vasily Belokurov. Inferred Evidence for Dark Matter Kinematic Substructure with SDSS–Gaia. *The Astrophysical Journal*, 874(1):3, 2019.
- [136] Jatan Buch, Shing Chau John Leung, and JiJi Fan. Using Gaia DR2 to constrain local dark matter density and thin dark disk. *Journal of Cosmology and Astroparticle Physics*, 2019(04):026, 2019.
- [137] Youjia Wu, Katherine Freese, Chris Kelso, Patrick Stengel, and Monica Valluri. Uncertainties in direct dark matter detection in light of Gaia’s escape velocity measurements. *Journal of Cosmology and Astroparticle Physics*, 2019(10):034, 2019.

- [138] O’Hare, Ciaran AJ and Evans, N Wyn and McCabe, Christopher and Myeong, GyuChul and Belokurov, Vasily. Velocity substructure from Gaia and direct searches for dark matter. *Physical Review D*, 101(2):023006, 2020.
- [139] Jatan Buch, JiJi Fan, and John Shing Chau Leung. Implications of the Gaia sausage for dark matter nuclear interactions. *Physical Review D*, 101(6):063026, 2020. 31
- [140] Jonathan D. Sloane, Matthew R. Buckley, Alyson M. Brooks, and Fabio Governato. Assessing Astrophysical Uncertainties in Direct Detection with Galaxy Simulations. *Astrophys. J.*, 831:93, 2016. 31
- [141] Chris Kelso, Christopher Savage, Monica Valluri, Katherine Freese, Gregory S. Stinson, and Jeremy Bailin. The impact of baryons on the direct detection of dark matter. *JCAP*, 1608:071, 2016. 31
- [142] Christopher McCabe. The Earth’s velocity for direct detection experiments. *JCAP*, 02:027, 2014. 31
- [143] Samuel K. Lee, Mariangela Lisanti, Annika H. G. Peter, and Benjamin R. Safdi. Effect of Gravitational Focusing on Annual Modulation in Dark-Matter Direct-Detection Experiments. *Phys. Rev. Lett.*, 112(1):011301, 2014. 32, 52
- [144] A. G. A. Brown, A. Vallenari, T. Prusti, J. H. J. de Bruijne, C. Babusiaux, C. A. L. Bailer-Jones, M. Biermann, D. W. Evans, L. Eyer, and et al. Gaia data release 2. *Astronomy & Astrophysics*, 616:A1, Aug 2018. 33
- [145] Ciaran AJ O’Hare, Christopher McCabe, N Wyn Evans, GyuChul Myeong, and Vasily Belokurov. Dark matter hurricane: Measuring the S1 stream with dark matter detectors. *Physical Review D*, 98(10):103006, 2018. 33
- [146] Francis Halzen and Alan D Martin. *Quark & Leptons: An Introductory Course In Modern Particle Physics*. John Wiley & Sons, 2008. 36
- [147] Marco Cirelli, Eugenio Del Nobile, and Paolo Panci. Tools for model-independent bounds in direct dark matter searches. *JCAP*, 10:019, 2013. 36, 37, 48, 65, 150
- [148] Nikhil Anand, A. Liam Fitzpatrick, and W. C. Haxton. Weakly interacting massive particle-nucleus elastic scattering response. *Phys. Rev.*, C89(6):065501, 2014. 36, 45, 47, 53, 80, 89
- [149] J. Engel, S. Pittel, and P. Vogel. Nuclear physics of dark matter detection. *Int. J. Mod. Phys. E*, 1:1–37, 1992. 36, 38
- [150] Gerard Jungman, Marc Kamionkowski, and Kim Griest. Supersymmetric dark matter. *Phys. Rept.*, 267:195–373, 1996. 36, 37
- [151] Richard H Helm. Inelastic and elastic scattering of 187-mev electrons from selected even-even nuclei. *Physical Review*, 104(5):1466, 1956. 37, 92

- [152] J.D. Lewin and P.F. Smith. Review of mathematics, numerical factors, and corrections for dark matter experiments based on elastic nuclear recoil. *Astropart. Phys.*, 6:87–112, 1996. 37
- [153] Mark W. Goodman and Edward Witten. Detectability of Certain Dark Matter Candidates. *Phys. Rev. D*, 31:3059, 1985. 38
- [154] Rouven Essig, Jeremy Mardon, and Tomer Volansky. Direct Detection of Sub-GeV Dark Matter. *Phys. Rev. D*, 85:076007, 2012. 39
- [155] Marc Schumann. Direct Detection of WIMP Dark Matter: Concepts and Status. *J. Phys. G*, 46(10):103003, 2019. 39, 40, 41
- [156] K. Schaeffner et al. A NaI-Based Cryogenic Scintillating Calorimeter: Results from a COSINUS Prototype Detector. *J. Low. Temp. Phys.*, 193(5-6):1174–1181, 2018. 39, 102, 103
- [157] R. Agnese et al. Results from the Super Cryogenic Dark Matter Search Experiment at Soudan. *Phys. Rev. Lett.*, 120(6):061802, 2018. 39, 40
- [158] R. Agnese et al. Search for Low-Mass Dark Matter with CDMSlite Using a Profile Likelihood Fit. *Phys. Rev. D*, 99(6):062001, 2019. 39, 40
- [159] Q. Arnaud et al. First results from the NEWS-G direct dark matter search experiment at the LSM. *Astropart. Phys.*, 97:54–62, 2018. 39, 74
- [160] R. Ajaj et al. Search for dark matter with a 231-day exposure of liquid argon using DEAP-3600 at SNOLAB. *Phys. Rev. D*, 100(2):022004, 2019. 39, 40
- [161] K. Abe et al. A direct dark matter search in XMASS-I. *Phys. Lett. B*, 789:45–53, 2019. 39
- [162] A. Aguilar-Arevalo et al. Search for low-mass WIMPs in a 0.6 kg day exposure of the DAMIC experiment at SNOLAB. *Phys. Rev. D*, 94(8):082006, 2016. 39, 74
- [163] C. Amole et al. Dark Matter Search Results from the Complete Exposure of the PICO-60 C₃F₈ Bubble Chamber. *Phys. Rev. D*, 100(2):022001, 2019. 39, 41, 78
- [164] E. Behnke et al. Final Results of the PICASSO Dark Matter Search Experiment. *Astropart. Phys.*, 90:85–92, 2017. 39, 41
- [165] AB Migdal. Ionization of atoms accompanying α - and β -decay. *J. Phys.(USSR)*, 4:449, 1941. 39
- [166] Masahiro Ibe, Wakutaka Nakano, Yutaro Shoji, and Kazumine Suzuki. Migdal effect in dark matter direct detection experiments. *Journal of High Energy Physics*, 2018(3):194, 2018. 39

- [167] Chris Kouvaris and Josef Pradler. Probing sub-GeV Dark Matter with conventional detectors. *Phys. Rev. Lett.*, 118(3):031803, 2017. 39
- [168] D.S. Akerib et al. Results of a Search for Sub-GeV Dark Matter Using 2013 LUX Data. *Phys. Rev. Lett.*, 122(13):131301, 2019. 39, 74
- [169] E Aprile, Jelle Aalbers, F Agostini, M Alfonsi, L Althueser, FD Amaro, Vasile C Antochi, E Angelino, F Arneodo, Derek Barge, et al. Search for light dark matter interactions enhanced by the migdal effect or bremsstrahlung in xenon1t. *Physical Review Letters*, 123(24):241803, 2019. 39
- [170] E. Aprile et al. XENON100 Dark Matter Results from a Combination of 477 Live Days. *Phys. Rev. D*, 94(12):122001, 2016. 40, 41
- [171] E. Aprile et al. Constraining the spin-dependent WIMP-nucleon cross sections with XENON1T. *Phys. Rev. Lett.*, 122(14):141301, 2019. 41
- [172] D.S. Akerib et al. Limits on spin-dependent WIMP-nucleon cross section obtained from the complete LUX exposure. *Phys. Rev. Lett.*, 118(25):251302, 2017. 41, 78
- [173] M.G. Aartsen et al. Search for annihilating dark matter in the Sun with 3 years of IceCube data. *Eur. Phys. J. C*, 77(3):146, 2017. [Erratum: *Eur.Phys.J.C* 79, 214 (2019)]. 41
- [174] K. Choi et al. Search for neutrinos from annihilation of captured low-mass dark matter particles in the Sun by Super-Kamiokande. *Phys. Rev. Lett.*, 114(14):141301, 2015. 41
- [175] R. Agnese et al. Low-mass dark matter search with CDMSlite. *Phys. Rev.*, D97(2):022002, 2018. 41, 78
- [176] Z. Ahmed et al. Search for Weakly Interacting Massive Particles with the First Five-Tower Data from the Cryogenic Dark Matter Search at the Soudan Underground Laboratory. *Phys. Rev. Lett.*, 102:011301, 2009. 41
- [177] R. Bernabei et al. The DAMA/LIBRA apparatus. *Nucl. Instrum. Meth.*, A592:297–315, 2008. 42, 99
- [178] R. Bernabei et al. Dark matter search. *Riv. Nuovo Cim.*, 26N1:1–73, 2003. 42
- [179] Enrico Morgante. *Aspects of WIMP Dark Matter searches at colliders and other probes*. PhD thesis, Geneva U., Dept. Theor. Phys., 9 2016. 44
- [180] Jalal Abdallah et al. Simplified Models for Dark Matter Searches at the LHC. *Phys. Dark Univ.*, 9-10:8–23, 2015. 44, 60
- [181] Eugenio Del Nobile. Complete Lorentz-to-Galileo dictionary for direct dark matter detection. *Phys. Rev.*, D98(12):123003, 2018. 45, 48

- [182] Sebastian Baum, Riccardo Catena, Jan Conrad, Katherine Freese, and Martin B. Krauss. Determining dark matter properties with a XENONnT/LZ signal and LHC Run 3 monojet searches. *Phys. Rev. D*, 97(8):083002, 2018. 45, 60, 62, 63, 85
- [183] R. Catena, K. Fridell, and M. B. Krauss. Non-relativistic Effective Interactions of Spin 1 Dark Matter. *JHEP*, 08:030, 2019. 45
- [184] James B. Dent, Lawrence M. Krauss, Jayden L. Newstead, and Subir Sabharwal. General analysis of direct dark matter detection: From microphysics to observational signatures. *Phys. Rev.*, D92(6):063515, 2015. 45, 47, 48, 60, 62, 63
- [185] Walter Greiner and Joachim Reinhardt. *Quantum electrodynamics*. Springer Science & Business Media, 2008. 45
- [186] Riccardo Catena and Bodo Schwabe. Form factors for dark matter capture by the Sun in effective theories. *JCAP*, 04:042, 2015. 46, 47, 48, 53, 57, 89, 95
- [187] K Schneck, B Cabrera, DG Cerdeño, V Mandic, HE Rogers, R Agnese, AJ Anderson, M Asai, D Balakishiyeva, D Barker, et al. Dark matter effective field theory scattering in direct detection experiments. *Physical Review D*, 91(9):092004, 2015. 47
- [188] Elena Aprile, J Aalbers, F Agostini, M Alfonsi, FD Amaro, M Anthony, Francesco Arneodo, P Barrow, L Baudis, Boris Bauermeister, et al. Effective field theory search for high-energy nuclear recoils using the xenon100 dark matter detector. *Physical Review D*, 96(4):042004, 2017. 47
- [189] Riccardo Catena and Paolo Gondolo. Global fits of the dark matter-nucleon effective interactions. *JCAP*, 09:045, 2014. 47, 100
- [190] Vincenzo Cirigliano, Michael L. Graesser, and Grigory Ovanessian. WIMP-nucleus scattering in chiral effective theory. *JHEP*, 10:025, 2012. 48
- [191] P. Klos, J. Menndez, D. Gazit, and A. Schwenk. Large-scale nuclear structure calculations for spin-dependent WIMP scattering with chiral effective field theory currents. *Phys. Rev. D*, 88(8):083516, 2013. [Erratum: Phys.Rev.D 89, 029901 (2014)]. 48
- [192] Martin Hoferichter, Philipp Klos, and Achim Schwenk. Chiral power counting of one- and two-body currents in direct detection of dark matter. *Phys. Lett. B*, 746:410–416, 2015.
- [193] Fady Bishara, Joachim Brod, Benjamin Grinstein, and Jure Zupan. Chiral Effective Theory of Dark Matter Direct Detection. *JCAP*, 02:009, 2017. 48
- [194] Fady Bishara, Joachim Brod, Benjamin Grinstein, and Jure Zupan. From quarks to nucleons in dark matter direct detection. *JHEP*, 11:059, 2017. 48

- [195] Martin Hoferichter, Philipp Klos, Javier Menndez, and Achim Schwenk. Analysis strategies for general spin-independent WIMP-nucleus scattering. *Phys. Rev. D*, 94(6):063505, 2016. 48
- [196] Daniel Gazda, Riccardo Catena, and Christian Forssn. Ab initio nuclear response functions for dark matter searches. *Phys. Rev. D*, 95(10):103011, 2017. 48
- [197] C. Krber, A. Nogga, and J. de Vries. First-principle calculations of Dark Matter scattering off light nuclei. *Phys. Rev. C*, 96(3):035805, 2017.
- [198] Alex Gnech, Michele Viviani, and Laura Elisa Marcucci. Calculation of the ${}^6\text{Li}$ ground state within the hyperspherical harmonic basis. 4 2020. 48, 72, 75
- [199] Francesco D’Eramo, Bradley J Kavanagh, and Paolo Panci. You can hide but you have to run: direct detection with vector mediators. *Journal of High Energy Physics*, 2016(8):111, 2016. 49
- [200] Fady Bishara, Joachim Brod, Benjamin Grinstein, and Jure Zupan. Renormalization Group Effects in Dark Matter Interactions. *JHEP*, 03:089, 2020. 49
- [201] Sebastian Baum, Katherine Freese, and Chris Kelso. Dark Matter implications of DAMA/LIBRA-phase2 results. *Phys. Lett. B*, 789:262–269, 2019. 49, 89
- [202] Felix Kahlhoefer, Florian Reindl, Karoline Schffner, Kai Schmidt-Hoberg, and Sebastian Wild. Model-independent comparison of annual modulation and total rate with direct detection experiments. *JCAP*, 05:074, 2018.
- [203] Sunghyun Kang, Stefano Scopel, Gaurav Tomar, and Jong-Hyun Yoon. DAMA/LIBRA-phase2 in WIMP effective models. *JCAP*, 1807(07):016, 2018. 49, 132
- [204] Xiaoyong Chu, Josef Pradler, and Lukas Semmelrock. Light dark states with electromagnetic form factors. *Phys. Rev. D*, 99(1):015040, 2019. 51
- [205] Jean-Francois Fortin and Tim M.P. Tait. Collider Constraints on Dipole-Interacting Dark Matter. *Phys. Rev. D*, 85:063506, 2012. 51
- [206] Eugenio Del Nobile, Graciela B. Gelmini, Paolo Gondolo, and Ji-Haeng Huh. Direct detection of Light Anapole and Magnetic Dipole DM. *JCAP*, 06:002, 2014. 51
- [207] Chiu Man Ho and Robert J. Scherrer. Anapole Dark Matter. *Phys. Lett. B*, 722:341–346, 2013. 51
- [208] Moira I. Gresham and Kathryn M. Zurek. Effect of nuclear response functions in dark matter direct detection. *Phys. Rev.*, D89(12):123521, 2014. 51

- [209] Tarso Franarin and Malcolm Fairbairn. Reducing the solar neutrino background in dark matter searches using polarized helium-3. *Phys. Rev. D*, 94(5):053004, 2016. 60
- [210] Paolo Gondolo. Recoil momentum spectrum in directional dark matter detectors. *Phys. Rev.*, D66:103513, 2002. 60
- [211] John Betteley Birks. *The theory and practice of scintillation counting: International series of monographs in electronics and instrumentation*, volume 27. Elsevier, 2013. 70, 113
- [212] R.F. Lang et al. Scintillator Non-Proportionality and Gamma Quenching in CaWO₄. 10 2009. 71, 114
- [213] R. Strauss et al. Energy-dependent light quenching in CaWO₄ crystals at mK temperatures. *Eur. Phys. J. C*, 74(7):2957, 2014. 71
- [214] M Mancuso, G Angloher, P Bauer, A Bento, C Bucci, L Canonica, A D’Addabbo, X Defay, A Erb, Franz von Feilitzsch, et al. A low nuclear recoil energy threshold for dark matter search with cressst-iii detectors. *Journal of Low Temperature Physics*, 193(3-4):441–448, 2018. 71, 75
- [215] G. Angloher et al. Results on light dark matter particles with a low-threshold CRESST-II detector. *Eur. Phys. J. C*, 76(1):25, 2016. 72, 74
- [216] G. Angloher et al. Results on MeV-scale dark matter from a gram-scale cryogenic calorimeter operated above ground. *Eur. Phys. J. C*, 77(9):637, 2017. 74, 75
- [217] Q. Yue et al. Limits on light weakly interacting massive particles from the cdex-1 experiment with a *p*-type point-contact germanium detector at the china jinping underground laboratory. *Phys. Rev. D*, 90:091701, Nov 2014. 74
- [218] R. Agnese et al. New Results from the Search for Low-Mass Weakly Interacting Massive Particles with the CDMS Low Ionization Threshold Experiment. *Phys. Rev. Lett.*, 116(7):071301, 2016. 74
- [219] L. Hehn et al. Improved EDELWEISS-III sensitivity for low-mass WIMPs using a profile likelihood approach. *Eur. Phys. J. C*, 76(10):548, 2016. 74
- [220] E. Armengaud et al. Searching for low-mass dark matter particles with a massive Ge bolometer operated above-ground. *Phys. Rev. D*, 99(8):082003, 2019. 74, 78
- [221] R. Agnese et al. Search for Low-Mass Weakly Interacting Massive Particles with SuperCDMS. *Phys. Rev. Lett.*, 112(24):241302, 2014. 74
- [222] C.E. Aalseth et al. CoGeNT: A Search for Low-Mass Dark Matter using *p*-type Point Contact Germanium Detectors. *Phys. Rev. D*, 88:012002, 2013. 74

- [223] E. Aprile et al. Low-mass dark matter search using ionization signals in XENON100. *Phys. Rev. D*, 94(9):092001, 2016. [Erratum: Phys.Rev.D 95, 059901 (2017)]. 74
- [224] Govinda Adhikari et al. An experiment to search for dark-matter interactions using sodium iodide detectors. *Nature*, 564(7734):83–86, 2018. [Erratum: Nature 566, E2 (2019)]. 74
- [225] J.I. Collar. Search for a nonrelativistic component in the spectrum of cosmic rays at Earth. *Phys. Rev. D*, 98(2):023005, 2018. 72, 74, 78
- [226] C. Amole et al. Dark matter search results from the PICO-60 CF₃I bubble chamber. *Phys. Rev. D*, 93(5):052014, 2016. 74
- [227] A. Gtlein et al. Impact of coherent neutrino nucleus scattering on direct dark matter searches based on CaWO₄ crystals. *Astropart. Phys.*, 69:44–49, 2015. 74
- [228] Marat Freytsis and Zoltan Ligeti. On dark matter models with uniquely spin-dependent detection possibilities. *Phys. Rev. D*, 83:115009, 2011. 72
- [229] A.F. Pacheco and D. Strottman. Nuclear Structure Corrections to Estimates of the Spin Dependent WIMP Nucleus Cross-section. *Phys. Rev. D*, 40:2131–2133, 1989. 75
- [230] V. A. Bednyakov and F. Simkovic. Nuclear spin structure in dark matter search: The Zero momentum transfer limit. *Phys. Part. Nucl.*, 36:131–152, 2005. [Fiz. Elem. Chast. Atom. Yadra36,257(2005)]. 75, 77, 79
- [231] Changbo Fu et al. Spin-Dependent Weakly-Interacting-Massive-Particle–Nucleon Cross Section Limits from First Data of PandaX-II Experiment. *Phys. Rev. Lett.*, 118(7):071301, 2017. [Erratum: Phys.Rev.Lett. 120, 049902 (2018)]. 78
- [232] XENON Collaboration, E Aprile, J Aalbers, F Agostini, M Alfonsi, L Althueser, FD Amaro, M Anthony, VC Antochi, F Arneodo, et al. Constraining the spin-dependent wimp-nucleon cross sections with xenon1t. *Physical review letters*, 122(14):141301, 2019. 78
- [233] Torsten Bringmann and Maxim Pospelov. Novel direct detection constraints on light dark matter. *Phys. Rev. Lett.*, 122(17):171801, 2019. 78
- [234] S. Yellin. Finding an upper limit in the presence of an unknown background. *Physical Review D*, 66(3), Aug 2002. 79
- [235] S. Yellin. Extending the optimum interval method, 2007. 79
- [236] Samuel J. Witte, Vera Gluscevic, and Samuel D. McDermott. Prospects for Distinguishing Dark Matter Models Using Annual Modulation. *JCAP*, 1702(02):044, 2017. 80, 94, 96, 132

- [237] A. H. Abdelhameed et al. Description of CRESST-III Data. 2019. 81
- [238] R. Brun and F. Rademakers. ROOT: An object oriented data analysis framework. *Nucl. Instrum. Meth.*, A389:81–86, 1997. 81
- [239] A. L. Robinson, J. H. Underwood, K. J. Kim, J. Kirz, I. Lindau, P. Pianetta, H. Winick, G. Williams, J. H. Scofield, and D. Vaughan. X-ray data booklet, 2009. 83
- [240] Glen Cowan. Statistics for searches at the lhc. In *LHC Phenomenology*, pages 321–355. Springer, 2015. 84
- [241] Sunghyun Kang, Stefano Scopel, Gaurav Tomar, and Jong-Hyun Yoon. Effective models of WIMP Direct Detection in DAMA/LIBRA-phase2. *PoS, ICHEP2018:353*, 2019. 89
- [242] E. Aprile et al. Light Dark Matter Search with Ionization Signals in XENON1T. *Phys. Rev. Lett.*, 123(25):251801, 2019. 93
- [243] E. Aprile et al. Search for Light Dark Matter Interactions Enhanced by the Migdal effect or Bremsstrahlung in XENON1T. *Phys. Rev. Lett.*, 123(24):241803, 2019. 93
- [244] R. Bernabei et al. First results from DAMA/LIBRA-phase2. *Nucl. Part. Phys. Proc.*, 303-305:74–79, 2018. 99
- [245] Franz Pröbst, Matthias Frank, S Cooper, P Colling, D Dummer, P Ferger, G Forster, A Nucciotti, W Seidel, and L Stodolsky. Model for cryogenic particle detectors with superconducting phase transition thermometers. *Journal of low temperature physics*, 100(1-2):69–104, 1995. 99
- [246] Gianfranco Bertone and Dan Hooper. History of dark matter. *Rev. Mod. Phys.*, 90(4):045002, 2018. 99
- [247] R Bernabei, P Belli, F Montecchia, W Di Nicolantonio, A Incicchitti, D Prospero, C Bacci, CJ Dai, LK Ding, HH Kuang, et al. Wimps search by scintillators: possible strategy for annual modulation search with large-mass highly-radiopure nai (ti). *Nuclear Physics B-Proceedings Supplements*, 70(1-3):79–84, 1999. 100
- [248] Paolo Gondolo and Graciela B. Gelmini. Halo independent comparison of direct dark matter detection data. *JCAP*, 12:015, 2012. 100
- [249] Josef Pradler, Balraj Singh, and Itay Yavin. On an unverified nuclear decay and its role in the DAMA experiment. *Phys. Lett. B*, 720:399–404, 2013. 100
- [250] R. Bernabei et al. No role for neutrons, muons and solar neutrinos in the DAMA annual modulation results. *Eur. Phys. J. C*, 74(12):3196, 2014. 100

- [251] Ken-Ichi Fushimi et al. High purity NaI(Tl) scintillator to search for dark matter. *JPS Conf. Proc.*, 11:020003, 2016. 100
- [252] G. Angloher et al. The COSINUS project - perspectives of a NaI scintillating calorimeter for dark matter search. *Eur. Phys. J.*, C76(8):441, 2016. 100
- [253] W. Seidel, G. Forster, W. Christen, F. Von Feilitzsch, H. Gobel, F. Probst, and R.L. Mossbauer. Phase Transition Thermometers With High Temperature Resolution for Calorimetric Particle Detectors Employing Dielectric Absorbers. *Phys. Lett. B*, 236:483–487, 1990. 100
- [254] J. strm et al. Fracture Processes Observed with A Cryogenic Detector. *Phys. Lett. A*, 356:262–266, 2006. 102
- [255] Richard B Firestone and Virginia S Shirley. Table of isotopes, 2 volume set. *Table of Isotopes, 2 Volume Set, by Richard B. Firestone, Virginia S. Shirley (Editor), pp. 3168. ISBN 0-471-33056-6. Wiley-VCH, December 1998.*, page 3168, 1998. 102, 156, 157
- [256] Y. Zhu et al. Production of ultra-low radioactivity NaI(Tl) crystals for Dark Matter detectors. In *2018 IEEE Nuclear Science Symposium and Medical Imaging Conference*, 2018. 103
- [257] Spencer Chang, Rafael F. Lang, and Neal Weiner. Effect of Thallium Impurities in the DAMA Experiment on the Allowed Parameter Space for Inelastic Dark Matter. *Phys. Rev. Lett.*, 106:011301, 2011. 103
- [258] Franco Conti, Paolo Acquistapace, and Anna Savojni. *Analisi matematica-Teoria e applicazioni*. The McGraw-Hill Companies, 2001. 106
- [259] Florian Reindl. *Exploring Light Dark Matter With CRESST-II Low-Threshold Detectors*. PhD thesis, Munich, Tech. U., 2016. 108
- [260] F. A. Danevich et al. Development of radiopure cadmium tungstate crystal scintillators from enriched ^{106}Cd and ^{116}Cd to search for double beta decay. *AIP Conf. Proc.*, 1549(1):201–204, 2013. 108, 109
- [261] Walter G Driscoll and William Vaughan. Handbook of optics. *New York: McGraw-Hill, 1978*, 1978. 109
- [262] Jelena Ninkovic. *Investigation of CaWO_4 Crystals for Simultaneous Phonon-Light Detection in the CRESST Dark Matter Search*. PhD thesis, Technische Universität München, 2005. 108, 109
- [263] Edward Creutz. *Nuclear Instrumentation II/Instrumentelle Hilfsmittel der Kernphysik II*, volume 8. Springer Science & Business Media, 2012. 108, 109
- [264] Neil W Ashcroft, N David Mermin, et al. Solid state physics [by] neil w. ashcroft [and] n. david mermin., 1976. 119, 120, 122, 124, 130

- [265] Peter Debye. Zur theorie der spezifischen wärmen. *Annalen der Physik*, 344(14):789–839, 1912. 119
- [266] David J Griffiths and Darrell F Schroeter. *Introduction to quantum mechanics*. Cambridge University Press, 2018. 119
- [267] Ling Ti Kong. Phonon dispersion measured directly from molecular dynamics simulations. *Computer Physics Communications*, 182(10):2201–2207, 2011. 120, 121
- [268] Kristin Persson. Materials data on uo2 (sg:225) by materials project. 1 2015. 121, 122
- [269] Annise Rivire, Stefano Lepri, Daniele Colognesi, and Francesco Piazza. Wavelet imaging of transient energy localization in nonlinear systems at thermal equilibrium: The case study of NaI crystals at high temperature. *Physical Review B*, 99(2), Jan 2019. 122, 123
- [270] Changyol Lee, David Vanderbilt, Kari Laasonen, Roberto Car, and M Parrinello. Ab initio studies on the structural and dynamical properties of ice. *Physical Review B*, 47(9):4863, 1993. 123
- [271] S. A. Kiselev and A. J. Sievers. Generation of intrinsic vibrational gap modes in three-dimensional ionic crystals. *Phys. Rev. B*, 55:5755–5758, Mar 1997. 124, 126, 129
- [272] D Nevedrov, V Hizhnyakov, and AJ Sievers. Anharmonic gap modes in alkali halides. In *Vibronic Interactions: Jahn-Teller Effect in Crystals and Molecules*, pages 343–347. Springer, 2001. 126
- [273] R Golub and JM Pendlebury. The electric dipole moment of the neutron. *Contemporary Physics*, 13(6):519–558, 1972. 134
- [274] Nicola Cabibbo. Simmetrie discrete. 2008. 134
- [275] Paul AM Dirac. Forms of relativistic dynamics. *Reviews of Modern Physics*, 21(3):392, 1949. 134
- [276] Maxim Pospelov and Adam Ritz. Electric dipole moments as probes of new physics. *Annals of physics*, 318(1):119–169, 2005. 135
- [277] CA Baker, DD Doyle, P Geltenbort, K Green, MGD Van der Grinten, PG Harris, P Iaydjiev, SN Ivanov, DJR May, JM Pendlebury, et al. Improved experimental limit on the electric dipole moment of the neutron. *Phys. Rev. Lett.*, 97(13):131801, 2006. 135
- [278] Palash B Pal. Dirac, majorana, and weyl fermions. *American Journal of Physics*, 79(5):485–498, 2011. 135

- [279] Carlo Giunti and Chung W Kim. *Fundamentals of neutrino physics and astrophysics*. Oxford university press, 2007. 138
- [280] Giorgio Arcadi, Abdelhak Djouadi, and Martti Raidal. Dark matter through the higgs portal. *Physics Reports*, 2019. 142
- [281] Savas Dimopoulos and Howard Georgi. Softly broken supersymmetry and su(5). *Nuclear Physics B*, 193(1):150 – 162, 1981. 142